Résumé

La thèse académique est composée de plusieurs chapitres, présente la synthèse et la caractérisation des matériaux pérovskites de formule générale ABO_3. Les travaux réalisés consistent en des études physico-chimiques. Les transitions de phase structurelles induites par la composition ont été étudiées dans trois systèmes de pérovskites, les informations structurelles ont été collectées et étudiées pour déterminer les conditions de stabilité et de formabilité de la structure. La morphologie et la croissance des grains ont été observées pour tous les matériaux et l'influence de la composition est rapportée. Nous avons également traité la dépendance des propriétés optiques aux paramètres structuraux et leur effet sur les mécanismes de gapping des pérovskites, ainsi que l'effet de la composition sur l'expansion du domaine d'absorption lumineuse. Les propriétés diélectriques des présentes séries ont été étudiées en fonction de la composition, de la température et de la fréquence ; les études visaient principalement à observer l'évolution de la constante diélectrique et des pertes diélectrique. De plus, nous rapportons la conductivité électrique à haute température.

Enfin, nous espérons que nos travaux et recherches fourniront des orientations utiles pour les futures études empiriques et théoriques.

ملخص

حظيت مواد المعروفة بالبيروفسكايت ذات الصيغة العامة ABO_3 باهتمام كبير بسبب مرونتها من حيث البنية والتركيب ، مما سمح للباحثين بضبط أو إحداث خصائص محددة داخل بالمادة. تظهر الأبحاث التي أجريت على البيروفسكايت نتائج واعدة لامتصاص الضوء المرئي. ثبت أيضًا أن الموصلية المختلطة ممكنة عن طريق استبدال التركيبي في الموقع A و / أو الموقع B في البنية ABO_3 ، إلخ. من المعروف أن البيروفسكايت يخضع لتغيرات شتى في تماثل البنية تحت تأثير التركيب أو درجة الحرارة أو الضغط. علاوة على ذلك ، تم الإبلاغ عن أن الخصائص الفيزيائية لهذه الفئة من المواد تعتمد على الهيكل و / أو التركيب ، مثل أنشطة التحفيز الضوئي ، و الطاقة ذات فجوة الحزمة ، إلخ

تتكون الأطروحة الأكاديمية من عدة فصول ، وتقدم توليف وتوصيف مواد البيروفسكايت للصيغة العامة ABO_3. يتكون العمل المنجز من دراسات فيزيائية كيميائية. تمت دراسة انتقالات المرحلة الهيكلية الناتجة عن التركيب في ثلاثة أنظمة بيروفسكايت ، وتم جمع المعلومات الهيكلية ودراستها لتحديد شروط الاستقرار والتشكيل للهيكل. لوحظ نمو ونمو الحبوب لجميع المواد وتم الإبلاغ عن تأثير التركيب. ناقشنا أيضًا اعتماد الخواص الضوئية على المعلمات الهيكلية وتأثيرها على آليات فجوة البيروفسكايت ، بالإضافة إلى تأثير التركيب على توسيع مجال امتصاص الضوء. تمت دراسة الخصائص العازلة للسلسلة الحالية كدالة للتركيب ودرجة الحرارة والتردد ؛ هدفت الدراسات بشكل أساسي إلى مراقبة تطور ثابت العزل وفقد العازل. بالإضافة إلى ذلك نقوم بالإبلاغ عن الموصلية الكهربائية عند درجة حرارة عالية.

أخيرًا ، نأمل أن يوفر عملنا وأبحاثنا إرشادات مفيدة للدراسات التجريبية والنظرية المستقبلية.

N° d'ordre

Prénom et NOM : Fatima EL BACHRAOUI

TITRE: The composition effect on the Structural, Optical, and Dielectric properties of ABO_3-type Perovskite materials

Année: 2021/2022
Initiale Formation doctorale : CAE

Université Hassan 1er
Centre d'Études Doctorales en Sciences et Techniques & Sciences Médicales

Faculté des Sciences et Techniques Settat

THÈSE DE DOCTORAT

Pour l'obtention de grade de Docteur en Chimie

Formation Doctorale: Chimie Appliquée et Environnement

Spécialité: Chimie Physique et Sciences des Matériaux

Sous le thème

The composition effect on the Structural, Optical, and Dielectric properties of ABO_3-type Perovskite materials

Présentée par :

Fatima EL BACHRAOUI

Soutenue le: *04 Février 2022*

A la Faculté des Sciences et Techniques de Settat devant le jury composé de :

Pr. HASNAOUI Abdellatif	**PES**	**USMS Béni Mellal**	Président
Pr. AMINE Khalil	**PES**	**ANL Chicago**	Rapporteur
Pr. SHAO Minhua	**PES**	**HKUST Hong Kong**	Rapporteur
Pr. FAHLI Ahmed	**PES**	**FST Settat**	Rapporteur
Pr. BIH Lahcen	**PES**	**UMI ENSAM Meknès**	Examinateur
Pr. ALAMI Jones	**PES**	**UM6P Benguérir**	Examinateur
Pr. TAMRAOUI Youssef	**PESA**	**UM6P Benguerir**	Invité
Pr. MANOUN Bouchaib	**PES**	**FST Settat**	Directeur de thèse

Année Universitaire: 2021/2022

Dedicated to

My parents "Khadija and Mohammed"

My sister "Choumicha"

My brothers "Ayoub and Abderrazak"

To all my dear friends

Preface

The research project presented in this thesis was carried out at Materials Science, Energy and Nano-engineering Department (MSN) – Mohammed VI Polytechnic University (UM6P), Benguerir, Morocco, in collaboration with the laboratory of Rayonnement-Matière et Instrumentation, S3M – Faculty of Science and Technology, University Hassan 1st, Settat, Morocco.

The research project described herein was conducted from 2017 to 2021 under the supervision of **Mr. Bouchaib MANOUN**, Full professor at the Faculty of Science and Technology, Hassan First University in Settat, and Adjunct Professor at Materials Science, Energy and Nano-engineering Department (MSN), and **Mr. Youssef TAMRAOUI**, Assistant professor at Materials Science, Energy and Nano-engineering Department (MSN).

The present work is based on experimental results obtained by using the structure of three research units:

- Laboratory of Rayonnement-Matière et Instrumentation, S3M – Faculty of Science and Technology, University Hassan 1st, Settat, Morocco. The carried tasks were the synthesis and characterizations of the studied materials
- Materials Science, Energy and Nano-engineering Department (MSN) – Mohammed VI Polytechnic University (UM6P), Benguerir, Morocco. The carried tasks were the synthesis and characterizations of the studied materials.
- Laboratoire des Sciences et Métiers de l'Ingénieur (LSMI), Département Matériaux et Procédés, ENSAM Meknès, Moulay Ismail University, Meknès, Morocco. The measurements carried are the dielectric and electric properties of perovskite materials.

This work has been presented as publications in international scientific journals and communications in national and international conferences.

Acknowledgement

In the Name of Allah who is Kind and Great Merciful

All prayers go to Allah; throughout my life I have felt and seen the countless blessings of Allah in every moment of my life, Allah has gifted me with peace and happiness and for that I am very grateful.

Foremost, I would like to pay respect and gratitude and express my sincere appreciations to my **supervisor Prof. Bouchaib MANOUN**, Full professor at the Faculty of Science and Technology, Hassan First University, Settat, and Adjunct Professor at Materials Science, Energy and Nano-engineering Department (MSN), and my **co-supervisor Prof. Youssef TAMRAOUI**, assistant professor at Materials Science, Energy and Nano-engineering Department (MSN), UM6P, Benguerir, for their generous support, advices, patience , time, encouragement and especially for their help to shape and reshape this work. They shared their knowledge and expertise and guided me throughout my doctoral studies and for that I am very grateful. It was an honor working under your supervision.

All my acknowledgements and deepest appreciation to the members of my dissertation committee, firstly for **Prof. Jones ALAMI**, Head of Materials Science, Energy and Nano-engineering Department (MSN), UM6P, Benguerir, for accepting to be the examination board's president of my thesis defense. For **Prof. Khalil AMIN** from Argonne National Laboratory, Chemical Sciences and Engineering Division, Illinois, USA, **Prof. Minhua SHAO** at Hong Kong University of Science and Technology, Shenzhen Research Institute, Hong Kong, And **Prof. FAHLI Ahmed** at Hassan First University, Settat, Morocco, for having agreed to report this thesis. Also a special thanks to **Prof. Lahcen BIH** at Université My Ismail, ENSAM, Meknès, Maroc, and **Prof. Abdelilah LAHMAR** Université de Picardie Jules Verne, France for accepting to examine my thesis work.

I own my deepest gratitude and respect to **Prof. Jones ALAMI**, Head of Materials Science, Energy and Nano-engineering Department (MSN), UM6P, Benguerir, for accepting me as a member of MSN department and giving me the opportunity to work under his direction. These four years of hard work have been fueled by his encouragements, support, and valuable advices that I will always remember. I sure have learnt so much from you, in direct and indirect way. For your trust on me, I would like to say, thank you very much.

I cannot express enough thanks to my mentor **Mrs. Siham ABAICHI**, Program Officer of Research and Education, very beautiful soul, for her patience, advices, the good vibes, and for her time listening to me. You were a source of positive energy and for that I am very lucky and grateful. Thank you very much.

I would like to extend my sincere thanks to all **MSN Department members**, Ph.D. students, Post-docs, Professors, and MSN-staff for being nice, cheerful and helpful, believe me it matters a lot.

I gratefully acknowledge **Prof. Lahcen BIH,** Professor at Faculty of Science, Moulay Ismail University, Meknès for his warm welcoming during my stay at "Laboratoire des Sciences et Métiers de l'Ingénieur (LSMI), Département Matériaux et Procédés, ENSAM Meknès" to carry the dielectric measurements. **Prof. Lahcen BIH** has not only gave me access to all the equipment that I needed during my stay, but also his precious time to discuss all the results and to guide me with his knowledge. I honestly enjoyed the scientific discussion and the in depth shared thoughts about science and development.

Thanks should also go to all my dear friends, **Miguel**, **Youssef**, **Meriam (s)**, and **Salim** to whom I am thankful for being proud of me, their support, encouragement, and the good moments and how patiently they were waiting for my graduation. Special thanks go to my good dear friend **Zineb KASSAB**, in this four year we shared a lot of unforgettable moments that I will cherish in my heart; your company had made my journey fun and joyful.

Finally, to my **parents** to whom I am forever indebted, there are no words that can express how grateful and proud I am that you are my parents, I learnt from you how to be kind, free, happy, and strong and how to never give up. To my sister **Choumicha**, thank you for caring and supporting everyone in you special way. To my brother **Ayoub** thank you for your kindness, for the funny moments. To my brother **Abderrazak**, thank you for the love. I would not be who I am today without your support.

Description by chapter

This chapter is organized in five chapters.

Chapter I is dedicated to gather the necessary information to understand the context of the research work and highlight the most important feature of the perovskite structure. Information concerning the condition of the formability and stability and the importance of the tolerance factor to determine the point of transition and or the degree of the distortion is treated. This chapter covers also the main properties of perovskites which will be treated in details in the following chapters. The reported mechanisms of gapping were reported as well as the dielectric properties of perovskite materials. Updates on the most treated applications of perovskites in the field of clean energy production are reported as well.

Chapter II presents the methodology used to carry the researches of this project. This chapter describes the synthesis method used to prepare three solid solutions ABO_3 type perovskites namely, $Ba_{1-x}La_xTi_{1-x}Fe_xO_3$, $Sr_{1-x}La_xTi_{1-x}Fe_xO_3$; $Ba_{1-x}Sr_xTi_{1-x}Fe_xO_{3-\delta}$ with the substitution amount varies between $0 \leq x \leq 1$. This chapter also describes the various experimental techniques used to investigate the structural and physical properties of the materials.

Chapter III discusses the effect of the composition on the structure formation, stability and phase transitions occurring. The structural investigations were carried out using Rietveld refinement technique, the visualization of the unit cell of the structure was performed using Vesta software. The evolution as function of the composition is treated for the unit cell parameter, and the unit cell volume. The tolerance factor evolution is used to investigate the stability of the structure and confirm the point of the phase transitions and the symmetry. Structural data were collected from the results obtained such as the bond angles B-O_1-B and B-O_2-B and the interatomic distances <B-O> and <A-O>.

Chapter IV treats the effect of the composition on the absorption of the materials under Uv-visible light. The chapter also treats the point of view of literature on the effect of the structure parameters mainly the B-O-B on the opening mechanisms of the band gap and the performance of the materials in terms of visible light harvesting. A part of this chapter is dedicated to discover other structural parameters governing the opening of the band gap, also to determine the position of the conduction band minimum and the valence band maximum.

Chapter V reports on the dielectric properties of the three series studied in this work. The effect of the composition on the electrical properties is discussed in details. The determination of the equivalent circuits gives insight on the conduction mechanism of the prepared materials. The evolution of the conduction as function of the composition is reported.

Résumé

Au cours des dernières années, due à l'augmentation de la consommation d'énergie, les matériaux de structure perovskite se sont placées au cœur de tous les type de recherches scientifique dans le domaine des énergies renouvelables. Les activités de recherche se sont accentuées récemment autour l'utilisation des matériaux perovskite comme des cathodes pour les piles à combustible (SOFCs), dans le domaine de la production d'hydrogène et comme des photocatalyst. La structure perovskite de type ABO_3 est connue par sa grande flexibilité structurale qui permet au matériau d'accueillir un grand nombre des éléments du tableau périodique. Ces caractéristiques permettent aux chercheurs d'ajuster ou d'induire des propriétés spécifiques dans la structure ABO_3 des pérovskites.

Dans ce travail, trois séries avec la formule générale $A_{(1-x)}A'_xTi_{(1-x)}Fe_xO_{3-\delta}$ (A = Ba, Sr, or La) avec $0 \leq x \leq 1$ et $\delta \geq 0$ ont été synthétisés par réaction à l'état solide à des températures élevée. L'effet de la composition sur l'évolution de la structure, la morphologie, les propriétés optique, diélectrique et électrique ont été évaluées.

- BLTF, SLTF, BSTF désignent respectivement les séries $Ba_{(1-x)}La_xTi_{(1-x)}Fe_xO_3$, $Sr_{(1-x)}La_xTi_{(1-x)}Fe_xO_3$, et $Ba_{(1-x)}Sr_xTi_{(1-x)}Fe_xO_{3-\delta}$

L'étude de l'effet de la composition dans les systèmes BLTF, SLTF et BSTF sur la structure a été réalisée par diffraction des rayons X, les diffractogrammes de la diffraction de rayons X ont été collectés à température ambiante et étudiés à l'aide de la méthode d'affinement de Rietveld. Les résultats ont montré que le system subit plusieurs transitions de phase, ceci est observé dans les trois system étudiés dans ce travail. Deux transitions de phase, Tétragonal → Cubique → Orthorhombique dans le système BLTF; une transition de la phase Cubique à Orthorhombique pour le système SLTF, et une transition de structure Tétragonal à Cubique dans le cas de BSTF. La stabilité de la structure est également été étudiée en termes de variation du facteur de tolérance en fonction de la composition et en fonction des distances interatomiques.

La morphologie des échantillons a été analysée à l'aide de la microscopie électronique à balayage; les résultats montrent que la variation de la composition a affecté la taille et la forme des particules ainsi que la porosité.

L'étude des propriétés optique par la spectroscopie UV-Vis montre l'effet positif sur l'amélioration de l'absorption de la lumière visible. L'effet de la composition ou la substitution a induit un décalage vers le domaine du visible du spectre, et a aussi créé de nouvelles bandes d'absorption. Les valeurs de la bande interdite estimées montrent une diminution avec l'augmentation du pourcentage de substitution dans les trois system BLTF, SLTF et BSTF. Ce comportement est dû à la création de nouveaux niveaux d'énergie qui ont également induit un décalage des bords de la bande interdite vers des positions plus adaptées. Les observations montrent que l'évolution de la band interdite est liée aux distances interatomiques <A-O> et <B-O>.

Les études diélectrique et électrique des matériaux préparés BLTF, SLTF, et BSTF ont été réalisé par la spectroscopie complexe d'impédance. L'objective est d'illustrer l'effet de la composition sur l'évolution thermique de la permittivité, les résultats montrent une diminution de la valeur de la permittivité diélectrique pour les trois cas d'étude. Sous l'effet de la température, une augmentation de la conductivité a été notée, en outre, sous l'effet de la composition l'évolution de la conductivité totale peut être classée comme suit : SLTF (x = 0.8) > BLTF (x = 0.6) > BSTF (x = 0.8), avec des valeurs estimées de l'ordre de 10^{-5} ($S.m^{-1}$), 10^{-6} ($S.m^{-1}$) and 10^{-7} ($S.m^{-1}$) respectivement. A température ambiante, SLTF séries présente des caractéristiques de conductivité prometteuses par rapport au BLTF et au BSTF séries.

Mot clés *: perovskite de type ABO_3, la double substitution, absorption de la lumière UV-visible, le minimum de la band de conduction, le maximum de la band de valence, permittivité diélectrique, transition de phase, la conductivité en fonction de température.*

ملخص

حظيت مواد المعروفة بالبيروفسكايت ذات الصيغة العامة ABO_3 باهتمام كبير بسبب مرونتها من حيث البنية والتركيب ، مما سمح للباحثين بضبط أو إحداث خصائص محددة داخل بالمادة. تظهر الأبحاث التي أجريت على البيروفسكايت نتائج واعدة لامتصاص الضوء المرئي. ثبت أيضًا أن الموصلية المختلطة ممكنة عن طريق استبدال التركيبي في الموقع A و / أو الموقع B في البنية ABO_3 ، إلخ. من المعروف أن البيروفسكايت يخضع لتغيرات شتى في تماثل البنية تحت تأثير التركيب أو درجة الحرارة أو الضغط. علاوة على ذلك ، تم الإبلاغ عن أن الخصائص الفيزيائية لهذه الفئة من المواد تعتمد على الهيكل و / أو التركيب ، مثل أنشطة التحفيز الضوئي ، و الطاقة ذات فجوة الحزمة ، إلخ.

في هذا التقرير ، نظام البيروفسكايت (A = Ba, Sr, La) $A_{(1-x)}A'_xTi_{(1-x)}Fe_xO_{3-\delta}$ مع $0 \leq x \leq 1$ and $\delta \geq 0$

تم تحضير المواد المدروسة في هذا العمل عبر تفاعل الكيميائي في الحالة الصلبة عند درجة حرارة عالية. تم دراسة تأثير التركيبة على التركيب و البنية والخصائص الفيزيائية. المواد المعدة هي: $Sr_{(1-x)}La_xTi_{(1-x)}Fe_xO_3$, $Ba_{(1-x)}L_xTi_{(1-x)}Fe_xO_3$, $Ba_{(1-x)}Sr_xTi_{(1-x)}Fe_xO_{3-\delta}$, والملقبة على التوالي بـ BLTF ، SLTF ، BSTF.

تم إجراء دراسة على تأثير التركيب على بنية BLTF و SLTF و BSTF بواسطة حيود الأشعة السينية. تم جمع نتائج الأشعة السينية في درجة حرارة الغرفة وفحصها باستخدام طريقة Rietveld للصقل. فيما يتعلق باختلاف التركيبات ومقدار الاستبدال ، لوحظت عدة انتقالات طور في المواد المدروسة وهي BLTF و SLTF و BSTF. انتقالات بين بنيتين من، رباعي الزوايا ← مكعب ← معينية مستقيمة بالنسبة ل BLTF؛ مرحلة واحدة من الانتقال من مكعب إلى معينية مستقيمة لنظام SLTF ، وانتقال من رباعي الزوايا إلى هيكل مكعب في حالة BSTF. تتم دراسة استقرار البنية أيضًا من حيث تباين عامل التسامح كدالة للتكون البنية. تم تحليل مورفولوجيا العينات باستخدام المجهر الإلكتروني الماسح. أظهرت النتائج أن التركيبة قد أثرت على حجم وشكل الجزيئات وكذلك المسامية.

أظهرت الخصائص البصرية التي تم فحصها عن طريق التحليل الطيفي للأشعة المرئية وفوق البنفسجية أن التركيبة قد أحدثت انزياحًا أحمر في نطاق الامتصاص وتعزيز امتصاص الضوء المرئي. تُظهر قيم فرقة فجوة الطاقة المقدرة انكماشًا في قيمة فرقة فجوة الطاقة الناتجة عن التركيبة. يرتبط تطور فجوة الطاقة بالمسافة بين الذرات <A-O> و <B-O> ؛ أدى إنشاء مستويات طاقة جديدة أيضًا إلى حدوث تحول في حواف فجوة الطاقة إلى أوضاع أكثر ملاءمة.

أظهرت دراسات الخواص العازلة والكهربائية أن هذه التركيبات قللت من سماحية العازل بشكل عام ، بينما تعزز موصلية المواد. يُلاحظ أن الموصلية تزداد مع زيادة درجة الحرارة لجميع التركيبات ويتم تقديمها بالترتيب التالي SLTF (x = 0.8)> BLTF (x = 0.6)> BSTF (x = 0.8)) ، للقيم التالية بالترتيب 5^{-10} (($S.m^{-1}$، $S.m^{-1}$) 10^{-6}) و 7^{-10} ($S.m^{-1}$) على التوالي. يُظهر SLTF ميزات موصلية واعدة في درجة حرارة الغرفة مقارنةً بـ BLTF و BSTF.

Abstract

Perovskite materials with the general formula ABO_3 have received considerable attention due to their flexibility in terms of structure and composition, which allowed researchers to tune or induce specific properties within the structure. The researches on perovskites show promising results on the visible light absorption; also mixed conductivity is proven to be possible by substituting the A-site and/or the B-site of the ABO_3 structure, etc. The perovskites are known to undergo various phase transitions under the effect of the composition, temperature or pressure. Moreover, it is reported that the physical properties of this class of materials depend on the structure and/or the composition, such as the order of transitions, the photocatalytic activities, and the band gap, etc.

In this report, the perovskite system $A_{(1-x)}A'_xTi_{(1-x)}Fe_xO_{3-\delta}$ (A = Ba, Sr, or La) with $0 \leq x \leq 1$ and $\delta \geq 0$, was prepared via the conventional solid state reaction at high temperature. The effect of the composition on the structure, morphology and physical properties are investigated. The prepared solid solutions are:

- $Ba_{(1-x)}La_xTi_{(1-x)}Fe_xO_3$, $Sr_{(1-x)}La_xTi_{(1-x)}Fe_xO_3$, and $Ba_{(1-x)}Sr_xTi_{(1-x)}Fe_xO_{3-\delta}$, labeled respectively as BLTF, SLTF, BSTF respectively.

The study of the composition effect on the structure of BLTF, SLTF and BSTF was carried out by the X-ray diffraction. The X-ray patterns were collected at room temperature and investigated by means of Rietveld refinement method. With regards to the variation of the compositions and the amount of the substitution several phase transitions were observed in the prepared solid solution namely BLTF, SLTF, and BSTF. Two phase transitions, Tetragonal → Cubic → orthorhombic for the BLTF systems; one phase transition from cubic to orthorhombic for SLTF system, and tetragonal to cubic structure transition in the case of BSTF. The stability of the structure is also studied in terms of the tolerance factor variation as function of the composition and as function of the interatomic distances.

The morphology of the samples was analyzed using the scanning electron microscopy; the results show that the composition has affected the size and the shape of the particles as well as the porosity.

The optical properties investigated by means of UV-Vis spectroscopy showed that the composition has induced a red shift of the absorption band and an enhancement of the visible light absorption. The estimated band gap values show a shrink of the band gap value induced by the composition. The evolution of the band gap is linked with the values of the interatomic distance <A-O> and <B-O>; the creation of new energy levels also induced a shift of the band gap edges to more suitable positions.

The dielectric and electric properties investigations have showed that these combinations reduce the dielectric permittivity in general, while enhances the conductivity of the materials. The conductivity is seen to increase with temperature for all the compositions and it is presented in the follow order SLTF (x = 0.8) > BLTF (x = 0.6) > BSTF (x = 0.8), for values in the order of 10^{-5} ($S.m^{-1}$), 10^{-6} ($S.m^{-1}$) and 10^{-7} ($S.m^{-1}$) respectively. The SLTF shows promising conductivity features at room temperature in comparison with BLTF and BSTF.

Keywords: *ABO_3 perovskites, Co-substitution, UV-visible light absorption, Conduction band minimum, Valence band maximum, Band gap, Dielectric permittivity, Phase transition, Conductivity as function of temperature*.

Abbreviation

E_b: breakdown electric field

W_{rec}: energy storage density

W_{loss}: loss energy density

E_g: band gap

ε: dielectric constant

CTE: coefficient of thermal expansion

IT-SOFCs: intermediate temperature solid oxide fuel cells

TPB: Triple phase boundary

SOFC: solid oxide fuel cell

P_r: Remanent polarization of ferroelectrics

SG: space group

XRD: X-Ray Diffraction patterns

SEM: Scanning electron microscopy

BLTF: $Ba_{1-x}La_xTi_{1-x}Fe_xO_3$

SLTF: $Sr_{1-x}La_xTi_{1-x}Fe_xO_3$

BSTF: $Ba_{1-x}Sr_xTi_{1-x}Fe_xO_{3-\delta}$

UV-Vis: Ultra violet to visible light

K-M: Kubelka Munk function

VBM: Valence Band Maximum

CBM: Conduction Band Minimum

R_g: Grain resistance

R_{gb}: Grain boundary resistance

CHAPTER I

State of the Art

LIST OF FIGURES

LIST OF TABLES

CHAPTER II

Experimental Details: Synthesis and Characterizations

LIST OF TABLES

CHAPTER III

Investigation of the composition effect on the structure and morphology in the solid solution systems $A_{(1-x)}A'_xTi_{(1-x)}Fe_xO_{3-\delta}$ (A = Ba, Sr, or La) with $0 \leq x \leq 1$ and $\delta \geq 0$: Rietveld refinement method studies

Part I: Investigation of the composition effect on the structure in the $Ba_{1-x}La_xTi_{1-x}Fe_xO_3$ $0 \leq x \leq 1$ perovskite system

LIST OF FIGURES

LIST OF TABLES

LIST OF FIGURES

LIST OF TABLES

CHAPTER IV

Effect of the composition and structure on the UV-Visible absorption and the band gap of the solid solution system $A A_{(1-x)}A'_{x}Ti_{(1-x)}Fe_{x}O_{3-\delta}$ (A = Ba, Sr, or La) with $0 \leq x \leq 1$ and $\delta \geq 0$

Part I: Investigation of the composition and structure effects on the optical properties of $Ba_{1-x}La_xTi_{1-x}Fe_xO_3$ perovskite system with $0 \leq x \leq 1$

LIST OF FIGURES

LIST OF TABLES

Part II: Investigation of the composition and structure effects on the optical properties of $Sr_{1-x}La_xTi_{1-x}Fe_xO_3$ perovskite system with $0 \leq x \leq 1$

LIST OF FIGURES

LIST OF TABLES

Part III: Investigation of the composition and the structure effects on the optical properties of $Ba_{1-x}Sr_xTi_{1-x}Fe_xO_{3-\delta}$ perovskite system with $0 \leq x \leq 1$

LIST OF FIGURES

LIST OF TABLES

CHAPTER V

Dielectric and electric studies at room and high temperature as function of the frequency of the solid solution system $A_{(1-x)}A'_xTi_{(1-x)}Fe_xO_{3-\delta}$ for (a= ba, la and sr) with $0 \leq x \leq 1$ & $\delta \geq 0$

Part I: The study of the dielectric and electric properties of the perovskite series $Ba_{1-x}La_xTi_{1-x}Fe_xO_3$ with $0 \leq x \leq 1$ at room and high temperature in a wide range of frequency

LIST OF FIGURES

LIST OF TABLES

Part II: The study of the dielectric and electric properties of the perovskite series $Sr_{1-x}La_xTi_{1-x}Fe_xO_3$ with $0 \leq x \leq 1$ at room and high temperature in a wide range of frequency

LIST OF FIGURES

LIST OF TABLES

Part III: The study of the dielectric and electric properties of the perovskite series $Ba_{1-x}Sr_xTi_{1-x}Fe_xO_{3-\delta}$ with $0 \leq x \leq 1$ at room and high temperature in a wide range of frequency

LIST OF TABLES

LIST OF FIGURES

Acknowledgement

Description by chapter

Summary

Résumé

Abbreviation

TABLE OF CONTENT

CHAPTER III

INVESTIGATION OF THE COMPOSITION EFFECT ON THE STRUCTURE AND MORPHOLOGY IN THE SOLID SOLUTION SYSTEM $A_{(1-x)}A'_xTi_{(1-x)}Fe_xO_{3-\delta}$ FOR (A= Ba, La AND Sr) WITH $0 \leq x \leq 1$ & $\delta \geq 0$: RIETVELD REFINEMENT METHOD STUDIES

CHAPTER IV

EFFECT OF THE COMPOSITION AND STRUCTURE ON THE UV-VISIBLE ABSORPTION AND THE BAND GAP OF THE SOLID SOLUTION SYSTEM $A_{(1-x)}A'_xTi_{(1-x)}Fe_xO_{3-\delta}$ FOR (A= Ba, La AND Sr) WITH $0 \leq x \leq 1$ & $\delta \geq 0$

CHAPTER V

DIELECTRIC AND ELECTRIC STUDIES AT ROOM AND HIGH TEMPERATURE AS FUNCTION OF THE FREQUENCY OF THE SOLID SOLUTION SYSTEM $A_{(1-x)}A'_xTi_{(1-x)}Fe_xO_{3-\delta}$ FOR (A= Ba, La AND Sr) WITH $0 \leq x \leq 1$ & $\delta \geq 0$

Chapter -I

State of the Art

I.1. Introduction: Journey of perovskite discovery, brief narration

The discovery of the mineral perovskite belongs to a journey of 15000 km with the objective of enlarging the geological, biological and geographical knowledge of the Russian region. Gustav Rose, the geology and mineralogy expert has examined unknown crystals suspected as new minerals, which confirmed later on that the crystals belong to a new mineral that is composed of calcium and titanium oxides [1,2]. The mineral was reported to adopt cubic symmetry, and then named after the well-known aristocrat and mineral collector Count Lev Alekseevich Von Perovskiy [1,2]. It was until 1844 where Heinrich the brother of Gustav Rose has analyzed and determined the exact chemical composition $CaTiO_3$. The journey of the discovery and establishment of the perovskite mineral crystal structure has lasted more than 60 years; the mystery was resolved at the beginning of the 19th century by Böggild [3]. Böggild has critically reviewed all the previous data with his work and reported an orthorhombic structure for $CaTiO_3$ [3,4].

Soon afterward, the discovery of X- ray diffraction has provided researchers with the necessary tool for a direct investigation of the structure of crystals. Discussions between different researchers have aroused again to answer the real structure of perovskite [5]. In the mid of 1940s, Helen Megaw being the first woman working in perovskite issues has proven that researchers have underestimated the perovskite structure [6,7]. Megaw's work has become then a reference and her contribution in the synthesis of $CaTiO_3$ and its investigation using X-ray diffraction has led to very important funding of the exact structure of perovskites [7]. 10 years later, the scientific community was finally able to prove the results proposed by Megaw, and in 1957 the final structure model was defined. The journey of structure investigation has taken more than 100 years after their discovery, after which, continuous attempts of preparing synthetic perovskite has led to find that the majority of these compound crystallize in the perovskite type structure, thus, the perovskite name now refers to every compound having similar structure as $CaTiO_3$.

Between 1930 and 1950s, Perovskite structure diffuses to the field of materials. In this era, Goldschmidt and his group worked on the classifications of perovskites adopting the idea proposed by Gustav F. Hüttig for coordination compounds [4,8]. Goldschmidt and his group were able to classify the perovskite structure into different types, their funding is still nowadays used for ABO_3 compounds and it is known as the tolerance factor, t, given in equation 1 [9]:

$$t = r_A + r_X / \sqrt{2}(r_B + r_X) \qquad \text{(Eq. 1)}$$

Soon after their publications, William Zachariasen under the supervision of Goldschmidt and the Physics Nobel Prize W.H.L. Bragg in 1915 has expanded the researches on the crystal structure of perovskites. William Zachariasen has classified the perovskite oxides in terms of B-site coordination and r_B/r_O and r_A/r_O ratios as he also reduced the tolerance factor values to $0.9 \leq t \leq 1$ [10]. With the continuity of researches it became known that these materials have the ability to accommodate any type of ion; Robert Evans [11] in his book mentioned that the oxidation state of ions is of secondary importance and that any pair of ions that have appropriate radii to the co-ordination and aggregate valence of 6 to maintain the neutrality in the structure is capable to adopt the perovskite structure. Moreover, in the beginning of 1970s and as a result of the extensive work of Megaw and her postdoc Mike Glazer [12]; another feature was discovered in perovskite structure referred to as system distortion. Their funding revealed that the distortion appearing in simple perovskites are the results of oxygen displacement of the BX_6 octahedron which tend to adapts to the space left by the A-cations [13,14]. Later on Glazer has established a notation that is still used, after some adjustment, to describe the BX_6 rotations [12,13,15,16].

A rapid growth was seen in the number of synthesized compounds with the perovskite structure between 1950 and 1960s. The legacy of this era was reflected not only in the fabrication of other new compounds [4,7,17], but it is seen nowadays knowing that PZT materials [18–21] for examples are still in the trend and constitute the benchmark of ceramic capacitors, as well as their application in several technologies. From 1970s up to now, researches are committed and dedicated to the discovery and investigation of properties diversity of perovskite and related crystal structure such as anti-perovskites, double and triple perovskites, etc. Fig-I.1 presents the most active researches related perovskite and their applications in different technologies mainly energy production and storage.

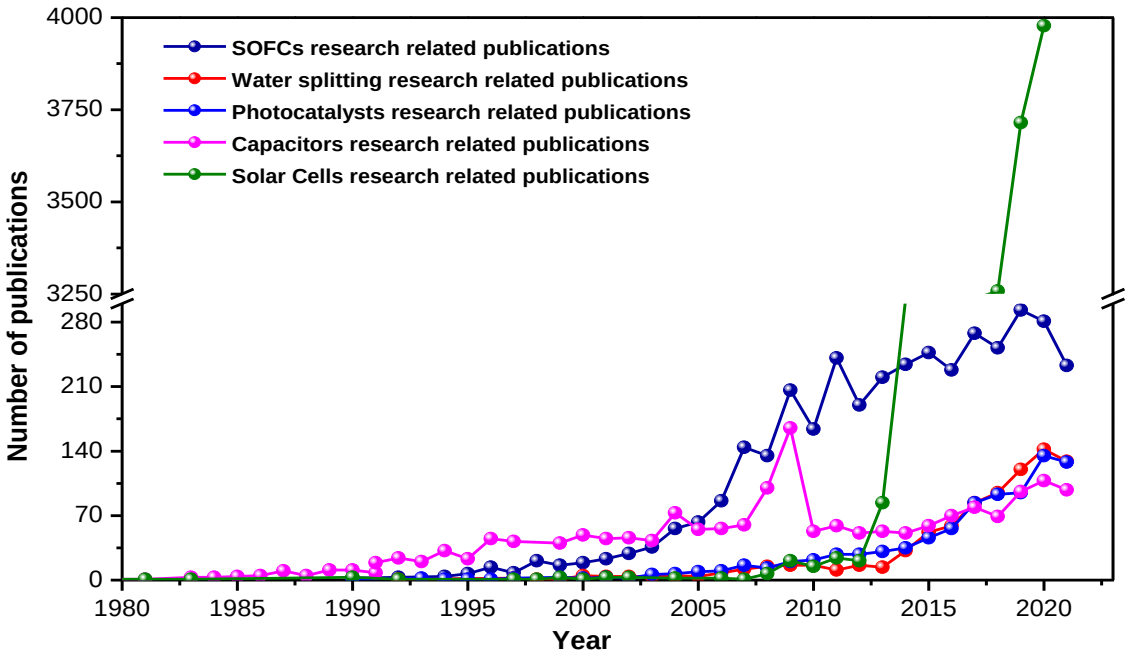

Fig-I.1: Amount of literature published from 1980 to 2017 on five different perovskite-related research fields that are still active. Data were obtained from SCOPUS database.

I.2. Perovskite structure

By the time when Megaw Helen put an end to the mystery of naming, the scientific community agreed on the fact that perovskites structure describes any material crystallizing in the form of ABX_3. Common compounds with the perovskite structure are oxides (*e.g.* $BaTiO_3$, $PbTiO_3$) [7,22–24], furthermore some hybrids [25–27], halides [28,29], nitrides [30,31], carbides [32,33] also crystallize in this structure. With a number more than 20K of publications in the field of perovskites structure and their applications, it is demonstrated that around 90% of the periodic table elements, namely transition metals, rare and alkali earth elements are stable in the ABO_3 perovskite structure [34].

ABO_3 perovskites oxides structure is commonly described by a set of corner sharing BO_6 octahedra in a 3D dimensional network. The A and B elements are cations of different size and O (oxygen) is the anion. The A-site elements (*e.g.* Ba^{2+}, La^{3+}, Pb^{2+}, and Nd^{3+} etc.) are twelvefold-oxygen coordination elements and are larger in size compared to the B-sites cations. The B-site elements are transition metals (*e.g.* Ti^{4+}, Fe^{3+}, Mn^{3+}, and Sc^{3+} etc.); and reside in an octahedral environment of sixfold-oxygen coordination [4,34,35]. The ideal perovskite structure belongs to

the cubic $SrTiO_3$ refined with *Pm*-3*m* (No. 221) space group at room temperature [36]. The structure of an ideal cubic perovskite presented for $SrTiO_3$ case is shown in **Fig-I.2**, where the B cations occupy the center with oxygen ions in the face centered positions; the A cations are shown in the corner of the cube.

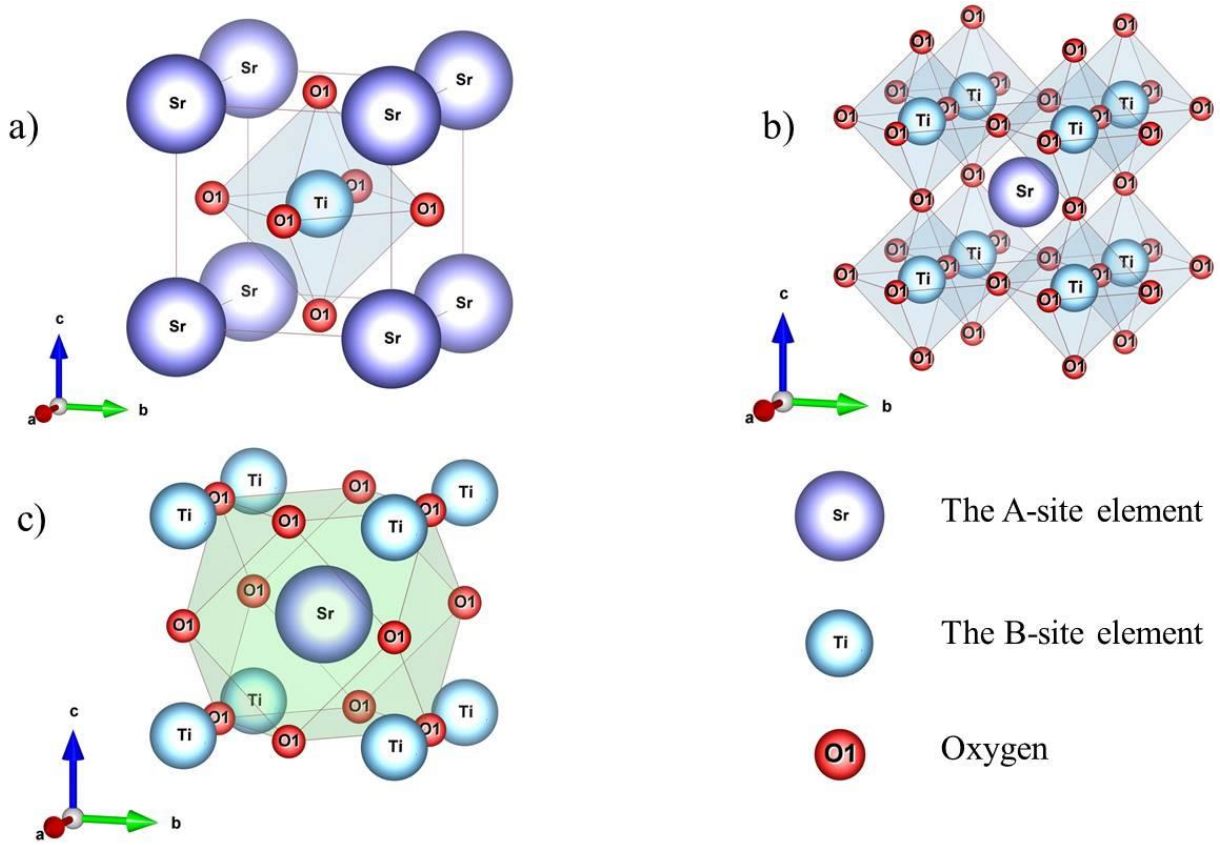

Fig-I.2: The ideal model of Cubic $SrTiO_3$ SG: Pm-3m (No. 221) at room temperature (a), the other different presentations show the unit cell with A cation at the center and B cations at the origin (b), and cuboctahedra environment of A cation.

The perovskite structure is no longer considered a mystery as it used to face doubt and conflict in assigning the exact nature of structure, however, the investigation of the variety of combinations that the structure may accommodate [37–39], the condition of the structure formability and stability [40–42], the octahedral tilt [43–45] and the variety of properties within the structure are still the topics of enormous researches.

I.3. Condition of formation and stability: Tolerance factor

The stability and formability of the perovskite structure depend on the ionic radii of A-site elements and B-site elements, as well as the electronegativity between the cations. Goldschmidt [9] in early 1920s has introduced a parameter known as the tolerance factor to determine the structure stability. The tolerance factor is expressed as function of the ionic radii of the A-site elements and the B-site elements. In the case of ideal perovskites, the cubic structure, the half of the unit cell parameter 'a' is equal to the bond B-O, and across the diagonal of face of the unit cell, A-O bond is equal to ($\frac{a}{\sqrt{2}} = r_A + r_o$). Goldschmidt and his group developed the formula of the tolerance factor and established the ratio between the ionic radii of the cations A and B and the anion, resulting in the following expression:

$$t = (r_A + r_O)/\sqrt{2}(r_B + r_O) \qquad \text{(Eq. 2)}$$

r_A, r_B and r_O, represent the ionic radii of the A-site element, the B-site element and oxygen. For an ideal perovskite structure (*Pm*-3*m*), t=1.

The value of the tolerance factor varies according to the ionic radii size and/or the oxidation state of the cations, thus, the tolerance factor of most perovskite have values varying between $0.75 < t < 1.03$ [46,47]. Bellow the range of structure formability of perovskites, other type of perovskites such as *e.g.* ilmenite tends to crystallize. For $t < 1$ and according to the tolerance factor formula, the term $\sqrt{2}(r_B + r_O)$ is higher than $(r_A + r_O)$, thus, sort of distortion or BO_6 tilts appear due to the compression of the bond B-O. The structure then will be either rhombohedral (R-3c) [48] or orthorhombic (Pbnm) [49]. For perovskites with $t > 1$, and according to the tolerance factor formula, the term $(r_A + r_O)$ is higher than $\sqrt{2}(r_B + r_O)$, thus compression along the A-O bond is applied by the size mismatch of the cations, $r_A > r_B$, in this case there is a displacement of the B cations from the octahedra center of BO_6, and then the structure will adopt the hexagonal symmetry. For values between $0.75 < t < 0.9$, the elements constituting the perovskite structure within this range give enlarged orthorhombic unit cell such as $GdFeO_3$ [50].

Notably, the tolerance factor now is considered as a solid statement used to determine the structure stability [46,51]. G. Pilania et al. [52] worked in the formability of perovskite using

machine Learning. The group has used different sets of feature pairs namely, the tolerance factor, the octahedral factor, the ionic radii size of A and B cations and the bond valence distances A-O and B-O. Machine learning was used to create a hyper-dimensional of structure dependency to the structural features used in the input data. Chonghe Li et al. [53] have investigated the regularities governing the formability of ABO_3 perovskites using the tolerance factor. 197 binary oxide systems were included in the study, combination of A_2O–B_2O_5; AO–BO_2 and A_2O_3–B_2O_3 groups were adopted. Chonghe Li et al. [53] investigation results, proved that the tolerance factor is necessary condition but not sufficient to fully predict the formability of the structure, it is found that, r_B/r_O, octahedral factor is as important as the tolerance factor. Huan Zhang et al. [46] have studied the structural stability and formability of ABO_3 perovskite, the likelihood of perovskite structure formability and non-formability was based on the tolerance factor and the bond-valence model (BVM). 376 ABO_3-type perovskites were included in the study, where 232 were found to adopt the perovskite structure. Huan Zhang et al. [46] established the following order of the perovskite structure stability: $A^{+}B^{5+}O_3 > A^{2+}B^{4+}O_3 > A^{3+}B^{3+}O_3$.

Structure prediction remains a challenge for researchers since resolving it, is time and cost saving as well as to discover new functional materials. Thus, additionally to the tolerance factor established by Goldschmidt, researcher continued the expansion of structure stability and formability of perovskite structure by establishing other new parameters that enable us to predict the formability of the structure. Christopher J. Bartel et al. [54] have developed a new tolerance factor to predict the stability of perovskite oxides and halides using computational selection 'SISSO algorithm' based on a data set containing the traditional tolerance factor, the electronegativity of A and B elements, the ionic radii and the oxidation states. The new proposed form of the tolerance factor is as follow:

$$\tau = \frac{r_X}{r_B} - n_A\left(n_A - \frac{{}^{r_A}/_{r_B}}{Ln\left({}^{r_A}/_{r_B}\right)}\right) \qquad \text{(Eq. 3)}$$

Where n_A is the oxidation state of A, r_A, r_B and r_X are the ionic radius of the cations, and $\tau < 4.18$ indicates perovskite structure stability. The new tolerance factor established by Christopher J. Bartel et al. [54] predict of about 92% of perovskite compounds of an experimental data set of 576 ABX_3.

I.4. Distortions and phase transitions of perovskites

Due to the rich composition that this class of materials is capable to host, varieties of symmetries are found in addition to the observed tilts and transitions phases occurring in the ABO_3 perovskites. Composition, temperature or pressure phase transitions were reported in several works [55–58]. The effect of A-site on the structure was emphasized by Pian Pian Ma. et al. [59] in the solid solution $La_{1-x}M_xMnO_3$ ($M=Sr^{2+}$, Ca^{2+}; x=0.15)*;* the A-site substitution effect on $LaMnO_3$ by Ca^{2+} and Sr^{2+} has showed that the orthorhombic structure of $LaMnO_3$ was preserved when substituting La^{3+} by Ca^{2+}, while in the case of La^{3+} substituted Sr^{2+}, the structure was identified to adopt a rhombohedral $R\bar{3}c$ phase. Moreover, composition inducing phase transition was reported in Jiayao Lu et al. [60] work on the electrochemical stability of A-site deficient in the solid solution $Li_{3x-y}La_{1-x}Al_{1-y}Ti_yO_3$ (x = 5y/12); one phase transition from cubic structure SG: *Pm*-3*m* to the tetragonal structure SG: *P*4*mm* as the amount of Ti increases is reported; Ti=0.9, and 1. $La_{1-x}Sr_xFeO_{3-\delta}$ (x = 0, 0.1, 0.5, 0.9, 1) was reported by O. Hass et al. [61]; the substitution of La^{3+} by Sr^{2+} induces two phase transitions from Orthorhombic (*Pbnm*) to rhombohedral ($R\bar{3}c$) to cubic (*Pm*-3*m*). As the amount of Sr^{2+} increases, the symmetry of the crystal structure in the solid solution $La_{1-x}Sr_xFeO_{3-\delta}$ evolves to higher symmetry. Phase transitions induced by temperature and pressure were studied by Tetsuya K. et al [62] on $CaSiO_3$, a transition from tetragonal to cubic structure was reported to occurs between 490 – 580 k and 30 – 70 GPa.

One of the ways to detect the changes of the structure is to calculate the tolerance factor. Nevertheless, the tolerance factor remains not sufficient condition to specify and indicate the type of distortion within the structure. Generally the distortion in the perovskite structure occurs under various constraints namely the composition, pressure or temperature, these distortions is at the core of the appearance or not of one or several structural phase transition. The structure variations of perovskite materials are very subtle and it is often difficult to define the new adopted system because the variant may slightly differ from the original structure, which makes it a challenging task for researcher. With regard to the ideal cubic structure, these distortions are classified according to three types of mechanisms: B cations displacement with the BO_6 octahedron, distortion of the BO_6 octahedra unit, and the octahedral tilting which is considered as the common occurring distortion in perovskites.

I.4.1. Glazer classifications

The tilting of BO_6 octahedra occurs around one or more of their axes of symmetry, the flexibility of perovskites is clearly observed in this case knowing that the octahedra preserves both the regularity of the octahedra, approximately, while the corner of connectivity are strictly maintained. Glazer in 1972, and 1975, has studied the octahedra tilting of perovskite and established simple ways of determining the perovskite structure [13]. Glazer's published work is a description of the methodology he considered to determine the different possible octahedra tilting around the pseudo-cubic axes. Glazer [13] has noted that the one octahedra tilt around the pseudo-cubic axes can determine the tilts of the octahedra in the plane perpendicular to this axis while along the axis the tilt can occurs either in the same of opposite direction as shown in **Fig-I.3**.

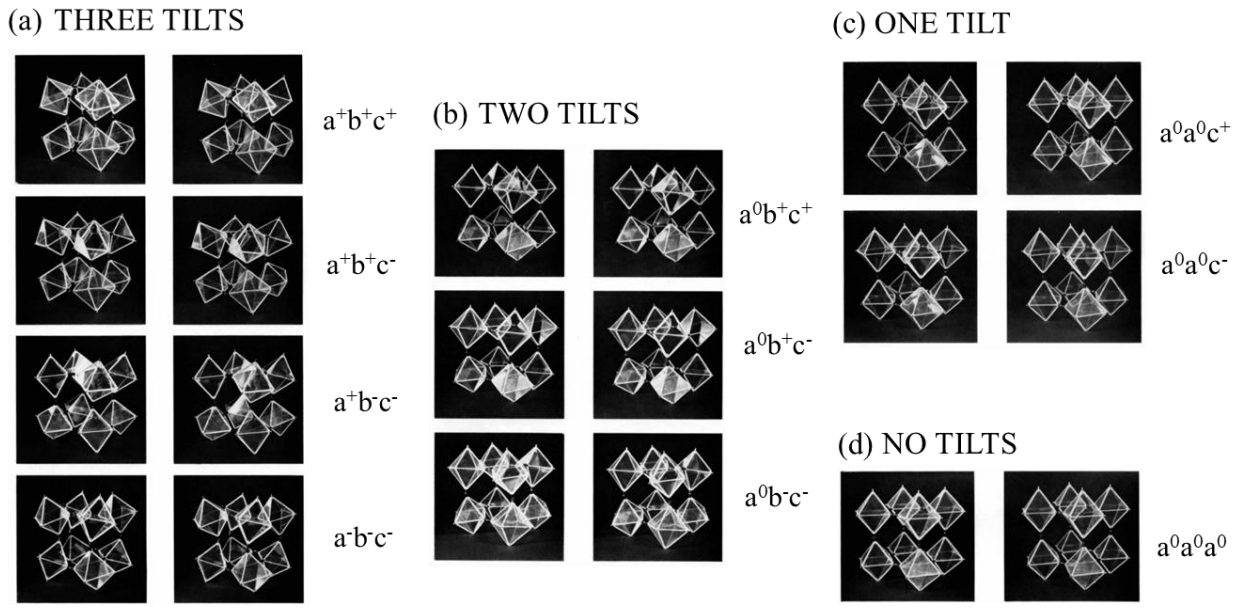

Fig-I.3: Series of **s**tereo-photographs by glazer [13] of the octahedra in each arrangement. The axes used are right-handed with [001] vertical and [010] to the right. The origin is taken at the center of any octahedron.

The notation $a^{\#}b^{\#}c^{\#}$ was assigned by glazer and it describes the sense of tilting in the perovskite system around the axes in the x, y, z directions of the $Pm\bar{3}m$, *(i.e.* $[100]_p$, $[010]_p$ and $[001]_p$ 'pseudo-cubic axes'). The superscript # is assigned as + or – and it describes the successive tilt of one layer of octahedra 'n' to the next layer 'n+1' around the relevant axis; the

symbol '+' describes an in-phase tilt while the symbol '–' is an out-phase tilt of when the octahedra of layer 'n' rotate in the opposite directions with 'n+1'. For cases, where there is no octahedra tilting the superscript # is referred to as 0, moreover, the case of which the letters are repeated, it indicates the identical magnitude rotations of the tilts [12,63,64].

Glazer [13] has defined 23 possible tilts of the system in the case of ABO_3 perovskites, and assigned to each a specific space group. Later on, considering the group theory, Howard and Stokes [16] have reduced the number of possible space groups to 15 as shown in **Fig-I.4**. **Table-I.1** resumes the different identified space groups according the glazer notation [13] and to Howard and Stokes notation [16].

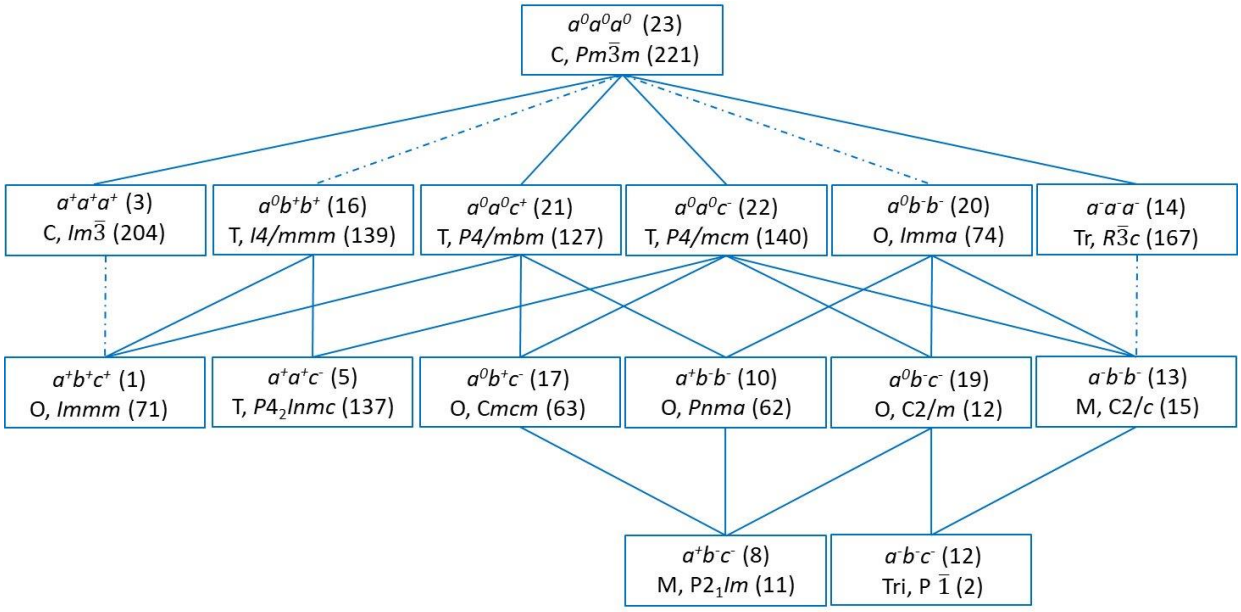

Fig-I.4: The possible space groups adopted by the perovskite structure due to octahedral tilts are given with the corresponding symbol and tilt systems [13]. Dashed lines connect the space groups among which the phase transitions must be first order. Continuous lines represent the relations for which second order transitions are allowed [16].

Table-I.1. Spatial groups for different simple perovskites with rotations of the octahedra according to Glazer notation (*)*[13]*, and according to Howard and Stokes (#)*[16]*.

Number	Symbol	No. order (*)	No. order (♯)
3-tiltd system			
1	$a^+b^+c^+$	*Immm* (71)	*Immm* (71)
2	$a^+b^+b^+$	*Immm* (71)	
3	$a^+a^+a^+$	*Im*$\bar{3}$ (204)	*Im*$\bar{3}$ (204)
4	$a^+b^+c^-$	*Pmmm* (59)	
5	$a^+a^+c^-$	*P*4_2*/nmc* (137)	*P*4_2*/nmc* (137)
6	$a^+b^+b^-$	*Pmmm* (59)	
7	$a^+a^+a^-$	*P*4_2*/nmc* (137)	
8	$a^+b^-c^-$	*P*2_1*/m* (11)	*P*2_1*/m* (11)
9	$a^+a^-c^-$	*P*2_1*/m* (11)	
10	$a^+b^-b^-$	*Pnma* (62)	*Pnma* (62)
11	$a^+a^-a^-$	*Pnma* (62)	
12	$a^-b^-c^-$	*F*$\bar{1}$ (2)	*P*$\bar{1}$ (2)
13	$a^-b^-b^-$	*I2/a* (15)	*C2/a* (15)
14	$a^-a^-a^-$	*R*$\bar{3}$*c* (167)	*R*$\bar{3}$*c* (167)
3-tiltd system			
15	$a^0b^+c^+$	*Immm* (70)	
16	$a^0b^+b^+$	*I4/mmm* (139)	*I4/mmm* (139)
17	$a^0b^+c^-$	*Cmcm* (63)	*Cmcm* (63)
18	$a^0b^+b^-$	*Cmcm* (63)	
19	$a^0b^-c^-$	*I2/m* (12)	*C2/m* (12)
20	$a^0b^-b^-$	*Imma* (74)	*Imma* (74)
1-tiltd system			
21	$a^0a^0c^+$	*P4/mbm* (127)	*P4/mbm* (127)
22	$a^0a^0c^-$	*I4/mcm* (140)	*I4/mcm* (140)
0-tiltd system			
23	$a^0a^0a^0$	*Pm*$\bar{3}$*m* (221)	*Pm*$\bar{3}$*m* (221)

I.5. Optical properties: Absorption and visible light harvesting

Recently, perovskite oxides are under intense research for various important applications such as catalytic membrane reactors, photocatalysts, solid oxide fuel cells, and optoelectronics, etc. The performance of these materials strongly depends on their light harvesting capabilities, and/or to the nature of the band gap Eg (eV) and its value. Recently, the Titanate perovskite family such $BaTiO_3$ and $SrTiO_3$ perovskite material have been attractive materials for photocatalysts applications owing to their stability, high and efficient photocatalytic activity [65–67]. Perovskite based titanium, $ATiO_3$, tends to show strong absorption in the Ultra-Violet region [68–71], whereas orthoferrite, $AFeO_3$, Cobaltite $ACoO_3$ and manganite $AMnO_3$ perovskites show expanded visible light absorption [72,73]. Knowing that perovskite materials are capable of accommodating wide range of the periodic table elements, the design of complex perovskites based 3d material was the topic of several researches aiming to combine the various properties in one compound.

$SrTiO_3$ is highly active under the UV light with no response to the visible light [65]. Co-doping or substituting an amount of the hosting structure's elements was adopted as a strategy for light absorption enhancement. Nanocrystalline of $SrTiO_3$ doped Fe ions was prepared via solid state reaction; the $SrTi_{0.9}Fe_{0.1}O_{2.968}$ nanocrystalline with a band gap equal to 1.34 eV, showed a broad and intense absorption extending from 0.5 to 6 eV covering from UV-visible domain to near IR [74]. The observed shrink of the band gap compared to $SrTiO_3$ was related to the appearance of defect centers across the gap [74]. Chao Zhan et al. [70] have reported DFT study of Rare earth and N co-doped $SrTiO_3$ toward high visible photocatalytic activity. Chao Zhan et al. [70] results proved that $SrTiO_3$ may serve as important candidate for water splitting application when doped by La-N, Ce-N, Pr-N and Nd-N due to the great absorption of visible light and the shrink occurred in the band gap.

In another study, the control of the optical absorption of $La_{1-x}Sr_xFeO_3$ perovskite films by both heterovalent A-substitution and oxygen vacancies was reported. It is found that Sr^{2+} substitution induces the formation of new states bellow the bottom of the conduction band which resulted in a redshift of the absorption[75]. La-Fe co-doped $SrTiO_3$ system was studied as visible light photocatalysts. Different dopant concentration up to 5 wt % were prepared, the samples showed a reduction of the optical band gap from 3.2 to 2.72 eV as the amount of the

substitution increases and resulted in a red shift of the absorption. This reduction was related to the formation of impurity energy levels, due to the doping and to the charge transfer transitions [76]. Other group of researcher has reported on the band gap of $LaFe_{1-x}Ti_xO_3$ system, the experiments show an increase from 2.05 to 2.61 eV of the band gap values as the amount of Fe^{3+} decreases[77].

$BaTiO_3$ ferroelectric perovskite materials, has been proposed as effective photocatalysts candidate for wastewater treatment. Schindra et al. [78] have critically reviewed the strategies adopted to improve the efficiency of $BaTiO_3$, among the methods reviewed; the group stated doping is a conventional method to efficiently enhance the photocatalytic activities of $BaTiO_3$. Metal doped $BaTiO_3$ including copper, iron manganese tungsten cerium and chromium demonstrated great ability to degrade organic pollutants. Additionally improving the hydrogen evolution activity of $BaTiO_3$ has also been the topic of research done by Pengcheng Xie et al. [79]. The group has studied the effect of Mo doping on $BaTiO_3$, and reported the efficiency of narrowing the band gap that resulted in a redshift of the absorption band confirming the improvement of the photocatalytic activity under visible light. Jiafeng Cao et al. [80] worked on nitrogen doped $BaTiO_3$, their results showed an improved photodegradation activities to Rhodamine-B under visible light irradiation ($420\ nm < \lambda < 780\ nm$) which is due to the enlargement of the valence band width. $BaTiO_3$ has found its way to solar driven methanation, Diego Mateo et al. [81] worked on Nickel nanoparticle supported on $BaTiO_3$ and studied the photothermal conversion of CO_2 under visible light. Diego Mateo et al. [81] reported an efficiency of 100% to hydrogenate CO_2 to CH_4 under Ultra Violet and visible irradiation with a production rate of 103.7 mmol g^{-1} h^{-1} and 40.3 mmol g^{-1} h^{-1} respectively.

Muhammad Aamir et al. [82] have reported the good activity of Co and Fe doped $LaCrO_3$ perovskite under solar light. Li Zeng et al. [83] have reported the synthesis of the perovskite series $LaNi_{1-x}Fe_xO_3$ and evaluated the photocatalytic activity under visible light. Li Zeng et al. [83] reported good performance of photocatalytic activities for $LaNi_{0.95}Fe_{0.05}O_3$; the materials showed 98.89% of degradation rate of methyl orange within 120 min. Enqi Yu et al. [84] studied the photothermocatalytic of $LaTi_{1-x}Mn_xO_{3-\delta}$, the introduction of Mn cations led to an increase of the catalytic activity under the light absorption, this was accompanied by an enhancement of light to heat conversion. The photocatalytic evolution of H_2 under simulated solar light of $LaMO_3$ (M:

Co, Mn, and Fe) was reported by Luz I et al [73]. Among the studied cases, $LaMnO_3$ showed the highest activity, while the lowest was obtained by $LaFeO_3$. In Luz I et al. [73] work the synthesis method was as well evaluated showing that materials prepared via sol gel showed better photocatalytic performances due to the large surface area. The effect of doping solves the issue of the fast recombination rate, WeiWei Li and al. [85] reported that Ti 3d and Fe 3d orbital hybridization in $BiFeO_3$-$SrTiO_3$ system creates trap states that suppress the fast recombination rate.

I.6. Band gap in perovskite materials: formation and modification

Owing to the structural flexibility, stability and ability to tune the physical properties of perovskite materials, the extensive studies of doping with 3d transition metals are still ongoing and emerging to all type of elements in the periodic table [56,86–88]. The purpose of researches is to enhance the visible light response of perovskite for a good benefit in the field of energy harvesting applications and clean energy production [89–94]. The band gap is one of the most important features and with a direct link to the absorption performance of oxides. The band gap is a parameter that controls the amount of energy absorbed from the UV-visible to near infrared region and has a critical role for energy harvesting applications as the properties related to the band gap nature are, but not limited to, the conductivity, photocatalytic and photoelectric conversion, etc., [95–100].

The wide band gap of perovskites such $SrTiO_3$, $BaTiO_3$ and other perovskites, is due to the fundamental characteristic nature of A-O and B-O interatomic distances and to the large difference in electronegativity between the oxygen and the transition-metal cations [101]. Julien Varignon et al. [98] have published their investigation on the gapping mechanisms of perovskite. This group of researchers has defined four generic mechanisms that affect the gapping or the opening of the band gap, where two are related to the intrinsic behavior of transition metals: compounds with two electrons, and compounds with instable single local electronic occupation patterns. The two others mechanisms originate due to structural symmetry breaking such as octahedral titling and rotations [98]: compounds forming subshells by octahedral breaking of atomic symmetry, compounds lifting electronic degeneracies due to the octahedral rotations, and those which are retaining the electronic degeneracies due to small or absent octahedral rotations. Elsewhere, Tingting Qi et al. [102] have examined the key factors for band structure engineering

in tetragonal systems. The group assumes that B-site ordering and the octahedral tilts in the perovskite structure strongly affect the opening of the band gap. These results are proven to be valid in the case of tetragonal system with fully d states or empty d states cations which are respectively located at the valence band maximum and the conduction band minimum. These combinations are found to raise the energy of the valence band, while choosing B cation with higher electronegativity may lower the conduction band energies. Moreover, Tingting Qi et al. [102] shows that suppressing the octahedral tilt in the perovskite structure can increase the bandwidth for both the conduction and the valence band, thus decreasing the band gap Eg (eV).

Theoretically, it is proven that the structural parameters have an effect on the gapping mechanisms, however, experimentally there are only few works stating the effect of the structure on the values of the band gap. This case was reported by C-C Hu et al. [103] and X. Zhou et al. [104] for tantalite materials $ATaO_3$. The band gap was found to decrease from 4.7, to 4.0, to 3.6 eV as the bond angle Ta-O-Ta deviates with 37°, 17° and 0° respectively. These results show that the factors affecting the band gap could be of structural origin and/or chemical factor. As the conduction band and the valence band are constituted respectively by s or d states of the B-cation and the p orbitals of the anion, the choice of the B cation plays a major role in the value of the band gap and mainly with cations exhibiting high energy occupied s^2 or d^{10} orbitals that can shift the valence band and couple with p orbitals of anions [103–105]. This fact, will results in the creation of new energy levels between the valence band and the conduction band resulting in a shrink of the band gap of the material [65,67,106]. Thus combining the two factors, namely structural and chemical factors, is a promising strategy to enhance the optical and electrical properties of perovskites.

I.7. Dielectric properties of perovskites and its importance for energy storage

Perovskites are part of the electroceramics class of materials, and they are considered as advanced materials known by their dielectric properties and high electrical resistivity greater than 10^8 Ω [107]. The dielectric materials are classified by their relative permittivity ε_r which represents the ability of the material to store electrical energy via different mechanisms originating from the orientation of electric dipoles by an external applied electric field. When a dielectric materials is under the effect of the electric field, ions or atoms either locally react and oppose the external electric field or creates dipoles moments that oppose this later [107,108].

These features make dielectric materials in general, and perovskite in particular good capacitors that can quickly deliver charger, and thus contribute in the search of producing efficient energy storage systems. Dielectric capacitors show low energy density which is the energy stored expressed in volume (Wh/L or J/cm^3), despite this limitation, they show several advantages that encourage scientists to target this class of energy storage devices such as higher operating voltage, size flexibility, safety, thermal and cyclic stability [20,109–111], etc.

Depending on the variation of the polarization upon the external electric field, dielectric materials can be categorized as linear dielectric or as nonlinear dielectric. For linear dielectrics, the dielectric constant "ε" is independent to the electric field and the polarization strength is linearly related to the electric field strength and small, in comparison with nonlinear dielectrics, they show a maximum of polarization at E_b, the breakdown electric field, and then decreases to non-zero values with the suppression of the external field. For non-linear dielectrics there are two types of stored energy, the effective energy storage density W_{rec} and the loss energy density W_{loss} which is the energy that cannot be released; this fact is due to presence of P_r remanent polarization of ferroelectric material [108,111]. Additionally, the dielectric constant of non-linear dielectrics changes with the applied external field; knowing that for dielectric materials there are five basic type of electric polarizations that molecules can show: electronic polarization, atomic or ionic polarization, dipole polarization, spontaneous polarization and interface or space charge polarization; each type of polarization requires time to perform which make the dielectric constant dependent to the frequency of the alternating electric field or the rate of the change of time-varying field which explain the fact of studying the dielectric properties at various frequencies and temperature [19,109,112–116]. The aforementioned polarization can be grouped into two regimes. First regime is associated with the vibrations of atoms or ions, when vibrating at certain frequency, a resonance occurs when the frequency of the excitation is close to the natural frequency of the vibration or oscillation system, this regime is called the resonance regime. When the polarization involves the motion of charges by migration or by orientation, the system belongs to the relaxation regime because of time required for the charge carriers to overcome the inertia arising from the surrounding medium in order to proceed in their movement during the polarization or the depolarization processes [108]. Therefore, there are ferroelectrics such as $BaTiO_3$, $(Ba_{0.70}Ca_{0.30})TiO_3$ (BCT), $Ba_{0.4}Sr_{0.6}TiO_3$ (BST) and, $Ba(Zr_{0.2}Ti_{0.8})O_3$ (BZT) [117–121]; relaxor ferroelectrics such as $BaTiO_3$-$BiScO_3$, $(1-x)BaTiO_3$-$xBi(Ni_{0.5}Sn_{0.5})O_3$

((1-*x*)BT-*x*BNS), $BaTiO_3$–$Bi(Mg_{2/3}Nb_{1/3})O_3$ (BT-BMN), and (1-x)$BaTiO_{3-x}Bi(Mg_{0.5}Zr_{0.5})O_3$ ((1-x)BT-xBMZ) [122–125]; antiferroelectrics such as Mn-doped $Ag_{0.97}La_{0.01}NbO_3$, and (1-x)$NaNbO_3$-x$CaZrO_3$ [126,127]; and relaxor antiferroelectrics such as $Bi_{0.5}Na_{0.5}TiO_3$–$SrTiO_3$–$(K_{0.5}Na_{0.5})NbO_3$, and $NaNbO_3$-$Bi_{0.5}Na_{0.5}TiO_3$ [128,129]. **Table-I.2** summarizes some of the different dielectrics cited, their type, Energy breakdown, and density storage.

Table-I.2. Energy storage properties of dielectric ceramics classified by type: Ferroelectrics, Relaxor ferroelectrics and Relaxor antiferroelectrics.

Composition	Type	E_b (kV cm^{-1})	W_{rec} (J cm^{-3})	Ref
$BaTiO_3/Al_2O_3$-SiO_2-ZnO	Ferroelectrics	150	0.83	[130]
$BaTiO_3/SrTiO_3$		47	0.198	[131]
$Ba_{0.7}Ca_{0.3}TiO_3$		150	1.41	[132]
$0.85(BaZr_{0.2}Ti_{0.8})O_3$-$0.15(Ba_{0.7}Ca_{0.3})TiO_3$		170	0.68	[109]
$0.88BaTiO_3$-$0.12Bi(Mg_{1/2}Ti_{1/2})O_3$	Relaxor ferroelectrics	150	1.6	[133]
$0.9BaTiO_3$-$0.1Bi(Mg_{2/3}Nb_{1/3})O_3$+0.3wt% $MnCO_3$		210	1.7	[134]
$0.9(0.92Bi_{0.5}Na_{0.5}TiO_3$-$0.08BaTiO_3)$-$0.1NaTaO_3$		100	1.2	[135]
$0.85(0.93Bi_{0.5}Na_{0.5}TiO_3$-$0.07BaTiO_3)$-$0.15Na_{0.73}Bi_{0.09}NbO_3$		127	0.9	[136]
$0.93NaNbO_3$-$0.07Bi(Mg_{1/2}Zr_{1/2})O_3$	Relaxor antiferroelectrics	255	2.31	[137]
$0.9NaNbO_3$-$0.1Bi(Mg_{2/3}Nb_{1/3})O_3$		300	2.8	[138]
$0.86NaNbO_3$-$0.14(Bi_{0.5}Na_{0.5})HfO_3$		350	3.51	[139]
$Na_{0.7}Bi_{0.1}NbO_3$		250	3.44	[140]
$0.80NaNbO_3$-$0.20SrTiO_3$		323	3.02	[110]

I.8. Recent perovskite oxides development and trend applications

In the past century, and after the discovery of ferroelectricity in $BaTiO_3$, perovskites were extensively studied for their physical properties such as ferroelectric, dielectric, ferromagnetic, piezoelectric, multiferroic and magneto-resistance. Nowadays and driven by the pressing concerns of clean energy production and the growing energy demands, perovskites have found

their way to energy production related technologies sector [89,104,141–143]. The following paragraphs will describe few of the most extensively tested technologies for perovskite materials.

I.8.1. Perovskite materials in Solid Oxide Fuel Cells SOFCs

Among the different type of fuel cells, Solid oxide fuel cells (SOFCs) can be subdivided into four major cells: the anode-supported cell (ASC), electrolyte-supported cells (ECSs), the metal-supported cell (MSC), inert-supported cell (ISC) [144]. Among the aforementioned classes the ISC potentially fulfills all the requirements of low cost SOFC; it utilizes cheap porous materials as a support. Fabian Grimm et al. [145,146] have reported on forsterite material (Mg_2SiO_4) doped Zn and Ca as support for SOFCs. This support was chosen due to its abundant nature and therefore inexpensive, which will reduce the manufacturing costs of SOCF. Fabian Grimm et al. [145,146] have studied the reactivity of seven different cathodes based perovskites in order to identify the less reactive cathode with forsterite; therefore, double layered pellets, mixed pellets and screen printed cathodes were prepared. The seven different cathodes are LSCF ($La_{0.58}Sr_{0.4}Co_{0.2}Fe_{0.8}O_3$), LSC ($La_{0.58}Sr_{0.4}CoO_3$), LSF ($La_{0.58}Sr_{0.4}FeO_3$), PSCF ($Pr_{0.58}Sr_{0.4}Co_{0.2}Fe_{0.8}O3$), LCCF ($La_{0.58}Ca_{0.4}Co_{0.2}Fe_{0.8}O_3$), LSFM 95S1M3 ($(La_{0.9}Sr_{0.1})0.95Fe_{0.7}Mn_{0.3}O_3$), and LSFM 95S2M8 ($(La_{0.8}Sr_{0.2})_{0.95}Fe_{0.2}Mn_{0.8}O_3$) [146]. The tested cathodes, LSC, LSF, LSCF, PSCF, and LCCF tend to react with forsterite and new phases are detected and form reaction layers with a thickness ranges between 1.8 μm and 30 μm. Whereas LSFM 95S2M8 and LSFM 95S1M3 show Fe_3O_4, $La_{9.33}(Si_6O_{26})$ as new phases, but no reaction layers are formed. Si, Sr, and Zn are reported to be the cause of the formation of reaction layers, whereas, La and Pr are identified as non-reactive elements with forsterite. Their reactivity was as follows: LSFM > LSF > LSC > PSCF > LSCF > LCCF (ascending order) [146].

The complex perovskite cathodes tested in the work of Fabian Grimm et al. are, but not limited to, the most popular cathodes applied for SOFCs. There are other combinations that form structurally and thermo-chemically stable materials, such $La_{0.8}Sr_{0.2}MnO_3$ (LSM). LSM is a cathode with electronic conduction type, low over-potential and it shows an excess of oxygen at oxidizing atmospheres [147,148]. The researches were directed toward extending the triple phase boundary (TPB) of LSM and inducing or enhancing the ionic conductivity of the material. However, at low operating temperature, the electrochemical deteriorate because of the polarization losses at the cathode side and the increase of electrode-electrolyte resistivity [147–

151]. Generally, SOFCs cathodes can be classified in term of composition, i.e. (La, Pr, Nd, Sr, Gd, Sm, Y, Sr, and Ca)-based materials, while in the B-sites the used elements are mainly Co, Fe and Mn; varying the composition gives different responses and performances for the cathodes and match differently with the electrolyte [152–160]. At high operating temperature, SLM is recommended as it fulfills almost all the requirement of good cathode. For low operating temperature $PrBa_{1-x}Sr_xCo_2O_{5+\delta}$ [161] and $NdBa_{0.5}Sr_{0.5}Co_{2-x}Mn_xO_{5+\delta}$ [162] show the highest conductivity with value close to 3000 Scm^{-1}. Cobalt based perovskite tend to show high conductivity like in the case of PBSC and NBSC, however their high CTE coefficient which causes thermal stress in the cell, make them unsuitable cathodes [152,156,161]. Much research is needed for Fe and Mn based cathode in term enhancing their conductivity to match the cobalt based materials. **Table-I.3** resumes the performance of some cathodes based perovskite in term of conductivity, and CTE coefficient.

Table-I.3. CTE and conductivity values of the different studied solid oxide fuel cells cathodes.

Cathodes	Conductivity (S cm^{-1})	CTE (x 10^{-6}) K^{-1}	Ref
$YBaCo_{2-x}Fe_xO_{5+\delta}$	16.3–18.0	-	[163]
$GdBaCuCo_{0.5}Fe_{0.5}O_{5+\delta}$	14.49	13	[164]
$NdBa_{0.5}Sr_{0.5}Co_{2-x}Mn_xO_{5+\delta}$	-	3000	[162]
$SmSrCo_{2-x}Mn_xO_{5+\delta}$	22.6–13.7	1000	[165]
$YBa_{1-x}Sr_xCo_2O_{5+\delta}$	–	449	[166]
$GdBaCo_2O_{5+\delta}$	20.1	512	[157]
$SmBa_{1-x}Sr_xCo_2O_{5+\delta}$	–	400	[167]
$Gd_{1-x}A_xCo_{1-y}Mn_yO_3$	–	250	[168]
$GdBa_{0.5}Sr_{0.5}Co_{2-x}Fe_xO_{5+\delta}$	24.01	1000	[169]
$Nd_{1-x}Ba_xCo_2O_{6-\delta}$	20.7	370	[170]
$Sm_{0.5}Sr_{0.5}Mn_xCo_{1-x}O_{3-\delta}$	–	100	[171]

SOFC is a complex field because it requires searching and optimizing large number of parameters. For example, the ORR reaction occurs at the electrode-electrolyte interface, thus, the reaction pathway depends then to the structure of the catalyst surface. Moreover cathode performance is related to the length of the TPB and the porosity; these properties are determined

and controlled by the synthesis method and fabrication of the cathode. Several studies suggested the Nano-structuring strategy to modify the morphology and microstructure, which showed an increase of the TPB resulting in the enhancement of the cell performance [172–175]. Electrospinning is found to be suitable method to produce high catalytic and porous materials; the reported properties of $GdBaCo_2O_{5-\delta}$ [176], $Pr_{0.6}Sr_{0.4}FeO_{3-\delta}$-$Ce_{0.9}Pr_{0.1}O_{2-\delta}$ [177], and $La_{0.58}Sr_{0.4}Co_{0.2}Fe_{0.8}O_3$ [178] showed good thermal stability and electrochemical activity; the materials were prepared via electrospinning and presented as nanofibers, and found to be good for IT-SOFCs. Furthermore, perovskites are also applied as electrolyte and in the anode side of SOFCs.

I.8.2. Perovskite materials in Photocatalysis

The past few years and among the large library of materials based perovskite structure, lanthanum $LaBO_3$ (B = Fe, Mn, and Co) and titanium $ATiO_3$ (A = Ba, Sr, Ca, etc) based perovskite are extensively investigated and have demonstrated good performance in different photocatalysts application [68–73]. La-based perovskites show narrow band gap, good optoelectronic and electrical properties, among these, $LaFeO_3$ has attracted the interest of researchers to enhance its photocatalytic properties by altering the surface area and or by doping new elements in A-site and and/or the B-site, capable of expanding the visible light absorption [179,180]. S. Thirumalairajan et al. [181] have prepared microsphere $LaFeO_3$ nanoparticles demonstrating a strong absorption at 554 nm and a good photocatalytic degradation of RhB within 3h. N. Yahya et al. [182] have reported the effect of the synthesis method on the photocatalytic performance of $LaFeO_3$ nanoparticles; via the combustion method, two routes were adopted using glucose only and Citric acid addition. Different morphologies were obtained; the $LaFeO_3$ prepared based on using only glucose exhibits agglomerated particles lowering the surface area of the sample, whereas $LaFeO_3$ prepared adding citric acid present less agglomerated particles with an average particle size of 70 nm and a better absorption of RB5. Thi To Nga Phan et al. [183] worked on the optimization of the photocatalytic performance of $LaFeO_3$ by tailoring the materials properties and the operating conditions; the group reported a dependency of the photocatalytic activity toward the iron precursor in the hydrothermal reaction. Thi To Nga Phan et al. [183] demonstrated that the morphology is a critical parameter, whereas the highest photocatalytic performance is shown for the material with the highest surface area equal to

17.63 m^2/g. The introduction of metal ion known as substitution in the B-site and or the A-site counts as a strategy to create new energy levels within the bands of the band gap, which plays the role of a trap that prevents the fast recombination of charge carrier. Parrino et al. [184] prepared the solid solution $LaFe_{1-x}Cu_xO_{3-\delta}$, where x = 0.05, 0.10, 0.20, and 0.40; they reported a good photocatalytic activity for a substitution amount less than 10% of Fe^{3+} by Cu^{2+}. Cu^{2+} doping has reduced the recombination rate of electron–hole, and the high photocatalytic activity observed for Cu^{2+} doped $LaFeO_3$ is reported to be due to the presence of oxygen vacancies. Based on Jauher et al. [185] work, Dhiman et al. [186] investigated the photocatalytic properties of the solid solution $LaMn_{0.2}Fe_{0.6}M_{0.2}O_3$ (M = Cr^{2+}, Co^{2+}, Ni^{2+}, Cu^{2+}, and Zn^{2+}), the higher photocatalytic degradation rate of dye was seen for Co, Ni, Cu and Zn, which was attributed to the generated vacancies defects and the narrow value of the band gap. Chiang, T.H et al. [187] reported on $RhCrO_x$/M-$LaFeO_3$ (M = Pr, Eu, Y, In, Ca, Tb and Mg) and the photocatalytic hydrogen production under the visible light. The highest H_2 evolution rate of 127 µmol h^{-1} g^{-1}, is obtained for the samples with 0.5 wt.% $RhCrO_x$ loading and 0.1 M Pr-doped $LaFeO_3$, this performance is 34% higher than undoped $LaFeO_3$ photocatalysts (94.8 µmol h^{-1} g^{-1}).

Titanate based perovskites with the typical formula $ATiO_3$ (A = Sr, Ba, Ca, Zn, Mn, Mg, etc.) are considered as potential photocatalysts for light-driven; however they exhibit wide band gap around 3 ~ 3.3 eV, with poor absorption of visible light [65–67]. $SrTiO_3$ band gap levels are suitable for water splitting and its performance for H_2 production was reported by Phoon et al. [188] and Bui et al. [189] demonstrating the good photocatalytic capability under the UV-light. Doping with new elements generates new donors or acceptors, creates new energy levels which induces a shrink of the band gap, and expands its absorption domain to the visible light. Rh-Ta-F: $SrTiO_3$ three doping strategy was reported by Kang et al. [190], this method has significantly promoted the H_2 evolution rate to attain a value close to 4123.7 µmol h^{-1} g^{-1}. López-Vàsquez et al. [191] have prepared $Sr_{0.97}Eu_{0.02}Zr_{0.1}Ti_{0.9}O_3$ to produce H_2, reporting the very high evolution rate (358,905.6 µmol·g^{-1}·h^{-1}). The group has optimized the participation of different parameters in the reaction such as the pH, dose of the photocatalysts, and concentration of the sacrificial agent; 70 mM ethylenediaminetetra acetic acid (EDTA), 0.01 g/L photocatalyst under a pH = 9.0 are the optimal condition according to their studies.

The two common problems of Photocatalysis semiconductors are the fast recombination of photogenerated charge carrier and the low light absorption. Various researches rely on the structural flexibility of perovskite materials to tailor the photocatalytic properties and overcome these limitations of semiconductors. The research in this regard are classified in terms of methods of preparation [183,189], the morphology effect [188], the electronic properties and the structural parameters such as the crystal structure or by composition [184,185,190]. However, few work studied the effect of the B-O-B on the band gap and the electron-hole pair separation [104,192].

I.9. Conclusion

This chapter has been devoted to a bibliographic study of the ABO_3 type perovskite and their history that carry with it years of discussions and focus to establish the law of structure formability and stability. The ABO_3 perovskites structure and their flexibility and variety in term of composition are presented and explained. The condition of the formation and stability of the structure using the established conditions by goldsmiths are discussed. The advancement and the modifications carried on the tolerance factor and its usability in theoretical studies was emphasized. The structural flexibility and distortions were discussed using glazer classifications showing the type of distortions and transitions that the ABO_3 undergoes. Reported researches and investigations carried out on perovskites properties namely the optical properties, the elements and parameters responsible for the opening mechanism of the band gap, and the dielectric properties. The last part concerns the last advancements and application in the field of energy conversion and photocatalysts and the usability of perovskite materials.

I.10. References

[1] A.R. Chakhmouradian, P.M. Woodward, Celebrating 175 years of perovskite research: a tribute to Roger H. Mitchell, Phys. Chem. Miner. 2014 416. 41 (2014) 387–391. https://doi.org/10.1007/S00269-014-0678-9.

[2] W.D. Navrosky A, Perovskite: A Structure of Great Interest to Geophysics and Materials Science, Am Geophys Union, Washington, D.C. (1989). https://doi.org/10.1029/GM045.

[3] O.B. Böggild, XXX. Krystallform und Zwillingsbildungen des Kryoliths, des Perowskits und des Boracits, Zeitschrift Für Krist. - Cryst. Mater. 50 (1912) 349–429. https://doi.org/10.1524/ZKRI.1912.50.1.349.

[4] N.S. Arul, V.D. Nithya, Revolution of Perovskite Synthesis, Properties and Applications, (2020).

[5] Barth TFW (1925) Die Kristallstruktur von Perowskit und verwandten Verbidungen. Nor Geol Tidsskr, (1925) 8:201-216.

[6] Megaw HD (1956) Ferroelectricity In Crystals. Methuen, Methuen, London, (n.d.).

[7] H.D. Megaw, Crystal structure of double oxides of the perovskite type, Proc. Phys. Soc. 58 (1946) 133–152. https://doi.org/10.1088/0959-5309/58/2/301.

[8] W.B. Jensen, The Origin of the Ionic-Radius Ratio Rules, J. Chem. Educ. 87 (2010) 587–588. https://doi.org/10.1021/ED100258F.

[9] G. Beskow, V. M. Goldschmidt: Geochemische Verteilungsgesetze der Elemente, Http://Dx.Doi.Org/10.1080/11035892409454037. 46 (2010) 738–743. https://doi.org/10.1080/11035892409454037.

[10] Zachariasen WH (1928) The crystal structure of sesquioxides and compounds of the type ABO3. Skr Nor Vidensk Akad Oslo I, Mat Naturv Klasse 4:7–165, (n.d.).

[11] R.C. Evans, An introduction to crystal chemistry, (1966) 410.

[12] A.M. Glazer, Distortion modes, A Journey into Reciprocal Sp. (Second Ed. (2021). https://doi.org/10.1088/978-0-7503-3875-2CH7.

[13] A.M. Glazer, IUCr, The classification of tilted octahedra in perovskites, Urn:Issn:0567-7408. 28 (1972) 3384–3392. https://doi.org/10.1107/S0567740872007976.

[14] A.M. Glazer, Simple ways of determining perovskite structures, Acta Crystallogr. Sect. A. 31 (1975) 756–762. https://doi.org/10.1107/S0567739475001635.

[15] C.J. Howard, H.T. Stokes, IUCr, Structures and phase transitions in perovskites – a group-theoretical approach, Urn:Issn:0108-7673. 61 (2004) 93–111. https://doi.org/10.1107/S0108767304024493.

[16] H.T. Stokes, E.H. Kisi, D.M. Hatch, C.J. Howard, IUCr, Group-theoretical analysis of octahedral tilting in ferroelectric perovskites, Urn:Issn:0108-7681. 58 (2002) 934–938. https://doi.org/10.1107/S0108768102015756.

[17] et al Mitsui T, Abe R, Furuhata Y, Mitsui T, Abe R, Furuhata Y, et al (1969) Ferro and antiferroelectric substances. Landolt-Bornstein numerical data and functional relationships, (n.d.) vol 3. Springer, Berlin. = (accessed August 25, 2021).

[18] M. Ito, M. Hagiwara, S. Fujihara, Ferroelectric and piezoelectric properties of (Bi1/2K1/2)(ZrxTi1−x)O3 lead-free ceramics, Mater. Lett. 271 (2020) 127776. https://doi.org/10.1016/j.matlet.2020.127776.

[19] H. li Lian, X. jing Shao, R. xue Cheng, Dielectric, ferroelectric, and piezoelectric properties of (Na0.47Bi0.47Ba0.06)1−xSrxTiO3 lead-free ceramics with different mean radii of the A-site cations, J. Mater. Sci. Mater. Electron. 30 (2019) 18539–18547. https://doi.org/10.1007/s10854-019-02207-x.

[20] B. Tiwari, T. Babu, R.N.P. Choudhary, Piezoelectric lead zirconate titanate as an energy material: A review study, Mater. Today Proc. 43 (2021) 407–412. https://doi.org/10.1016/J.MATPR.2020.11.692.

[21] L.F. Zhu, B.P. Zhang, S. Li, L. Zhao, N. Wang, X.C. Shi, Enhanced piezoelectric properties of Bi(Mg1/2Ti1/2)O3

modified BiFeO3-BaTiO3 ceramics near the morphotropic phase boundary, J. Alloys Compd. 664 (2016) 602–608. https://doi.org/10.1016/j.jallcom.2016.01.003.

[22] K. Itoh, L.Z. Zeng, E. Nakamura, N. Mishima, Crystal structure of BaTiO3 in the cubic phase, Ferroelectrics. 63 (1985) 29–37. https://doi.org/10.1080/00150198508221381.

[23] M. Arshad, W. Khan, M. Abushad, M. Nadeem, S. Husain, A. Ansari, V.K. Chakradhary, Correlation between structure, dielectric and multiferroic properties of lead free Ni modified BaTiO3 solid solution, Ceram. Int. 46 (2020) 27336–27351. https://doi.org/10.1016/j.ceramint.2020.07.219.

[24] A. Chawla, A. Singh, M. Singh, Effect of decreasing Mg2+ and Zr4+ substitution on the structural, ferroelectric and magnetic properties of BF-PT solid solutions, Mater. Today Commun. 14 (2018) 47–52. https://doi.org/10.1016/j.mtcomm.2017.12.010.

[25] M.M. Lee, J. Teuscher, T. Miyasaka, T.N. Murakami, H.J. Snaith, Efficient Hybrid Solar Cells Based on Meso-Superstructured Organometal Halide Perovskites, Science (80-.). 338 (2012) 643–647. https://doi.org/10.1126/SCIENCE.1228604.

[26] M.B. Johnston, L.M. Herz, Hybrid Perovskites for Photovoltaics: Charge-Carrier Recombination, Diffusion, and Radiative Efficiencies, Acc. Chem. Res. 49 (2015) 146–154. https://doi.org/10.1021/ACS.ACCOUNTS.5B00411.

[27] G. Grancini, M.K. Nazeeruddin, Dimensional tailoring of hybrid perovskites for photovoltaics, Nat. Rev. Mater. 2018 41. 4 (2018) 4–22. https://doi.org/10.1038/s41578-018-0065-0.

[28] S.D. Stranks, H.J. Snaith, Metal-halide perovskites for photovoltaic and light-emitting devices, Nat. Nanotechnol. 2015 105. 10 (2015) 391–402. https://doi.org/10.1038/nnano.2015.90.

[29] C. Li, X. Lu, W. Ding, L. Feng, Y. Gao, Z. Guo, IUCr, Formability of ABX3 (X = F, Cl, Br, I) halide perovskites, Urn:Issn:0108-7681. 64 (2008) 702–707. https://doi.org/10.1107/S0108768108032734.

[30] V. V. Bannikov, I.R. Shein, A.L. Ivanovskii, Electronic structure, chemical bonding and elastic properties of the first thorium-containing nitride perovskite TaThN3, Phys. Status Solidi – Rapid Res. Lett. 1 (2007) 89–91. https://doi.org/10.1002/PSSR.200600116.

[31] A. Fuertes, Nitride tuning of transition metal perovskites, APL Mater. 8 (2020) 020903. https://doi.org/10.1063/1.5140056.

[32] Y. Benhouria, M. Kibbou, N. Khossossi, J. Foshi, I. Essaoudi, A. Oubelkacem, A. Ainane, R. Ahuja, Carbides-anti-perovskites Mn3(Sn, Zn)C: Potential candidates for an application in magnetic refrigeration, Phys. E Low-Dimensional Syst. Nanostructures. 124 (2020) 114317. https://doi.org/10.1016/J.PHYSE.2020.114317.

[33] R.E. Schaak, M. Avdeev, W.L. Lee, G. Lawes, H.W. Zandbergen, J.D. Jorgensen, N.P. Ong, A.P. Ramirez, R.J. Cava, Formation of transition metal boride and carbide perovskites related to superconducting MgCNi3, J. Solid State Chem. 177 (2004) 1244–1251. https://doi.org/10.1016/J.JSSC.2003.10.032.

[34] T. Application, T. Wu, P. Gao, Development of Perovskite-Type Materials for, (2018) 1–32. https://doi.org/10.3390/ma11060999.

[35] Z. Zhang, Y. Zhu, Y. Zhong, W. Zhou, Z. Shao, Anion Doping: A New Strategy for Developing High-Performance Perovskite-Type Cathode Materials of Solid Oxide Fuel Cells, Adv. Energy Mater. 7 (2017) 1–9. https://doi.org/10.1002/aenm.201700242.

[36] H. Zhang, S. Liu, M.E. Scofield, S.S. Wong, X. Hong, V.B. Prakapenka, E. Greenberg, T.A. Tyson, Structural phase transitions in $SrTiO_3$ nanoparticles, Appl. Phys. Lett. 111 (2017) 052904. https://doi.org/10.1063/1.4997332.

[37] M. Dhiman, M. Tripathi, S. Singhal, Structural, optical and photocatalytic properties of different metal ions (Cr3+, Co2+, Ni2+, Cu2+ and Zn2+) substituted quaternary perovskites, Mater. Chem. Phys. 202 (2017) 40–49. https://doi.org/10.1016/j.matchemphys.2017.09.003.

[38] P. Sciences, Anion Substitution in Perovskite Related Materials For Fuel Cell Applications By Cathryn Hancock Supervisor : Prof Peter Slater Collaborative Supervisor : Dr John Varcoe, (2012).

[39] S. Pradhan, G.S. Roy, Study the Crystal Structure and Phase Transition of BaTiO 3 – A Pervoskite, Researcher. 55

(2013) 63–67. https://doi.org/10.7537/marsrsj050313.10.

[40] S. Lin, M. Zhang, Z. Wang, Y. Pan, First-principle investigation on multiferroicity in cubic perovskite LaMn3Fe4O12 compound, Comput. Mater. Sci. 133 (2017) 116–121. https://doi.org/10.1016/j.commatsci.2017.03.015.

[41] J. Hwang, R.R. Rao, L. Giordano, Y. Katayama, Y. Yu, Y. Shao-Horn, Perovskites in catalysis and electrocatalysis., Science. 358 (2017) 751–756. https://doi.org/10.1126/science.aam7092.

[42] A. Grimaud, K.J. May, C.E. Carlton, Y.-L. Lee, M. Risch, W.T. Hong, J. Zhou, Y. Shao-Horn, Double perovskites as a family of highly active catalysts for oxygen evolution in alkaline solution, Nat. Commun. 4 (2013) 1–7. https://doi.org/10.1038/ncomms3439.

[43] D.V. West, P.K. Davies, Triclinic and monoclinic structures of SrLaCuNbO6 and SrLaCuTaO6 double perovskites, J. Appl. Crystallogr. 44 (2011) 595–602. https://doi.org/10.1107/S0021889811012131.

[44] L.T. Tsymbal, Y.B. Bazaliy, V.N. Derkachenko, V.I. Kamenev, G.N. Kakazei, F.J. Palomares, P.E. Wigen, Magnetic and structural properties of spin-reorientation transitions in orthoferrites, J. Appl. Phys. 101 (2007) 123919. https://doi.org/10.1063/1.2749404.

[45] L.F. Da Silva, J.C. M'Peko, J. Andrés, A. Beltrán, L. Gracia, M.I.B. Bernardi, A. Mesquita, E. Antonelli, M.L. Moreira, V.R. Mastelaro, Insight into the effects of fe addition on the local structure and electronic properties of SrTiO3, J. Phys. Chem. C. 118 (2014) 4930–4940. https://doi.org/10.1021/jp408839q.

[46] H. Zhang, N. Li, K. Li, D. Xue, Structural stability and formability of ABO3-type perovskite compounds, Acta Crystallogr. Sect. B Struct. Sci. 63 (2007) 812–818. https://doi.org/10.1107/S0108768107046174.

[47] C.J. Howard, H.T. Stokes, Structures and phase transitions in perovskites - A group-theoretical approach, Acta Crystallogr. Sect. A Found. Crystallogr. 61 (2005) 93–111. https://doi.org/10.1107/S0108767304024493.

[48] H. Lehnert, H. Boysen, P. Dreier, Y. Yu, Room temperature structure of LaAlO3, Zeitschrift Für Krist. - Cryst. Mater. 215 (2000) 145–147. https://doi.org/10.1524/ZKRI.2000.215.3.145.

[49] A.E. Giannakas, A.K. Ladavos, P.J. Pomonis, Preparation, characterization and investigation of catalytic activity for NO + CO reaction of LaMnO3and LaFeO3perovskites prepared via microemulsion method, Appl. Catal. B Environ. 49 (2004) 147–148. https://doi.org/10.1016/j.apcatb.2003.12.002.

[50] L. Chonghe, T. Yihao, Z. Yingzhi, W. Chunmei, W. Ping, Prediction of lattice constant in perovskites of GdFeO3 structure, J. Phys. Chem. Solids. 64 (2003) 2147–2156. https://doi.org/10.1016/S0022-3697(03)00209-9.

[51] M. Troccaz, P. Gonnard, Y. Fetiveau, L. Eyraud, G. Grange, Goldschmidt factor and phase diagrams of doped titanate zirconates, Ferroelectrics. 14 (1976) 679–681. https://doi.org/10.1080/00150197608236699.

[52] G. Pilania, P. V. Balachandran, J.E. Gubernatis, T. Lookman, Classification of ABO3 perovskite solids: A machine learning study, Acta Crystallogr. Sect. B Struct. Sci. Cryst. Eng. Mater. 71 (2015) 507–513. https://doi.org/10.1107/S2052520615013979.

[53] C. Li, K.C.K. Soh, P. Wu, Formability of ABO3 perovskites, J. Alloys Compd. 372 (2004) 40–48. https://doi.org/10.1016/J.JALLCOM.2003.10.017.

[54] C.J. Bartel, C. Sutton, B.R. Goldsmith, R. Ouyang, C.B. Musgrave, L.M. Ghiringhelli, M. Scheffler, New tolerance factor to predict the stability of perovskite oxides and halides, Sci. Adv. 5 (2019) eaav0693. https://doi.org/10.1126/SCIADV.AAV0693.

[55] Y. Tamraoui, B. Manoun, F. Mirinioui, I. Saadoune, R. Haloui, A. Elhachmi, E. Saad, P. Lazor, Temperature and composition induced phase transitions in Sr2−xCa1+xTeO6 ($0 \leq x \leq 2$) double perovskite oxides, J. Mol. Struct. 1131 (2017) 103–113. https://doi.org/10.1016/j.molstruc.2016.11.036.

[56] Y. Tamraoui, B. Manoun, F. Mirinioui, R. Haloui, P. Lazor, X-ray diffraction and Raman spectroscopy studies of temperature and composition induced phase transitions in Ba2-xSrxMgTeO6($0 \leq x \leq 2$), J. Alloys Compd. 603 (2014). https://doi.org/10.1016/j.jallcom.2014.03.037.

[57] B. Manoun, A. Ezzahi, S. Benmokhtar, L. Bih, Y. Tamraoui, R. Haloui, F. Mirinioui, S. Addakiri, J.M. Igartua, P. Lazor, X-ray diffraction and Raman spectroscopy studies of temperature and composition induced phase transitions in Ba2-xSr

xMWO6 (M = Ni, Co and 0 ≤ x ≤ 2) double perovskite oxides, J. Mol. Struct. 1045 (2013) 1–14. https://doi.org/10.1016/j.molstruc.2013.03.059.

[58] M. Etter, M. Müller, M. Hanfland, R.E. Dinnebier, High-pressure phase transitions in the rare-earth orthoferrite LaFeO3, Acta Crystallogr. Sect. B Struct. Sci. Cryst. Eng. Mater. 70 (2014) 452–458. https://doi.org/10.1107/S2052520614007379.

[59] P.P. Ma, Q.L. Lu, N. Lei, Y.K. Liu, B. Yu, J.M. Dai, S.H. Li, G.H. Jiang, Effect of A-site substitution by Ca or Sr on the structure and electrochemical performance of LaMnO3 perovskite, Electrochim. Acta. 332 (2020) 135489. https://doi.org/10.1016/J.ELECTACTA.2019.135489.

[60] J. Lu, Y. Li, Y. Ding, Li-ion conductivity and electrochemical stability of A-site deficient perovskite-structured Li3x-yLa1-xAl1-yTiyO3 electrolytes, Mater. Res. Bull. 133 (2021) 111019. https://doi.org/10.1016/J.MATERRESBULL.2020.111019.

[61] O. Haas, U.F. Vogt, C. Soltmann, A. Braun, W.S. Yoon, X.Q. Yang, T. Graule, The Fe K-edge X-ray absorption characteristics of La1−xSrxFeO3−δ prepared by solid state reaction, Mater. Res. Bull. 44 (2009) 1397–1404. https://doi.org/10.1016/J.MATERRESBULL.2008.11.026.

[62] T. Komabayashi, K. Hirose, N. Sata, Y. Ohishi, L.S. Dubrovinsky, Phase transition in CaSiO3 perovskite, Earth Planet. Sci. Lett. 260 (2007) 564–569. https://doi.org/10.1016/J.EPSL.2007.06.015.

[63] A.M. Glazer, The classification of tilted octahedra in perovskites, Acta Crystallogr. Sect. B Struct. Crystallogr. Cryst. Chem. 28 (1972) 3384–3392. https://doi.org/10.1107/S0567740872007976.

[64] M.W. Lufaso, P.M. Woodward, IUCr, Prediction of the crystal structures of perovskites using the software program SPuDS, Urn:Issn:0108-7681. 57 (2001) 725–738. https://doi.org/10.1107/S0108768101015282.

[65] J. Wang, S. Yin, M. Komatsu, T. Sato, Lanthanum and nitrogen co-doped SrTiO3 powders as visible light sensitive photocatalyst, J. Eur. Ceram. Soc. 25 (2005) 3207–3212. https://doi.org/10.1016/j.jeurceramsoc.2004.07.027.

[66] H.C. Chen, C.W. Huang, J.C.S. Wu, S.T. Lin, Theoretical investigation of the metal-doped SrTiO 3 photocatalysts for water splitting, J. Phys. Chem. C. 116 (2012) 7897–7903. https://doi.org/10.1021/jp300910e.

[67] K. Kato, J. Jiang, Y. Sakata, A. Yamakata, Effect of Na-Doping on Electron Decay Kinetics in $SrTiO_3$ Photocatalyst, ChemCatChem. 11 (2019) 6349–6354. https://doi.org/10.1002/cctc.201901669.

[68] A. Alshoaibi, O. Saber, F. Ahmed, Enhancement of Optical Activity and Properties of Barium Titanium Oxides to Be Active in Sunlight through Using Hollandite Phase Instead of Perovskite Phase, Cryst. 2021, Vol. 11, Page 550. 11 (2021) 550. https://doi.org/10.3390/CRYST11050550.

[69] W. Zhou, H. Deng, L. Yu, P. Yang, J. Chu, Optical band-gap narrowing in perovskite ferroelectric ABO3 ceramics (A=Pb, Ba; B=Ti) by ion substitution technique, Ceram. Int. 41 (2015) 13389–13392. https://doi.org/10.1016/J.CERAMINT.2015.07.127.

[70] Chao Zhang, Nan Jiang, Shiai Xu, Zheng Li, Xingliang Liu, Tianle Cheng, Aixia Han, Haitang Lv, Wenliang Sun, Yunlei Hou, Towards high visible light photocatalytic activity in rare earth and N co-doped SrTiO 3 : a first principles evaluation and prediction, RSC Adv. 7 (2017) 16282–16289. https://doi.org/10.1039/C6RA27840J.

[71] Y.-Q. Wang, 汪月琴, Y. Liu, 刘银, M.-X. Zhang, 张明旭, F.-F. Min, 闵凡飞, Electronic Structure and Visible-Light Absorption of Transition Metals (TM=Cr, Mn, Fe, Co) and Zn-Codoped SrTiO3: a First-Principles Study*, Chinese Phys. Lett. 35 (2018) 017101. https://doi.org/10.1088/0256-307X/35/1/017101.

[72] G. Jácome-Acatitla, M. Álvarez-Lemus, R. López-González, C. García-Mendoza, A. Sánchez-López, D. Hernández-Acosta, Photodegradation of 4-chloropehol in aqueous media using LaBO3 (B = Fe, Mn, Co) perovskites: Study of the influence of the transition metal ion in the photocatalytic activity, J. Photochem. Photobiol. A Chem. 390 (2020) 112330. https://doi.org/10.1016/J.JPHOTOCHEM.2019.112330.

[73] L.I. Ibarra-Rodriguez, A.M. Huerta-Flores, J.M. Mora-Hernandez, L.M. Torres-Martínez, Photocatalytic evolution of H2 over visible-light active LaMO3 (M: Co, Mn, Fe) perovskite materials: Roles of oxygenated species in catalytic performance, J. Phys. Chem. Solids. 136 (2020) 109189. https://doi.org/10.1016/J.JPCS.2019.109189.

[74] K. Sedeek, S.A. Said, T.Z. Amer, N. Makram, H. Hantour, Band gap tuning in nanocrystalline SrTi0.9Fe0.1O2.968

perovskite type for photocatalytic and photovoltaic applications, Ceram. Int. 45 (2019) 1202–1207. https://doi.org/10.1016/j.ceramint.2018.09.305.

[75] S.Y. Smolin, M.D. Scafetta, A.K. Choquette, M.Y. Sfeir, J.B. Baxter, S.J. May, Static and Dynamic Optical Properties of La1-xSrxFeO3-δ: The Effects of A-Site and Oxygen Stoichiometry, Chem. Mater. 28 (2016) 97–105. https://doi.org/10.1021/acs.chemmater.5b03273.

[76] M. Abdi, V. Mahdikhah, S. Sheibani, Visible light photocatalytic performance of La-Fe co-doped SrTiO3 perovskite powder, Opt. Mater. (Amst). 102 (2020) 109803. https://doi.org/10.1016/j.optmat.2020.109803.

[77] C. Sasikala, N. Durairaj, I. Baskaran, B. Sathyaseelan, M. Henini, E. Manikandan, Transition metal titanium (Ti) doped LaFeO3nanoparticles for enhanced optical structural and magnetic properties, J. Alloys Compd. 712 (2017) 870–877. https://doi.org/10.1016/j.jallcom.2017.04.133.

[78] S.K. Ray, J. Cho, J. Hur, A critical review on strategies for improving efficiency of BaTiO3-based photocatalysts for wastewater treatment, J. Environ. Manage. 290 (2021) 112679. https://doi.org/10.1016/J.JENVMAN.2021.112679.

[79] P. Xie, F. Yang, R. Li, C. Ai, C. Lin, S. Lin, Improving hydrogen evolution activity of perovskite BaTiO3 with Mo doping: Experiments and first-principles analysis, Int. J. Hydrogen Energy. 44 (2019) 11695–11704. https://doi.org/10.1016/J.IJHYDENE.2019.03.145.

[80] J. Cao, Y. Ji, C. Tian, Z. Yi, Synthesis and enhancement of visible light activities of nitrogen-doped BaTiO3, J. Alloys Compd. 615 (2014) 243–248. https://doi.org/10.1016/J.JALLCOM.2014.07.008.

[81] D. Mateo, N. Morlanes, P. Maity, G. Shterk, O.F. Mohammed, J. Gascon, Efficient Visible-Light Driven Photothermal Conversion of CO2 to Methane by Nickel Nanoparticles Supported on Barium Titanate, Adv. Funct. Mater. 31 (2021) 2008244. https://doi.org/10.1002/ADFM.202008244.

[82] M. Aamir, I. Bibi, S. Ata, F. Majid, S. Kamal, N. Alwadai, M. Sultan, S. Iqbal, M. Aadil, M. Iqbal, Graphene oxide nanocomposite with Co and Fe doped LaCrO3 perovskite active under solar light irradiation for the enhanced degradation of crystal violet dye, J. Mol. Liq. 322 (2021) 114895. https://doi.org/10.1016/J.MOLLIQ.2020.114895.

[83] L. Zeng, T. Peng, H. Sun, J. Yang, Y. Li, Y. Qin, Fe-doped LaNi1-xFexO3 perovskite oxides for enhanced visible-light-driven photocatalytic activity, J. Solid State Chem. 297 (2021) 122033. https://doi.org/10.1016/J.JSSC.2021.122033.

[84] E. Yu, J. Chen, H. Jia, Enhanced light-driven photothermocatalytic activity on selectively dissolved LaTi1−xMnxO3+δ perovskites by photoactivation, J. Hazard. Mater. 399 (2020) 122942. https://doi.org/10.1016/J.JHAZMAT.2020.122942.

[85] W. Li, K. Jiang, Z. Li, S. Gong, R.L.Z. Hoye, Z. Hu, Y. Song, C. Tian, J. Kim, K.H.L. Zhang, S. Cho, J.L. MacManus-Driscoll, Origin of Improved Photoelectrochemical Water Splitting in Mixed Perovskite Oxides, Adv. Energy Mater. 8 (2018) 1801972. https://doi.org/10.1002/aenm.201801972.

[86] A. El Hachmi, F. El Bachraoui, S. Louihi, Y. Tamraoui, S. Benmokhtar, L. Bih, M. Sajieddine, P. Lazor, B. Manoun, Structural, Magnetic and Optical Properties Study of Tellurium-Based Perovskites: Sr<inf>3−x</inf>Pb<inf>x</inf>Fe<inf>2</inf>TeO<inf>9</inf> (0 ≤ x ≤ 2.25), J. Inorg. Organomet. Polym. Mater. 30 (2020). https://doi.org/10.1007/s10904-020-01446-4.

[87] M. Azdouz, B. Manoun, M. Azrour, L. Bih, L. El Ammari, S. Benmokhtar, P. Lazor, Synthesis, Rietveld refinements and Raman spectroscopy studies of the solid solution Na1−xKxPb4(VO4)3 (0⩽x⩽1), J. Mol. Struct. 963 (2010) 258–266. https://doi.org/10.1016/j.molstruc.2009.10.047.

[88] M. Li, M. Zhao, F. Li, W. Zhou, V.K. Peterson, X. Xu, Z. Shao, I. Gentle, Z. Zhu, A niobium and tantalum co-doped perovskite cathode for solid oxide fuel cells operating below 500 °c, Nat. Commun. 8 (2017). https://doi.org/10.1038/ncomms13990.

[89] L. Shu, J. Sunarso, S.S. Hashim, J. Mao, W. Zhou, F. Liang, Advanced perovskite anodes for solid oxide fuel cells: A review, Int. J. Hydrogen Energy. 44 (2019) 31275–31304. https://doi.org/10.1016/j.ijhydene.2019.09.220.

[90] A. Lahmar, S. Habouti, C.H. Solterbeck, M. Es-Souni, B. Elouadi, Correlation between structure, dielectric, and ferroelectric properties in BiFeO3 - LaMnO3 solid solution thin films, J. Appl. Phys. 105 (2009). https://doi.org/10.1063/1.3063813.

[91] A. Puhan, B. Bhushan, V. Kumar, H.S. Panda, A. Priyam, D. Das, D. Rout, Tailoring the structural, optical and magnetic

properties of BiFeO 3 multiferroic nanoparticles by Ba, Cr co-doping, Mater. Sci. Eng. B Solid-State Mater. Adv. Technol. 241 (2019) 48–54. https://doi.org/10.1016/j.mseb.2019.02.009.

[92] F. Casanova Monteiro, P. de Jesus Cubas, V. Sena Kosera, J.F. Haas Leandro Monteiro, S.T. Fujiwara, Photocatalytic activity of BiFeO3 in pellet form synthetized using solid state reaction and modified Pechini method, J. Photochem. Photobiol. A Chem. 367 (2018) 390–396. https://doi.org/10.1016/j.jphotochem.2018.08.051.

[93] R. Asahi, T. Morikawa, T. Ohwaki, K. Aoki, Y. Taga, Visible-light photocatalysis in nitrogen-doped titanium oxides, Science (80-.). 293 (2001) 269–271. https://doi.org/10.1126/science.1061051.

[94] R. Xiao, R. Qin, C. Zhang, S. Chen, J. Wang, Catalytic decomposition of ethyl acetate over La-modified Cu-Mn oxide supported on Honeycomb ceramic, J. Rare Earths. (2020). https://doi.org/10.1016/j.jre.2020.10.015.

[95] K. Sedeek, S.A. Said, T.Z. Amer, N. Makram, H. Hantour, Band gap tuning in nanocrystalline SrTi0.9Fe0.1O2.968 perovskite type for photocatalytic and photovoltaic applications, Ceram. Int. 45 (2019) 1202–1207. https://doi.org/10.1016/J.CERAMINT.2018.09.305.

[96] B. Ghosh, B. Febriansyah, P.C. Harikesh, T.M. Koh, S. Hadke, L.H. Wong, J. England, S.G. Mhaisalkar, N. Mathews, Direct Band Gap Mixed-Valence Organic-inorganic Gold Perovskite as Visible Light Absorbers, Chem. Mater. 32 (2020) 6318–6325. https://doi.org/10.1021/acs.chemmater.0c00345.

[97] Z. Hu, Z. Lin, J. Su, J. Zhang, J. Chang, Y. Hao, A Review on Energy Band-Gap Engineering for Perovskite Photovoltaics, Sol. RRL. 3 (2019) 1900304. https://doi.org/10.1002/solr.201900304.

[98] J. Varignon, M. Bibes, A. Zunger, Origin of band gaps in 3d perovskite oxides, Nat. Commun. 10 (2019) 1658. https://doi.org/10.1038/s41467-019-09698-6.

[99] C. Wang, H. Qiu, T. Inoue, Q. Yao, Band gap engineering of SrTiO3 for water splitting under visible light irradiation, Int. J. Hydrogen Energy. 39 (2014) 12507–12514. https://doi.org/10.1016/J.IJHYDENE.2014.06.059.

[100] E. Kim, Z.-T. Jiang, K. No, Measurement and Calculation of Optical Band Gap of Chromium Aluminum Oxide Films, Jpn. J. Appl. Phys. 39 (2000) 4820–4825. https://doi.org/10.1143/JJAP.39.4820.

[101] I. Grinberg, D.V. West, M. Torres, G. Gou, D.M. Stein, L. Wu, G. Chen, E.M. Gallo, A.R. Akbashev, P.K. Davies, J.E. Spanier, A.M. Rappe, Perovskite oxides for visible-light-absorbing ferroelectric and photovoltaic materials, Nature. 503 (2013) 509–512. https://doi.org/10.1038/nature12622.

[102] T. Qi, I. Grinberg, A.M. Rappe, Band-gap engineering via local environment in complex oxides, Phys. Rev. B - Condens. Matter Mater. Phys. 83 (2011) 224108. https://doi.org/10.1103/PhysRevB.83.224108.

[103] C.-C. Hu, C.-C. Tsai, H. Teng, Structure Characterization and Tuning of Perovskite-Like NaTaO 3 for Applications in Photoluminescence and Photocatalysis, J. Am. Ceram. Soc. 92 (2009) 460–466. https://doi.org/10.1111/j.1551-2916.2008.02869.x.

[104] X. Zhou, J. Shi, C. Li, Effect of metal doping on electronic structure and visible light absorption of SrTiO3 and NaTaO3 (Metal = Mn, Fe, and Co), J. Phys. Chem. C. 115 (2011) 8305–8311. https://doi.org/10.1021/jp200022x.

[105] A. Kudo, Y. Miseki, Heterogeneous photocatalyst materials for water splitting, Chem. Soc. Rev. 38 (2009) 253–278. https://doi.org/10.1039/b800489g.

[106] H. Li, S. Yin, Y. Wang, T. Sekino, S.W. Lee, T. Sato, Roles of Cr3+ doping and oxygen vacancies in SrTiO3 photocatalysts with high visible light activity for NO removal, J. Catal. 297 (2013) 65–69. https://doi.org/10.1016/j.jcat.2012.09.019.

[107] V. F. lvovich, Impedance Spectroscopy: Applications to Electrochemical and Dielectric Phenomena - Vadim F. Lvovich - Google Boeken, (2012).

[108] K.C. Kao, Dielectric Phenomena in Solids, Dielectr. Phenom. Solids. (2004) 1–581. https://doi.org/10.1016/B978-0-12-396561-5.X5010-5.

[109] V.S. Puli, D.K. Pradhan, D.B. Chrisey, M. Tomozawa, G.L. Sharma, J.F. Scott, R.S. Katiyar, Structure, dielectric, ferroelectric, and energy density properties of (1 − x)BZT–xBCT ceramic capacitors for energy storage applications, J. Mater. Sci. 2012 485. 48 (2012) 2151–2157. https://doi.org/10.1007/S10853-012-6990-1.

[110] M. Zhou, R. Liang, Z. Zhou, S. Yan, X. Dong, Novel Sodium Niobate-Based Lead-Free Ceramics as New Environment-Friendly Energy Storage Materials with High Energy Density, High Power Density, and Excellent Stability, ACS Sustain. Chem. Eng. 6 (2018) 12755–12765. https://doi.org/10.1021/ACSSUSCHEMENG.8B01926.

[111] H. Zhang, T. Wei, Q. Zhang, W. Ma, P. Fan, D. Salamon, S.-T. Zhang, B. Nan, H. Tan, Z.-G. Ye, A review on the development of lead-free ferroelectric energy-storage ceramics and multilayer capacitors, J. Mater. Chem. C. 8 (2020) 16648–16667. https://doi.org/10.1039/D0TC04381H.

[112] B. Luo, X. Wang, E. Tian, H. Song, G. Li, L. Li, Electronic, dielectric and optical properties of orthorhombic lanthanum gallate perovskite, J. Alloys Compd. 708 (2017) 187–193. https://doi.org/10.1016/j.jallcom.2017.02.267.

[113] W. Payne, V. Tennery, Dielectric and Structural Investigations of the System BaTi03-BaHfO3, J. Am. Ceram. Soc. 418 (1965) 413. https://doi.org/10.1111/j.1151-2916.1965.tb14779.x.

[114] X.H. Wang, R.Z. Chen, Z.L. Gui, L.T. Li, The grain size effect on dielectric properties of BaTiO3 based ceramics, in: Mater. Sci. Eng. B Solid-State Mater. Adv. Technol., Elsevier, 2003: pp. 199–202. https://doi.org/10.1016/S0921-5107(02)00520-2.

[115] H. Felhi, R. Lahouli, M. Smari, H. Rahmouni, K. Khirouni, E. Dhahri, Study of the structural, electric and dielectric proprieties of Bi1-xNdxMn2O5 (x=0, x=0.1 and x=0.2), J. Mol. Struct. 1179 (2019) 1–10. https://doi.org/10.1016/j.molstruc.2018.10.086.

[116] D. Czekaj, Fabrication and dielectric properties of donor doped BaTiO3 ceramics, Arch. Metall. Mater. 54 (2009) 923–933. https://doi.org/10.2478/amm-2013-0163.

[117] Z. Zhao, V. Buscaglia, M. Viviani, M.T. Buscaglia, L. Mitoseriu, A. Testino, M. Nygren, M. Johnsson, P. Nanni, Grain-size effects on the ferroelectric behavior of dense nanocrystalline <span class, Phys. Rev. B. 70 (2004) 024107. https://doi.org/10.1103/PhysRevB.70.024107.

[118] V.S. Puli, A. Kumar, D.B. Chrisey, M. Tomozawa, J.F. Scott, R.S. Katiyar, Barium zirconate-titanate/barium calcium-titanate ceramics via sol–gel process: novel high-energy-density capacitors, J. Phys. D. Appl. Phys. 44 (2011) 395403. https://doi.org/10.1088/0022-3727/44/39/395403.

[119] W. Li, Z. Xu, R. Chu, P. Fu, G. Zang, Large Piezoelectric Coefficient in (Ba1−xCax)(Ti0.96Sn0.04)O3 Lead-Free Ceramics, J. Am. Ceram. Soc. 94 (2011) 4131–4133. https://doi.org/10.1111/J.1551-2916.2011.04888.X.

[120] A. Jalalian, A.M. Grishin, X.L. Wang, Z.X. Cheng, S.X. Dou, Large piezoelectric coefficient and ferroelectric nanodomain switching in Ba(Ti0.80Zr0.20)O3-0.5(Ba0.70Ca0.30)TiO3 nanofibers and thin films, Appl. Phys. Lett. 104 (2014) 103112. https://doi.org/10.1063/1.4867013.

[121] G.H. Jaffari, M.A. Iqbal, S.K. Hasanain, A. Ali, A.S. Bhatti, S.I. Shah, A. Mumtaz, Effect of densification on the ferroelectric response of Ba0.4Sr0.6TiO3, Solid State Commun. 205 (2015) 46–50. https://doi.org/10.1016/J.SSC.2015.01.001.

[122] W. Abbas, D. Ho, A. Pramanick, High energy storage efficiency and thermal stability of A-site-deficient and 110-textured BaTiO3–BiScO3 thin films, J. Am. Ceram. Soc. 103 (2020) 3168–3177. https://doi.org/10.1111/JACE.17002.

[123] F. Si, B. Tang, Z. Fang, H. Li, S. Zhang, Enhanced energy storage and fast charge-discharge properties of (1-x)BaTiO3-xBi(Ni1/2Sn1/2)O3 relaxor ferroelectric ceramics, Ceram. Int. 45 (2019) 17580–17590. https://doi.org/10.1016/J.CERAMINT.2019.05.323.

[124] B. Xiong, H. Hao, S. Zhang, H. Liu, M. Cao, Structure, Dielectric Properties and Temperature Stability of BaTiO3–Bi(Mg1/2Ti1/2)O3 Perovskite Solid Solutions, J. Am. Ceram. Soc. 94 (2011) 3412–3417. https://doi.org/10.1111/J.1551-2916.2011.04519.X.

[125] T. Wang, L. Jin, C. Li, Q. Hu, X. Wei, Relaxor Ferroelectric BaTiO3–Bi(Mg2/3Nb1/3)O3 Ceramics for Energy Storage Application, J. Am. Ceram. Soc. 98 (2015) 559–566. https://doi.org/10.1111/JACE.13325.

[126] H. Guo, H. Shimizu, Y. Mizuno, C.A. Randall, Strategy for stabilization of the antiferroelectric phase (Pbma) over the metastable ferroelectric phase (P21ma) to establish double loop hysteresis in lead-free (1−x)NaNbO3-xSrZrO3 solid solution, J. Appl. Phys. 117 (2015) 214103. https://doi.org/10.1063/1.4921876.

[127] C. Xu, Z. Fu, Z. Liu, L. Wang, S. Yan, X. Chen, F. Cao, X. Dong, G. Wang, La/Mn Codoped AgNbO3 Lead-Free

Antiferroelectric Ceramics with Large Energy Density and Power Density, ACS Sustain. Chem. Eng. 6 (2018) 16151–16159. https://doi.org/10.1021/ACSSUSCHEMENG.8B02821.

[128] Q. Xu, Z. Song, W. Tang, H. Hao, L. Zhang, M. Appiah, M. Cao, Z. Yao, Z. He, H. Liu, Ultra-Wide Temperature Stable Dielectrics Based on Bi0.5Na0.5TiO3–NaNbO3 System, J. Am. Ceram. Soc. 98 (2015) 3119–3126. https://doi.org/10.1111/JACE.13693.

[129] L. Liu, D. Shi, M. Knapp, H. Ehrenberg, L. Fang, J. Chen, Large strain response based on relaxor-antiferroelectric coherence in Bi0.5Na0.5TiO3–SrTiO3–(K0.5Na0.5)NbO3 solid solutions, J. Appl. Phys. 116 (2014) 184104. https://doi.org/10.1063/1.4901549.

[130] B. Liu, X. Wang, R. Zhang, L. Li, Grain size effect and microstructure influence on the energy storage properties of fine-grained BaTiO3-based ceramics, J. Am. Ceram. Soc. 100 (2017) 3599–3607. https://doi.org/10.1111/JACE.14802.

[131] L. Wu, X. Wang, H. Gong, Y. Hao, Z. Shen, L. Li, Core-satellite BaTiO3@SrTiO3 assemblies for a local compositionally graded relaxor ferroelectric capacitor with enhanced energy storage density and high energy efficiency, J. Mater. Chem. C. 3 (2015) 750–758. https://doi.org/10.1039/C4TC02291B.

[132] V.S. Puli, D.K. Pradhan, B.C. Riggs, D.B. Chrisey, R.S. Katiyar, Investigations on structure, ferroelectric, piezoelectric and energy storage properties of barium calcium titanate (BCT) ceramics, J. Alloys Compd. 584 (2014) 369–373. https://doi.org/10.1016/J.JALLCOM.2013.09.108.

[133] Q. Hu, T. Wang, L. Zhao, L. Jin, Z. Xu, X. Wei, Dielectric and energy storage properties of BaTiO3–Bi(Mg1/2Ti1/2)O3 ceramic: Influence of glass addition and biasing electric field, Ceram. Int. 43 (2017) 35–39. https://doi.org/10.1016/J.CERAMINT.2016.08.005.

[134] W.-B. Li, D. Zhou, L.-X. Pang, Enhanced energy storage density by inducing defect dipoles in lead free relaxor ferroelectric BaTiO3-based ceramics, Appl. Phys. Lett. 110 (2017) 132902. https://doi.org/10.1063/1.4979467.

[135] Qi Xu, Hanxing Liu, Lin Zhang, Juan Xie, Hua Hao, Minghe Cao, Zhonghua Yao, M. T. Lanagan, Structure and electrical properties of lead-free Bi 0.5 Na 0.5 TiO 3 -based ceramics for energy-storage applications, RSC Adv. 6 (2016) 59280–59291. https://doi.org/10.1039/C6RA11744A.

[136] Q. Xu, M.T. Lanagan, X. Huang, J. Xie, L. Zhang, H. Hao, H. Liu, Dielectric behavior and impedance spectroscopy in lead-free BNT–BT–NBN perovskite ceramics for energy storage, Ceram. Int. 42 (2016) 9728–9736. https://doi.org/10.1016/J.CERAMINT.2016.03.062.

[137] N. Qu, H. Du, X. Hao, A new strategy to realize high comprehensive energy storage properties in lead-free bulk ceramics, J. Mater. Chem. C. 7 (2019) 7993–8002. https://doi.org/10.1039/C9TC02088H.

[138] J. Ye, G. Wang, M. Zhou, N. Liu, X. Chen, S. Li, F. Cao, X. Dong, Excellent comprehensive energy storage properties of novel lead-free NaNbO3-based ceramics for dielectric capacitor applications, J. Mater. Chem. C. 7 (2019) 5639–5645. https://doi.org/10.1039/C9TC01414D.

[139] Z. Yang, H. Du, L. Jin, Q. Hu, H. Wang, Y. Li, J. Wang, F. Gao, S. Qu, Realizing high comprehensive energy storage performance in lead-free bulk ceramics via designing an unmatched temperature range, J. Mater. Chem. A. 7 (2019) 27256–27266. https://doi.org/10.1039/C9TA11314B.

[140] M. Zhou, R. Liang, Z. Zhou, X. Dong, Superior energy storage properties and excellent stability of novel NaNbO3-based lead-free ceramics with A-site vacancy obtained via a Bi2O3 substitution strategy, J. Mater. Chem. A. 6 (2018) 17896–17904. https://doi.org/10.1039/C8TA07303A.

[141] S. Suthirakun, S.C. Ammal, G. Xiao, F. Chen, K. Huang, H.-C. zur Loye, A. Heyden, Obtaining mixed ionic/electronic conductivity in perovskite oxides in a reducing environment: A computational prediction for doped SrTiO3, Solid State Ionics. 228 (2012) 37–45. https://doi.org/10.1016/J.SSI.2012.09.013.

[142] J. Kim, S. Seo, J. Lee, H. Choi, S. Kim, G. Piao, Y.R. Kim, B. Park, J. Lee, Y. Jung, H. Park, S. Lee, K. Lee, Efficient and Stable Perovskite-Based Photocathode for Photoelectrochemical Hydrogen Production, Adv. Funct. Mater. (2021) 2008277. https://doi.org/10.1002/adfm.202008277.

[143] A. Kostopoulou, K. Brintakis, N.K. Nasikas, E. Stratakis, Perovskite nanocrystals for energy conversion and storage, Nanophotonics. 0 (2019). https://doi.org/10.1515/nanoph-2019-0119.

[144] L. Blum, W.A. Meulenberg, H. Nabielek, R. Steinberger-Wilckens, Worldwide SOFC Technology Overview and Benchmark, Int. J. Appl. Ceram. Technol. 2 (2005) 482–492. https://doi.org/10.1111/J.1744-7402.2005.02049.X.

[145] F. Grimm, M. Neubert, J. Karl, N.H. Menzler, O. Guillon, Selection of cathode materials for forsterite-supported solid oxide fuel cells – Part II: Electro-catalytic activity, J. Power Sources. 451 (2020) 227811. https://doi.org/10.1016/J.JPOWSOUR.2020.227811.

[146] F. Grimm, N.H. Menzler, O. Guillon, Selection of cathode materials for forsterite supported solid oxide fuel cells – Part I: Materials interactions, J. Power Sources. 451 (2020) 227607. https://doi.org/10.1016/J.JPOWSOUR.2019.227607.

[147] M. Zhang, M. Yang, Z. Hou, Y. Dong, M. Cheng, A bi-layered composite cathode of La0.8Sr0.2MnO3-YSZ and La0.8Sr0.2MnO3-La0.4Ce0.6O1.8 for IT-SOFCs, Electrochim. Acta. 53 (2008) 4998–5006. https://doi.org/10.1016/J.ELECTACTA.2008.01.095.

[148] R. Radhakrishnan, A. V. Virkar, S.C. Singhal, Estimation of Charge-Transfer Resistivity of La0.8Sr0.2MnO3 Cathode on Y 0.16Zr0.84 O 2 Electrolyte Using Patterned Electrodes, J. Electrochem. Soc. 152 (2004) A210. https://doi.org/10.1149/1.1829415.

[149] T. Suzuki, M. Awano, P. Jasinski, V. Petrovsky, H.U. Anderson, Composite (La, Sr)MnO3–YSZ cathode for SOFC, Solid State Ionics. 177 (2006) 2071–2074. https://doi.org/10.1016/J.SSI.2005.12.016.

[150] R.K. Gupta, E.Y. Kim, Y.H. Kim, C.M. Whang, Effect of strontium ion doping on structural, thermal, morphological and electrical properties of a co-doped lanthanum manganite system, J. Alloys Compd. 490 (2010) 56–61. https://doi.org/10.1016/J.JALLCOM.2009.10.095.

[151] T. Noh, J. Ryu, J. Kim, Y.N. Kim, H. Lee, Structural and impedance analysis of copper doped LSM cathode for IT-SOFCs, J. Alloys Compd. 557 (2013) 196–201. https://doi.org/10.1016/J.JALLCOM.2013.01.002.

[152] P. Zhang, G. Guan, D.S. Khaerudini, X. Hao, C. Xue, M. Han, Y. Kasai, A. Abudula, B-site Mo-doped perovskite Pr0.4Sr0.6 (Co0.2Fe0.8)1−xMoxO3−σ (x = 0, 0.05, 0.1 and 0.2) as electrode for symmetrical solid oxide fuel cell, J. Power Sources. 276 (2015) 347–356. https://doi.org/10.1016/J.JPOWSOUR.2014.11.141.

[153] K.K. Hansen, A-Site Deficient (Pr0.6Sr0.4) 1 − sFe0.8Co0.2O3 − δ Perovskites as Solid Oxide Fuel Cell Cathodes, J. Electrochem. Soc. 156 (2009) B1257. https://doi.org/10.1149/1.3194786.

[154] J.-H. Kim, A. Manthiram, LnBaCo2O5 + δ Oxides as Cathodes for Intermediate-Temperature Solid Oxide Fuel Cells, J. Electrochem. Soc. 155 (2008) B385. https://doi.org/10.1149/1.2839028.

[155] Q. Zhou, W.C.J. Wei, Y. Guo, D. Jia, LaSrMnCoO5+δ as cathode for intermediate-temperature solid oxide fuel cells, Electrochem. Commun. 19 (2012) 36–38. https://doi.org/10.1016/J.ELECOM.2012.03.001.

[156] J.H. Kim, J.T.S. Irvine, Characterization of layered perovskite oxides NdBa1−xSrxCo2O5+δ (x = 0 and 0.5) as cathode materials for IT-SOFC, Int. J. Hydrogen Energy. 37 (2012) 5920–5929. https://doi.org/10.1016/J.IJHYDENE.2011.12.150.

[157] N. Li, Z. Lü, B. Wei, X. Huang, K. Chen, Y. Zhang, W. Su, Characterization of GdBaCo2O5+δ cathode for IT-SOFCs, J. Alloys Compd. 454 (2008) 274–279. https://doi.org/10.1016/J.JALLCOM.2006.12.017.

[158] E. V. Tsipis, M. V. Patrakeev, V. V. Kharton, A.A. Yaremchenko, G.C. Mather, A.L. Shaula, I.A. Leonidov, V.L. Kozhevnikov, J.R. Frade, Transport properties and thermal expansion of Ti-substituted La1−xSrxFeO3−δ (x=0.5–0.7), Solid State Sci. 7 (2005) 355–365. https://doi.org/10.1016/J.SOLIDSTATESCIENCES.2005.01.001.

[159] V. V. Kharton, A. V. Kovalevsky, A.P. Viskup, J.R. Jurado, F.M. Figueiredo, E.N. Naumovich, J.R. Frade, Transport Properties and Thermal Expansion of Sr0.97Ti1−xFexO3−δ (x=0.2–0.8), J. Solid State Chem. 156 (2001) 437–444. https://doi.org/10.1006/JSSC.2000.9019.

[160] J.H. Park, K.Y. Kim, S. Do Park, Oxygen permeation and stability of La0.6Sr0.4TixFe1−xO3−δ (x = 0.2 and 0.3) membrane, Desalination. 245 (2009) 559–569. https://doi.org/10.1016/J.DESAL.2009.02.021.

[161] S. Park, S. Choi, J. Kim, J. Shin, G. Kim, Strontium Doping Effect on High-Performance PrBa1−xSrxCo2O5+δ as a Cathode Material for IT-SOFCs, ECS Electrochem. Lett. 1 (2012) F29. https://doi.org/10.1149/2.007205EEL.

[162] J. Kim, S. Choi, S. Park, C. Kim, J. Shin, G. Kim, Effect of Mn on the electrochemical properties of a layered perovskite

NdBa0.5Sr0.5Co2 − xMnxO5 + δ (x = 0, 0.25, and 0.5) for intermediate-temperature solid oxide fuel cells, Electrochim. Acta. 112 (2013) 712–718. https://doi.org/10.1016/J.ELECTACTA.2013.09.014.

[163] J. Xue, Y. Shen, T. He, Double-perovskites YBaCo2−xFexO5+δ cathodes for intermediate-temperature solid oxide fuel cells, J. Power Sources. 196 (2011) 3729–3735. https://doi.org/10.1016/J.JPOWSOUR.2010.12.071.

[164] Q. Zhou, T. Wei, S. Guo, X. Qi, R. Ruan, Y. Li, Y. Wu, Q. Liu, Evaluation of GdBaCuCo0.5Fe0.5O5+δ as cathode material for intermediate temperature solid oxide fuel cells, Ceram. Int. 38 (2012) 2899–2903. https://doi.org/10.1016/J.CERAMINT.2011.11.064.

[165] Y. Wang, X. Zhao, S. Lü, X. Meng, Y. Zhang, B. Yu, X. Li, Y. Sui, J. Yang, C. Fu, Y. Ji, Synthesis and characterization of SmSrCo2−xMnxO5+δ (x=0.0, 0.2, 0.4, 0.6, 0.8, 1.0) cathode materials for intermediate-temperature solid-oxide fuel cells, Ceram. Int. 40 (2014) 11343–11350. https://doi.org/10.1016/J.CERAMINT.2014.03.113.

[166] F. Meng, T. Xia, J. Wang, Z. Shi, J. Lian, H. Zhao, J.M. Bassat, J.C. Grenier, Evaluation of layered perovskites YBa1−xSrxCo2O5+δ as cathodes for intermediate-temperature solid oxide fuel cells, Int. J. Hydrogen Energy. 39 (2014) 4531–4543. https://doi.org/10.1016/J.IJHYDENE.2014.01.008.

[167] A. Jun, J. Kim, J. Shin, G. Kim, Optimization of Sr content in layered SmBa1–xSrxCo2O5+δ perovskite cathodes for intermediate-temperature solid oxide fuel cells, Int. J. Hydrogen Energy. 37 (2012) 18381–18388. https://doi.org/10.1016/J.IJHYDENE.2012.09.048.

[168] M.B. Phillipps, N.M. Sammes, O. Yamamoto, Gd1−xAxCo1−yMnyO3 (A=Sr, Ca) as a cathode for the SOFC, Solid State Ionics. 123 (1999) 131–138. https://doi.org/10.1016/S0167-2738(99)00082-X.

[169] C. Kuroda, K. Zheng, K. Świerczek, Characterization of novel GdBa0.5Sr0.5Co2−xFexO5+δ perovskites for application in IT-SOFC cells, Int. J. Hydrogen Energy. 38 (2013) 1027–1038. https://doi.org/10.1016/J.IJHYDENE.2012.10.085.

[170] K. Yi, L. Sun, Q. Li, T. Xia, L. Huo, H. Zhao, J. Li, Z. Lü, J.M. Bassat, A. Rougier, S. Fourcade, J.C. Grenier, Effect of Nd-deficiency on electrochemical properties of NdBaCo2O6−δ cathode for intermediate-temperature solid oxide fuel cells, Int. J. Hydrogen Energy. 41 (2016) 10228–10238. https://doi.org/10.1016/J.IJHYDENE.2016.04.248.

[171] H. Lv, B.Y. Zhao, Y.J. Wu, G. Sun, G. Chen, K.A. Hu, Effect of B-site doping on Sm0.5Sr0.5MxCo1−xO3−δ properties for IT-SOFC cathode material (M = Fe, Mn), Mater. Res. Bull. 42 (2007) 1999–2012. https://doi.org/10.1016/J.MATERRESBULL.2007.02.007.

[172] J.D. Kim, G.D. Kim, J.W. Moon, Y. il Park, W.H. Lee, K. Kobayashi, M. Nagai, C.E. Kim, Characterization of LSM–YSZ composite electrode by ac impedance spectroscopy, Solid State Ionics. 143 (2001) 379–389. https://doi.org/10.1016/S0167-2738(01)00877-3.

[173] S.P. Jiang, Nanoscale and nano-structured electrodes of solid oxide fuel cells by infiltration: Advances and challenges, Int. J. Hydrogen Energy. 37 (2012) 449–470. https://doi.org/10.1016/J.IJHYDENE.2011.09.067.

[174] S. Paydar, M.H. Shariat, S. Javadpour, Investigation on electrical conductivity of LSM/YSZ8, LSM/Ce0.84Y0.16O0.96 and LSM/Ce0.42Zr0.42Y0.16O0.96 composite cathodes of SOFCs, Int. J. Hydrogen Energy. 41 (2016) 23145–23155. https://doi.org/10.1016/J.IJHYDENE.2016.10.092.

[175] A. Banerjee, O. Deutschmann, Elementary kinetics of the oxygen reduction reaction on LSM-YSZ composite cathodes, J. Catal. 346 (2017) 30–49. https://doi.org/10.1016/J.JCAT.2016.11.035.

[176] X. Jiang, H. Xu, Q. Wang, L. Jiang, X. Li, Q. Xu, Y. Shi, Q. Zhang, Fabrication of GdBaCo2O5+δ cathode using electrospun composite nanofibers and its improved electrochemical performance, J. Alloys Compd. 557 (2013) 184–189. https://doi.org/10.1016/J.JALLCOM.2013.01.015.

[177] C. Jin, Y. Mao, D.W. Rooney, N. Zhang, K. Sun, Preparation and characterization of Pr0.6Sr0.4FeO3−δ–Ce0.9Pr0.1O2−δ nanofiber structured composite cathode for IT-SOFCs, Ceram. Int. 42 (2016) 9311–9314. https://doi.org/10.1016/J.CERAMINT.2016.02.121.

[178] A. Enrico, W. Zhang, M. Lund Traulsen, E.M. Sala, P. Costamagna, P. Holtappels, La0.6Sr0.4Co0.2Fe0.8O3-δ nanofiber cathode for intermediate-temperature solid oxide fuel cells by water-based sol-gel electrospinning: Synthesis and electrochemical behaviour, J. Eur. Ceram. Soc. 38 (2018) 2677–2686. https://doi.org/10.1016/J.JEURCERAMSOC.2018.01.034.

[179] J. Faye, A. Baylet, M. Trentesaux, S. Royer, F. Dumeignil, D. Duprez, S. Valange, J.M. Tatibouët, Influence of lanthanum stoichiometry in La 1-xFeO 3-δ perovskites on their structure and catalytic performance in CH 4 total oxidation, Appl. Catal. B Environ. 126 (2012) 134–143. https://doi.org/10.1016/j.apcatb.2012.07.001.

[180] P. Xiao, J. Zhu, D. Zhao, Z. Zhao, F. Zaera, Y. Zhu, Porous $LaFeO_3$ Prepared by an in Situ Carbon Templating Method for Catalytic Transfer Hydrogenation Reactions, ACS Appl. Mater. Interfaces. 11 (2019) 15517–15527. https://doi.org/10.1021/acsami.9b00506.

[181] S. Thirumalairajan, K. Girija, I. Ganesh, D. Mangalaraj, C. Viswanathan, A. Balamurugan, N. Ponpandian, Controlled synthesis of perovskite LaFeO3 microsphere composed of nanoparticles via self-assembly process and their associated photocatalytic activity, Chem. Eng. J. 209 (2012) 420–428. https://doi.org/10.1016/J.CEJ.2012.08.012.

[182] N. Yahya, F. Aziz, A. Jamaludin, A. Aizat, M.A. Mutalib, J. Jaafar, W.J. Lau, N. Yusof, W.N.W. Salleh, A.F. Ismail, Effects of the Citric Acid Addition on the Morphology, Surface Area, and Photocatalytic Activity of LaFeO3 Nanoparticles Prepared by Glucose-Based Gel Combustion Methods, Ind. Eng. Chem. Res. 58 (2018) 609–617. https://doi.org/10.1021/ACS.IECR.8B04263.

[183] T.T.N. Phan, A.N. Nikoloski, P.A. Bahri, D. Li, Optimizing photocatalytic performance of hydrothermally synthesized LaFeO3 by tuning material properties and operating conditions, J. Environ. Chem. Eng. 6 (2018) 1209–1218. https://doi.org/10.1016/J.JECE.2018.01.033.

[184] F. Parrino, E. García-López, G. Marcì, L. Palmisano, V. Felice, I.N. Sora, L. Armelao, Cu-substituted lanthanum ferrite perovskites: Preparation, characterization and photocatalytic activity in gas-solid regime under simulated solar light irradiation, J. Alloys Compd. 682 (2016) 686–694. https://doi.org/10.1016/J.JALLCOM.2016.05.017.

[185] S. Jauhar, M. Dhiman, S. Bansal, S. Singhal, Mn3+ ion in perovskite lattice: a potential Fenton's reagent exhibiting remarkably enhanced degradation of cationic and anionic dyes, J. Sol-Gel Sci. Technol. 2015 751. 75 (2015) 124–133. https://doi.org/10.1007/S10971-015-3682-8.

[186] M. Dhiman, M. Tripathi, S. Singhal, Structural, optical and photocatalytic properties of different metal ions (Cr3+, Co2+, Ni2+, Cu2+ and Zn2+) substituted quaternary perovskites, Mater. Chem. Phys. 202 (2017) 40–49. https://doi.org/10.1016/J.MATCHEMPHYS.2017.09.003.

[187] T.H. Chiang, G. Viswanath, Y.-S. Chen, Effects of RhCrOx Cocatalyst Loaded on Different Metal Doped LaFeO3 Perovskites with Photocatalytic Hydrogen Performance under Visible Light Irradiation, Catal. 2021, Vol. 11, Page 612. 11 (2021) 612. https://doi.org/10.3390/CATAL11050612.

[188] B.L. Phoon, C.W. Lai, J.C. Juan, P.-L. Show, W.-H. Chen, A review of synthesis and morphology of SrTiO3 for energy and other applications, Int. J. Energy Res. 43 (2019) 5151–5174. https://doi.org/10.1002/ER.4505.

[189] D.N. Bui, J. Mu, L. Wang, S.Z. Kang, X. Li, Preparation of Cu-loaded SrTiO3 nanoparticles and their photocatalytic activity for hydrogen evolution from methanol aqueous solution, Appl. Surf. Sci. 274 (2013) 328–333. https://doi.org/10.1016/J.APSUSC.2013.03.054.

[190] H.W. Kang, S. Bin Park, Improved performance of tri-doped photocatalyst SrTiO3:Rh/Ta/F for H2 evolution under visible light irradiation, Int. J. Hydrogen Energy. 41 (2016) 13970–13978. https://doi.org/10.1016/J.IJHYDENE.2016.06.213.

[191] A. López-Vásquez, P. Delgado-Niño, D. Salas-Siado, Photocatalytic hydrogen production by strontium titanate-based perovskite doped europium (Sr0.97Eu0.02Zr0.1Ti0.9O3), Environ. Sci. Pollut. Res. 2018 265. 26 (2018) 4202–4214. https://doi.org/10.1007/S11356-018-3116-6.

[192] C.-C. Hu, C.-C. Tsai, H. Teng, Structure Characterization and Tuning of Perovskite-Like $NaTaO_3$ for Applications in Photoluminescence and Photocatalysis, J. Am. Ceram. Soc. 92 (2009) 460–466. https://doi.org/10.1111/j.1551-2916.2008.02869.x.

Chapter -II

Experimental Details: Synthesis and Characterizations

II.1. Introduction

This chapter presents the technical methodology adopted to achieve the purpose of the thesis project. It covers the synthesis method and the different experimental techniques used throughout this thesis work. The tools used to investigate and understand the effects of the structure and the composition on the physical properties of the based perovskite materials are covered in general sense. The various properties investigated in this work are:

- The evolution of the structure in terms of symmetry and phase transitions induced by the substitution effect: X-ray diffraction coupled with Rietveld refinement.
- The UV-Visible absorption of the prepared materials and experimentally estimating the band gap values of the samples: UV-vis spectroscopy using diffuse reflectance method.
- The morphology of the materials and the effect of the composition on the size and shape of the particles: Scanning electron microscopy (SEM).
- The dielectric properties, Nyquist plots and equivalent circuits describing the conductivity mechanisms present in the materials: Complex impedance spectroscopy

II.2. Synthesis technique

II.2.1. Solid state reactions

The conventional solid state reaction was used to prepare all the compositions studied in this work. High purity binary oxides and/or carbonates of appropriate cations were used to prepare the perovskite solid solutions, and are presented in **Table-II.1**. The starting precursors are mixed in the correct stoichiometric ratio with respect to the following chemical reactions:

$$(1-x)\,BaCO_3 + x/2\,La_2O_3 + (1-x)\,TiO_2 + x/2\,Fe_2O_3 \text{ --- > } Ba_{(1-x)}La_xTi_{(1-x)}Fe_xO_3 + (1-x)\,CO_2\uparrow$$

$$(1-x)\,SrCO_3 + x/2\,La_2O_2 + (1-x)\,TiO_2 + x/2\,Fe_2O_3 \text{ ---- > } Sr_{(1-x)}La_xTi_{(1-x)}Fe_xO_3 + (1-x)\,CO_2\uparrow$$

$$(1-x)\,BaCO_3 + x\,SrCO_2 + (1-x)\,TiO_2 + x/2\,Fe_2O_3 \text{ ---- > } Ba_{(1-x)}Sr_xTi_{(1-x)}Fe_xO_{3-\delta} + CO_2\uparrow$$

The mixture is ground together in an agate mortar placed into crucibles and heated in air at progressively higher temperatures (400°C /24h, 600°C /24h, 800°C /24h, 1200°C /24h), followed by an intermediate regrinding. The heat treatment program and duration of the synthesis depends strongly on the chosen precursors and the material being synthesized. The requirements

of high temperature and the long time are to provide the reagent materials with enough energy to break their initial structure and immigrate to form new bond according to the reaction. It is important to follow the reaction with an intermediate regrinding to speed up the process, ensure the homogeneity of the mixture and the contact between the reagents. This method of preparation was chosen because it produces high crystalline materials which facilitate the structural investigations and provide us with high responses regarding their dielectric properties.

Table-II.1. List of the precursors with their purity grade used to synthesis the perovskites solid solutions studied in this work.

Precursors	Purity Grade
$SrCO_3$	99.995%
$BaCO_3$	99.995%
La_2O_3	99.999%
TiO_2	99.9997%
Fe_2O_3	99.97%

II.3. X-Ray Powder Diffraction Technique

Scientifically understanding and predicting the properties of materials depends greatly on the knowledge of the geometrical structure at the atomic scale. Powder diffraction is a technique frequently used for the determination of crystal structure since it provides information on the bulk material. The analysis of the diffracted intensity distribution in space of the studied material makes it possible to characterize its structure. Bragg equation is at the core of the X-ray powder diffraction principle in terms of reflection of incident X-ray by sets of lattice planes described by miller indices (*hkl*) [1].

X-ray characterizations were carried out on the different synthesized solid solutions based perovskites structure. The analyses were performed by means of:

- D2 PHASER diffractometer in the bragg-brentano geometry (CuKα radiation, λ= 1.5406 Å) at 30 KV and 10 mA. The patterns were scanned in 2θ-steps of 0.01, in the range $10 < 2\theta < 105°$.
- D8 PHASER diffractometer in the bragg-brentano geometry (CuKα radiation, λ= 1.5406 Å) at 40 KV and 40 mA. The patterns were scanned in 2θ-steps of 0.01, in the range $10 < 2\theta < 105°$.

The X-ray diffraction characterization were performed in order to investigate the phase formation of the new perovskites materials and to later on, understand at the atomic level the effect of the structural parameters on the physical properties.

II.4. Rietveld Refinement method

In order to benefit the most from the information collected in the X-ray powder diffraction patterns, it is mostly coupled with structure resolution technique. Rietveld refinement technique is generally used to confirm the phase formation by defining the structure adopted by new synthesized materials and thus, extracting the necessary structural data information to conduct the investigation [2–4].

The powder diffraction is collected in digitized form in order to be treated by the software. Hence the patterns are recorded as a numerical intensity value y_i, at each specific increments or steps *i*. For constant wavelength data, the increments are steps in scattering angle 2θ and ranges from 0.01° to 0.05°. H.M. Rietveld [5] realized that the appropriate way to extract the maximum of information from X-ray powder diffraction patterns is to write a mathematical expression to represent the observed intensity at every step in this pattern, equation 1:

$$Y_c = Y_b + \sum Y_h \qquad \text{(Eq. 1)}$$

This equation, has each of Bragg reflections (Y_h; **h**= *hkl*) near the powder patterns step and the background contribution. The least squares method, which is a powerful technique for estimating the values of the adjustable parameters, is used to minimizing the weighted differences between the observed $\{y_i\}_{i=1,..n}$ and calculated intensities $\{y_{c,i}(\alpha)\}_{i=1,..n}$ [5,6]. The function minimized in the Rietveld Method is shown in equation 3:

$$\chi^2 = \sum_{i=1}^{n} w_i\{y_i - y_{c,i}(\alpha)\}^2 \qquad \text{(Eq. 2)}$$

With $w_i = \frac{1}{\sigma_i^2}$, the variance of the observation y_i. Programs such *FullProf*, have been developed for Rietveld Refinement analysis of Neutron or X-ray powder diffraction patterns collected at constant or variable step in scattering angle 2θ.

For structural investigation carried out throughout the thesis work, Rietveld Refinement method was adopted in order to investigate the structures of the new synthesized materials and to

study the effect of the substitution on the variation and or phase transitions occurred. All the perovskites series and samples prepared during this work were treated by WinPLOTR software integrated in the FullProf program. The number of refined parameters varies between 26 and 33 depending on the structure. The refined parameters include the different structural and instrumental factors such as: scale factor, lattice parameters, zero shift, background coefficients, space group, peak profile, atomic positions, occupancy and isotropic atomic displacement parameters of individual atoms. The background is fitted with fifth order polynomial and the peak shape is fitted with a pseudo-Voigt profile function [7–9].

II.5. UV-Visible spectroscopy

The optical properties investigation of the samples was performed by means of PerkinElmer UV/VIS/NIR spectrometer Lambda 1050 equipped with an integrating sphere. The diffuse reflectance spectra F(R) of all the studied compounds was collected at room temperature in the range of 250-1800 nm. The powders were then shaped into cylindrical pellets using 1mm diameter steel dies and pressed with a hydraulic press under a pressure of 6t. The pellets were then sintered in air at 900°C overnight.

The absorbance of the solid solutions was studied using the Kubelka-Munk function theory (F(R)) using equation 3:

$$\frac{K}{S} = \frac{(1-R)^2}{2R} \equiv F(R) \qquad \text{(Eq. 3)}$$

The parameter R represents the diffuse reflectance, which is collected from the UV-vis analysis. K and S are respectively the absorption coefficient and the scattering coefficient. The method adopted to investigate the absorption of the compounds is the most general theory developed by Kubelka and Munk [10,11]. According to equation 4, the kubelka-Munk function reads a plot of $F(R_\infty)$ as a function of the extinction coefficient k.

McLean analysis was adopted to estimate the absorption edge and thus calculate the optical band gap using tauc plot. Equation 4, expresses the relation between the coefficient of absorption (F(R)) and the band gap energy and the type of the band gap.

$$F(R)h\nu = A(h\nu - E_g)^n \qquad \text{(Eq. 4)}$$

Where "A" is the band tailing parameter, the "n" index is dependent to the inter-band transitions mechanisms; the possible values for the index n are equal to 1/2, 2, 3/2 or 3, each denotes respectively direct allowed, indirect allowed, direct forbidden and indirect forbidden transitions types. The E_g values were derived by the extrapolation of the tangential line from high photon energy to zero F(R) → 0 [11].

The Conduction band minimum and the valence band maximum were estimated using the following empirical equations 5 and 6 [12,13]:

$$E_{CB} = \chi - E_e - 0.5E_g \qquad \text{(Eq. 5)}$$

$$E_{VB} = E_{CB} + E_g \qquad \text{(Eq. 6)}$$

E_g represents the band gap calculated from the experimental results. E_e is equal to 4.5 and represent the free electron energy, while E_{CB} and E_{VB} are respectively the conduction band and the valence band potential. χ is the electronegativity of semiconductions and can be calculated using equation 7 [12,13]:

$$\chi = [\chi(A)^a \chi(B)^b \chi(C)^c \chi(D)^d \chi(E)^e]^{\frac{1}{a+b+c+d+e}} \qquad \text{(Eq. 7)}$$

The indexes "a, b, c, d and e" are the number of atoms in each composition and $\chi(y)$ is the electronegativity of each elements of the compound.

II.6. Scanning electron microscopy

The morphology and the microstructure of the prepared samples were observed by field emission scanning electron microscopy (SEM) JEOL LSM-IT500HRLA. The Images were captured for the samples at 5 nm and 500 nm.

II.7. Complex impedance spectroscopy

Ceramic pellets were prepared and sintered at high temperature 900°C, the dielectric and electric properties of the prepared ceramics were analyzed using the data acquisition system based on Modulab XM MTS which is connected to the probostat cell support system and driven by a microcomputer. The ceramic pellets were painted using silver lacquer, and then placed between two electrodes placed in the sample's holder stored in a programmable heating chamber.

The measurements were recorded in a wide range of frequency, high, medium, and low frequency (10 Hz – 1 MHz) at temperatures ranging from 27°C to 390°C. The results obtained consists of the dielectric vs. temperature and complex impedance Z'' *vs*. Z' known as Nyquist plots.

The complex impedance Z* is defined by its real and imaginary parts as:

$$Z^*(\omega) = Z'(\omega) - jZ''(\omega) \qquad (8)$$

Where Z' and Z'' are the real and imaginary parts of complex impedance, respectively. $\omega = 2\pi f$ is the angular frequency Due to the different contributions existing in polycrystalline ceramics such as grain, grain boundary and electrode interface, the Nyquist plots (Z'' *vs* Z') can be obtained in the form of incomplete semi-circle, one depressed semicircle due to the inhomogeneity of polycrystalline materials, or as multiple semicircles [14]. The real (Z') and imaginary (Z") parts of the complex impedance expressions are as following [15]:

$$Z' = \frac{R_g}{1 + \left(\omega R_g C_g\right)^2} + \frac{R_{gb}\left[1 + Q_{gb}R_{gb}\omega^{\alpha}\cos\left(\frac{\alpha\pi}{2}\right)\right]}{\left[1 + Q_{gb}R_{gb}\omega^{\alpha}\cos\left(\frac{\alpha\pi}{2}\right)\right]^2 + \left[Q_{gb}R_{gb}\omega^{\alpha}\sin\left(\frac{\alpha\pi}{2}\right)\right]^2} \qquad (9)$$

$$Z'' = \frac{\omega R_g^2 C_g}{1 + \left(\omega R_g C_g\right)^2} + \frac{Q_{gb}R_{gb}^2\omega^{\alpha}\sin\left(\frac{\alpha\pi}{2}\right)}{\left[1 + Q_{gb}R_{gb}\omega^{\alpha}\cos\left(\frac{\alpha\pi}{2}\right)\right]^2 + \left[Q_{gb}R_{gb}\omega^{\alpha}\sin\left(\frac{\alpha\pi}{2}\right)\right]^2} \qquad (10)$$

R_g and C_g represent grain resistance and capacitance, respectively. R_{gb} and Q_{gb} (CPE) are grain-boundaries resistance and capacitance, respectively. ω is the angular frequency and α ($0 < \alpha < 1$) is the parameter which describes the capacitive nature of CPE_{gb} element, $\alpha = 0$ for the pure ohmic resistor and $\alpha = 1$ for the ideal capacitor.

The experimental data of the complex impedance were fitted using Zview software in order to find the equivalent circuit of each material and to separate the contribution of grain, grain boundary and the electrode interface. Equations (9) and (10), are used to fit the the impedance data (Z" vs Z') and the parameters R_g, R_{gb}, C_g and Q_{gb} (CPE) for the ceramics under study are extracted and presented.

II.8. Conclusion

In this chapter, we have presented the method adopted for the preparation of three solid solutions ABO_3-type perovskites and the different characterization techniques used in this study. The materials were characterized using the X-ray diffraction for structure determination and phase transition investigations. Scanning electron microscopy is used to have insight on the morphology of the prepared materials. The UV-vis spectroscopy is used to investigate the light absorption performance and estimated experimentally the values of the band gap. The impedance spectroscopy is used to study the dielectric and electric properties of the materials.

The methodology used in this work relies on the elaboration of the samples with the suitable synthesis method in this case the conventional solid state. This method allows the materials to form high crystalline materials, which is a characteristic that helps carry in depth investigation of the structure of the materials. Additionally, high crystalline structures allow achieving the best performance of the materials when studying thier dielectric properties. The prepared samples are labeled as follow:

- $Ba_{(1-x)}La_xTi_{(1-x)}Fe_xO_3$: BLTF
- $Sr_{(1-x)}La_xTi_{(1-x)}Fe_xO_3$: SLTF
- $Ba_{(1-x)}Sr_xTi_{(1-x)}Fe_xO_{3-\delta}$: BSTF

II.9. References

[1] A. Le Bail, Chapter 5:The Profile of a Bragg Reflection for Extracting Intensities, Powder Diffr. (2008) 134–165. https://doi.org/10.1039/9781847558237-00134.

[2] F. Bhadala, L. Suthar, P. Kumari, M. Roy, Rietveld refinement, morphological, vibrational, Raman, optical and electrical properties of Ca/Mn co-doped BiFeO3, Mater. Chem. Phys. 247 (2020) 122719. https://doi.org/10.1016/j.matchemphys.2020.122719.

[3] M. Azdouz, B. Manoun, M. Azrour, L. Bih, L. El Ammari, S. Benmokhtar, P. Lazor, Synthesis, Rietveld refinements and Raman spectroscopy studies of the solid solution Na1−xKxPb4(VO4)3 (0⩽x⩽1), J. Mol. Struct. 963 (2010) 258–266. https://doi.org/10.1016/j.molstruc.2009.10.047.

[4] A. El Hachmi, B. Manoun, Y. Tamraoui, S. Louihi, L. Bih, M. Sajieddine, P. Lazor, Structural and Mössbauer Studies of Sr1.5Ca1.5Fe2.25Mo0.75O9−δ and Sr1.92Ca1.08Fe2.04W0.96O9−δ Double Perovskites, J. Struct. Chem. 61 (2020) 861–872. https://doi.org/10.1134/s0022476620060049.

[5] H.M. Rietveld, A profile refinement method for nuclear and magnetic structures, J. Appl. Crystallogr. 2 (1969) 65–71. https://doi.org/10.1107/s0021889869006558.

[6] Powder Diffraction, Powder Diffr. (2008). https://doi.org/10.1039/9781847558237.

[7] J. Rodriguez-Carvajal, FULLPROF 2000: A Rietveld Refinement and Pattern Matching Analysis Program, 2008.

[8] J. Rodríguez-Carvajal, FULLPROF: A Program for Rietveld Refinement and Pattern Matching Analysis, in: Abstr. Satell. Meet. Powder Diffr. XV Congr. IUCr, 1990.

[9] Y. Tamraoui, B. Manoun, F. Mirinioui, I. Saadoune, R. Haloui, A. Elhachmi, E. Saad, P. Lazor, Temperature and composition induced phase transitions in Sr<inf>2−x</inf>Ca<inf>1+x</inf>TeO<inf>6</inf> (0 ≤ x ≤ 2) double perovskite oxides, J. Mol. Struct. 1131 (2017). https://doi.org/10.1016/j.molstruc.2016.11.036.

[10] P. Kubelka, F. Munk, An Article on Optics of Paint Layers (engl. Übersetzung), Z. Tech. Phys. 12 (1931) 593–601.

[11] M. Nowak, B. Kauch, P. Szperlich, Determination of energy band gap of nanocrystalline SbSI using diffuse reflectance spectroscopy, Rev. Sci. Instrum. 80 (2009) 4–7. https://doi.org/10.1063/1.3103603.

[12] T. Xian, H. Yang, L. Di, J. Ma, H. Zhang, J. Dai, Photocatalytic reduction synthesis of SrTiO3-graphene nanocomposites and their enhanced photocatalytic activity, Nanoscale Res. Lett. 9 (2014) 1–9. https://doi.org/10.1186/1556-276X-9-327.

[13] M. Abdi, V. Mahdikhah, S. Sheibani, Visible light photocatalytic performance of La-Fe co-doped SrTiO3 perovskite powder, Opt. Mater. (Amst). 102 (2020) 109803. https://doi.org/10.1016/j.optmat.2020.109803.

[14] D.K. Mahato, A. Dutta, T.P. Sinha, Electrical properties and scaling behaviour of rare earth based Ho 2 CoZrO 6 double perovskite ceramics, Mater. Res. Bull. 47 (2012) 4226–4232. https://doi.org/10.1016/j.materresbull.2012.09.028.

[15] F.B. Abdallah, A. Benali, M. Triki, E. Dhahri, M.P.F. Graça, M.A. Valente, Effect of annealing temperature on structural, morphology and dielectric properties of La0.75Ba0.25FeO3 perovskite, Superlattices Microstruct. 117 (2018)

260–270. https://doi.org/10.1016/j.spmi.2018.03.048.

Chapter -III

Investigation of the composition effect on the structure and morphology in the solid solution systems $A_{(1-x)}A'_xTi_{(1-x)}Fe_xO_{3-\delta}$ for (A = Ba, La and Sr) with $0 \leq x \leq 1$ & $\delta \geq 0$: Rietveld refinement method studies

III.1. Introduction

This chapter constitutes the first part of the research project; it is dedicated to study the effect of the composition on the ABO_3 perovskite structure as it is to our interest to map the system symmetry and the structural characteristic for further investigations. Systematic studies of the evolution of the structure as well as the various parameters as function of the composition will be discussed in details. The system stability within a wide range of the substitution amount ($0 \leq x \leq 1$), the phase transitions, the correct symmetry adopted are investigated and reported. The effect of the composition on the morphology and the growth of the grains is also treated in this chapter for all the compositions of the three solid solutions.

The main objective of the structural investigations is to collect information on the various parameters namely: the unit cell parameters, unit cell volume, the interatomic distances, the bond angles etc., and prepare a dataset that will allow us to link the effect of the symmetry and/or the structure parameters to the physical properties of the synthesized perovskite series $A_{(1-x)}A'_xTi_{(1-x)}Fe_xO_{3-\delta}$ (A = Ba, La, Sr) with $0 \leq x \leq 1$. The observations concerning the morphology evolution as function of the compositions will serve to explain the effect of the morphology on the dielectric and electric properties of the treated solid solutions under the formula $A_{(1-x)}A'_xTi_{(1-x)}Fe_xO_{3-\delta}$ (A = Ba, La, Sr) with $0 \leq x \leq 1$.

Part I - Chapter III studies the effect of the composition on the structure and morphology of the system $A_{(1-x)}A'_xTi_{(1-x)}Fe_xO_{3-\delta}$. In this case of study, the A-sites are occupied by Ba^{2+} and La^{3+} cations while the B-sites are occupied by Fe^{3+} and Ti^{4+} cations, thus, the chemical formula of the perovskite system is written as $Ba_{1-x}La_xTi_{1-x}Fe_xO_3$ with the substitution amount varies between $0 \leq x \leq 1$. The $Ba_{1-x}La_xTi_{1-x}Fe_xO_3$ will be abbreviated as BLTF in the following paragraphs.

Part II - Chapter III studies the effect of the composition on the structure and morphology of the system $A_{(1-x)}A'_xTi_{(1-x)}Fe_xO_{3-\delta}$. In this case of study, the A-sites are occupied by Sr^{2+} and La^{3+} cations while the B-sites are occupied by Fe^{3+} and Ti^{4+} cations, thus, the chemical formula of the perovskite system is written as $Sr_{1-x}La_xTi_{1-x}Fe_xO_3$ with the substitution amount varies between $0 \leq x \leq 1$. The $Sr_{-x}La_xTi_{1-x}Fe_xO_3$ will be abbreviated as SLTF in the following paragraphs.

Part III - Chapter III studies the effect of the composition on the structure and morphology of the system $A_{(1-x)}A'_xTi_{(1-x)}Fe_xO_{3-\delta}$. In this case of study, the A-sites are occupied by Ba^{2+} and Sr^{2+} cations while the B-sites are occupied by Fe^{3+} and Ti^{4+} cations, thus, the chemical formula of the perovskite system is written as $Ba_{1-x}Sr_xTi_{1-x}Fe_xO_{3-\delta}$ with the substitution amount varies between $0 \leq x \leq 1$. The $Ba_{1-x}Sr_xTi_{1-x}Fe_xO_{3-\delta}$ will be abbreviated as BSTF in the following paragraphs.

III.2. Part I: Investigation of the composition effect on the structure in $Ba_{1-x}La_xTi_{1-x}Fe_xO_3$ perovskite system with $0 \leq x \leq 1$

III.2.1. Introduction

$BaTiO_3$ is considered the state of the art of ABO_3 perovskite materials, as it was and still extensively studied for its dielectric properties [1–4]. Across literature, it is agreed that $BaTiO_3$ crystallizes in the tetragonal structure with *P*4*mm* space group [5], and the effect of the composition on its structure is seen in several works. The incorporation of Fe^{3+} in the B-site of $BaTiO_3$ perovskite showed the formation of hexagonal phase for $BaTi_{1-x}Fe_xO_3$ ceramics for a substitution amount x = 7, 30 and 70% as it is reported by *Fangting Lin et al* [6]. The hexagonal structure was reported in another work of Fe doped $BaTiO_3$ (x = 1% - 10%) by *QIU Shen-yu et al.* [7], it is reported that the hexagonal phase appears for a substitution amount above 2% of Fe^{3+} doping. However, *I.C. Amaechi et al.* [8] have reported a tetragonal structure for $BaTiO_3$ doped Fe^{3+} for Fe contents ranging from 2 to 8%. The electrical properties of $BaTiO_3$ were studied by *Finlay D. et al.* [9] after doping with La^{3+} for a content bellow x = 0.20, the solid solution $Ba_{1-x}La_xTi_{1-x/4}O_3$ was reported to adopt the tetragonal structure for composition with x < 0.04 while above x > 0.04 the patterns were indexed for cubic structure. *B. H. Devmunde et al.* [10] reported a tetragonal phase for La^{3+} doped $BaTiO_3$ forming the solid solution $Ba_{1-x}La_xTiO_3$ for a content ranging between x = 0 to 0.02.

$LaFeO_3$ is reported to adopt the orthorhombic structure with *Pbnm* as space group [11, 12]. Co-substitution by Dy^{3+} and Ti^{4+} of $LaFeO_3$ has been reported by *A. Mitra et al*. [13], the solid solution $La_{1-x}Dy_xFe_{1-y}Ti_yO_3$ for x/y =0.02 showed orthorhombic structure with same space group as $LaFeO_3$. Same structure was reported by *A. Rai et al.* [14] while studying the solid solution $La_{1-x}Na_xFe_{1-x}Mn_xO_3$ (x = 0 - 0.2), however *Pnma* was adopted as space group. Ti doped $LaFeO_3$ as well showed the orthorhombic structure for a substitution amount of 10 wt. % in the work reported by *P. Garcia-Munoz et al*. [15]. It is observed that small amount of the substitution might preserve the system unchanged; however it may induce a transition toward new space group within the same system.

On the other hand, solid solution based $LaFeO_3$-$BaTiO_3$ has been the topic of few works studying their dielectric and magnetic properties. *H. Chaabane et al*. [16] prepared the solid solution $Ba_{1-x}La_xTi_{1-x}Fe_xO_3$ (x = 0 – 0.15) by the conventional solid state reaction, where they

reported a tetragonal structure for compositions with x ≤ 0.05 with *P*4*mm*, above which indexation with cubic structure with $Pm\bar{3}m$ space group was assigned for the compositions with x ≥ 0.075. *R. Rajagukguk et al.* [17], as well reported on the magnetic ordering in the solid solution (1-x) $BaTiO_3$ - x $LaFeO_3$ (0.1 ≤ x ≤ 0.7) all the samples were indexed with a cubic structure. The reported structure by *Sushrisangita S. et al* [18] of the solid solution $Ba_{1-x}La_xTi_{1-x}Fe_xO_3$ (x = 0 – 0.5) is assumed to crystallize in tetragonal structure with unit cell parameters varying between 3.988 and 3.977 Å for the lattice parameter 'a = b' and between 3.997 and 0.996 Å for the lattice parameter 'c'.

Based on all the reported studied, it is seen that the same composition is indexed with different space groups leading to confusions. In this part we conduct structural investigations using the Rietveld refinement method and we report on the stability of the structure, the phase transitions induced by the substitution, the symmetry and the evolution of the structural parameters of the solid solution $Ba_{1-x}La_xTi_{1-x}Fe_xO_3$ in wide range of substitution amount 0 ≤ x ≤1.

III.2.2. X-Ray Diffraction patterns: results and discussion

The X-ray diffraction patterns of BLTF perovskite system are presented in **Fig-III.P1.1a.** The results prove that the samples are formed in the desired structure and substitution of Ba^{2+} and Ti^{4+} by La^{3+} and Fe^{3+} respectively at A-sites and B-sites of ABO_3 structure is achieved. The diffraction pattern of each sample is indexed using Dicvol software [19]**. Fig-III.P1.1b** shows the main peaks at *2θ (°)* in the ranges *31° ≤ 2θ ≤ 33°*, *44° ≤ 2θ ≤ 47°*, *55° ≤ 2θ ≤ 58°* corresponding to the reflections (101) (110), (002) (200) and (112) (211); a gradual shift toward higher *2θ (°)* is observed with increasing the substitution amount of Ba^{2+} and Ti^{4+} by La^{3+} and Fe^{3+} respectively. The shift observed is an indication of the lattice parameters contraction induced by substituting elements of higher ionic radius by elements with smaller ionic radius, thus the decrease of the unit cell volume. Respectively, the identified peaks gradationally overlap, up to x = 0.3 of Ba^{2+} and Ti^{4+} substitution, to form single reflections (110), (200) and (211). At x > 0.6, the samples adopt different crystallographic system: a split is now observed into, i.e. (200), (112), (020); (220), (004); and (321), (240), (123), (042) respectively as it is shown in **Fig-III.P1.1b**. It is thus postulated that the specific information obtained from these observations illustrates the occurrence of several phase transitions, and will be investigated in the following paragraphs.

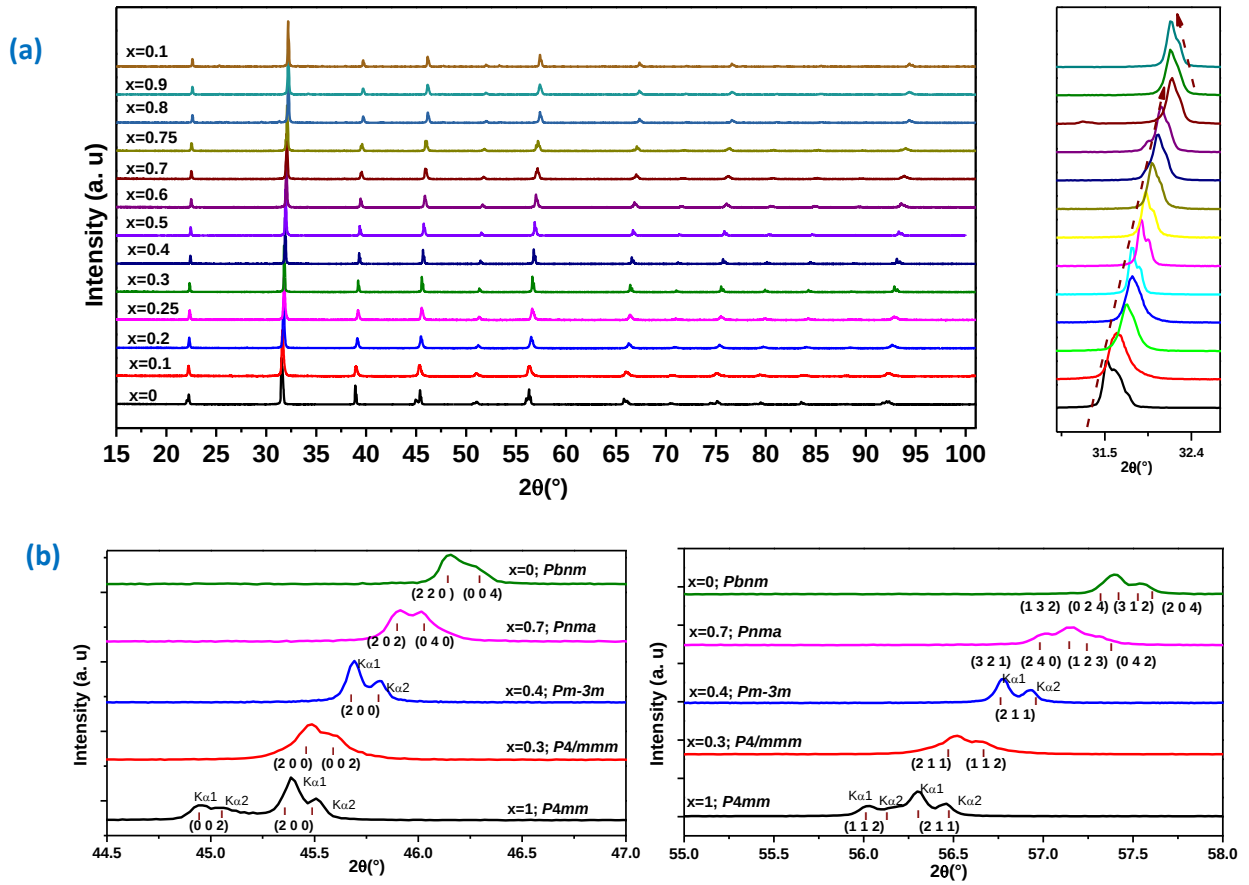

Fig-III.P1.1: X-ray powder diffraction patterns of $Ba_{1-x}La_xTi_{1-x}Fe_xO_3$ ($0 \leq x \leq 1$) presenting the peaks shape variation **(a)** and the separated main peaks **(b)**.

III.2.3. Rietveld refinement study of the structure and the phase transitions

To understand the effect of the substitution on the perovskite structure evolution, the X-ray diffraction patterns, seen in **Fig-III.P1.1a**, were refined using FullProf coupled with WinPLOTR software. The symmetries and the space group chosen for each sample were adjusted to the calculated ones. In comparison with the reported structure in literature [20–22] the refinement results demonstrate the existence of 5 phase transitions as function of the composition, the samples between $0 \leq x \leq 0.25$ adopt the tetragonal symmetry with two different space groups *P*4*mm* and *P*4*/mmm* corresponding respectively to x = 0 and x = 0.1, 0.2, 0.25. Due to the singlet feature of the peaks shown in the X-ray patterns of the samples within the composition range $0.3 \leq x \leq 0.6$, it is deduced that the samples adopt the cubic symmetry with *Pm*-3*m* as space group. For the composition range $0.7 \leq x \leq 1$, the main peaks start splitting showing orthorhombic X-ray pattern features. The refinement results reveal that the samples

within this range adopt the orthorhombic structure with two space groups *Pnma* and *Pbnm* for x = 0.7, 0.75 and x = 0.9, 0.8, 1 respectively. In the following sections, a detailed analysis of the different phase formation and transitions is given.

III.2.3.1. Tetragonal BLTF perovskite system with 0 ≤ x ≤ 0.25

Fig-III.P1.2 shows the final plot of the Rietveld refinement results obtained for the tetragonal BLTF perovskite system with 0 ≤ x ≤ 0.25, and the unit cell visualization along [010] projection. $BaTiO_3$ crystallizes in the tetragonal symmetry, with *P*4*mm* space group, at room temperature [23]. The X-ray pattern measured for $BaTiO_3$ sample fits perfectly to the model used for the Rietveld refinement. The results show low reliability factors R_F = 2.85**,** R_B = 4.50**,** R_p = 9.20**,** R_{wp} = 12.2**,** cR_p = 13.3, cR_{wp} = 15.6, χ = 2.83. The unit cell parameters a (Å) = b (Å) = 3.994(8), c(Å)= 4.029(8) and γ (°) = 90, are found to be close to the reported results [23], the crystallographic data issued from the Rietveld refinement results are presented in **Table-III.P1.1**. The compositions of BLTF perovskite system with x = 0.1, x = 0.2 and x = 0.25 were also refined using $BaTiO_3$ model as input data with the same space group *P*4*mm*. However, when studying the evolution of the unit cell parameters, it was observed that at x = 0.1 of Ba^{2+} and Ti^{4+} substitution, a relaxation along the (ab) plan has occurred. This causes lattice expansion for a (Å) = b (Å) = 4.002(2) Å, and contraction for the lattice parameter c (Å) = 3.992(3) Å. Above x=0.2, a contraction of the lattice parameters was observed which is in contradiction with the previous observations of the X-ray diffraction peaks presented in **Fig-III.P1.1b**. The shift toward higher *2θ (°)* and the overlap of the diffraction peaks were explained to be the result of system distortion, that gradually weakened as the amount of substitutions increased, i.e. a system that transforms into higher symmetry. Accordingly, we assumed that the samples still adopt the tetragonal symmetry, and since the BLTF system is evolving toward higher symmetry, the compositions x = 0.1, 0.2 and 0.25 are modeled using *P4/mmm* as space group. The fitting to this model showed satisfactory results with low reliability factors and the crystallographic data are collected and presented in **Table-III.P1.1**. Selected interatomic distances <Ti/Fe-O>**,** <Ba/La-O> and bond angles O–Ti–O, O–(Ba/La)–O & Ti–O–(Ba/La)) are summarized in **Table-III.P1.2;** these results are collected to study the evolution of the system as function of the composition in the following paragraph.

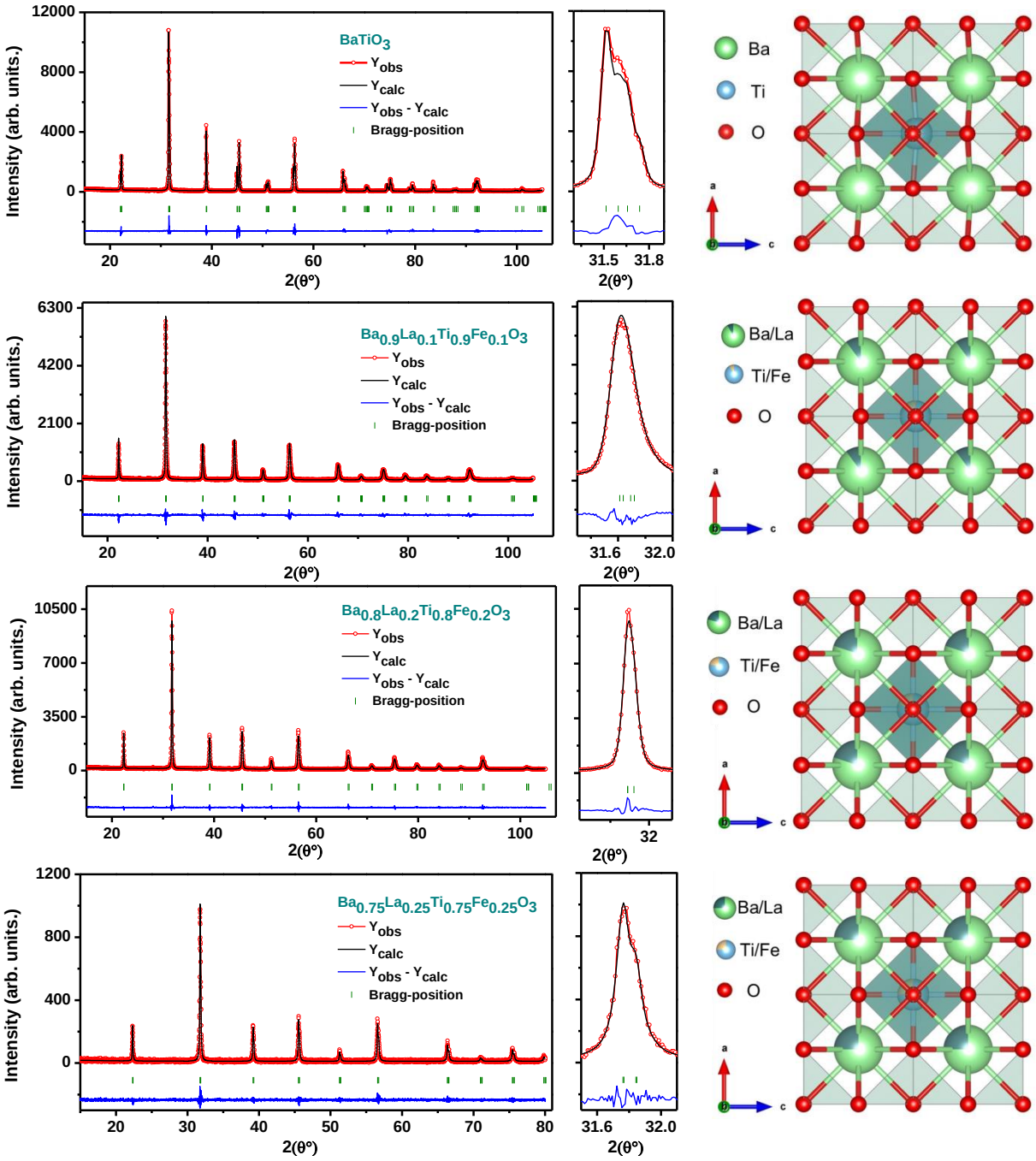

Fig-III.P1.2: Final Rietveld Refinement plots of Tetragonal BLTF system $0 \leq x \leq 0.25$ and [010] projection of the unit cell with *P4mm* and *P4/mmm*. The observed data and calculated profile are indicated by circles and solid trace respectively. The lowest trace shows the difference between the observed and calculated model. The vertical bars indicate the calculated bragg reflections positions.

Table-III.P1.1. Refined structural parameters for Tetragonal BLTF system $0 \le x \le 0.25$

$BaTiO_3$	Ba/La	Ti/Fe	O1	O2
	space group *P4mm*			
x	0	½	½	½
y	0	½	½	0
z	0	0.509(7)	-0.034(7)	0.474(8)
B (A^2)	0.32(5)	0.27(9)	0.74(2)	0.74(2)
Occupancy	1	1	1	2
a(Å)= 3.994(8), **c(Å)**= 4.029(8), **α(°)**= 90° **U**=0.047(4), **V**=-0.016(4), **W**= 0.008(7) R_F=2.85, R_B=4.50, R_p=9.20, R_{wp}=12.2, cR_p=13.3, cR_{wp}= 15.6, χ=2.83				
$Ba_{0.9}La_{0.1}Ti_{0.9}Fe_{0.1}O_3$	Ba/La	Ti/Fe	O1	O2
	space group *P4/mmm*			
x	0	½	½	½
y	0	½	½	0
z	0	½	0	½
B (A^2)	0.27(4)	0.14(6)	0.91(1)	0.91(1)
Occupancy	0.9/0.1	0.9/0.1	1	2
a(Å)= 3.996(2), **c(Å)**= 4.002(5), **α(°)**= 90° **U**= 0. 278(2), **V**=0.013(1), **W**= 0.007(3) R_F= 2.77, R_B= 4.09, R_p= 9.67, R_{wp}= 12.7, cR_p= 17.8, cR_{wp}= 19.0, χ=2.08				
$Ba_{0.8}La_{0.2}Ti_{0.8}Fe_{0.2}O_3$	Ba/La	Ti/Fe	O1	O2
	space group *P4/mmm*			
x	0	½	½	½
y	0	½	½	0
z	0	½	0	½
B (A^2)	0.40(4)	0.24(5)	0.95(2)	0.95(2)
Occupancy	0.8/0.2	0.8/0.2	1	2
a(Å)= 3.983(6), **c(Å)**= 3.991(1), **α(°)**= 90° **U**= 0.228(1), **V**= -0.008(2), **W**= 0.007(2) R_F= 2.56, R_B= 4.27, R_p= 7.14, R_{wp}= 8.98, cR_p= 15.3, cR_{wp}= 14.5, χ=1.59				
$Ba_{0.75}La_{0.25}Ti_{0.75}Fe_{0.25}O_3$	Ba/La	Ti/Fe	O1	O2
	space group *P4/mmm*			
x	0	½	½	½
y	0	½	½	0
z	0	½	0	½
B (A^2)	0.67(1)	0.32(1)	0.9(3)	0.9(3)
Occupancy	0.75/0.25	0.75/0.25	1	2
a(Å)= 3.981(8), **c(Å)**= 3.979(2), **α(°)**= 90° **U**=0.050(2), **V**=0.013(1), **W**= 0.002(2) R_F=4.87, R_B=6.32, R_p=13.9, R_{wp}=20.1, cR_p=25.2, cR_{wp}= 29.5, χ= 1. 98				

Table-III.P1.2. Selected interatomic distances (Å) and (O–Ti–O, O–(Ba/La)–O & Ti –O– (Ba/La)) angles for Tetragonal BLTF system ($0 \leq x \leq 0.25$).

Interatomic distances	x=0	Composition	x=0.1	x=0.2	x=0.25
1×Ti/Fe–O1	2.190(4)	2×Ti/Fe–O1	2.001(2)	1.994(4)	1.989(6)
1×Ti/Fe–O1	1.840(4)	4×Ti/Fe–O2	1.998(1)	1.992(20)	1.990(3)
4×Ti/Fe–O2	2.002(3)	<Ti/Fe–O>	1.999	1.993	1.989
<Ti/Fe–O>	2.006				
4×Ba/La–O1	2.827(1)	4×Ba/La–O1	2.826(1)	2.817(1)	2.815(3)
4×Ba/La–O2	2.910(2)	8×Ba/La–O2	2.828(2)	2.819(3)	2.814(4)
4×Ba/La–O2	2.760(2)	<Ba–O>	2.827	2.818	2.814
<Ba/La–O>	2.832				
1×O1–Ti/Fe–O1	179.960(4)	1×O1–Ti/Fe–O1	180.000(2)	180.000(4)	180.000(2)
2×O2–Ti/Fe–O2	171.920(1)	2×O2–Ti/Fe–O2	180.000(1)	180.000(18)	180.000(9)
8×O2–Ti/Fe–O2	89.720(1)	8×O2–Ti/Fe–O2	90.000(6)	90.000(9)	90.000(4)
4×O1–(Ba/La)–O1	89.870(4)	4×O1–(Ba/La)–O1	90.000(5)	90.000(2)	90.000(3)
2×O1–(Ba/La)–O1	174.450(4)	2×O1–(Ba/La)–O1	180.000(9)	180.000(1)	180.000(3)
4×O2–(Ba/La)–O2	177.000(2)	4×O2–(Ba/La)–O2	180.000(1)	180.000(2)	180.000(4)
1x(Ti/Fe)–O1-(Ti/Fe)	179.960(4)	1x(Ti/Fe)–O1-(Ti/Fe)	180.000(2)	180.000(4)	180.000(9)
1x(Ti/Fe)–O2-(Ti/Fe)	171.920(1)	1x(Ti/Fe)–O2-(Ti/Fe)	180.000(2)	180.000(4)	180.000(9)

III.2.3.2. Cubic BLTF perovskite system $0.3 \leq x \leq 0.6$

The diffraction peaks were observed to be singlet for the compositions within $0.3 \leq x \leq 0.6$. Thus, the space group *Pm*-3*m* (N°221) is suggested as a model for the refinement and the Rietveld refinement demonstrates good fitting with the experimental results and low reliability factors, the results of the Rietveld refinement are summarized in **Table-III.P1.3**. The decrease of the lattice parameters obtained from the final refinement results is convenient with the substitution due to the ionic radius size difference between Ba^{2+}/Ti^{4+} and La^{3+}/Fe^{3+} respectively. **Fig-III.P1.3** shows the final plot of the Rietveld refinement for the Cubic system, and a [010] projection visualization of the unit cell. The interatomic distances <Ti/Fe-O>**,** <Ba/La-O> and bond angles (O–Ti–O, O–(Ba/La)–O & Ti –O– (Ba/La)) for the cubic symmetry are summarized in **Table-III.P1.4.** The collected results will contribute to study the evolution of parameters of BLTF system as function of the composition.

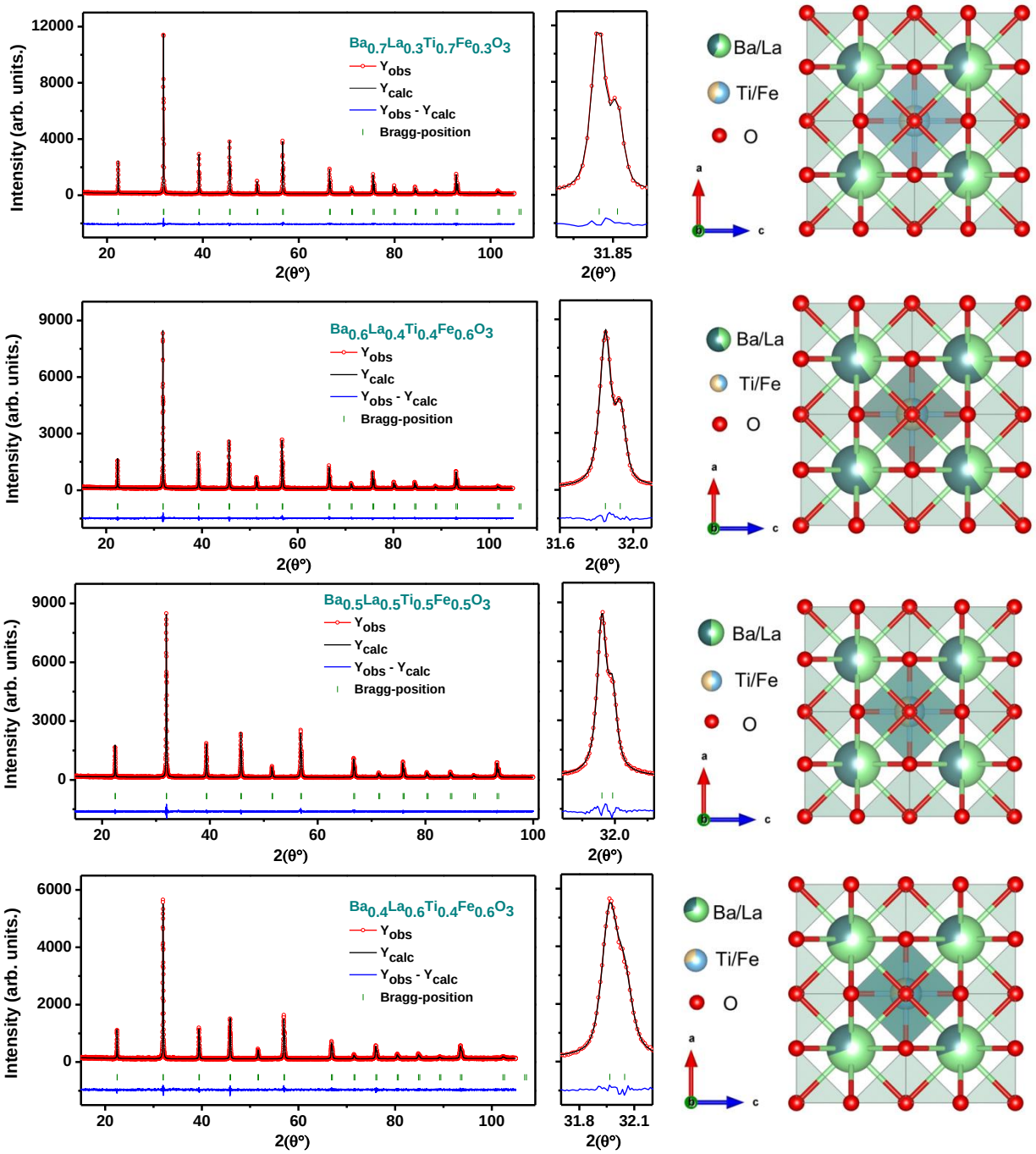

Fig-III.P1.3: Final Rietveld Refinement plots of Cubic BLTF system $0.3 \leq x \leq 0.6$ and [010] projection of the unit cell with *Pm*-3*m*. The observed data and calculated profile are indicated by circles and solid trace respectively. The lowest trace shows the difference between the observed and calculated model. The vertical bars indicate the calculated bragg reflections positions.

Table-III.P1.3. Refined structural parameters for Cubic BLTF system $0.3 \leq x \leq 0.6$

$Ba_{0.7}La_{0.3}Ti_{0.7}Fe_{0.3}O_3$	Ba/La	Ti/Fe	O1
	space group *Pm-3m*		
x	0	½	½
y	0	½	½
z	0	½	0
B (A^2)	0.28(3)	0.14(6)	0.96(2)
Occupancy	0.7/0.3	0.7/0.3	3
a(Å)=3.977(6), **α(°)**= 90° **U**= 0.015(3), **V**= -0.004(5), **W**= 0.005(4) R_F=1.54, R_B=2.21, R_p= 5.61, R_{wp}= 7.52, cR_p= 11.5, cR_{wp}= 11.7, χ= 2.31			
$Ba_{0.6}La_{0.4}Ti_{0.6}Fe_{0.4}O_3$	Ba/La	Ti/Fe	O1
	space group *Pm-3m*		
x	0	½	½
y	0	½	½
z	0	½	0
B (A^2)	0.37(3)	0.20(5)	1.28(2)
Occupancy	0.6/0.4	0.6/0.4	3
a(Å)=3.970(4), **α(°)**= 90° **U**=0.016(2), **V**= -0.002(2), **W**= 0.004(4) R_F=1.72, R_B=2.49, R_p=6.10, R_{wp}=8.17, cR_p=14.2, cR_{wp}=13.8, χ= 2.07			
$Ba_{0.5}La_{0.5}Ti_{0.5}Fe_{0.5}O_3$	Ba/La	Ti/Fe	O1
	space group *Pm-3m*		
x	0	½	½
y	0	½	½
z	0	½	0
B (A^2)	0.30(3)	0.07(3)	1.80(3)
Occupancy	0.5/0.5	0.5/0.5	3
a(Å)=3.964(6), **α(°)**= 90° **U**= 0.015(3), **V**= 0.011(249), **W**= 0.002(5) R_F=1.83, R_B=2.29, R_p= 5.66, R_{wp}= 7.32, cR_p= 15.3, cR_{wp}= 13.6, χ= 2.08			
$Ba_{0.4}La_{0.6}Ti_{0.4}Fe_{0.6}O_3$	Ba/La	Ti/Fe	O1
	space group *Pm-3m*		
x	0	½	½
y	0	½	½
z	0	½	0
B (A^2)	0.37(3)	0.11(5)	2.00(13)
Occupancy	0.4/0.6	0.4/0.6	3
a(Å)=3.956(9), **α(°)**= 90° **U**=0.090(6), **V**=-0.016(5), **W**= 0.007(2) R_F=2.71, R_B=2.96, R_p=6.32, R_{wp}=8.16, cR_p=22.0, cR_{wp}=17.6, χ= 1.54			

Table-III.P1.4. Selected interatomic distances (Å) and (O–Ti–O, O–(Ba/La)–O & Ti –O– (Ba/La)) angles for Cubic BLTF system ($0.3 \leq x \leq 0.6$).

Interatomic distances	x=0.3	x=0.4	x=0.5	x=0.6
Ti/Fe–O	1.989(2)	1.985(2)	1.982(3)	1.978(5)
Ba/La–O	2.813(3)	2.808(2)	2.803(3)	2.797(5)
3×O1–Ti/Fe–O1	180.000(3)	180.000(2)	180.000(4)	180.000(6)
12×O1–Ti/Fe–O1	90.000(1)	90.000(1)	90.000(2)	90.000(3)
6×O1–(Ba/La)–O1	180.000(2)	180.000(2)	180.000(3)	90.000(3)
12×O1–(Ba/La)–O1	90.000(2)	90.000(1)	90.000(2)	180.000(4)
(Ti/Fe)–O-(Ti/Fe)	180.000(3)	180.000(2)	180.000(4)	180.000(6)
4x(Ba/La)–O-(Ba/La)	90.000(2)	90.000(1)	90.000(2)	90.000(3)
2x(Ba/La)–O-(Ba/La)	180.000(2)	180.000(2)	180.000(3)	180.000(4)
8x(Ti/Fe)–O-(Ba/La)	90.000(1)	90.000(1)	90.000(2)	90.000(2)

III.2.3.3. Orthorhombic BLTF perovskite system $0.7 \leq x \leq 1$

The X-ray analysis demonstrates that the samples are formed in single phased ABO_3-type structure except for the composition x = 0.8; secondary phase is detected at 30.45° corresponding to $BaLa_2Ti_4O_{14}$. At x > 0.6, the X-ray diffraction peaks split into doublet, triplet and quadruplet, while the indexation shows similarities to $LaFeO_3$. For the compositions x = 0.7, x = 0.75 and x = 0.8, the peaks move toward higher *2θ (°)*, then a slight shift toward lower *2θ (°)* is observed for the composition x = 0.9 and x = 1. Unlike the samples with the compositions x = 0.7, x = 0.75 and x = 0.8, we noticed that the compounds x = 0.9 and x = 1 show an additional peak at around *2θ* = 24.50°. This additional peak corresponds to the crystallographic reflection (111). According to the mentioned observations, we assumed that the samples with the composition between $0.7 \leq x \leq 1$ crystalize in an orthorhombic structure with different space groups. It is known that $LaFeO_3$ crystallizes in an orthorhombic structure at room temperature with a *Pbnm* space group [24]. The fitting of the compositions x = 0.9 with this model showed good results and low reliability factors are obtained as presented in **Table-III.P1.5**. The *Pnma* space group was then suggested for x = 0.7, x = 0.75 and x = 0.8. All the peaks were successfully indexed and the model fitted perfectly to the experimental results showing low reliability factors. The final Rietveld refinement plots and a visualization of the unit cell parameters along [010] axis are presented in **Fig-III.P1.4.** For structural parameters evolution study, the data issued from the Rietveld refinement are collected and summarized in **Table-III.P1.6**.

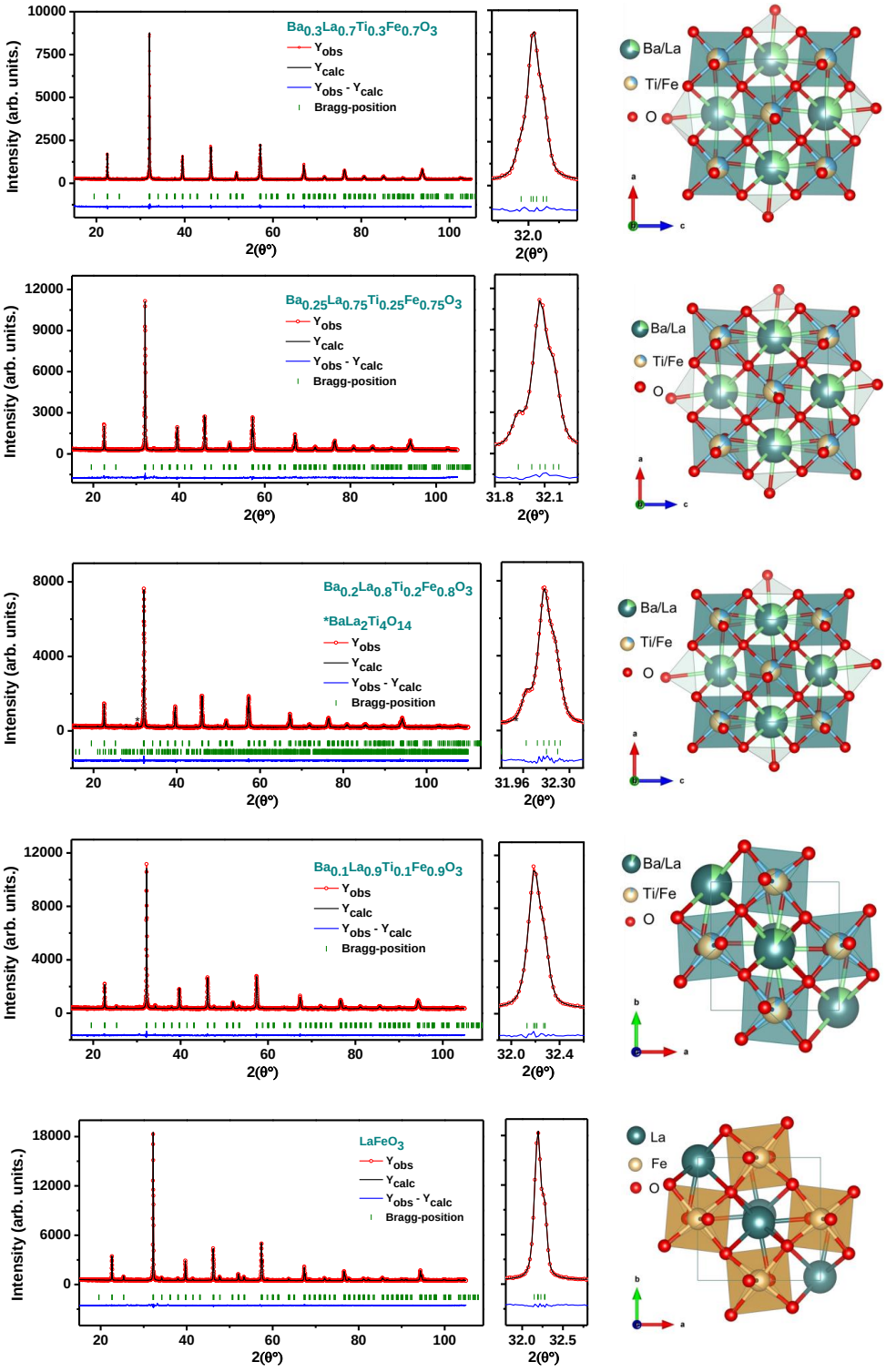

Fig-III.P1.4: Final Rietveld Refinement plots of Orthorhombic BLTF system $0.7 \leq x \leq 1$ and [010] projection of the unit cell with *Pnma* and [001] unit cell with *Pbnm*. The observed data and calculated profile are indicated by circles and solid trace respectively. The lowest trace shows the difference between the observed and calculated model. The vertical bars indicate the calculated bragg reflections positions.

Table-III.P1.5. Refined structural parameters for Orthorhombic BLTF system $0.7 \leq x \leq 1$

$Ba_{0.3}La_{0.7}Ti_{0.3}Fe_{0.7}O_3$	Ba/La	Ti/Fe	O1	O2
	space group *Pnma*			
x	-0.0008(1)	0	0.452(6)	0.248(8)
y	¼	0	¼	-0.023(5)
z	0.495(7)	0	0.533(11)	0.275(6)
B (A^2)	0.420(6)	0.080(8)	0.900(4)	0.900(4)
Occupancy	0.3/0.7	0.3/0.7	1	2
a(Å)= 5.599(2), **b(Å)**= 7.886(3), **c(Å)**= 5.578(2), **α(°)**= 90° **U**=0.057(7), **V**=-0.001(6), **W**= 0.007(1) R_F=13.8, R_B=6.75, R_p=4.93, R_{wp}=6.39, cR_p=23.0, cR_{wp}=16.2, χ= 1.34				
$Ba_{0.25}La_{0.75}Ti_{0.25}Fe_{0.75}O_3$	Ba/La	Ti/Fe	O1	O2
	space group *Pnma*			
x	-0.003(9)	0	0.436(4)	0.236(9)
y	¼	0	¼	-0.015 (5)
z	0.496(8)	0	0.543(9)	0.242(10)
B (A^2)	0.430(7)	0.130(9)	1.500(3)	1.500(3)
Occupancy	0.75/0.25	0.75/0.25	1	2
a(Å)= 5.599(2), **b(Å)**= 7.875(2), **c(Å)**= 5.571(2), **α(°)**= 90° **U**=0.015(4), **V**=0.003(4), **W**= 0.005(8) R_F=23.3, R_B=13.3, R_p=5.26, R_{wp}=6.78, cR_p=26.2, cR_{wp}=17.8, χ= 1.92				
$Ba_{0.2}La_{0.8}Ti_{0.2}Fe_{0.8}O_3$	Ba/La	Ti/Fe	O1	O2
	space group *Pnma*			
x	-0.0013(7)	0	0.435(3)	0.254(6)
y	¼	0	¼	-0.028(2)
z	0.494(7)	0	0.467(14)	0.269(5)
B (A^2)	0.56(5)	0.160(56)	1.7(3)	1.7(3)
Occupancy	0.2/0.8	0.2/0.8	1	2
a(Å)= 5.592(2), **b(Å)**= 7.867(2), **c(Å)**= 5.563(2), **α(°)**= 90° **U**= 0.027(3), **V**= 0.002(3), **W**= 0.004(6) R_F= 18.0, R_B= 9.14, R_p= 7.05, R_{wp}= 9.84, cR_p= 32.0, cR_{wp}= 25.9, χ= 2.42				
$Ba_{0.1}La_{0.9}Ti_{0.1}Fe_{0.9}O_3$	Ba/La	Ti/Fe	O1	O2
	space group *Pbnm*			
x	-0.0052(12)	0	0.080(7)	-0.238(7)
y	0.022 (3)	½	0.522(4)	0.223(6)
z	¼	0	¼	0.025(4)
B (A^2)	0.52(7)	0.22(8)	1.8(3)	1.8(3)
Occupancy	0.9/0.1	0.9/0.1	1	2
a(Å)= 5.567(2), **b(Å)**= 5.556(3), **c(Å)**= 7.854(3), **α(°)**= 90° **U**=0.087(1), **V**=-0.029(7), **W**= 0.001(1) R_F=10.1, R_B=4.20, R_p=4.28, R_{wp}= 5.39, cR_p=25.1, cR_{wp}=16.2, χ= 1.39				
$LaFeO_3$	Ba/La	Ti/Fe	O1	O2
	space group *Pbnm*			
x	-0.0038(15)	0	0.087(6)	-0.270(5)
y	0.029(2)	½	0.497(3)	0.278(3)
z	¼	0	¼	0.036(3)
B (A^2)	0.800(6)	0.440(8)	0.900(6)	0.900(6)
Occupancy	1	1	1	2

Table-III.P1.6. Selected interatomic distances (Å) and (O–Ti–O, O–(Ba/La)–O & Ti –O– (Ba/La)) angles for Orthorhombic BLTF system ($0.7 \leq x \leq 1$).

Composition	X=0.7	X=0.75	X=0.8	Composition	X=0.9	X=1
2×Ti/Fe–O1	1.998(7)	2.015(7)	2.008(8)	2×Ti/Fe–O1	2.017(9)	2.022(8)
2×Ti/Fe–O2	2.080(4)	1.890(5)	2.070(3)	2×Ti/Fe–O2	2.040(4)	1.960(3)
2×Ti/Fe–O2	1.900(4)	2.070(5)	1.900(3)	2×Ti/Fe–O2	1.920(4)	2.030(2)
<Ti/Fe–O>	1.992	1.991	1.992	<Ti/Fe–O>	1.992	2.004
Ba/La–O1	3.070(3)	3.150(2)	2.680(6)	Ba/La–O1	2.820(2)	3.003(2)
Ba/La–O1	2.540(3)	2.470(2)	2.940(6)	Ba/La–O1	2.820(2)	2.652(2)
Ba/La–O1	2.960(6)	3.020(5)	3.179(2)	Ba/La–O1	3.200(4)	3.250(3)
Ba/La–O1	2.650(6)	2.590(5)	2.419(2)	Ba/La–O1	2.370(4)	2.320(3)
2×Ba/La–O2	2.840(4)	2.850(5)	2.600(8)	2×Ba/La–O2	2.460(3)	2.630(3)
2×Ba/La–O2	2.980(4)	2.870(5)	2.950(7)	2×Ba/La–O2	2.980(3)	2.810(2)
2×Ba/La–O2	2.600(4)	2.690(5)	2.680(8)	2×Ba/La–O2	2.810(3)	2.520(2)
2×Ba/La–O2	2.770(4)	2.750(5)	2.920(3)	2×Ba/La–O2	2.890(3)	3.210(3)
<Ba/La–O>	2.800	2.795	2.793	<Ba/La–O>	2.790	2.797
1×O1–Ti/Fe–O1	180.0(7)	180.0(6)	180.0(5)	1×O1–Ti/Fe–O1	180.0(8)	180.000(2)
8×O2–Ti/Fe–O2	90(3)	90(4)	91(8)	4×O2–Ti/Fe–O2	91(3)	91.300(2)
2×O2–Ti/Fe–O2	180(3)	180(5)	180(9)	2×O2–Ti/Fe–O2	180(3)	180.000(2)
				4×O2–Ti/Fe–O2	89(2)	88.700(2)
1×O1–Ba/La–O1	171(2)	169.100(2)	163(4)	1×O1–Ba/La–O1	160.6(14)	159.800(7)
1×O1–Ba/La–O1	169(4)	166(3)	175(5)	2×O2–Ba/La–O2	176(2)	173.200(5)
4×O2–Ba/La–O2	174(3)	176(3)	174(5)	2×O2–Ba/La–O2	171(2)	167.400(2)
(Ti/Fe)–O1-(Ti/Fe)	161.200(3)	155.300(3)	155.600(2)	(Ti/Fe)–O1-(Ti/Fe)	153.5(3)	153.200(3)
(Ti/Fe)–O2-(Ti/Fe)	167.800(2)	173(2)	168(4)	(Ti/Fe)–O2-(Ti/Fe)	165.5(2)	159.600(9)

The results summarized in **Tables-III.P1.1**, **P1.3** and **P1.5** are expressed in the **Fig-III.P1.5 (a, b).** The unit cell parameters evolution as function of the composition shows a decrease as demonstrated in **Fig-III.P1.5a**. Respectively, the substitution of higher ionic radius cations (Ba^{2+} = 1.61Å) (Ti^{4+} = 0.605Å) by smaller ionic radius cations (La^{3+} = 1.36Å) and (Fe^{3+} = 0.55Å), has resulted in a compression along the c-axis leading to the increase or expansion of the "a" lattice parameter and decrease of "b" and "c" lattice parameters confirming the break from high symmetry toward low symmetry. This evolution is also reflected in **Fig-III.P1.5b,** as a continual decrease of the unit cell volume as the amount of the substitution increases. To illustrate the symmetry break, we calculated the experimental tolerance factor introduced by Goldschmidt et al. [25].

$$t = (r_A + r_O)/\sqrt{2}(r_B + r_O) \qquad \text{(Eq. 1)}$$

Where, r_A, r_B and r_O represent the ionic radius of the elements in the A-sites, B-sites and the oxygen ion respectively. In our Case $r_A = (1-x)*r_{Sr} + (x)*r_{La}$ and $r_B = (1-x)*r_{Ti} + (x)*r_{Fe}$. The evolution of the tolerance factor calculated from the experimental results proves that the system evolves toward higher symmetry as shown in **Fig-III.P1.5c**. The variation of the tolerance factor as function of substitution indicates the structure stability. It is demonstrated that specific percentages of La^{3+} and Fe^{3+} substitution build systems with high symmetry as for the compositions between ($0.2 \leq x \leq 0.6$), while at $x > 0.6$ the system evolves toward lower symmetry.

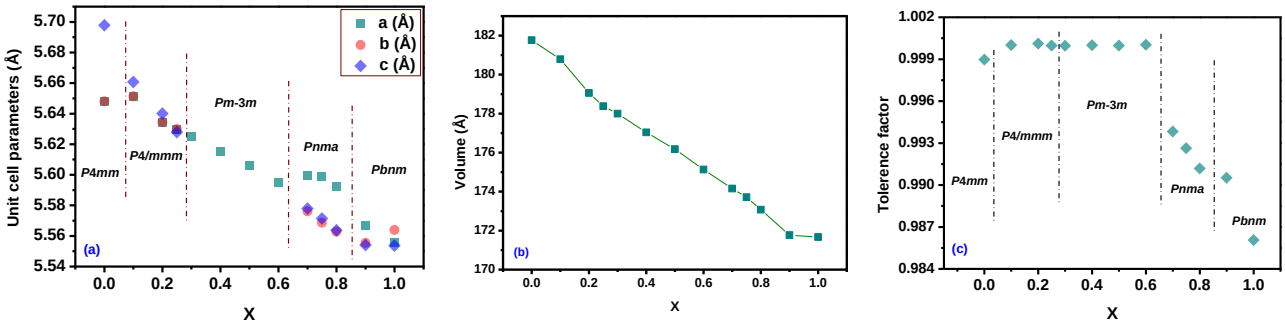

Fig-III.P1.5: The variation as function of the composition of the Unit cell parameters (a, b, c) **(a)**, the unit cell Volume **(b)** and the calculated experimental tolerance factor **(c).**

In **Fig-III.P1.6 (a, b)** the two <Ba/La-O> and <Ti/Fe-O> interatomic distances along with the tolerance factor were presented as function of the substitution amount. The further decrease of the <Ba/La-O> interatomic observed is consistent with substitution of higher ionic radius elements (Ba^{2+} = 1.61Å) (Ti^{4+} = 0.605Å) with smaller ionic radius elements (La^{3+} = 1.36Å) and (Fe^{3+} = 0.55Å). The observed Ti/Fe-O interatomic behavior is more significant to understand the symmetry evolution in the solid solution series. The samples with the composition between ($0.2 \leq x \leq 0.6$) show a decrement in <Ti/Fe-O> interatomic distance, and thus they present structures with higher symmetry, above $x > 0.6$ as shown in **Fig-III.P1.6a**, distorted and disordered systems are built as <Ti/Fe-O> interatomic distance starts to increase. With regard to the **equation 1** of the tolerance factor, it is concluded that <Ti/Fe-O> interatomic distance affects strongly the stability of the structure, and smaller the value, the close the tolerance factor is close to unity and this is observed clearly at compositions $x > 0.6$.

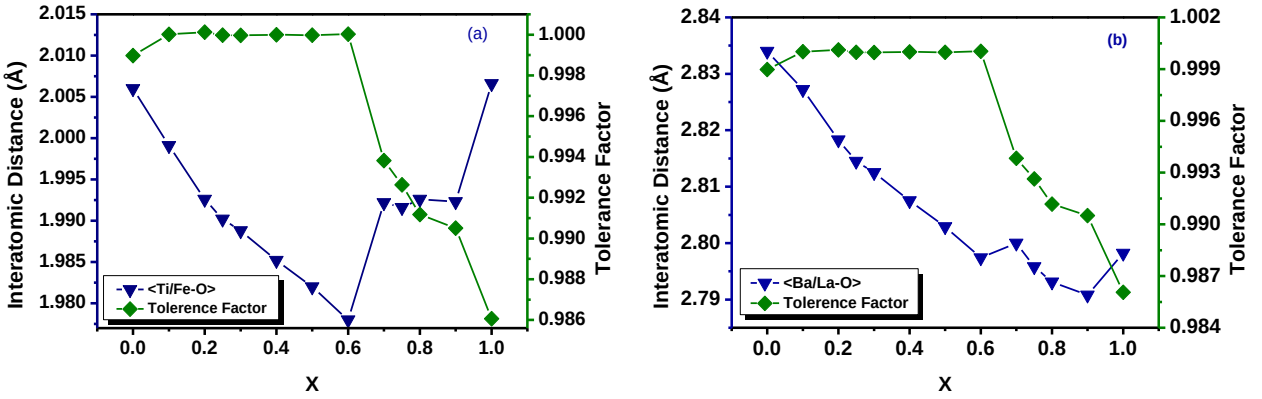

Fig-III.P1.6: The interatomic distance evolution presented along with the tolerance factor as function of the composition. <Ti/Fe-O> **(a)** and <Ba/La-O> **(b)** interatomic distances.

III.2.4. Morphological analysis and the effect of the compositions on the grain growth

The effect of the composition on the grain size, distribution and morphology is different from a composition to another in the BLTF solid solution. The Micrographs displayed in **Fig-III.P1.7** show the different morphologies of the samples. $BaTiO_3$ (x = 0) the grains are in irregular polyhedron form and largely agglomerated with an average size of 1.86 µm. The substitution of Ba^{2+} by La^{3+} in $BaTiO_3$ is reported to reduce the grain size only, while the shape of the grains is maintained in the form of polygonal [53, 54], similarly, the addition of Fe^{3+} reduces the grain size but tend to form secondary hexagonal phases [55]. In the current case, the composition with x = 0.25 shows inhomogeneous distribution of grains with spherical shape, the sample show agglomerated grains coexisting with porous and distributed grains with an average size between 0.089 and 0.48µm. Large grains are formed for the compositions x = 0.3 and 0.5 and constitute the majority, the grains are in irregular shape and few pores are observed. The grain size varies between 1.3 and 4.4 µm for x = 0.3 and between 0.68 and 2.702 µm. The composition x = 0.6 shows very different morphology with grain average size between 0.3 and 1.6 µm, the compounds is forms porous structure with grains of various forms like irregular cubic faced, and irregular polyhedrons grains distributed homogeneously. At x = 0.8, the grains are curved faces and more interconnected, and barely any grain boundaries is observed; meanwhile the composition x = 0.9 shows very porous structure with distributed large and small grains in the form of irregular polyhedrons, the average size is in the range 0.92 and 2.25 µm for x = 0.8 and between 0.24 and 1.50 µm for x = 0.9. Smaller grains are observed for $LaFeO_3$ with an average size of about 0.398 µm.

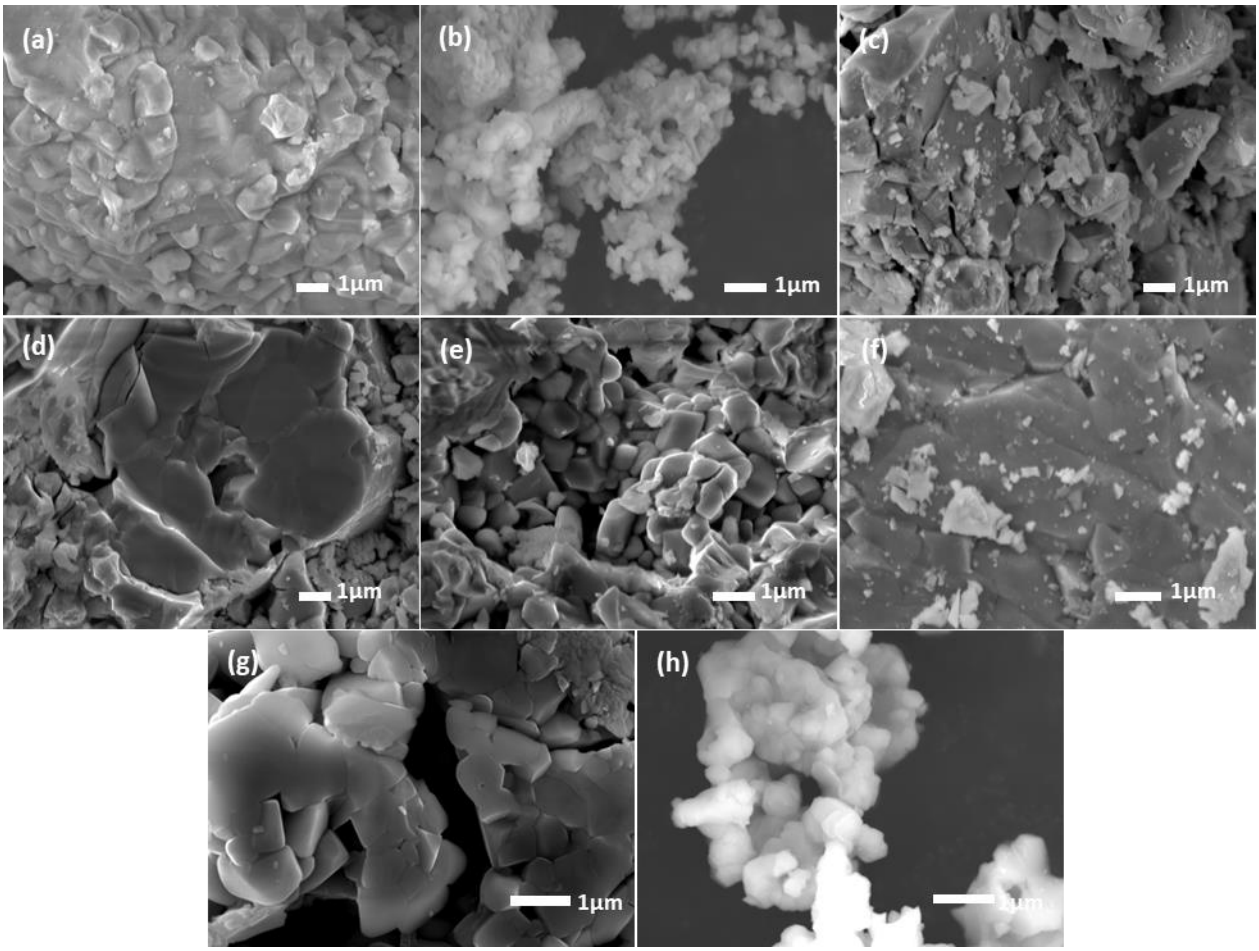

Fig-III.P1.7: SEM images showing the effect of the composition on the morphology of the solid solution BLTF for the compositions x = 0 **(a)**, x = 0.25 **(b)**, x = 0.3 **(c)**, x = 0.5 **(d)**, x = 0.6 **(e)**, x = 0.8 **(f)**, x = 0.9 **(g)**, and x = 1 **(h)**.

III.2.5. Conclusion

The structural studies of the solid solution of perovskite $Ba_{1-x}La_xTi_{1-x}Fe_xO_3$ $0 \leq x \leq 1$ demonstrates the complete dissolution of $LaFeO_3$ into $BaTiO_3$ and it is proven to be possible for an amount of substitution ranging between $0 \leq x \leq 1$. The substitution of high ionic radius elements by small ionic radius elements results in a decrements of the unit cell volume and thus the unit cell parameters. By means of the Rietveld refinement method, two main phase transitions, Tetragonal → Cubic → orthorhombic were found as the amount of the substitution increases. During our investigation we observed that the samples in the same symmetry adopt different space groups, for the compositions between $0.1 \leq x \leq 0.25$, the samples adopt the tetragonal structure with *P4/mmm* unlike $BaTiO_3$ that crystallize in the *P4mm.* As the amount of the substitution increases the system evolve toward structure with high symmetry adopting

Pm-3*m* space group for cubic system for the composition between $0.3 \leq x \leq 0.6$. At x = 0.7 there is a break in the symmetry and the samples show an orthorhombic structure with *Pnma* as space group for the composition between $0.7 \leq x \leq 0.8$ while *Pbnm* is found for the compositions x = 0.9 and x = 1. The structure stability was verified based on the calculated tolerance factor using the interatomic distances issued from Rietveld refinement results. Moreover, the system evolution was systematically studied with regard to the interatomic distance evolution; it is observed that the system forms highly symmetric structure for compositions between ($0.2 \leq x \leq 0.6$), and evolves toward distorted systems at $x > 0.6$. This evolution was correlated with the interatomic distances evolution as function of the composition. It is concluded that the system shows distorted structure as the interatomic distance Ti/Fe-O increases, and since Ba/La-O interatomic is in a continual decrease, the symmetry formation is more affected to Ti/Fe-O.

Various morphologies were observed for the BLTF ceramics; the incorporation of La^{3+} and Fe^{3+} formed structure with inhomogeneous grain size distribution, and more porous structure in comparison with $BaTiO_3$. The inhomogeneity observed in all the samples is also due to the synthesis method used to prepare BLTF which is known to produce non homogeneous powders, however the different shapes observed at each composition is purely related to the composition. Non continual decrease is reported in this case since the size decreased for the composition x = 0.25 and then start increasing at $x \geq 0.3$.

III.3. Part II: Investigations of the composition effect on the structure in $Sr_{1-x}La_xTi_{1-x}Fe_xO_3$ perovskite system with $0 \leq x \leq 1$

III.3.1. Introduction

$SrTiO_3$ is extensively investigated for photocatalytic, water splitting and other clean energy production applications due to its important properties [26–28]. $SrTiO_3$ is known to adopt the cubic structure with space group $Pm\bar{3}m$ [29, 30]; the doping effect of Ba and Ag on the properties and structure of $SrTiO_3$ was reported by *M. Ghasemifard et al.* [31]; $SrTiO_3$ and $Sr_{0.9}Ba_{0.1}TiO_3$ adopt the cubic structure while $Sr_{0.9}Ba_{0.1}Ti_{0.9}Ag_{0.1}O_3$ showed tetragonal symmetry. La and Cr Co-doped of $SrTiO_3$ for H_2 evolution photocatalysts is reported by *Yushuai Jia et al.* [32], cubic structure was assigned to the prepared samples where the effect of the substitution was shown on the full width at half maximum of the (110) XRD peak of the prepared samples.

The effect of Fe addition was reported by Luis F et al. [33]; the X-ray diffraction analysis showed that the network of the perovskite series $SrTi_{1-x}Fe_xO_3$ shrinks as the amount of the Fe^{3+} increases while all the prepared samples were indexed to the cubic structure. La-doped $SrTiO_3$ solid solution was studied as thermal conductive materials; M. T. Buscaglia et al. [34] reported cubic structure for an amount of La^{3+} 10% of Sr substitution. La-doped $SrTiO_3$ was as well studied for its colossal permittivity by *M. Qin et al.* [35] and for its thermoelectric properties by *S. P. Singh et al.* [36] both groups reported cubic structure. In other work *M. Abdi et al.* [37] studied the performance of La and Fe co-doped $SrTiO_3$ with the different concentrations: 1, 2, 3, 4 and 5 wt % and reported the cubic structure for all the prepared samples.

The reported results show that $SrTiO_3$ maintains the cubic structure for low amount of substitution in both cases of A-site or B-site substitution; it preserve as well the cubic structure in the case of co-substitution of small amount. This part will discuss the substitution effect in a wide range between $0 \leq x \leq 1$ of La and Fe co-doped $SrTiO_3$; $Sr_{1-x}La_xTi_{1-x}Fe_xO_3$ solid solution. The stability criteria of the structure, the phase transitions induced as well as the evolution of the structural parameters will be evaluated and discussed.

III.3.2. X-Ray Diffraction patterns: results and discussion

The X-ray diffraction patterns of the perovskite series SLTF is presented in **Fig-III.P2.1a**. $SrTiO_3$ and $LaFeO_3$ corresponding respectively to x=0 and x=1 show their typical perovskite structure pattern [38, 39]. The samples with compositions ranging between $0.2 \leq x \leq 0.8$ show similar X-ray diffraction patterns to $SrTiO_3$ and $LaFeO_3$, indicating that all the synthesized samples adopt the perovskite structure. This reveals that doping $SrTiO_3$ with La^{3+} and Fe^{3+} does not prevent the phase formation. Indexing of the resulted X-ray diffraction peaks was done by Dicvol software [19]. A gradual shift of the main peaks toward lower 2 theta is observed with the increase of the substitution amount as presented in **Fig-III.P2.1b**. This shift indicates that the structure evolution of samples undergoes lattice parameter relaxation and thus an increase of the unit volume must be observed. **Fig-III.P2.1b** shows the magnified main peaks at 2 theta in the ranges $32 \leq 2\theta \leq 33$, $46 \leq 2\theta \leq 47$, $57 \leq 2\theta \leq 58$ correspond respectively to the reflections (110), (200) and (211) for the samples x = 0 and x = 0.2. At a substitution amount higher than 20%, the reflections (110), (200), (211) split to doublets (002), (121); (202), (040) and (123), (042) and the

reflection (321) splits to triplet (125), (244), (163). These observations suggest the occurrence of phase transitions due to substitution of Sr^{2+} and Ti^{4+} elements by La^{3+} and Fe^{3+} respectively.

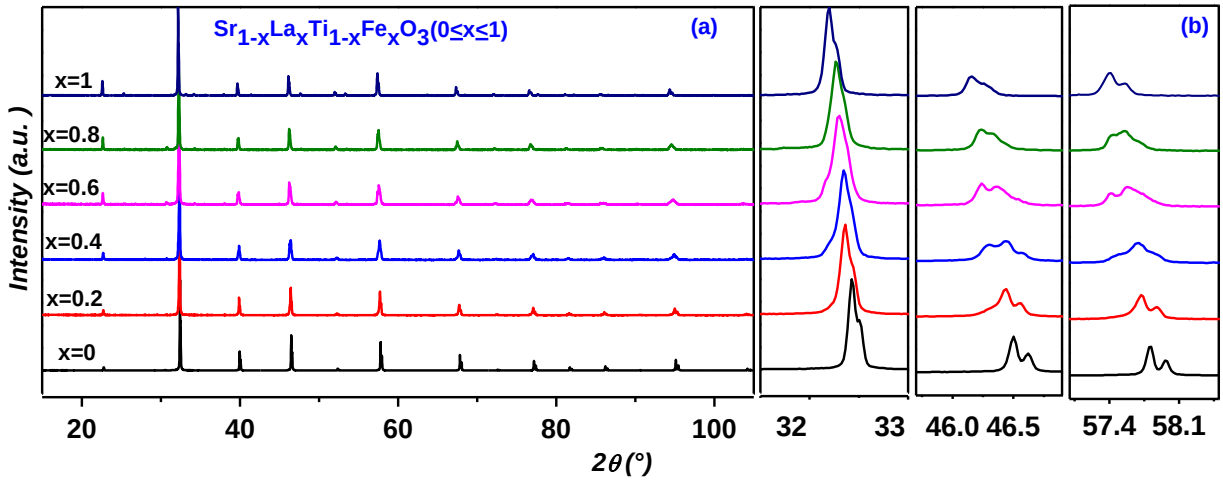

Fig-III.P2.1: X-ray powder diffraction patterns of $Sr_{1-x}La_xTi_{1-x}Fe_xO_3$ ($0 \leq x \leq 1$) presenting the peaks shape variation **(a)** and the separated main peaks **(b)**.

III.3.3. Rietveld refinement study of the structure and the phase transitions

Rietveld Refinement method was used in order to investigate the crystal structure formation and the effect of the substitution. Structure refinement of the X-ray diffraction patterns was conducted using FullProf [40] program coupled with WinPLOTR software [19]. Adjustment of the calculated profile to the experimental results led to satisfactory results as presented in **Table-III.P2.(2, 3)**. The results confirm that the system undergoes one phase transition at $x > 0.2$ from higher symmetry (SG: *Pm-3m*) to lower symmetry (SG: *Pnma/Pbnm*). The bond angles, and the interatomic distances issued from the Rietveld refinement are collected and summarized in **Table-III.P2.(1, 4)**.

III.3.3.1. Cubic SLTF perovskite system $0 \leq x \leq 0.2$

The compound with $x = 0.2$ was refined to the same cubic symmetry of $SrTiO_3$ with *Pm-3m* space group (N°221) [38]. The calculated profile fitted perfectly to the experimental pattern. The sample shows an increase in the unit cell parameter from 3.906 to 3.909 **Å**. This increase confirms our previous observations and the calculated tolerance factor is equal to unity, the final Rietveld refinement plots are presented in **Fig-III.P2.2**.

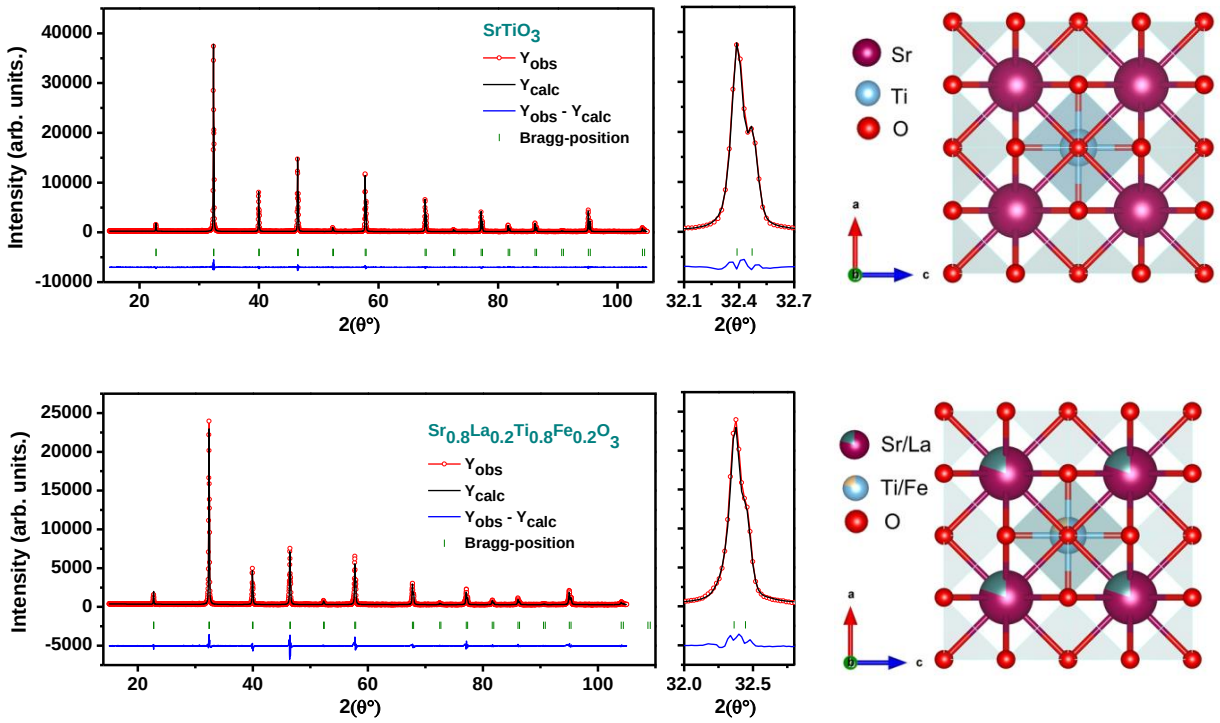

Fig-III.P2.2: Final Rietveld Refinement plots of Cubic SLTF system $0 \leq x \leq 0.2$ and [010] projection of the unit cell with *Pm*-3*m*. The observed data and calculated profile are indicated by circles and solid trace respectively. The lowest trace shows the difference between the observed and calculated model. The vertical bars indicate the calculated bragg reflections positions.

Table-III.P2.1. Selected interatomic distances (Å) and (O–Ti–O, O–(Sr/La)–O & Ti –O– (Sr/La)) angles for Cubic SLTF system ($0 \leq x \leq 0.2$).

Interatomic distances	x=0	x=0.2
Ti/Fe–O	1.9529(8)	1.9544(4)
Sr/La–O	2.7619(2)	2.7640(1)
3×O1–Ti/Fe–O1	180.000(3)	180.0 (2)
12×O1–Ti/Fe–O1	90.000(1)	90.0 (1)
6×O1–(Sr/La)–O1	180.000(2)	180.000(1)
12×O1–(Sr/La)–O1	90.000(2)	90.000(1)
(Ti/Fe)–O-(Ti/Fe)	180.000(3)	180.000(2)
4x(Sr/La)–O-(Sr/La)	90.000(2)	90.000(1)
2x(Sr/La)–O-(Sr/La)	180.000(2)	180.000(2)
8x(Ti/Fe)–O-(Sr/La)	90.000(1)	90.000(1)

Table-III.P2.2. Refined structural parameters for Cubic SLTF system $0 \leq x \leq 0.2$

$SrTiO_3$	Ba/La	Ti/Fe	O1
	space group *Pm-3m*		
x	0	0	0
y	0	0	0
z	0	0	0

B (A²)	0.60(2)	0.60(2)	0.60(2)
Occupancy	1	1	1
a(Å) = 3.90595(2), **γ(°)** = 90 **U** = 0.00834(8), **V** = -0.00191(9), **W** = 0.00494(2) **R_F** = 1.75, **R_B** = 2.63, **R_p**= 5.11, **R_{wp}**= 7.00, **cR_p**= 7.77, **cR_{wp}**= 9.10, **χ** = 4.49			
$Sr_{0.8}La_{0.2}Ti_{0.8}Fe_{0.2}O_3$	**Sr/La**	**Ti/Fe**	**O1**
	space group *Pm-3m*		
x	0	½	½
y	0	½	½
z	0	½	0
B (A²)	0.96(5)	0.45(6)	0.73(6)
Occupancy	0.8/0.2	0.8/0.2	3
a(Å) = 3.90888(9), **γ(°)** = 90 **U** = 0.01226(5), **V** = 0.02739(5) , **W** = -0.00108(1) **R_F** = 4.69, **R_B** = 6.60, **R_p**= 7.85, **R_{wp}**= 11.0, **cR_p**= 20.6, **cR_{wp}**= 19.8, **χ** = 5.85			

III.3.3.2. Orthorhombic SLTF perovskite system $0.4 \leq x \leq 1$

The compounds with the composition ranging between $0.4 \leq x \leq 0.8$ present similar X-ray patterns to that of $LaFeO_3$ [39]. Traces of La_2O_3 has been detected between 30.5° and 30.8° for the compositions x = 0.4, 0.6 and 0.8. The X-ray patterns show a difference in the shape of the main peaks as shown in **Fig-III.P2.1b**. Refining the structures to the orthorhombic symmetry with *Pbnm* space group led to high reliability factors and appropriate interatomic distances which confirm that these compositions may adopt different space group than the one given by $LaFeO_3$ (**Fig-III.P2.3)**. *Pnma* space group was suggested as the fitting model, the Rietveld refinement led to satisfactory results with low reliability factors. The refinement results showed that the samples within $0.4 \leq x \leq 1$ adopt the orthorhombic structure with two different space group *Pnma* and *Pbnm* for x = 0.4, 0.6, 0.8 and x = 1 respectively.

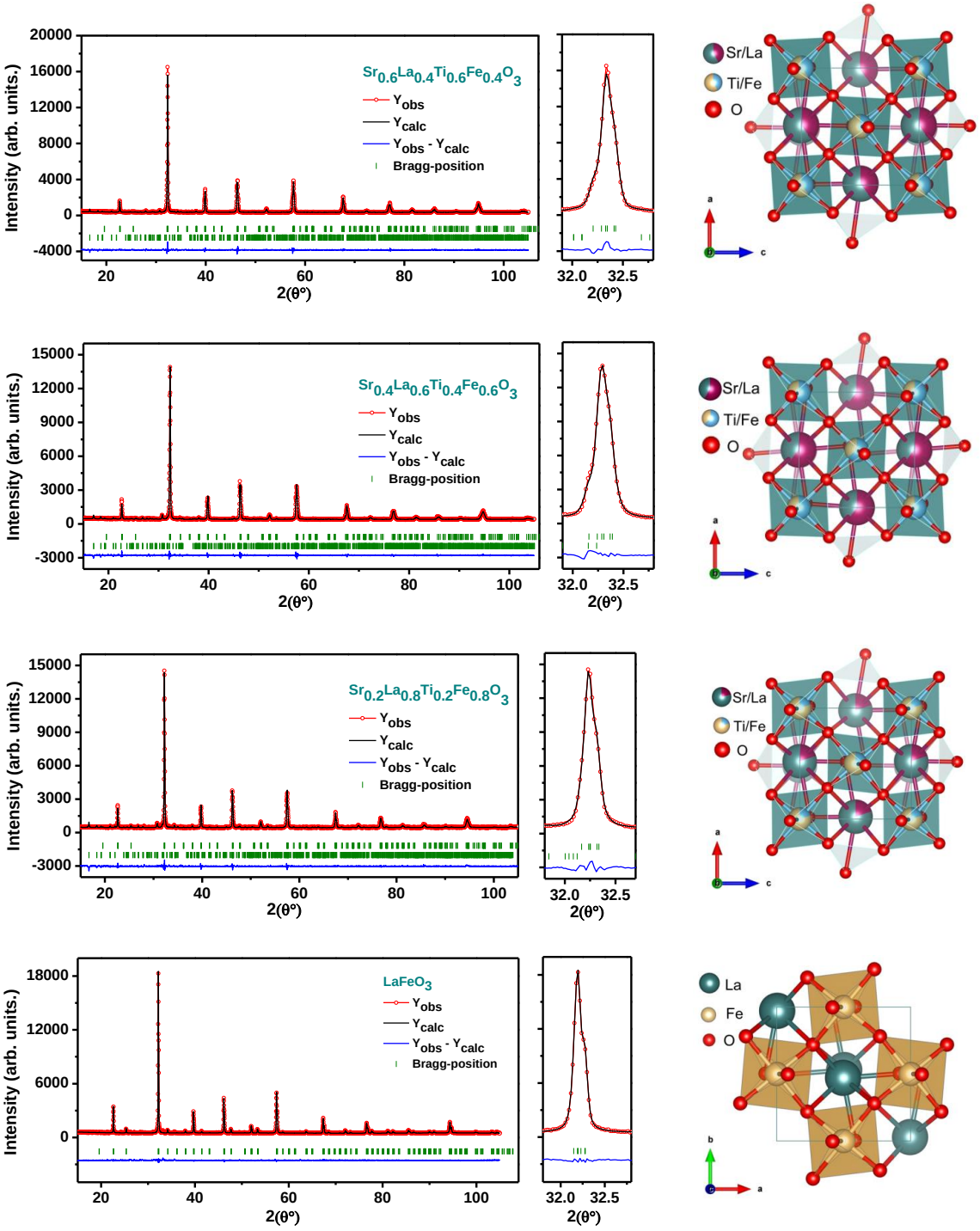

Fig-III.P2.3: Final Rietveld Refinement plots of Orthorhombic SLTF system $0.4 \leq x \leq 1$ and [010] projection of the unit cell with *Pnma* and [001] unit cell with *Pbnm*. The observed data and calculated profile are indicated by circles and solid trace respectively. The lowest trace shows the difference between the observed and calculated model. The vertical bars indicate the calculated bragg reflections positions.

Table-III.P1.3. Refined structural parameters for Orthorhombic SLTF system 0.4 ≤ x ≤ 1

$Sr_{0.6}La_{0.4}Ti_{0.6}Fe_{0.4}O_3$	Sr/La	Ti/Fe	O1	O2
	space group *Pnma*			
x	-0.0015(12)	0	0.465(6)	0.242(8)
y	¼	0	¼	0.010(2)
z	0.4971(8)	0	0.567(2)	0.239(5)
B (A²)	0.57(6)	0.56(7)	0.74(20)	0.74(20)
Occupancy	0.6/0.4	0.6/0.4	1	2
a(Å) = 5.5310(2), **b(Å)** = 7.8134(2), **c(Å)** = 5.5549(2), **γ(°)** = 90 **U** = 0.02829(6), **V** = 0.02321(6), **W** = 0.00079(12) $\mathbf{R_F}$ = 11.4, $\mathbf{R_B}$ = 6.24, $\mathbf{R_p}$= 4.66, $\mathbf{R_{wp}}$= 6.07, $\mathbf{cR_p}$= 20.1, $\mathbf{cR_{wp}}$= 14.6, **χ** = 1.71				
$Sr_{0.4}La_{0.6}Ti_{0.4}Fe_{0.6}O_3$	Sr/La	Ti/Fe	O1	O2
	space group *Pnma*			
x	-0.0115(5)	0	0.494(4)	0.263(7)
y	¼	0	¼	0.015(3)
z	0.4976(10)	0	0.569(3)	0.234(6)
B (A²)	0.89(7)	0.32(8)	0.82(2)	0.82(2)
Occupancy	0.4/0/6	0.4/0.6	1	2
a(Å) = 5.5368(2), **b(Å)** = 7.8236(3), **c(Å)** = 5.5619(2), **γ(°)** = 90 **U** = 0.08334(10), **V** = -0.02372(10), **W** = 0.01094(2) $\mathbf{R_F}$ = 14.5, $\mathbf{R_B}$ = 8.13, $\mathbf{R_p}$= 4.54, $\mathbf{R_{wp}}$= 6.05, $\mathbf{cR_p}$= 23.7, $\mathbf{cR_{wp}}$= 16.5, **χ** = 1.91				
$Sr_{0.2}La_{0.8}Ti_{0.2}Fe_{0.8}O_3$	Sr/La	Ti/Fe	O1	O2
	space group *Pnma*			
x	-0.0212(3)	0	0.484(3)	0.280(4)
y	¼	0	¼	0.020(2)
z	0.4995(12)	0	0.589(3)	0.248(5)
B (A²)	0.63(6)	0.19(8)	0.428(15)	0.428(15)
Occupancy	0.2/0.8	0.2/0.8	1	2
a(Å) = 5.5459(2), **b(Å)** = 7.8412(3), **c(Å)** = 5.56079(19), **γ(°)** = 90 **U** = 0.05103(6), **V** = -0.01839(6), **W** = 0.00861(1) $\mathbf{R_F}$ = 16.3, $\mathbf{R_B}$ = 9.74, $\mathbf{R_p}$= 4.23, $\mathbf{R_{wp}}$ = 5.65, $\mathbf{cR_p}$= 25.4, $\mathbf{cR_{wp}}$= 16.8, **χ** = 1.75				
$LaFeO_3$	Sr/La	Ti/Fe	O1	O2
	space group *Pbnm*			
x	-0.0027(15)	0	0.074(5)	-0.287(3)
y	0.0291(2)	½	0.492(2)	0.273(4)
z	¼	0	¼	0.041(3)
B (A²)	0.57(6)	0.25(7)	0.868(2)	0.868(2)
Occupancy	1	1	1	2
a(Å) = 5.55572(12), **b(Å)** = 5.56394(15), **c(Å)** = 7.85404(17), **γ(°)** = 90 **U** = 0.02325(3), **V** = -0.00538(3), **W** = 0.00510(6) $\mathbf{R_F}$ = 6.60, $\mathbf{R_B}$ = 7.28, $\mathbf{R_p}$ = 3.86, $\mathbf{R_{wp}}$ = 4.93, $\mathbf{cR_p}$ = 22.6, $\mathbf{cR_{wp}}$ = 14.5, **χ** = 1.46				

Table-III.P2.4. Selected interatomic distances (Å) and (O–Ti–O, O–(Sr/La)–O & Ti –O– (Sr/La)) angles for Orthorhombic SLTF system ($0.4 \leq x \leq 1$).

Composition	X=0.7	X=0.75	X=0.8	Composition	X=1
2×Ti/Fe–O1	1.998(4)	1.993(3)	2.024(4)	2×Ti/Fe–O1	2.007(6)
2×Ti/Fe–O2	1.89(4)	1.96(4)	2.08(2)	2×Ti/Fe–O2	2.059(2)
2×Ti/Fe–O2	2.04(4)	1.98(4)	1.86(3)	2×Ti/Fe–O2	1.95(2)
<Ti/Fe–O>	1.976	1.977	1.979	<Ti/Fe–O>	2.005
Sr/La–O1	2.98(3)	2.77(2)	2.789(2)	Sr/La–O1	3.019(1)
Sr/La–O1	2.61(3)	2.83(2)	2.846(2)	Sr/La–O1	2.611(1)
Sr/La–O1	3.139(1)	3.152(2)	3.273(2)	Sr/La–O1	3.18(3)
Sr/La–O1	2.428(1)	2.411(2)	2.288(2)	Sr/La–O1	2.39(3)
2×Sr/La–O2	2.72(3)	2.80(3)	2.83(2)	2× Sr/La–O2	2.65(2)
2× Sr/La–O2	2.69(3)	2.57(3)	2.52(2)	2× Sr/La–O2	2.81(2)
2× Sr/La–O2	2.84(3)	2.91(3)	2.92(2)	2× Sr/La–O2	2.47(2)
2× Sr/La–O2	2.83(3)	2.81(3)	2.86(2)	2× Sr/La–O2	3.26(2)
< Sr/La–O>	2.776	2.778	2.788	< Sr/La –O>	2.798
1×O1–Ti/Fe–O1	180.0(3)	180.0(3)	180.0(5)	1×O1–Ti/Fe–O1	180.0(5)
8×O2–Ti/Fe–O2	90(3)	90(4)	90.9(2)	4×O2–Ti/Fe–O2	91.0(1)
2×O2–Ti/Fe–O2	180(4)	180(3)	180(2)	2×O2–Ti/Fe–O2	180.0(2)
				4×O2–Ti/Fe–O2	89.0(2)
1×O1–Sr/La–O1	172.2(7)	163.7(1)	178.8(1)	1×O1–Sr/La–O1	162.5(7)
1×O1–Sr/La–O1	164(2)	178.7(1)	159.6(1)	2×O2–Sr/La–O2	172.5(1)
2×O2–Sr/La–O2	177.8(2)	175.1(2)	172.4(1)	2×O2–Sr/La–O2	166.1(1)
2×O2–Sr/La–O2	178.2(2)	178(2)	175.8(1)		
(Ti/Fe)–O1-(Ti/Fe)	161.200(3)	155.300(3)	155.600(2)	(Ti/Fe)–O1-(Ti/Fe)	156.2(2)
(Ti/Fe)–O2-(Ti/Fe)	167.800(2)	173(2)	168(4)	(Ti/Fe)–O2-(Ti/Fe)	157.0(8)

The refinement results of the structural and instrumental parameters are resumed in **Table-III.P2.3** and **Table-III.P2.4**. The effect of the substitution led to the relaxation of the unit cell parameters resulting in a linear increase of the unit cell volume and thus an increase of the interatomic distances as illustrated in **Fig-III.P2.4 (a, b)** and **Fig-III.P2.5 (a, b)**. To evaluate the transition occurred by doping $SrTiO_3$ and the degree of deviation from its ideal cubic structure, we calculated the experimental tolerance factor introduced by Goldschmidt et al. [25].

$$t = (r_A + r_O)/\sqrt{2}(r_B + r_O) \qquad \text{(Eq. 1)}$$

Where, r_A, r_B and r_O represent the ionic radius of the elements in the A-sites, B-sites and the oxygen ion respectively. In our Case $r_A = (1-x)*r_{Sr} + (x)*r_{La}$ and $r_B = (1-x)*r_{Ti} + (x)*r_{Fe}$.

The calculated tolerance factor of the perovskite series ranges between 1.000 and 0.987. **Fig-III.P2.4c** illustrates the evolution of this factor versus the amount of the substitution "x". The evolution of the tolerance factor shows a decrease above x > 0.2 demonstrating that the samples adopt more distorted structure. Thus, the continual increase of the substitution apply a strain leading the perovskite structure to adopt more distorted systems which results in the appearance of the phase transition at x > 0.2. In **Fig-III.P2.5 (a, b),** it is observed that the as the amount of the substitution increases, the interatomic distances increases. Smaller interatomic distances form high symmetrical structures.

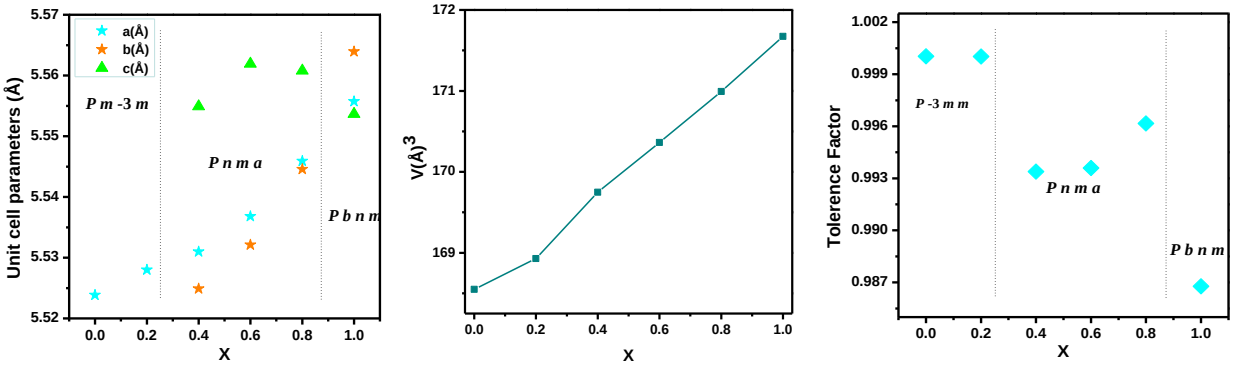

Fig-III.P2.4: The variation as function of the composition of the Unit cell parameters (a, b, c) **(a)**, the unit cell Volume **(b)** and the calculated experimental tolerance factor **(c).**

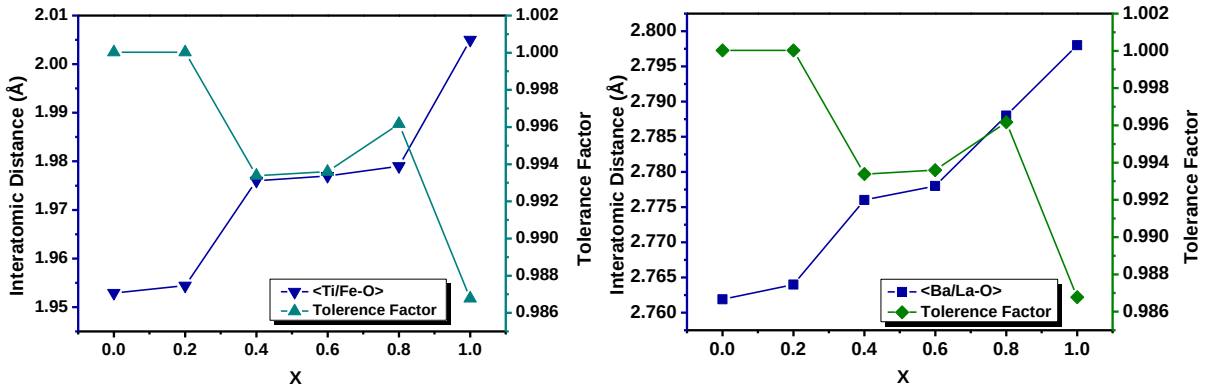

Fig-III.P2.5: The interatomic distance evolution presented along with the tolerance factor as function of the composition. <Ti/Fe-O> **(a)** and <Sr/La-O> **(b)** interatomic distances.

III.3.4. Morphological analysis and the effect of the compositions on the grain growth

The micrographs displayed in **Fig-III.P2.6** show the effect of the compositions on the grain growth, the size and morphology. The SEM Image of undoped $SrTiO_3$ (x = 0) shows porous

structure with non-uniform grains of an average size 0.83 μm; small grains are clustered spherical (0.247 μm) and co-exist with the large particles are irregular polyhedron (2.60 μm) as shown in **Fig-III.P2.6a**. With the substitution effect, the grains are in the form of flat plate like shape with varying size between 0.23 and 1.03 μm for x = 0.2 and 1.47 and 1.36 μm for x = 0.4. The compositions with x ≥ 0.6, broad range of grain size is manifested in inhomogeneous distributions of non-uniform and irregular shape of grains and in the form of clustered spherical grains for x = 0.8, this observation is valid for the substitution amount up to x = 0.8. The grain size varies between 0.67 and 1.12 μm for x = 0.6, and between 0.38 and 1.75 μm. $LaFeO_3$ micrograph displays denser and connected grains in the form of irregular small and large polyhedron with grain size ranging between 0.13 and 0.85 μm. Overall, the samples shows porous structure mainly for the compositions x = 0, 0.2 and 0.4; as the substitution amount increases (x ≥ 0.6), the grains become more interconnected however, they still show porous structure. The effect of the substitution is observed in both reducing the grain size and the morphology evolution from irregular shape to flat plate like grains with polygon surface.

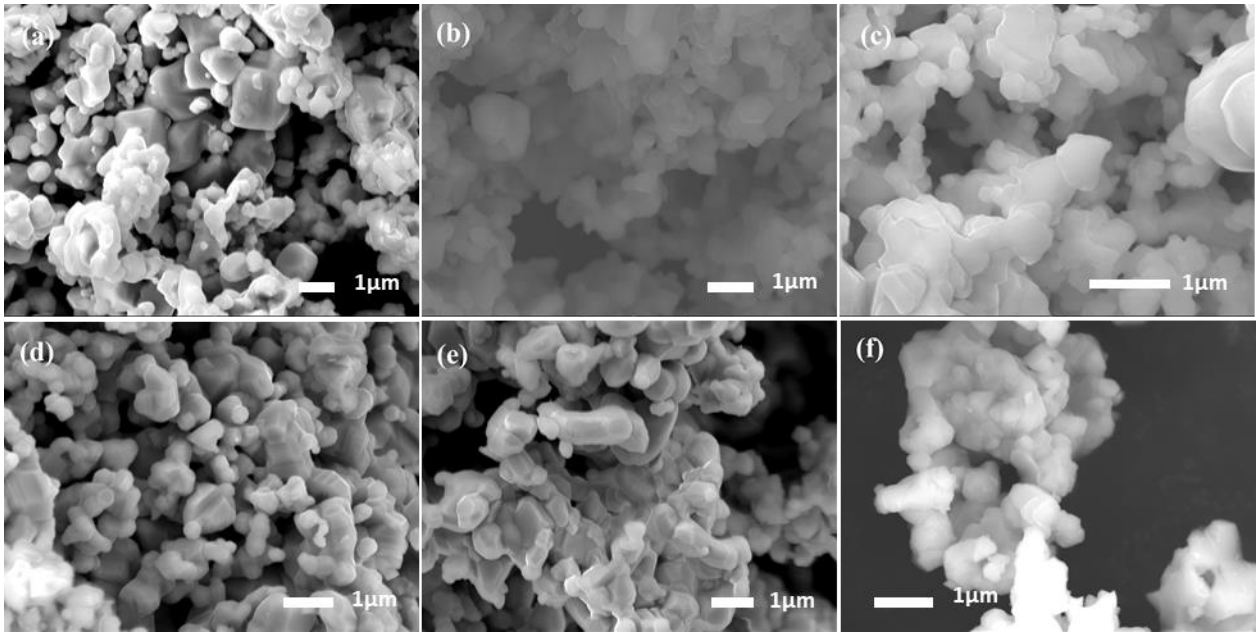

Fig-III.P2.6: SEM images showing the effect of the composition on the morphology of the solid solution BLTF for the compositions x = 0 **(a)**, x = 0.2 **(b)**, x = 0.4 **(c)**, x = 0.6 **(d)**, x = 0.8 **(e)**, and x = 0.1 **(f)**.

III.3.5. Conclusion

The ability of $SrTiO_3$ perovskite to accommodate La^{3+} cations in the A-site and Fe^{3+} cations in the B-site ranges between $0 \leq x \leq 1$ is examined and the final products are expressed following the chemical formula $Sr_{1-x}La_xTi_{1-x}Fe_xO_3$. Typical X-ray diffraction patterns of ABO_3 perovskites were obtained with a gradual shift toward lower 2 theta. The structural investigation by Rietveld refinement methods shows that compositions with $0.2 \leq x$ adopt high symmetry structure with *Pm*-3*m* space group, while the compositions with $x \geq 0.4$ adopt more distorted structure with *Pnma* space group for x = 0.4, 0.6 and 0.8 and *Pbnm* space group for x = 1. These results prove that high amount of Fe^{3+} and La^{3+} tend to form more distorted structures. These results were confirmed by the tolerance factor calculated using the interatomic distances as input data. The compositions with $0.2 \leq x$ showed a value close of $t \approx 1$ while the compositions with $x \geq 0.4$ showed values lower than $t < 1$.

Consistently with the shift of the main peaks of X-ray patterns observed, an increase of the unit cell parameters and thus the unit cell volume has been observed as the amount of the substitution increases. The co-substitution of Sr^{2+} and Ti^{4+} by La^{3+} and Fe^{3+} respectively induces relaxation along the three axis a, b and c; in this case Fe^{3+} ionic radius is larger for high spin and smaller in low spin compared to Ti^{4+} while La^{3+} has smaller ionic radius compared to Sr^{2+}. The volume is expected to decrease as we substituted larger ionic radius by smaller ionic radius elements, however, the results showed a continual increase as the amount of the substitution increases. The evolution of the interatomic distances B-O and A-O demonstrates that the volume expansion is more likely to follow the behavior of the A-O interatomic distance as they show similar response to the substitution effect. The interatomic distance B-O affects more the degree of distortion in the system, it is observed that the tolerance factor evolves oppositely to the B-O interatomic and larger values tends to form low symmetry structure.

For the morphologic characteristics, as the amount of the substitution increases, two different forms of grains were observed: Flat plat like shape for the compositions $x \leq 0.4$, whereas at $x > 0.4$, the samples are non-uniform and in irregular forms. Besides, more porous structure is obtained with the incorporation of La^{3+} and Fe^{3+}. The reduction of the grain size is also observed as an effect of the substitution.

Part III: Investigation of the composition effect on the structure in $Ba_{1-x}Sr_xTi_{1-x}Fe_xO_{3-\delta}$ perovskite system with $0 \leq x \leq 1$

III.3.6.Introduction

The strontium iron oxide material $SrFeO_{3-\delta}$ ($0.5 \leq \delta \leq 0$) is a non-stoichiometric perovskite. Depending on the value 'δ' that describes the vacancy ordering of oxygen, $SrFeO_{3-\delta}$ crystallizes in different forms [41–44]. The cubic structure is reported for $\delta = 0$; in this form $SrFeO_3$ is a helical antiferromagnetic insulator material and iron cations are octahedrally coordinated by oxygen; for $\delta = 0.5$ the material shows semiconductor features and adopt an orthorhombic brownmillerite-like structure. In comparison with the perovskite structure, the oxygen ions aligned along a particular direction are absent for $SrFeO_{2.5}$. The compositions when $\delta \sim 0.125$ and $\delta \sim 0.25$ shows respectively tetragonal phase and orthorhombic phase, as both composition show mixed conductivity and finite band gap [41]. *Y.takeda et al.* [43] reported different structures for four single phases in relation with the oxygen nonstoichiometry of $SrFeO_{3-\delta}$ ($0.5 \leq x \leq 0$); $SrFeO_3$ with cubic structure, $SrFeO_{2.86}$, $SrFeO_{2.73}$ with tetragonal and orthorhombic structure respectively, and $SrFeO_{2.5}$ with brownmillerite-like structure. *J. P. Hodges* [42] showed that $SrFeO_{2.75}$ adopt orthorhombic structure, space group *Cmmm*; on the other hand the correct crystal structure for $SrFeO_{2.875}$ is tetragonal, space group *I4/mmm*.

The heat treatment in literature shows great effect on the stoichiometry of $SrFeO_{3-\delta}$, as it is as well governed by the pressure (p_{O_2}). *L. Fournès et al.* [45] reported in their work that $SrFeO_{2.68}$ is obtained under a slow heat treatment in air at 950°C then reground and treated again for two days at 1300°C. The annealing $SrFeO_{2.68}$ for 24h under dynamic vacuum in quartz tube at 850°C led to obtain $SrFeO_{2.5}$ as final product. Moreover, $SrFeO_{2.75}$ composition is reached after 24h annealing at 650°C and fast quenching; very slow cooling from 800°C to room temperature resulted in the formation of $SrFeO_{2.83}$. Similarly to *J.P. Hodges et al.*, $SrFeO_{3-\delta}$ was obtained by mixing stoichiometric amounts of $SrCO_3$ and Fe_2O_3, this mixture was fired at 1250°C for 24H followed by a slow cooling to room temperature and an oxygen content equal to 2.870 was determined, then the sample was treated under controlled environment of pure oxygen for 24h under 30 MPa and slowly cooled to room temperature, to find a content of oxygen equal to 2.998.

Intense investigations were given to $SrFeO_{3-\delta}$ as it is considered good model to study the effects of oxygen-vacancy ordering on the electronics and structural properties. However, co-substituted $SrFeO_{3-\delta}$ is now gaining interest aiming to enhancing the properties and stabilizing the perovskite structure of $SrFeO_{3-\delta}$. *Hiroshi Yamamura et al.* [46] reported the effect of the substitution on the stability of the structure in the perovskite-type solid solution $Sr_{1-x}M_xFeO_{3-\delta}$, $SrFeO_{2.5}$ showed a transition from the brownmillerite structure to the cubic structure for Mn^{3+} amount ranging between ($0.30 \leq x \leq 0.60$). Similar results were obtained when studying the solid solution $SrFeO_{2.5}$ – $LaFeO_3$; they reported a phase transition to cubic structure for substitution amounts between ($0.0 \leq x \leq 0.20$). The effect of Ti^{4+} was studied by *Avner Rothschild et al.* [47] and *Nicola H. Perry et al.* [48] for different purposes, however no information related to structure were emphasized.

In this part we conduct structural investigations using the Rietveld refinement method and we report the stability of the structure, the phase transitions induced by the substitution, the symmetry and the evolution of the structural parameters of the solid solution $Ba_{1-x}Sr_xTi_{1-x}Fe_xO_{3-\delta}$ in wide range of substitution amount $0 \leq x \leq 1$.

III.3.7.X-Ray diffraction patterns: results and discussion

The X-ray diffraction patterns were recorded at room temperature and indexed using Dicvol program [49] for the perovskite series $Ba_{1-x}Sr_xTi_{1-x}Fe_xO_{3-\delta}$ with $0 \leq x \leq 1$. The Results show that the samples adopt the perovskites like structure. This indicates that all the samples have been successfully synthesized and adopt the desired phase. The X-ray diffraction patterns of the perovskite series are presented in **Fig-III.P3.1a**. The partial substitution of Sr^{2+} in A-sites and Fe^{3+} in B-sites is confirmed to be possible and do not inhibit the phase formation. Besides, the effect of the substitution is reflected by a change in the structure which is clearly observed in the X-ray patterns presented in **Fig-III.P3.1b**. The observed shift of the X-ray patterns toward higher 2 theta is continual with a step of about 0.24 ± 0.01° as the amount of the substitution increases. The evolution of the X-ray diffraction patterns indicates that the system evolve toward higher symmetry. As shown in **Fig-III.P3.1a**, the main peaks of $BaTiO_3$ gradually overlap to form singlet at $x \geq 0.6$. Based on these observations, we suggest that a phase transition is taking place between x = 0.4 and x = 0.6, from tetragonal symmetry for the samples with x=0; 0.2; 0.4 to cubic symmetry for the samples x=0.6, 0.8 and 1.

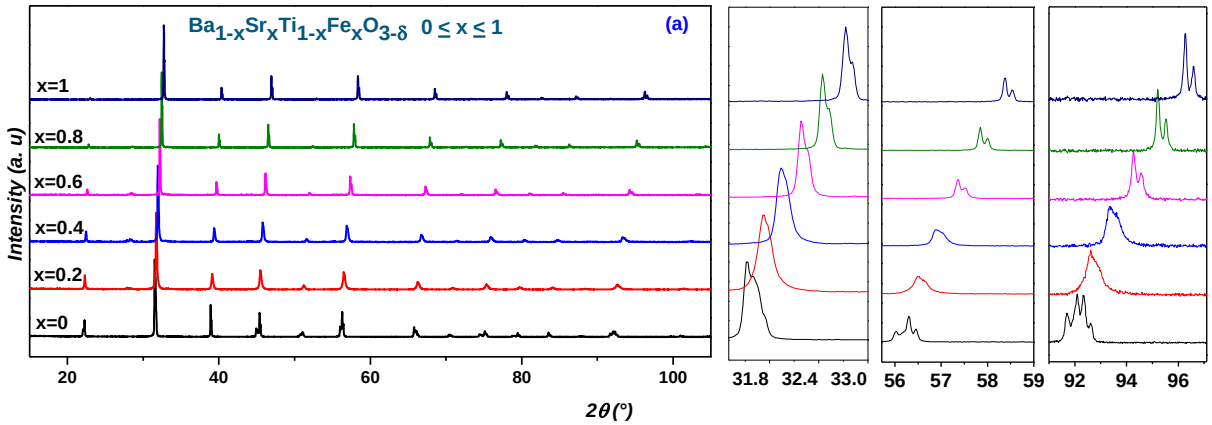

Fig-III.P3.1: X-ray powder diffraction patterns of $Ba_{1-x}Sr_xTi_{1-x}Fe_xO_3$ ($0 \leq x \leq 1$) presenting the peaks shape variation **(a)** and the separated main peaks **(b)**.

III.3.8.Rietveld refinement study of the structure and the phase transitions

For further investigations, the Rietveld refinement method is used to investigate the effect of the substitution on the structure and to determine the phase transition occurred. It is defined in the literature that $BaTiO_3$ adopts the tetragonal (SG: *P*4*mm*); and $SrFeO_{3-\delta}$ structure is dependent to the value of 'δ' [50, 51]. Traces of impurities were detected at $2\theta = 27.88°$ of BaO for the composition x=0.2; BaO and $BaFe_2O_4$ at $27° < 2\theta < 28°$ for the composition x = 0.4 and traces of $BaFe_2O_4$ for the composition x = 0.6. The choice of the matching profile for each of the synthesized samples is done based on the X-ray diffraction patterns comparison to the end members.

III.4.2.1. Tetragonal BSTF perovskite system $0 \leq x \leq 0.4$

Tetragonal symmetry with *P*4*mm* space group was first assigned to the samples x = 0.2; 0.4 considering the similarities of their X-ray patterns compared to that of $BaTiO_3$. The Rietveld refinement for this model showed unsatisfactory results given the negative Biso coefficient obtained indicating the incorrectness of the atomic positions and thus the model. Since the system evolves toward higher symmetry, *P*4*/mmm* space group is suggested. The final plot of the Rietveld refinement and the structure visualization in the [010] direction are shown in **Fig-III.P3.2**, the fitting to this model showed satisfactory results with low reliability factors as presented in **Table-III.P3.1**. The bond angles and the interatomic distances are summarized in **Table-III.P3.2**.

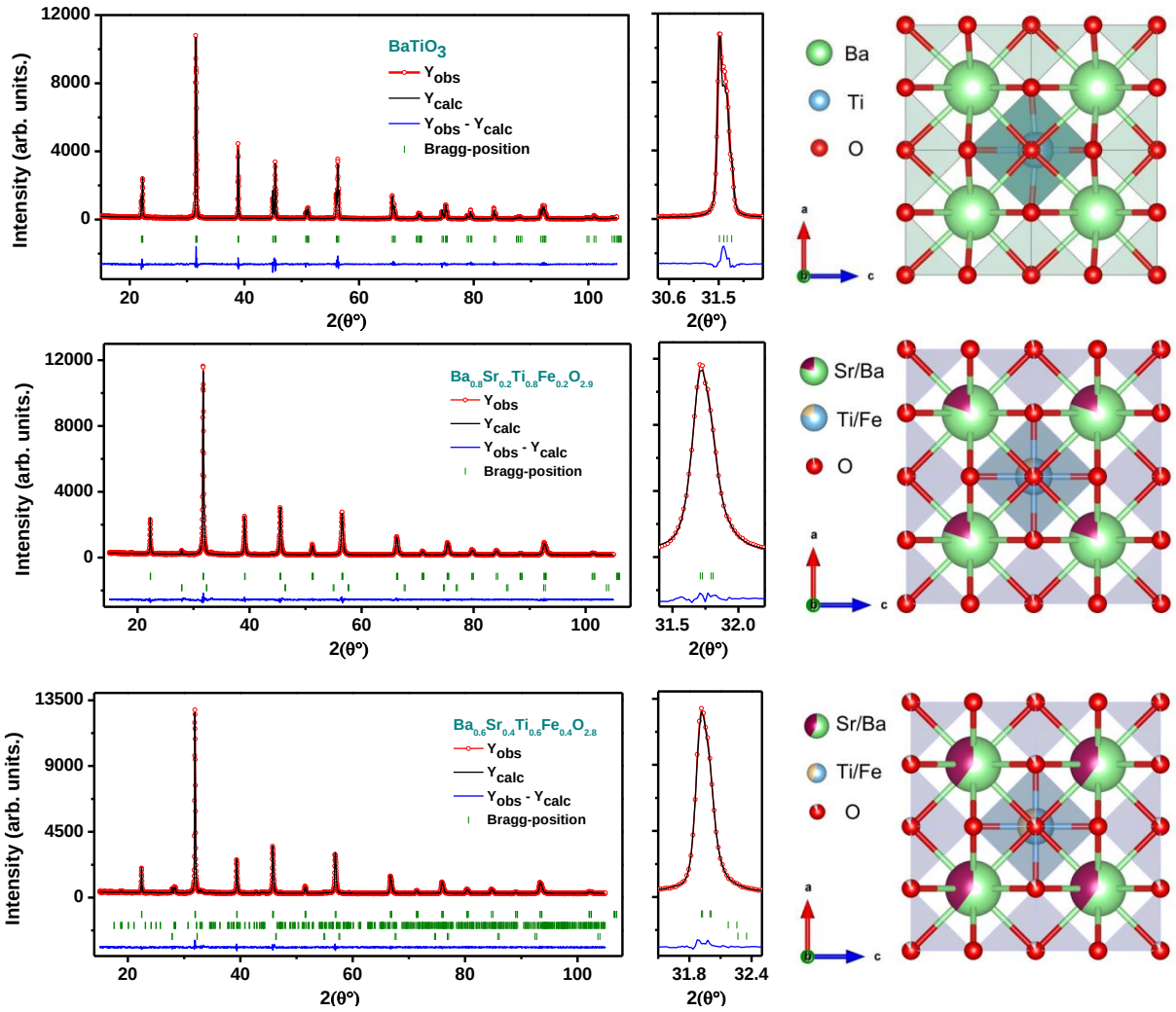

Fig-III.P3.2: Final Rietveld Refinement plots of Tetragonal BSTF system $0 \leq x \leq 0.4$ and [010] projection of the unit cell with *P*4*mm* and *P*4/*mmm*. The observed data and calculated profile are indicated by circles and solid trace respectively. The lowest trace shows the difference between the observed and calculated model. The vertical bars indicate the calculated bragg reflections positions.

Table-III.P3.1. Refined structural parameters for Tetragonal BSTF system $0 \leq x \leq 0.4$

$BaTiO_3$	**Sr/Ba**	**Ti/Fe**	**O1**	**O2**
	space group *P4mm*			
x	0	½	½	½
y	0	½	½	0
z	0	0.491(7)	0.033(7)	0.524(9)
B (A^2)	0.30(3)	0.27(8)	0.75(17)	0.75(17)
Occupancy	1	1	1	2
a(Å) = 3.99383(8), **c(Å)** = 4.02896(8), **γ(°)** = 90 **U** = 0.04719(3), **V** = -0.01654(3), **W** = 0.00797(7) $\mathbf{R_F}$ = 2.81, $\mathbf{R_B}$ = 4.55, $\mathbf{R_p}$= 9.26, $\mathbf{R_{wp}}$ = 12.2, $\mathbf{cR_p}$ = 13.4, $\mathbf{cR_{wp}}$ = 15.6, **χ** = 3.44				
$Sr_{0.8}Ba_{0.2}Ti_{0.8}Fe_{0.2}O_{2.9}$	**Sr/Ba**	**Ti/Fe**	**O1**	**O2**

	space group *P4/mmm*			
x	0	½	½	½
y	0	½	½	0
z	0	½	0	½
B (A²)	0.49(6)	0.50(7)	0.88(13)	0.88(13)
Occupancy	0.8/0.2	0.8/0.2	1	1.9
a(Å) = 3.9851(3), **c(Å)** = 3.9894(5), **γ(°)** = 90 **U** = 0.17256(15), **V** = 0.01895(11), **W** = 0.00241(2) **R_F** = 4.71, **R_B** = 6.33, **R_p** = 6.35, **R_{wp}** = 8.46, **cR_p** = 15.1, **cR_{wp}** = 14.8, **χ** = 2.03				
$Sr_{0.6}Ba_{0.4}Ti_{0.6}Fe_{0.4}O_{2.8}$	**Sr/Ba**	**Ti/Fe**	**O1**	**O2**
	space group *P4/mmm*			
x	0	½	½	½
y	0	½	½	0
z	0	½	0	½
B (A²)	0.61(7)	0.44(8)	0.82(14)	0.82(14)
Occupancy	0.6/0.4	0.6/0.4	1	1.8
a(Å) = 3.9603(3), **c(Å)** = 3.9627(6), **γ(°)** = 90 **U** = 0.13734(13), **V** = 0.00154(1), **W** = 0.00361(2) **R_F** = 7.83, **R_B** = 7.85, **R_p** = 5.44, **R_{wp}** = 7.17, **cR_p** = 19.9, **cR_{wp}** = 16.0, **χ** = 2.09				

Table-III.P3.2. Selected interatomic distances (Å) and (O–Ti–O, O–(Ba/Sr)–O & Ti –O– (Ba/Sr)) angles for Tetragonal BSTF system ($0 \leq x \leq 0.4$).

Interatomic distances / bond angles	x=0	Interatomic distances / bond angles	x=0.2	x=0.3
1×Ti/Fe–O1	1.85(4)	2×Ti/Fe–O1	1.99(5)	1.990(8)
1×Ti/Fe–O1	2.18(4)	4×Ti/Fe–O2	1.992(6)	1.991(4)
4×Ti/Fe–O2	2.001(3)	<Ti/Fe–O>	1.991	1.990
<Ti/Fe–O>	2.005			
4×Ba/Sr–O1	2.8272(1)	4×Ba/Sr–O1	2.817(9)	2.815(4)
4×Ba/Sr–O2	2.77(3)	8×Ba/Sr–O2	2.819(4)	2.815(6)
4×Ba/Sr–O2	2.91(3)	<Ba/Sr–O>	2.818	2.814
<Ba/Sr–O>	2.835			
1×O1–Ti/Fe–O1	180(3)	1×O1–Ti/Fe–O1	180.00	180.00
2×O2–Ti/Fe–O2	172.38(1)	2×O2–Ti/Fe–O2	180.00	180.00
8×O2–Ti/Fe–O2	89.75(1)	8×O2–Ti/Fe–O2	90.00	90.00
4×O1–(Ba/Sr)–O1	89.87(4)	4×O1–(Ba/Sr)–O1	90.00	90.00
2×O1–(Ba/Sr)–O1	174.61(4)	2×O1–(Ba/Sr)–O1	180.00	180.00
4×O2–(Ba/Sr)–O2	177.2(2)	4×O2–(Ba/Sr)–O2	180.000	180.000
1x(Ti/Fe)–O1-(Ti/Fe)	180(3)	1x(Ti/Fe)–O1-(Ti/Fe)	180.00	180.00(9)
1x(Ti/Fe)–O2-(Ti/Fe)	172.38(1)	1x(Ti/Fe)–O2-(Ti/Fe)	180.00	180.00(5)

III.4.2.2. Cubic BSTF perovskite system $0.6 \leq x \leq 1$

The attributed model for the samples with the compositions x=0.6; 0.8 consist of that of $SrFeO_3$ [51]. The Rietveld refinement results show that both samples adopt the cubic structure showing low reliability factors, the structural information is presented in **Table-III.P3.3** and

Table-III.P3.4. The final Rietveld refinement plots is given in **Fig-III.P3.3**; the visualization of the structure shows the unit cell in the [010] projection. The calculated tolerance factor from the Rietveld refinement results are shown in **Fig-III.P3.4**. The evolution of the tolerance factor as function of the composition is in good agreement with the previous observations. This evolution demonstrates that the system evolves toward higher symmetries when the strontium and iron contents become important.

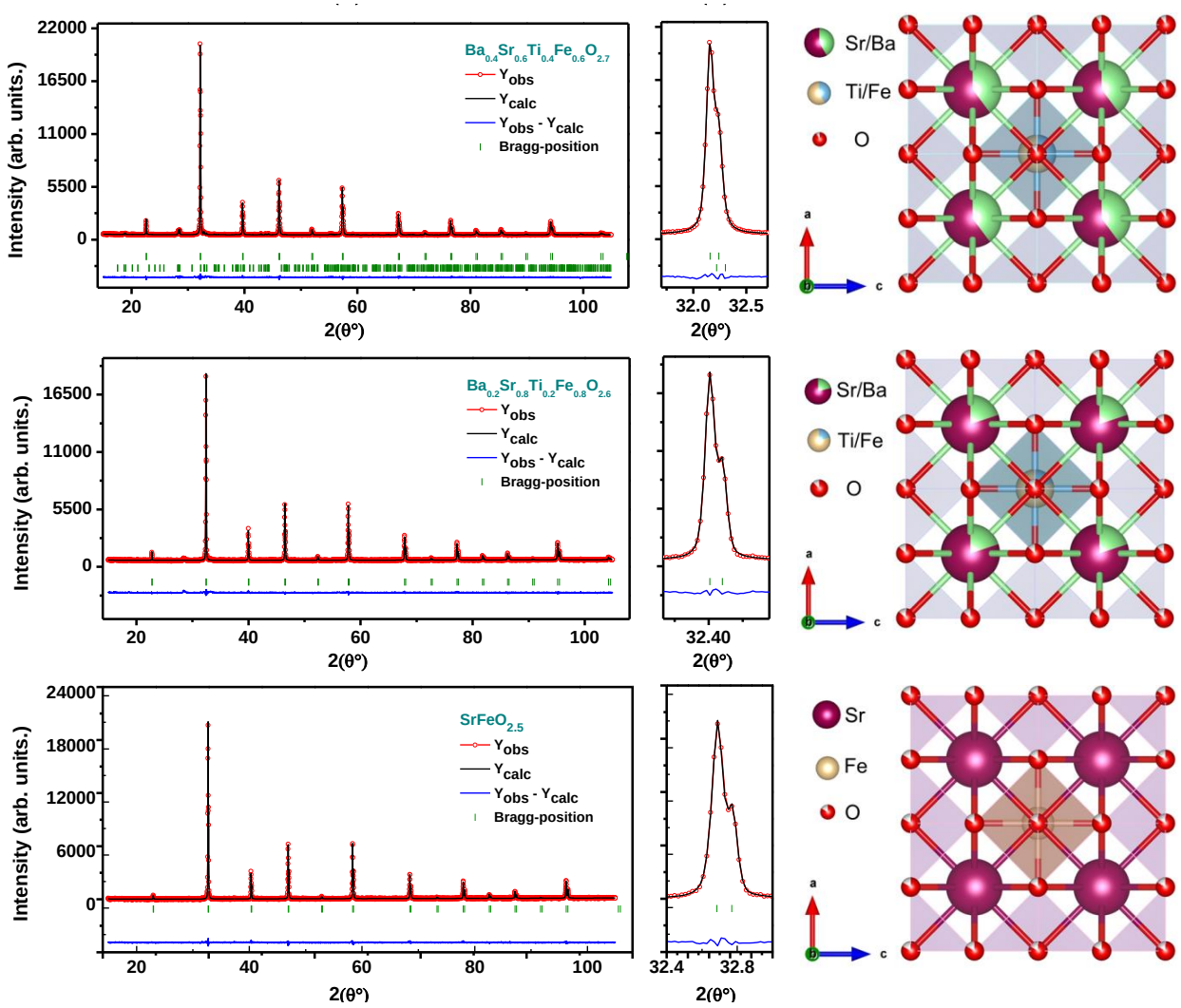

Fig-III.P3.3: Final Rietveld Refinement plots of Cubic BSTF system $0.6 \leq x \leq 1$ and [010] projection of the unit cell with *Pm*-3*m*. The observed data and calculated profile are indicated by circles and solid trace respectively. The lowest trace shows the difference between the observed and calculated model. The vertical bars indicate the calculated bragg reflections positions.

Table-III.P3.3. Refined structural parameters for Cubic SLTF system $0.6 \leq x \leq 1$

$Sr_{0.4}Ba_{0.6}Ti_{0.4}Fe_{0.6}O_{2.7}$	Sr/Ba	Ti/Fe	O1
	space group *Pm-3m*		
x	0	½	½
y	0	½	½
z	0	½	0
B (Å²)	0.87(5)	0.62(7)	0.85(14)
Occupancy	0.4/0.6	0.4/0.6	2.7
a(Å) = 3.93303(9), **γ(°)** = 90 **U** = 0.03693(4), **V** = -0.00547(4), **W** = 0.00524(9) $\mathbf{R_F}$ = 3.07, $\mathbf{R_B}$ = 4.82, $\mathbf{R_p}$ = 3.79, $\mathbf{R_{wp}}$ = 5.05, $\mathbf{cR_p}$= 16.8, $\mathbf{cR_{wp}}$ = 12.4, **χ** = 3.69			
$Sr_{0.2}Ba_{0.8}Ti_{0.4}Fe_{0.8}O_{2.6}$	Sr/Ba	Ti/Fe	O1
	space group *Pm-3m*		
x	0	½	½
y	0	½	½
z	0	½	0
B (Å²)	0.43(5)	0.52(6)	0.75(13)
Occupancy	0.2/0.8	0.2/0.8	2.6
a(Å) = 3.90373(6), **γ(°)** = 90 **U** = 0.01824(2), **V** = -0.00057(2), **W** = 0.00378(5) $\mathbf{R_F}$ = 4.04, $\mathbf{R_B}$ = 4.44, $\mathbf{R_p}$ = 3.13, $\mathbf{R_{wp}}$ = 4.02, $\mathbf{cR_p}$ =18.6, $\mathbf{cR_{wp}}$ = 11.7, **χ** = 2.42			
$SrFeO_{2.5}$	Sr/Ba	Ti/Fe	O1
	space group *Pm-3m*		
x	0	½	½
y	0	½	½
z	0	½	0
B (Å²)	0.37(5)	0.49(7)	0.39(13)
Occupancy	1	1	2.5
a(Å) = 3.87141(5), **γ(°)** = 90 **U** = 0.01854(2), **V** = -0.00500(2), **W** = 0.00517(5) $\mathbf{R_F}$ = 5.22, $\mathbf{R_B}$ = 4.68, $\mathbf{R_p}$ = 2.52, $\mathbf{R_{wp}}$ = 3.20, $\mathbf{cR_p}$ = 20.9, $\mathbf{cR_{wp}}$ = 11.4, **χ** = 2.17			

Table-III.P3.4. Selected interatomic distances (Å) and (O–Ti–O, O–(Ba/Sr)–O & Ti –O– (Ba/Sr)) angles for Cubic SLTF system ($0.6 \leq x \leq 1$).

Interatomic distances / bond angles	x=0.6	x=0.8	x=1
Ti/Fe–O	1.9665(5)	1.9519(3)	1.9357(2)
Sr/Ba–O	2.7811(5)	2.7604(3)	2.7375(2)
3×O1–Ti/Fe–O1	180.00(6)	180.00 (4)	180.00(3)
12×O1–Ti/Fe–O1	90.00(3)	90.00(2)	90.00(2)
6×O1–(Sr/Ba)–O1	180.00(4)	180.00(3)	180.00(2)
12×O1–(Sr/Ba)–O1	90.00(3)	90.00(2)	90.00(2)
(Ti/Fe)–O-(Ti/Fe)	180.00(6)	180.00(4)	180.00(3)
4x(Sr/Ba)–O-(Sr/Ba)	90.00(3)	90.00(2)	90.00(2)
2x(Sr/Ba)–O-(Sr/Ba)	180.00(4)	180.00(3)	180.000(2)
8x(Ti/Ba)–O-(Sr/Ba)	90.00(2)	90.00(2)	90.00(1)

The unit cell parameters are plotted and presented in **Fig-III.P3.4a**. A continual decrease is observed for the unit cell parameter "c" of about 0.03 ± 0.01 Å as the amount of the substitution increases. This decrease can be expressed by c_x-0.03 ≈ $c_{0.2+x}$ ± 0.01 Å, meaning that at each new composition a decrease of about 0.03 ± 0.01 Å of the unit cell "c" is expected. In this case, the effect of the substitution can be seen as a constant strain applied along the c-axis leading to a decrease of the unit cell with a constant step. The contraction along the c-axis is also observed in **Fig-III.P3.4a** confirming our observations which can be expressed by A*c_x ≈ $c_{0.2+x}$ ± 0.02 Å, where A is approximately equal to ≈ 0.99.

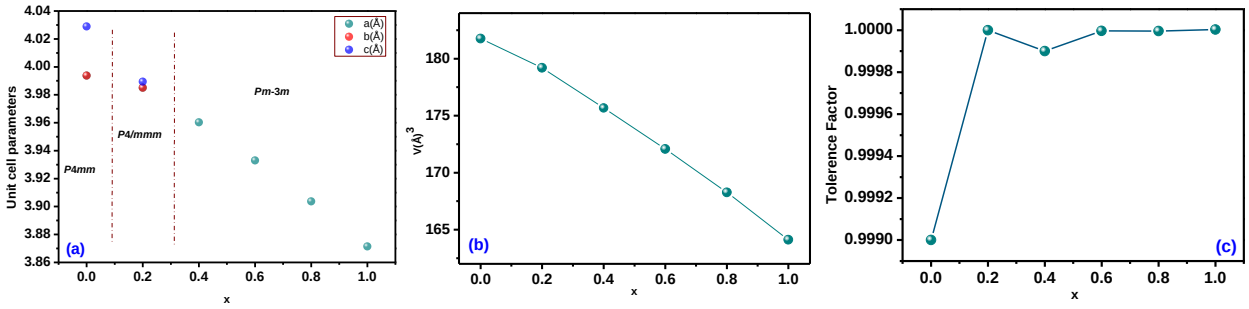

Fig-III.P3.4: The variation as function of the composition of the Unit cell parameters (a, b, c) **(a)**, the unit cell Volume **(b)** and the calculated experimental tolerance factor **(c).**

The chemical strain as an effect of the substitution is mainly applied along the c-axis leading the structure to evolve toward system with higher symmetry and this is observed starting from x ≥ 0.2 above which a continual and linear decrease of the unit cell parameters is seen. As a consequence a linear decrease in the unit cell volume is also observed which result also in a decrease in the interatomic distances A-O and B-O **Fig-III.P3.5 (a, b)**. This decrease explains the shift observed in the X-ray diffraction peaks toward higher 2tetha with a constant step of about 0.24 ± 0.01°. The substitution has as well an effect on the composition, as the amount of the substitution increases oxygen vacancies are created to maintain charge neutrality. A linear evolution of the unit cell parameters, mainly the 'c' parameter, and the unit volume is observed as the amount of the substitution increases. This linearity might be due to the oxygen vacancies created in the samples by the effect of the substitution.

The tolerance factor was calculated to confirm the evolution of the system toward high symmetries. The experimental tolerance factor introduced by Goldschmidt et al. [25] was calculated using equation 1:

$$t = (r_A + r_O)/\sqrt{2}(r_B + r_O) \qquad \text{(Eq. 1)}$$

Where, r_A, r_B are respectively the ionic radius of the elements in the A-sites, B-sites and r_O is the oxygen ion respectively. In our Case $r_A = (1\text{-}x)*r_{Sr} + (x)*r_{Ba}$ and $r_B = (1\text{-}x)*r_{Ti} + (x)*r_{Fe}$ and $r_O = 1.4$. **Fig-III.P3.5 (a, b)** presents the evolution of the tolerance factor and the interatomic distances A-O and B-O versus the substitution showing that at $x \geq 0.2$ the factor is close to unity confirming the results reported previously. According to the behavior of the interatomic distances observed in **Fig-III.P3.5 (a, b),** it is demonstrated that both interatomic distances contributes equally to the formation of either high symmetry systems or low symmetry systems.

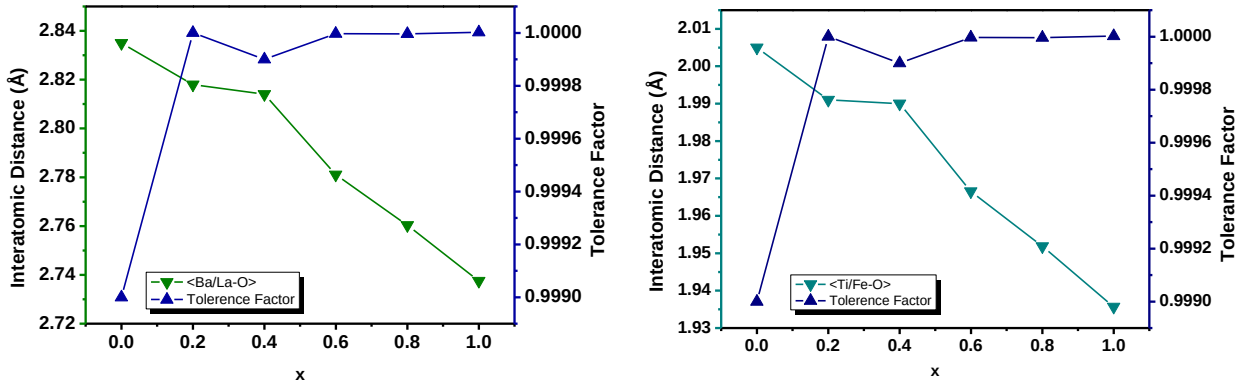

Fig-III.P3.5: The interatomic distance evolution presented along with the tolerance factor as function of the composition. <Ti/Fe-O> **(a)** and <Ba/Sr-O> **(b)** interatomic distances.

III.4.4. Morphological analysis and the effect of the compositions on the grain growth

The morphology and particle sizes were determined for all compositions of BSTF solid solution. The evolution of the morphology as function of the composition is shown in the SEM micrographs displayed in **Fig-III.P3.6**. The composition x = 0 have irregular shape of grains and form large agglomerates, as we can also observe in some region the succession of layers uniformly distributed close remark was mentioned by M. Ganguly et al [52]. With the insertion of Fe^{3+} and Sr^{2+} the morphology of the samples changes, the compositions x = 0.2, 0.4, and 0.6 show layered flat plate like grains, meanwhile, the composition x = 0.8 the powder is formed by polygonal shape grains and defined grain boundaries with varied sizes. The composition x = 1

shows very different surface morphology in comparison with the rest of the compositions; the SEM images shows irregular shape and large agglomerate grains, the discontinuity of the growth of the grain is observed in this case. Approximately the average grain size decreases from 1.86 µm for the composition x = 0 to 0.342, then 0.537 µm, for the compositions x = 0.2, and 0.4. As the amount of the substitution increases, the average grain size began to increase for the compositions x = 0.6, 0.8, and 1 respectively from 1.217, 1.247 to 2.734 µm. These results shows that only a small amount of the substitution ranging between $0.2 \leq x \leq 0.4$ can reduce the grain size. In the current case study, the incorporation of Sr^{2+} and Fe^{3+} form between $0.2 \leq x \leq 0.6$ flat plate like grains, and the grain size is reduced only for the compositions x = 0.2, and 0.4.

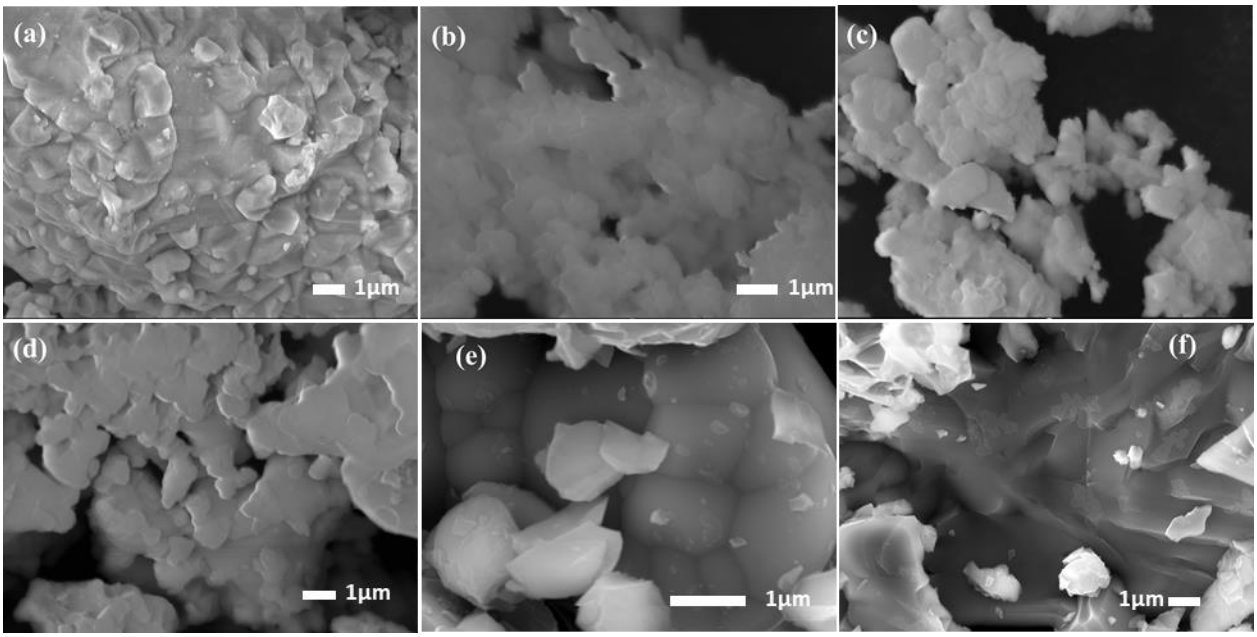

Fig-III.P2.6: SEM images showing the effect of the composition on the morphology of the solid solution BLTF for the compositions x = 0 **(a)**, x = 0.2 **(b)**, x = 0.4 **(c)**, x = 0.6 **(d)**, x = 0.8 **(e)**, and x = 0.1 **(f)**.

III.4.5. Conclusion

The information transmitted from the X-ray diffraction patterns indicates an evolution toward high symmetry systems. The main peaks were observed to shift with a step of 0.24 ± 0.01°, which later on was found to reflect the uniform decrease of the unit cell parameters. Consistently with the evolution of the X-ray pattern, the detailed structural investigations confirmed the evolution of the system toward high symmetry structure while revealing one phase transition from tetragonal structure to cubic structure. The calculated tolerance factor was in

agreements with the results found, where values close to unity were obtained as "x" increases. As a function of the substitution, the unit cell parameters and thus the unit cell volume parameters showed a linear decrease. It was observed that the substitution effect acts as a strain applied along the c axis and it was expressed as $A*c_x \approx c_{0.2+x} \pm 0.02$ Å, where A is approximately equal to $A \approx 0.99$. The decrease of the unit cell parameters "c" was found to be 0.03 ± 0.01 Å at each new composition and it was expressed by $c_x - 0.03 \approx c_{0.2+x} \pm 0.01$ Å.

The evolution of the experimental tolerance factors issued from the interatomic distances was in agreement with the X-ray diffraction patterns results. High symmetry systems were observed for low interatomic distances A-O and B-O, where both distances behave similarly and both contributes equally to the formation of the perovskite structure with defined symmetry.

The SEM micrographs showed that only small amount of Sr^{2+} and Fe^{3+} will reduce the grain size. The grains are in different shapes, the morphology evolve from flat plate like grains (x = 0.2, 0.4 and 0.6) to non-uniform polygonal shape grains (x = 0.8), additionally the grain boundaries can be easily observed and detected in the case of x = 0.8.

III.5. Chapter conclusion

The effect of the composition on the ABO_3 perovskite structure was studied in three different systems within a large percentage of substitution. The ability to synthesis stable complex perovskite structure has been proven to be possible for (1-x) $BaTiO_3$ – x $LaFeO_3$, (1-x) $SrTiO_3$ – x $LaFeO_3$, and (1-x) $BaTiO_3$ – x $SrFeO_{3-\delta}$ solid solution at a range of composition between $0 \leq x \leq 1$ labeled as BLTF, SLTF and BSTF respectively. The prepared solid solutions showed good stability according to the calculated tolerance factor, the values obtained ranges between 1 and 0.976 which is framed within the conditions of structure formability established by Goldschmidt for ABO_3 perovskites. Substitution of higher ionic radii elements with lower ionic radii tends to decrease the volume and a shift of the X-ray patterns is observed and vis-versa.

The systems showed phase transition as function of the substitution: for BLTF system undergoes two phase transitions from tetragonal, cubic to orthorhombic; SLTF system undergoes one phase transitions from cubic to orthorhombic, and same with BSTF system that shows a transition from tetragonal to cubic. In general and from the effect of composition percentages perspective, the structure of the prepared samples tends to take the form of either the composition of x = 0 for values less than 20% or 30% of the substitution amount, or the form of the composition with x = 1 for composition higher than 60%. However, more insights on the preferred structure were obtained by studying the evolution of the different structural parameters as the unit cell volume and the interatomic distances with comparison to the evolution of the tolerance factor.

The interatomic distances showed that the B-O governs more the symmetry, while the A-O affects the unit cell volume. For the three cases studied in this chapter, a decrease or an increase of the A-O distances is followed by a decrease or an increase of the unit cell volume respectively. Meanwhile the B-O distance showed more significant results when studying the symmetry evolution in comparison with the evolution of the tolerance factor. The cubic structure is formed for values ranging between 1.99 and 1.94Å for Ti/Fe-O interatomic distances with condition that A-O ranges between 2.72 and 2.81Å. The tetragonal structure is formed for Ti/Fe-O values between 1.991 and 2.006Å, and for A-O values close to 2.83Å. The orthorhombic structure is observed for values of Ti/Fe-O between 1.978 and 2.006Å and for A-O the values are close to 2.77 and 2.79Å.

The effect of the compositions on the morphology and the grains growth was studied for BLTF, SLTF, and BSTF. In the three cases, it is observed that specific amount of the substitution is capable of forming small grain size above which the grains are largely agglomerated: BLTF, x = 0.25; SLTF, x = 0.2 ≤ x ≤ 0.4; and BSTF, 0.2 ≤ x ≤ 0.4. In all the $A_{1-x}A_xTi_{1-x}Fe_xO_3$ (A = Ba, La, Sr) system with 0 ≤ x ≤ 1, it is observed that a combination of Sr^{2+}/La^{3+} and Ba^{2+}/Sr^{2+} in the A-site can form flat plat like grains for a substitution amount ranging between 0.2 ≤ x ≤ 0.4 and 0.2 ≤ x ≤ 0.6 respectively. The substitution of $BaTiO_3$ in all the cases is found to form porous structures in comparison with the large agglomerated grains of $BaTiO_3$. However, the smaller grains size was obtained for BLTF at x = 0.25, while the larger particles were observed for BLTF at x = 0.8.

III.6. References

1. Hu Q, Wang T, Zhao L, et al (2017) Dielectric and energy storage properties of BaTiO3–Bi(Mg1/2Ti1/2)O3 ceramic: Influence of glass addition and biasing electric field. Ceram Int 43:35–39. https://doi.org/10.1016/J.CERAMINT.2016.08.005

2. Wang XH, Chen RZ, Gui ZL, Li LT (2003) The grain size effect on dielectric properties of BaTiO3 based ceramics. In: Materials Science and Engineering B: Solid-State Materials for Advanced Technology. Elsevier, pp 199–202

3. Xu Q, Lanagan MT, Huang X, et al (2016) Dielectric behavior and impedance spectroscopy in lead-free BNT–BT–NBN perovskite ceramics for energy storage. Ceram Int 42:9728–9736. https://doi.org/10.1016/J.CERAMINT.2016.03.062

4. Zhang H, Jo W, Wang K, Webber KG (2014) Compositional dependence of dielectric and ferroelectric properties in BiFeO 3 – BaTiO 3 solid solutions. 40:4759–4765. https://doi.org/10.1016/j.ceramint.2013.09.020

5. Pradhan S, Roy GS (2013) Study the Crystal Structure and Phase Transition of BaTiO 3 – A Pervoskite. Researcher 55:63–67. https://doi.org/10.7537/marsrsj050313.10

6. Lin F, Jiang D, Ma X, Shi W (2008) Influence of doping concentration on room-temperature ferromagnetism for Fe-doped BaTiO3 ceramics. J Magn Magn Mater 320:691–694. https://doi.org/10.1016/J.JMMM.2007.08.008

7. Qiu SY, Li W, Liu Y, et al (2010) Phase evolution and room temperature ferroelectric and magnetic properties of Fe-doped BaTiO3 ceramics. Trans Nonferrous Met Soc China 20:1911–1915. https://doi.org/10.1016/S1003-6326(09)60394-0

8. Amaechi IC, Hadj Youssef A, Kolhatkar G, et al (2021) Ultrafast microwave-assisted hydrothermal synthesis and photocatalytic behaviour of ferroelectric Fe3+-doped BaTiO3 nanoparticles under simulated sunlight. Catal Today 360:90–98. https://doi.org/10.1016/J.CATTOD.2019.07.021

9. Morrison FD, Coats AM, Sinclair DC, West AR (2001) Charge Compensation Mechanisms in La-Doped BaTiO3. J Electroceramics 2001 63 6:219–232. https://doi.org/10.1023/A:1011400630449

10. Devmunde BH, Somwanshi SB, Kharat PB, Solunke MB (2020) Rare Earth Ion (La3+) Doped BaTiO3 Perovskite Nanoceramics for Spintronic Applications. J Phys Conf Ser 1644:012055. https://doi.org/10.1088/1742-6596/1644/1/012055

11. Geller S, Wood E a. (1956) Crystallographic studies of perovskite-like compounds. I. Rare earth orthoferrites and YFeO 3 , YCrO 3 , YAlO 3. Acta Crystallogr 9:563–568. https://doi.org/10.1107/S0365110X56001571

12. Bellakki MB, Kelly BJ, Manivannan V (2010) Synthesis, characterization, and property studies of (La, Ag) FeO3($0.0 \leq x \leq 0.3$) perovskites. J Alloys Compd 489:64–71. https://doi.org/10.1016/j.jallcom.2009.08.059

13. Mitra A, Mahapatra AS, Mallick A, et al (2017) Simultaneous enhancement of magnetic and ferroelectric properties of LaFeO3 by co-doping with Dy3+ and Ti4+. J Alloys Compd 726:1195–1204. https://doi.org/10.1016/J.JALLCOM.2017.08.074

14. Rai A, Thakur AK (2017) Effect of co-substitution on structural, optical, dielectric and magnetic behavior of LaFeO3. J Alloys Compd 695:3579–3588. https://doi.org/10.1016/J.JALLCOM.2016.11.407

15. Garcia-Muñoz P, Fresno F, Lefevre C, et al (2020) Synergy effect between photocatalysis and heterogeneous photo-Fenton catalysis on Ti-doped LaFeO3 perovskite for high efficiency light-assisted water treatment. Catal Sci Technol 10:1299–1310. https://doi.org/10.1039/C9CY02269D

16. Chaabane H, Abdelmoula N, Khemakhem H, et al (2011) Dielectric and ferroelectric properties of lead-free Ba1−xLaxTi1−xFexO3 ceramics. Phys status solidi 208:180–185. https://doi.org/10.1002/PSSA.201026083

17. Rajagukguk R ;Shin. DG ;Lee. BW. (2011) Magnetic Ordering in (1-x)$BaTiO_3$-x$LaFeO_3$ Solid Solutions. J Magn 16:101–103. https://doi.org/10.4283/JMAG.2011.16.2.101

18. Sahoo S, Das S, Mahapatra PK, Choudhary RNP (2018) Fabrication and characterization of LaFeO3-BaTiO3 electroceramics. Mater Chem Phys 216:158–169. https://doi.org/10.1016/J.MATCHEMPHYS.2018.05.032

19. Roisnel T, Rodríguez-Carvajal J WinPLOTR: a Windows tool for powder diffraction patterns analysis

20. Rajagukguk R, Shin DG, Lee BW (2011) Magnetic ordering in (1-x)BaTiO3-xLaFeO3 solid solutions. J Magn 16:101–103. https://doi.org/10.4283/JMAG.2011.16.2.101

21. Sahoo S, Das S, Mahapatra PK, Choudhary RNP (2018) Fabrication and characterization of LaFeO3-BaTiO3 electroceramics. Mater Chem Phys 216:158–169. https://doi.org/10.1016/j.matchemphys.2018.05.032

22. Chaabane H, Abdelmoula N, Khemakhem H, et al (2011) Dielectric and ferroelectric properties of lead-free Ba1−xLaxTi1−xFexO3 ceramics. Phys status solidi 208:180–185. https://doi.org/10.1002/pssa.201026083

23. Itoh K, Zeng LZ, Nakamura E, Mishima N (1985) Crystal structure of BaTiO3 in the cubic phase. Ferroelectrics 63:29–37. https://doi.org/10.1080/00150198508221381

24. Etter M, Müller M, Hanfland M, et al (2014) High-pressure phase transitions in the rare-earth orthoferrite $LaFeO_3$. Acta Crystallogr Sect B Struct Sci Cryst Eng Mater 70:452–458. https://doi.org/10.1107/S2052520614007379

25. Troccaz M, Gonnard P, Fetiveau Y, et al (1976) Goldschmidt factor and phase diagrams of doped titanate zirconates. Ferroelectrics 14:679–681. https://doi.org/10.1080/00150197608236699

26. Xian T, Yang H, Di L, et al (2014) Photocatalytic reduction synthesis of SrTiO3-graphene nanocomposites and their enhanced photocatalytic activity. Nanoscale Res Lett 9:1–9. https://doi.org/10.1186/1556-276X-9-327

27. Li H, Yin S, Wang Y, et al (2013) Roles of Cr3+ doping and oxygen vacancies in SrTiO3 photocatalysts with high visible light activity for NO removal. J Catal 297:65–69. https://doi.org/10.1016/j.jcat.2012.09.019

28. Li W, Jiang K, Li Z, et al (2018) Origin of Improved Photoelectrochemical Water Splitting in Mixed Perovskite Oxides. Adv Energy Mater 8:1801972. https://doi.org/10.1002/AENM.201801972

29. Rizwan M, Ali A, Usman Z, et al (2019) Structural, electronic and optical properties of copper-doped SrTiO3 perovskite: A DFT study. Phys B Condens Matter 552:52–57. https://doi.org/10.1016/j.physb.2018.09.022

30. Hayward SA, Salje EKH (1999) Cubic-tetragonal phase transition in SrTiO3 revisited: Landau theory and transition mechanism. Phase Transitions 68:501–522. https://doi.org/10.1080/01411599908224530

31. Ghasemifard M, Abrishami ME, Iziy M (2015) Effect of different dopants Ba and Ag on the properties of SrTiO3 nanopowders. Results Phys 5:309–313. https://doi.org/10.1016/J.RINP.2015.10.005

32. Jia Y, Zhao D, Li M, et al (2018) La and Cr Co-doped SrTiO3 as an H2 evolution photocatalyst for construction of a Z-scheme overall water splitting system. Chinese J Catal 39:421–430. https://doi.org/10.1016/S1872-2067(18)63027-X

33. Silva LF da, M'Peko J-C, Andrés J, et al (2014) Insight into the Effects of Fe Addition on the Local Structure and Electronic Properties of SrTiO3. J Phys Chem C 118:4930–4940. https://doi.org/10.1021/JP408839Q

34. Buscaglia MT, Maglia F, Anselmi-Tamburini U, et al (2014) Effect of nanostructure on the thermal conductivity of La-doped SrTiO3 ceramics. J Eur Ceram Soc 34:307–316. https://doi.org/10.1016/J.JEURCERAMSOC.2013.08.009

35. Qin M, Gao F, Cizek J, et al (2019) Point defect structure of La-doped SrTiO3 ceramics with colossal permittivity. Acta Mater 164:76–89. https://doi.org/10.1016/J.ACTAMAT.2018.10.025

36. Singh SP, Kanas N, Desissa TD, et al (2020) Thermoelectric properties of A-site deficient La-doped SrTiO3 at 100–900 °C under reducing conditions. J Eur Ceram Soc 40:401–407. https://doi.org/10.1016/J.JEURCERAMSOC.2019.09.024

37. Abdi M, Mahdikhah V, Sheibani S (2020) Visible light photocatalytic performance of La-Fe co-doped SrTiO3 perovskite powder. Opt Mater (Amst) 102:109803. https://doi.org/10.1016/J.OPTMAT.2020.109803

38. Da Silva LF, M'Peko JC, Andrés J, et al (2014) Insight into the effects of fe addition on the local structure and electronic properties of SrTiO3. J Phys Chem C 118:4930–4940. https://doi.org/10.1021/jp408839q

39. Marezio M, Dernier PD (1971) The bond lengths in LaFeO3. Mater Res Bull 6:23–29. https://doi.org/10.1016/0025-5408(71)90155-3

40. Rodriguez-Carvajal J (2008) FULLPROF 2000: A Rietveld Refinement and Pattern Matching Analysis Program

41. Jia T, Zeng Z, Zhang X, et al (2019) The influence of oxygen vacancy on the electronic and optical properties of ABO3−δ (A = La, Sr, B = Fe, Co) perovskites. Phys Chem Chem Phys 21:20454–20462. https://doi.org/10.1039/C9CP03883C

42. Hodges JP, Short S, Jorgensen JD, et al (2000) Evolution of Oxygen-Vacancy Ordered Crystal Structures in the Perovskite Series SrnFenO3n−1 (n=2, 4, 8, and ∞), and the Relationship to Electronic and Magnetic Properties. J Solid State Chem 151:190–209. https://doi.org/10.1006/JSSC.1999.8640

43. Takeda Y, Kanno K, Takada T, et al (1986) Phase relation in the oxygen nonstoichiometric system, SrFeOx (2.5 ≤ x ≤ 3.0). J Solid State Chem 63:237–249. https://doi.org/10.1016/0022-4596(86)90174-X

44. Maity A, Dutta R, Penkala B, et al (2015) Solid-state reactivity explored in situ by synchrotron radiation on single crystals: from SrFeO2.5 to SrFeO3 via electrochemical oxygen intercalation*. J Phys D Appl Phys 48:504004. https://doi.org/10.1088/0022-3727/48/50/504004

45. Fournès L, Potin Y, Grenier JC, et al (1987) High temperature Mössbauer spectroscopy of some SrFeO3−y phases. Solid State Commun 62:239–244. https://doi.org/10.1016/0038-1098(87)90803-9

46. YamamuraHiroshi, KiriyamaRyôiti (2006) Oxygen Vacancies in the Perovskite-type Ferrites. II. Mössbauer Effect in the SrFeO2.5 -LaFeO3 Solid-solution System. http://dx.doi.org/101246/bcsj452702 45:2702–2708. https://doi.org/10.1246/BCSJ.45.2702

47. Avner Rothschild *,†, Wolfgang Menesklou ‡, Harry L. Tuller † and, Ivers-Tiffée‡ E (2006) Electronic Structure, Defect Chemistry, and Transport Properties of SrTi1-xFexO3-y Solid Solutions. Chem Mater 18:3651–3659. https://doi.org/10.1021/CM052803X

48. Perry NH, Kim N, Ertekin E, Tuller HL (2019) Origins and Control of Optical Absorption in a Nondilute Oxide Solid Solution: Sr(Ti,Fe)O3–x Perovskite Case Study. Chem Mater 31:1030–1041. https://doi.org/10.1021/ACS.CHEMMATER.8B04580

49. Roisnel T, Rodríquez-Carvajal J (2001) WinPLOTR: A Windows Tool for Powder Diffraction Pattern Analysis. Mater Sci Forum 378–381:118–123. https://doi.org/10.4028/www.scientific.net/MSF.378-381.118

50. Itoh K, Zeng LZ, Nakamura E, Mishima N (1985) Crystal structure of $BaTiO_3$ in the cubic phase. Ferroelectrics 63:29–37. https://doi.org/10.1080/00150198508221381

51. Haas O, Vogt UF, Soltmann C, et al (2009) The Fe K-edge X-ray absorption characteristics of La1-xSrxFeO3-δ prepared by solid state reaction. Mater Res Bull 44:1397–1404. https://doi.org/10.1016/j.materresbull.2008.11.026

52. Ganguly M, Rout SK, Sinha TP, et al (2013) Characterization and Rietveld Refinement of A-site deficient Lanthanum doped Barium Titanate. J Alloys Compd 579:473–484. https://doi.org/10.1016/J.JALLCOM.2013.06.104

53. Billah M, Rahman MM (2017) Investigation on the Correlation between Structural and Electrical Properties of Lanthanum Doped Barium Titanate Ceramics. Appl Mech Mater 860:99–104. https://doi.org/10.4028/WWW.SCIENTIFIC.NET/AMM.860.99

54. Petrović MMV, Bobić JD, Ramoška T, et al (2011) Electrical properties of lanthanum doped barium titanate ceramics. Mater Charact 62:1000–1006. https://doi.org/10.1016/J.MATCHAR.2011.07.013

55. Cortés-Vega FD, Montero-Tavera C, Yañez-Limón JM (2020) Influence of diluted Fe3+ doping on the physical properties of BaTiO3. J Alloys Compd 847:156513. https://doi.org/10.1016/J.JALLCOM.2020.156513

Chapter -IV

Effect of the composition and structure on the UV-Visible absorption and the band gap of the solid solution system $A_{(1-x)}A'_xTi_{(1-x)}Fe_xO_{3-\delta}$ for (A = Ba, La and Sr) with $0 \leq x \leq 1$

IV.1. Introduction

This chapter forms the second part of the research project; the capability of the UV-Visible light absorption of BLTF, SLTF, and BSTF was tested between 250 – 800 nm. Due to the sensitivity of the physical properties to the structural variation, the objective of this chapter is to investigate the effect of the composition and the structure on the absorption performance in the UV-Visible domain, as well as the various factors governing the opening of the band gap. The correlation between the composition, structure and the optical properties will be established. The strategy adopted to carry this research relies mainly on the observation of the evolution of the optical band gap as function of the composition, the volume, the symmetry, the bond angles, and the interatomic distances. The different cases of **chapter III** are studied in order to hold into an ensemble of information enough to confirm the reported theories about the opening of the band gap in perovskites; and to conduct in-depth studies oriented toward understanding the influence of the different parameters on the optical properties of perovskites.

Part I - chapter IV will treat the effect of the composition and the structural parameters on the opening of the band gap. The case study of this part is the solid solution of $Ba_{1-x}La_xTi_{1-x}Fe_xO_3$ perovskite system with the substitution amount varies between $0 \leq x \leq 1$. The elements of the A-sites consist of La^{3+} and Ba^{2+} while the B-sites consist of Fe^{3+} and Ti^{4+}. In this study the variation of the band gap as function of the composition is emphasized, additionally its evolution is systematically studied with regards to the structural parameters variation, naming: the volume, the distortion degree, the interatomic distances between the B-sites and oxygen <Ti/Fe-O> as well as the A-sites elements and oxygen <Ba/La-O>, and the bond angles Ti/Fe-O_1-Ti/Fe and Ti/Fe-O_2-Ti/Fe. To explain the new values of the band gap, a visualization of the variation the band gap edges positions are estimated and linked to the results issued from the UV-visible results.

The objective of this study is to first confirm the results obtained from the literature and to establish a good understanding on the governing factors of the band gap opening and build a vision on the specific combination of structure composition that will estimate the nature of the band gap.

Part II - Chapter IV is the continuity of the study objective, which consists of using similar strategy to understand the effect of the composition and the structural parameters on the

opening of the band gap. The solid solution of the case study consist of the perovskite structure $Sr_{1-x}La_xTi_{1-x}Fe_xO_3$ where the Ba^{2+} are replaced by Sr^{2+} which is an element that belong to the same group as the Barium, the substitution amount in this case varies between $0 \leq x \leq 1$. The elements of the A-sites consist of La^{3+} and Sr^{2+} while the B-sites consist of Fe^{3+} and Ti^{4+}. The variation of the band gap as function of the composition is emphasized, additionally, its evolution is systematically studied with regards to the structural parameters variation, naming: the volume, the distortion degree, the interatomic distances between the B-sites and oxygen <Ti/Fe-O> as well as the A-sites elements and oxygen <Sr/La-O>, and the bond angles Ti/Fe-O_1-Ti/Fe and Ti/Fe-O_2-Ti/Fe. The objective of this part is to confirm the previous observation obtained from **Part I - chapter IV**.

Following the same objective of understanding the governing factors of the band gap opening, the information obtained in this part will add to the aim of the study the necessary results to define the specific combination of structure-composition that will give a small band gap. To explain the new values of the band gap, a visualization of the variation the band gap edges positions are estimated and linked to the results issued from the UV-visible results.

Part III - Chapter IV is used as a confirmation case of the previous results of **Part (I) (II) - chapter IV**. The case study of this part is the solid solution of $Ba_{1-x}Sr_xTi_{1-x}Fe_xO_{3-\delta}$ perovskite system with the substitution amount varies between $0 \leq x \leq 1$. The A-site in this case is shared between Ba^{2+} and Sr^{2+}, while the B-sites consist of the elements Fe^{3+} and Ti^{4+}. In this study the variation of the band gap as function of the composition is emphasized, additionally the evolution of the band gap is systematically studied with regards to the structural parameters variation, naming: the volume, the distortion degree, the interatomic distances between the B-sites and oxygen <Ti/Fe-O> as well as the A-sites elements and oxygen <Ba/Sr-O>, and the bond angles Ti/Fe-O_1-Ti/Fe and Ti/Fe-O_2-Ti/Fe. A visualization of the band gap edges namely the conduction band minimum and the valence band maximum are estimated and linked to the results issued from the UV-visible results.

The objective of this part is to confirm the previous results and collect the necessary information that will facilitate the understanding of the governing factors of the band gap opening and conclude the band gap dependency to the composition and structural parameters.

IV.2. Part I: Investigation of the composition and structure effects on the optical properties of $Ba_{1-x}La_xTi_{1-x}Fe_xO_3$ perovskite system with ($0 \leq x \leq 1$)

IV.2.1. Introduction

The band gap is one of the important characteristics of oxide materials as it consists one of the best way to get access to solar energy. Numerous applications rely now on the efficient use of solar light such as photocatalytic, photovoltaic and water splitting [1–3]. Substantial efforts have been made to design materials capable of absorbing large amount of visible light which constitutes 40% of solar spectrum [4]. Perovskite oxides materials with the general formula (ABO_3) are a class of oxides emerging to technological field due to their interesting structural and physical properties [5]. The perovskite structure is able of hosting a wide range of rare and alkaline earth element and transition metal cation. Thus, there is high possibility of tuning their physical properties, among which the optical band gap was the topic of several studies [6–8]. Researchers have tried to understand the link between the composition, the structure and the optical band gap. It is stated that the titling of BO_6 octahedral strongly influence the bang gap of perovskites. Moreover, a group of researcher studied the origin of the band gap opening where they succeeded to identify structural generic mechanisms in 3d perovskite such as the symmetry, the octahedral tilting and rotations [9]. It is found that a small difference in B-O-B bond angles led to obvious change of the physical properties, the samples with bond angles close to 180° showed high photocatalytic activity [10].

In order to investigate the structural and optical properties correlation in perovskites, different compositions of the perovskite solid solution $Ba_{1-x}La_xTi_{1-x}Fe_xO_3$ are prepared via solid state reaction. The change of their macroscopic properties caused by the change of the elemental composition and/or the structural parameters is investigated. Detailed study of the structural variation and phase transition occurred in the system are emphasized. Enhancement of the optical responses of the perovskites series $Ba_{1-x}La_xTi_{1-x}Fe_xO_3$ and its dependency to structural and composition variation is reported.

IV.2.2. The UV-visible absorption performance

The optical absorption is analyzed employing the UV/Vis absorption spectroscopy. The absorbance results were approximately expressed by the Kubelka-Munk [11] function using the following equation:

$$\frac{K}{S} = \frac{(1-R)^2}{2R} \equiv F(R) \qquad (Eq.\ 1)$$

K, S and R parameters are described respectively as the absorption coefficient, the scattering coefficient and the diffuse reflectance. F(R) is the Kubelka-Munk function proposed by P. Kubelka and F. Munk [11], which is proportional to the absorbance coefficient.

Fig-IV.P1.1a shows the absorption coefficient F(R) calculated using the Kubelka-Munk function; at $x \geq 0.1$, the samples present strong absorption in the UV-Vis regions ranging from 276.34 nm to 592.11 nm, the absorption regions of each sample are listed in **Table-IV.P1.1**. The peaks observed especially in the visible range indicate that the samples exhibit high absorption of the visible light, which makes these samples promising photocatalysts materials. For further investigations, the compositions are classified by symmetry, the absorption peak of $BaTiO_3$ with *P*4*mm* is expanding to the visible region and new absorptions appear between 492 nm and 500 nm as shown in **Fig-IV.P1.1b** for the samples with *P*4/*mmm* space group, x = 0.1, 0.2 and 0.25. As the amount of the substitution increases, the absorptions of the compositions ($0.3 \leq x \leq 0.6$) with cubic *Pm*-3*m* space group shift toward the visible range between 376 nm and 550 nm, as presented in **Fig-IV.P1.1c**. Above x=0.6, the transition of the absorption toward the visible range is still observed for the samples adopting the orthorhombic structure with *Pnma* and *Pbnm* space groups, hence additional absorption peaks are detected between 455 nm and 540 nm as observed in the absorption spectra at **Fig-IV.P1.1d**. The absorption intensities decrement for the compositions between $0.1 \leq x \leq 0.9$ could be related to the enhanced conductivity due to the substitution [12]. The absorption peaks of $LaFeO_3$ observed in the UV and the visible light regions at around 230 nm, 390 nm, 530 nm and 700 nm [12] attract great attention of researchers to enhance the optical absorption and develop $LaFeO_3$ a promising catalyst material [13, 14]. Based on several studies, the absorption spectrum was systematically compared to that of α-Fe_2O_3 and found to be similar [15]. It is thus suggested that the absorption regions of $LaFeO_3$ are associated to the modes: charge transfer, at around 298.01 nm from the O2p non-bonding level

to the $3de_g$ orbital; the absorptions at 365.37 nm and 456.68 nm are related to the charge transfer mechanisms between the O2p non-bonding orbital and the lowest unoccupied orbital 3dt2g; and spin forbidden ligand field transitions for the absorptions appearing between 500 nm and 800 nm. According to our results and referring to the absorption spectra observed, the co-existence of Ti^{4+} along with Fe^{3+} led to the disappearance of the charge transfer mechanisms between the O2p non-bonding level and the $3de_g$ orbital. As a result, an enhancement of the charge transfer mechanism (O^{2+}-Fe^{3+}) and of spin forbidden ligand field transitions is induced in the samples.

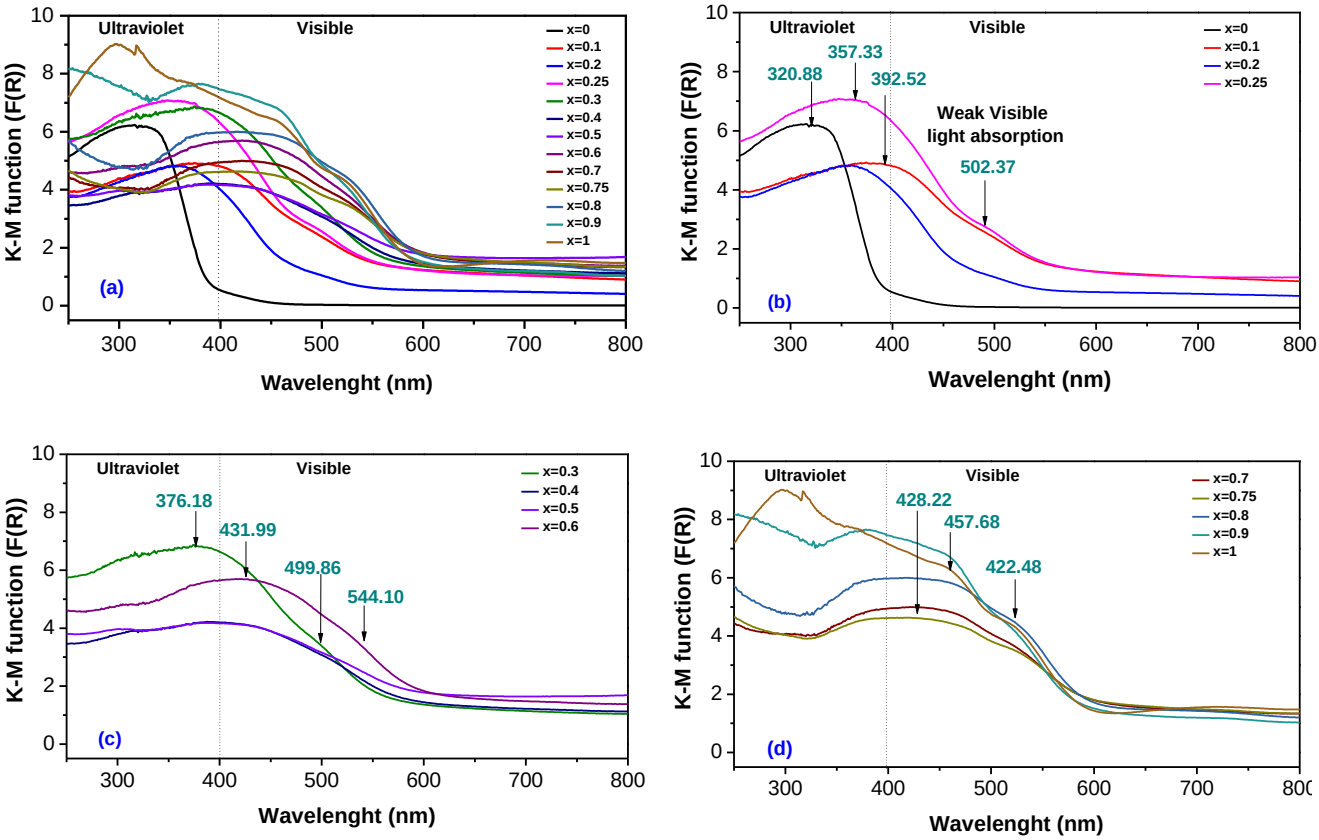

Fig-IV.P1.1: UV-vis Spectra of the series $Ba_{1-x}La_xTi_{1-x}Fe_xO_3$ ($0 \leq x \leq 1$), showing the evolution of the absorption coefficient (K-M function) in the range of wavelength between 250 and 800 nm **(a),** the evolution of the absorption coefficient for the tetragonal samples with ($0 \leq x \leq 0.25$) **(b),** the cubic samples with ($0.3 \leq x \leq 0.6$) **(c)** and for the orthorhombic samples with ($0.7 \leq x \leq 1$)**(d)**.

IV.2.3. Band Gap values determination

The F(R) function is used to examine the inter-band transitions type by applying the McLean [11] analysis; the optical band gap (E_g) can be calculated using the Tauc plot relation, as demonstrated in **Fig-IV.P1.2**:

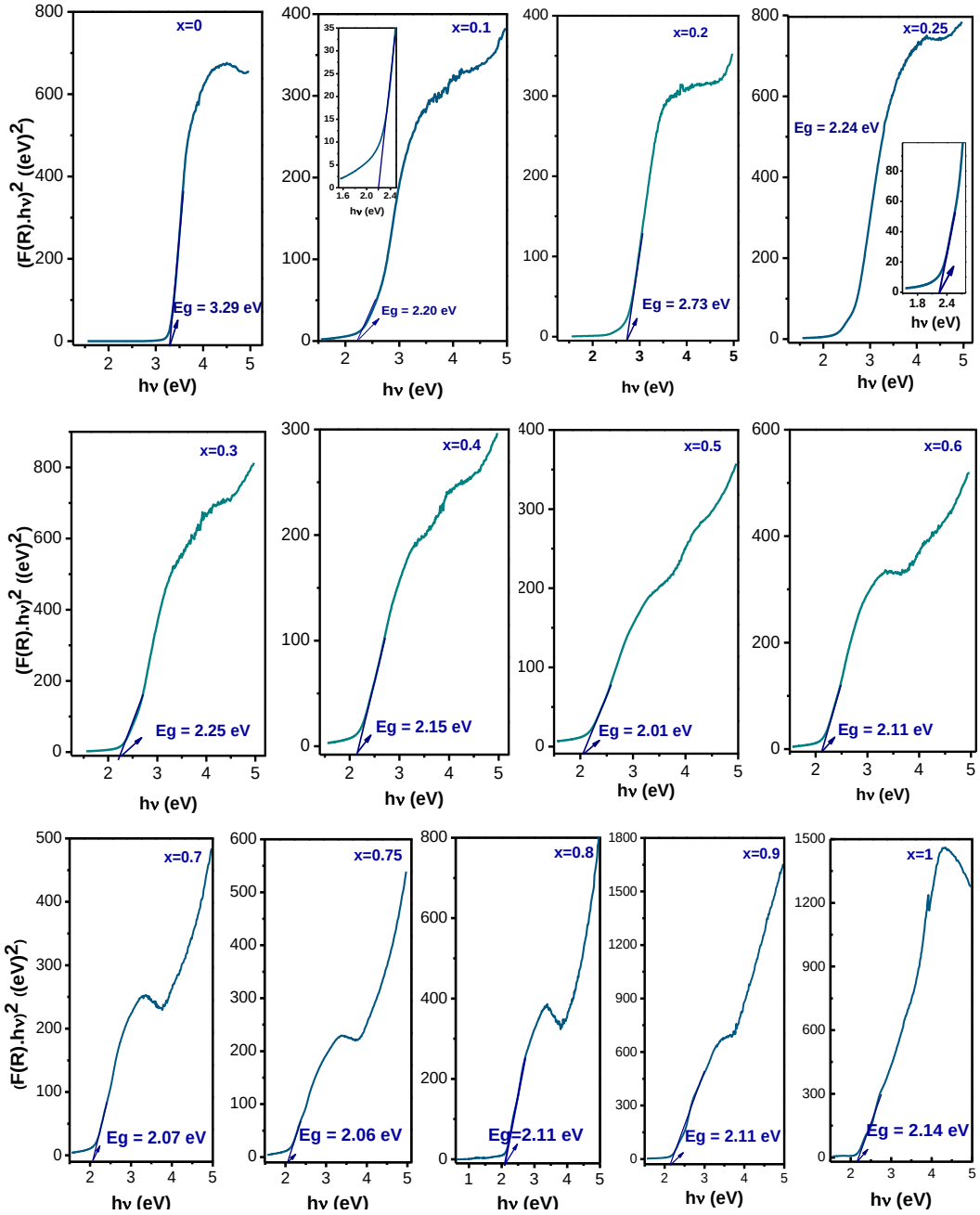

Fig-IV.P1.2: The kubelka-Munk function (F(R)hν)½ variation of the series $Ba_{1-x}La_xTi_{1-x}Fe_xO_3$ ($0 \leq x \leq 1$).

$$F(R)h\nu = A(h\nu - E_g)^n \qquad (Eq.\,2)$$

Where $F(R) \equiv \alpha(\lambda) = \frac{K}{S}$ is the absorption coefficient, A is a constant dependent to the transmittance, called the band tailing parameter. The coefficient $\upsilon = C/\lambda$ is the light frequency and h is Planks constant ($h = 6.626\times10^{-34}$ Joules sec). The possible values for the index ***n*** are equal to 1/2, 2, 3/2 or 3 and each describes respectively direct allowed, indirect allowed, direct forbidden and indirect forbidden transitions type. From equation 2, the extrapolation of the tangential line from high photon energy gives the optical band gap value.

The reported band gaps of $BaTiO_3$ and $LaFeO_3$ correspond respectively to ~3.23 eV and ~2.1 eV [16–18]. **Table-IV.P1.1** regroups all the calculated band gaps estimated using Tauc plot method. The wide band gap was observed mainly for $BaTiO_3$ and it is found to be equal to ~ 3.29 eV which is close to the reported band gap value [17]. **Fig-IV.P1.3** shows the evolution of the band gap as function of the composition. For the samples $0 \leq x \leq 0.3$, a decrease of the band gap values is observed as function of the substitution. For the samples with $0.3 \leq x \leq 0.9$, the decrease is continual and the band gap values are within $2.01\ eV \leq E_g \leq 2.15\ eV$. Aiming to link the structural variation to the opening of the band gap, a study as function of several crystallographic parameters are emphasized as shown in **Fig-IV.P1.4.** The variation of the unit cell volume indicates that a decrease of the unit cell volume is followed by a shrink in the band gap as shown in **Fig-IV.P1.4a**. Moreover the evolution of the band gap as function of the distortion degree was as well studied; the results are presented in **Fig-IV.P1.4a,** and shows that as the amount of the substitution increases, an increase of the distortion degree is observed mainly for the high symmetry compositions between $0.1 \leq x \leq 0.6$, and it is accompanied by a decrease of the band gap values. The point of transition from the high symmetry system to the orthorhombic system show a decrease of the distortion degree, where the evolution of the band gap values remains

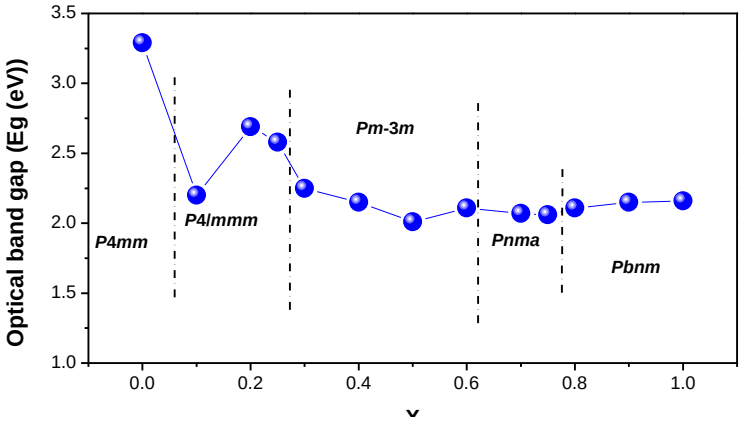

Fig-IV.P1.3: The evolution of the optical band gap as function of the composition of the series $Ba_{1-x}La_xTi_{1-x}Fe_xO_3$ ($0 \leq x \leq 1$).

steady, but to be more precise a slide increase that might be neglected is observed as shown in **Fig-IV.P1.4b**. These results demonstrate that the distortion degree in this case do not affect the opening of the band gap. Additionally, the observation of the dependency of the optical band gap to the crystallographic parameters was treated in terms of the bond angles and the interatomic distances. It is stated that at high symmetry the Ti/Fe-O-Ti/Fe bond angle is equal to 180° resulting in a complete overlap of the O(2p) and the 3d levels [19]. In this case, it is found that as the amount of La^{3+}/Fe^{3+} increases, the system evolves toward lower symmetry resulting in a deviation of the B-O-B bond angles from the ideal value "180°" into values lower than "165°". We suggest that the decrease of the band gap values observed for the compositions with high symmetry is mainly due to the ideal B-O-B bond angle despite the low amount of La^{3+}/Fe^{3+} introduced in the system. As for the compositions $0.7 \leq x \leq 0.9$ adopting systems with low symmetry, the high amount of substitution contributed to reduce the electronegativity between A-site/B-site elements and the oxygen. **Fig-IV.P1.4 (a, b)** show the evolution of the Ti/Fe-O_1-Ti/Fe and Ti/Fe-O_2-Ti/Fe bond angles as a function of "x". It is shown that in the range $0.7 \leq x \leq 1$, as the substitution increases the bond angle deviate to lower values and an increase in the band gap is observed. This indicates that the band gap is still affected by the bond angles that influences the overlap between the O(2p) and the 3d levels. These observations indicate that the crystallographic parameters B-O-B and mainly Ti/Fe-O_2-Ti/Fe is as important as the substitution in the mechanisms of band gap opening, and thus the improvement of the absorption in the visible region. Knowing that the band gap opening is governed mainly by O2p non-bonding level and the $3de_g$ orbital of transition metals in the B site, the interatomic distances are important parameters that can also affect the opening mechanism of the band gap. The evolution of the Ba/La-O and Ti/Fe-O are shown respectively in **Fig-IV.P1.4 (e, f)** the evolution of the Ba/La-O interatomic distance follows a similar behavior as the volume, while the Ti/Fe-O variation shows two different behaviors depending on the symmetry. For the compositions with high symmetry a continual decrease of the Ti/Fe-O is observed followed by a decrease in the band gap value; the compositions $0.7 \leq x \leq 0.9$ present an increase of the interatomic distance while a slight increase of the band gap values in this interval is observed as shown in **Fig-IV.P1.4f**.

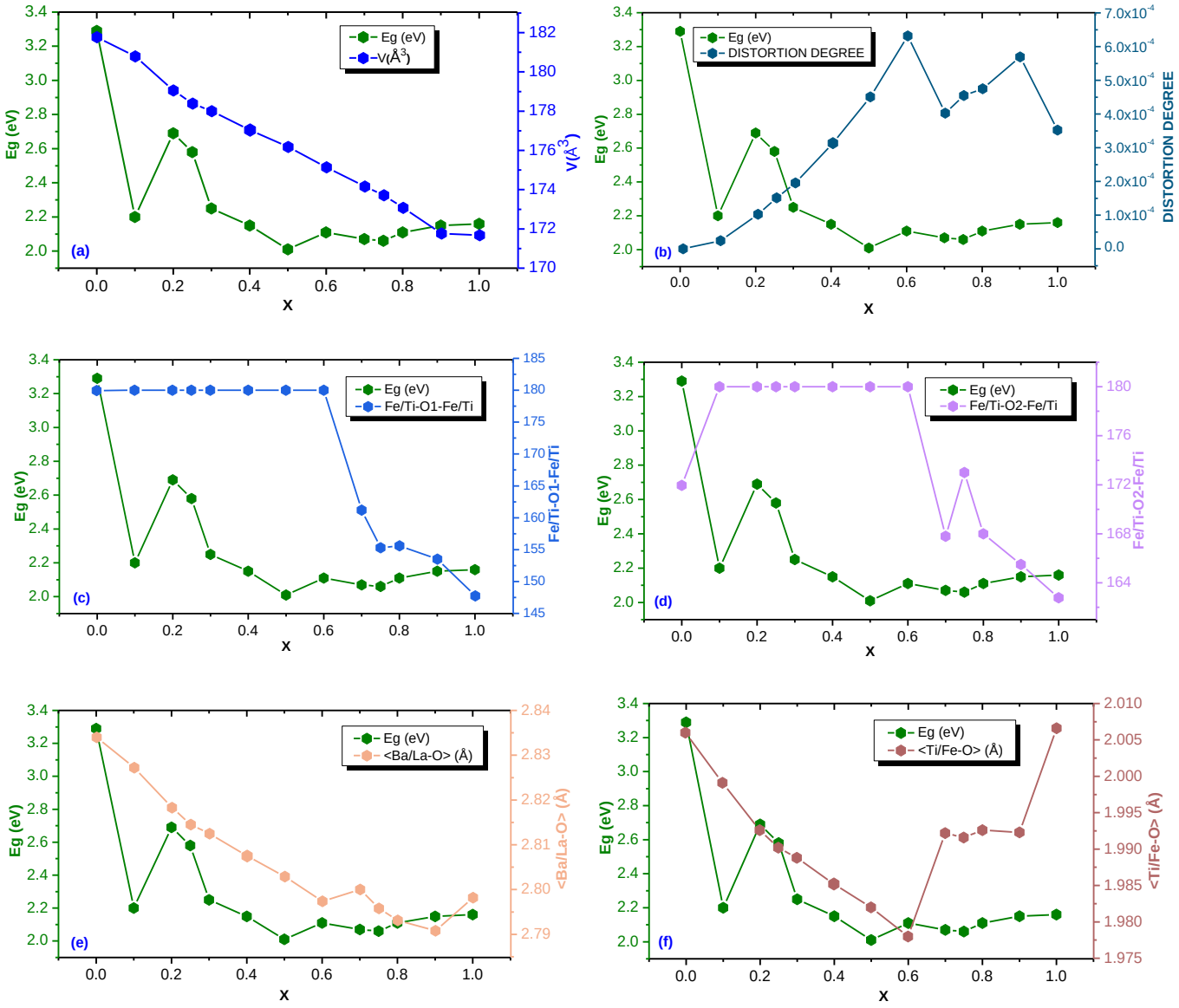

Fig-IV.P1.4: The optical band gap dependence to the crystallographic parameters. The evolution of E_g vs the volume **(a)**, the evolution of E_g vs the distortion degree **(b)**, the evolution of E_g vs the bond angles Fe/Ti-O_1-Fe/Ti **(c)** and Fe/Ti-O_2-Fe/Ti **(d)**, the evolution of E_g vs the interatomic distance <Ba/La-O>**(e)** and <Ti/Fe-O>**(f)**.

Table-IV.P1.1. The main absorptions peak in the UV-visible light (250 nm ≤ λ ≤ 800 nm), and the calculated optical indirect allowed energy gap using Tauc's relationship of the series $Ba_{(1-x)}La_xTi_{(1-x)}Fe_xO_3$ ($0 \leq x \leq 1$).

Composition	UV light absorption (nm)	visible light absorption (nm)	Eg (Tauc plot) (eV)
0	321.58	---	3.29
0.1	390.20	493.07	2.2
0.2	359.14	499.86	2.69
0.25	362.19	496.85	2.58
0.3	392.44	494.33	2.25
0.4	315.35	403.08	2.15
0.5	299.26	414.19	2.01
0.6	304.54	425.54	2.11
0.7	---	434.68 521.27	2.07
0.75	---	436.32 525.75	2.06
0.8	---	431.54 523.24	2.11
0.9	379.95	455.37 503.63	2.15
1	298.01 364.37	454.61 524.74	2.16

IV.2.4. Band gap edges estimation

As discussed previously, the band gap estimated from the reflectance results is affected by both the structure parameters and the composition. The new optical band gaps obtained are the result of the valence and conduction band edges displacement. In order to visualize this shift, the conduction band minimum (CBM) and the valence band maximum (VBM) were calculated using the following equation:

$$E_{CB} = \chi - E_e - 0.5E_g \qquad \text{(Eq. 3)}$$

$$E_{VB} = E_{CB} + E_g \qquad \text{(Eq. 4)}$$

Where, E_{CB} and E_{VB} are respectively the conduction band and the valence band potentials. E_g is the band gap estimated from the UV-vis collected results. E_e is equal to 4.5 and represents the

energy of the free electrons *vs* hydrogen. χ is the electronegativity of semi-conduction and can be calculated as following:

$$\chi = [\chi(A)^a \chi(B)^b \chi(C)^c \chi(D)^d \chi(E)^e]^{\frac{1}{a+b+c+d+e}} \qquad \text{(Eq. 5)}$$

The parameters a, b, c, d and e are the number of atoms in each composition and $\chi(y)$ is the electronegativity of each elements of the compound. **Fig-IV.P1.5**, presents the shift of the CBM and VBM which is in accordance with the shrink of the band gap. Both bands were affected as the amount of the substitution increases, downward shift is observed for the conduction band minimum while the valence band maximum shifts upwards. **Table-IV.P1.2** summarizes the calculated electronegativity, the conduction band edge and the valence band edge potentials.

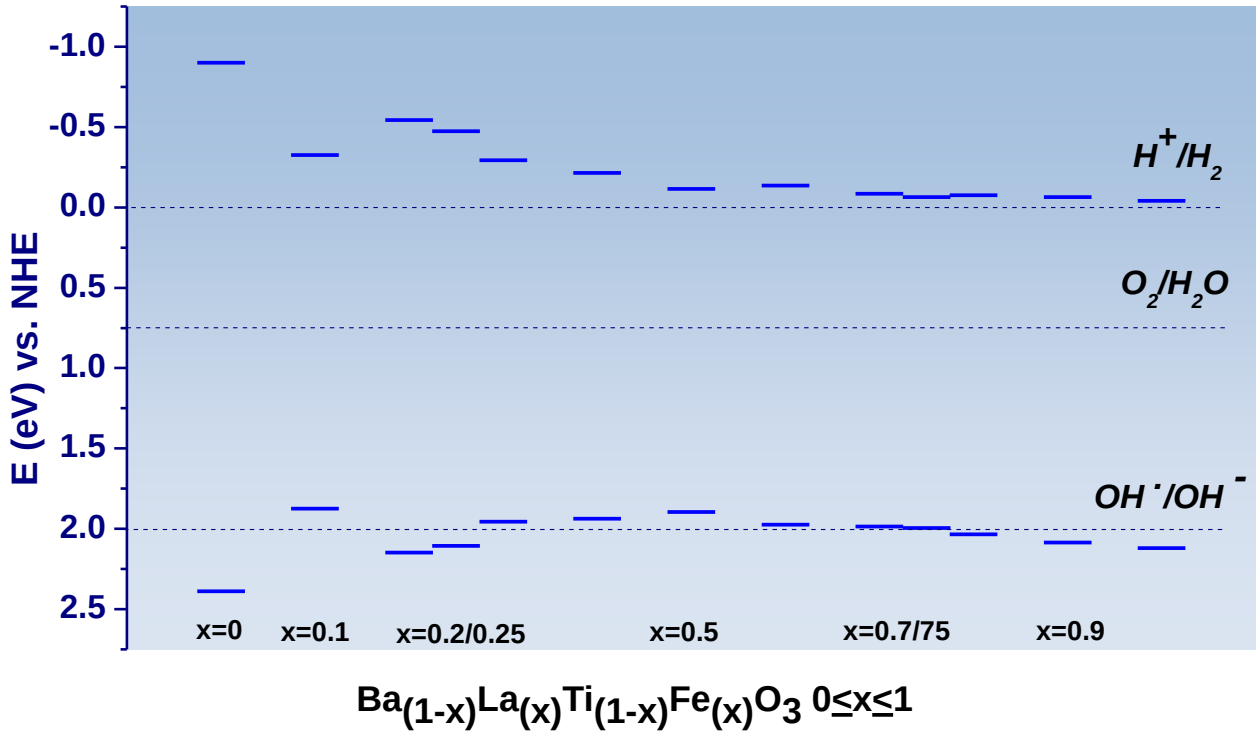

Fig-IV.P1.5: Schematic representations of the calculated conduction band minimum and the valence band maximum for the perovskite series $Ba_{1-x}La_xTi_{1-x}Fe_xO_3$ ($0 \leq x \leq 1$).

Table-IV.P1.2. The calculated values of the absolute electronegativity, the band gap Eg, and the CB and VB potentials for the perovskites series $Ba_{(1-x)}La_xTi_{(1-x)}Fe_xO_3$ ($0 \leq x \leq 1$).

Composition	χ	E_g	E_{CB}	E_{VB}
0	5.244607848	3.29	-0.90039	2.389608
0.1	5.27343803	2.2	-0.32656	1.873438
0.2	5.302426695	2.69	-0.54257	2.147427
0.25	5.31698073	2.58	-0.47302	2.106981
0.3	5.331574713	2.25	-0.29343	1.956575
0.4	5.360882961	2.15	-0.21412	1.935883
0.5	5.39035232	2.01	-0.11465	1.895352
0.6	5.419983675	2.11	-0.13502	1.974984
0.7	5.449777917	2.07	-0.08522	1.984778
0.75	5.4647364	2.06	-0.06526	1.994736
0.8	5.479735941	2.11	-0.07526	2.034736
0.9	5.509858647	2.15	-0.06514	2.084859
1	5.540146942	2.16	-0.03985	2.120147

IV.2.5. Conclusion

The UV-vis measurements revealed that starting from the composition x = 1, all the samples showed very large and board absorption in the UV-Vis regions which show their ability of absorbing notable amount of light in the visible region, which make these samples promising materials for photocatalysis. As the amount of La^{3+} and Fe^{3+} content increases, a continual shift and expansion of the absorption toward the visible range is observed: for the tetragonal symmetry between 492 – 500nm, for the cubic symmetry between 376 – 550nm, while new absorption bands appeared between 455 – 540nm.

The dependency of optical properties to the structural parameters is established. The evolution of the volume is close from the evolution of the band gap as both parameters shows a decrease as function of the composition. Additionally, the correlation between the optical band gap and the structural parameters was observed more to be dependent to Ti/Fe-O_2-Ti/Fe. It is assumed that the low optical band gap values observed in high symmetry structures is due to the

ideal angle 180° presents in this symmetry, which ensures the complete overlap between 2p (O2) and 3d (Ti/Fe) energy levels. Meanwhile, for the composition with orthorhombic structure, the deviation of this bond angles is followed by a slight increase of the band gap. Similar observations in the case of the interatomic distances Ti/Fe-O, it is observed that the band gap decreases when Ti/Fe-O decreases, and slightly increases with the increase of this distance.

Both the CBM and VBM were affected by the substitution, an upward shift was observed for the Valence band maximum while the conduction band minimum shifts downward and this was observed for all the compositions studied in this work.

IV.3. Part II: Investigation of the composition and structure effects on the optical properties of $Sr_{1-x}La_xTi_{1-x}Fe_xO_3$ perovskite system with ($0 \leq x \leq 1$)

IV.3.1. Introduction

Researches toward visible light active materials dedicated for solar harvesting applications have received enormous interest [20–23]. The ABO_3 structure is generally composed of rare earth and alkali metal occupying the A site with 12-fold coordination (A= Ba^{2+}, La^{3+}, Sr^{2+}, Pb^{2+}, etc.), while transition metals are positioned at the B-site of 6-fold coordination (B= Fe^{3+}, Ti^{4+}, etc.). Recently, the Titanate perovskite family and mainly $SrTiO_3$ perovskite material has been an attractive material for photocatalysts applications owing to its stability, high and efficient photocatalysts activity [4, 24, 25]. However, due to the wide band gap value (3.2 eV) it is found that $SrTiO_3$ is highly active under the UV light with no response to the visible light [4]. The wide band gap of perovskites such as $SrTiO_3$ is due to the fundamental characteristic nature of A-O and B-O interatomic distances and to the large difference in electronegativity between the oxygen and the transition-metal cations [26]. Co-doping or substituting an amount of the hosting structure's elements will enable us to create and generate new energy level between the valence band and the conduction band resulting in a shrink of the band gap of the material [4, 25, 27]. WeiWei Li and al. reported that Ti 3d and Fe 3d orbital hybridization in $BiFeO_3$-$SrTiO_3$ system creates trap states that suppress the fast recombination rate [28]. Nanocrystalline of $SrTiO_3$ doped Fe ions was prepared via solid state reaction; the $SrTi_{0.9}Fe_{0.1}O_{2.968}$ nanocrystalline with a band gap equal to 1.34 eV, showed a broad and intense absorption extending from 0.5 eV to 6 eV covering the UV-visible region to near IR. The observed shrink of the band gap compared to $SrTiO_3$ was related to the appearance of defect centers across the gap [29]. Other group of

researcher has reported on the band gap of $LaFe_{1-x}Ti_xO_3$ system, the experiments show an increase from 2.05 eV of 2.61 eV of the band gap values as the amount of Fe^{3+} decreases [30]. In another study, the control of the optical absorption of $La_{1-x}Sr_xFeO_3$ perovskite films by both heterovalent A-substitution and oxygen vacancies was reported. It is found that Sr substitution induces the formation of new states bellow the bottom of the conduction band which resulted in a redshift of the absorption [31]. Recently, La-Fe co-doped $SrTiO_3$ system was studied as visible light photocatalysts. Different dopant concentration up to 5 wt %, were prepared, the samples showed a reduction of the optical band gap as the amount of the substitution increases from 3.2 eV to 2.72 eV and a red shift of the absorption. This reduction was related to the formation of impurity energy levels, due to the doping and to the charge transfer transitions [32]. The intrinsic behavior and effect of the doping elements is not the only factor responsible for the shrink of the band gap, as it is stated by a group of researcher, the gapping in perovskite materials is also related to structural symmetry breaking such as octahedral titling and rotation [9].

The aim of this work is to study the effect of the structure and the composition on the optical band gap, as well as estimate the change occurred in both the conduction band minimum and the valence band maximum of their alignment with the redox potential. The co-substitution of $SrTiO_3$ by rare earth and transition metals is carried out using the solid state reaction. La^{3+} and Fe^{3+} elements were the chosen candidates to synthesis the perovskites series $Sr_{1-x}La_xTi_{1-x}Fe_xO_3$, the doping elements amount ranges between $0 \leq x \leq 1$. The choice of La^{3+} lies behind the capability of increasing the surface area and the prevention of electron-hole recombination [33–37] while Fe^{3+} ions will create new energy levels and enhances the absorption in the visible light domain [37–39] which are desired characteristics for photocatalysts applications. The effect of the substitution on the structural formation, optical properties, the band gap and the conduction/valence bands edges was studied.

IV.3.2. The UV-visible absorption performance

The Uv-vis diffuse reflectance (R%) spectra were collected between 200 nm and 800 nm at room temperature. The absorbance of the ceramics was expressed with the Kubelka-Munk function approximation F(R) using the following equation [40]:

$$\frac{K}{S} = \frac{(1-R)^2}{2R} \equiv F(R) \qquad (Eq.\,1).$$

The parameters K, S and R, are respectively the absorption coefficients, the scattering coefficient and the diffuse reflectance. **Fig-IV.P2.1** shows the absorption bands of the synthesized samples. $SrTiO_3$ sample presents two UV absorptions at 280 nm and 345 nm, these absorptions correspond to the inter-band transition between Ti(3d-t_{eg}) and O(2p) levels [41]. The effect of La, Fe-$SrTiO_3$ substitution is observed in the continual shift of the absorptions of about 23 nm from 280 nm to 303 nm and of about 33 nm from 345 nm to 378. Moreover, a high intense broad visible light absorption bands appear at around 455 nm and 527 nm indicating the strong response to the visible light. The red-shift of the absorption bands as well as the appearance of new intense broad absorptions is related to several factor among which we site, the interaction of Ti(3d) orbitals and Fe(3d) orbitals and/or to the charge transfer transition between La^{3+} / Fe^{3+} [39]. The significant contribution of the substituting elements La^{3+} / Fe^{3+} to create new energy levels is also possible, which results in new absorption bands [42]. **Table-IV.P2.1** summarizes the main absorption peaks in the UV-visible light ($250\ nm \leq \lambda \leq 800$).

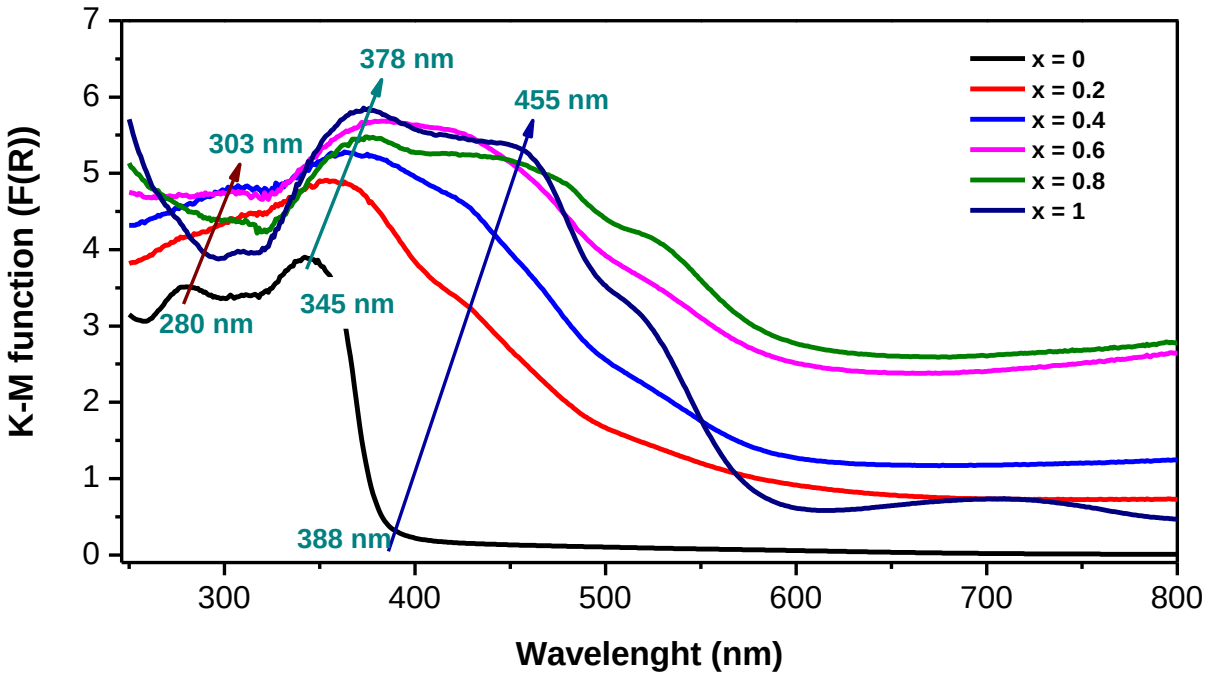

Fig-IV.P2.1: UV-vis Spectra of the series $Sr_{1-x}La_xTi_{1-x}Fe_xO_3$ ($0 \leq x \leq 1$), showing the evolution of absorption coefficient (K-M function) in the range of wavelength between 250 and 800 nm.

Table-IV.P2.1. The main absorptions peak in the UV-visible light (250 nm ≤ λ ≤ 800 nm), and the calculated optical indirect allowed energy gap using Tauc's relationship of the series $Sr_{(1-x)}La_xTi_{(1-x)}Fe_xO_3$ ($0 \leq x \leq 1$).

Composition	UV light absorption (nm)	visible light absorption (nm)	Eg (Tauc plot) (eV)
0	280 345	---- ----	3.34
0.2	303 355	428 ----	2.53
0.4	303 366	431 518	2.39
0.6	303 378	429 523	2.18
0.8	309 372	455 526	2.00
1	372 ----	455 518	2.19

IV.3.3. Band Gap values determination

The optical band gap values E_g is estimated by McLean analysis of the absorption edge using the equation (2) [40]:

$$F(R)h\nu = A(h\nu - E_g)^n \qquad (Eq.\,2)$$

Where $F(R) \equiv \alpha(\lambda) = \frac{K}{S}$ is the absorption coefficient, the constant "A" is the band tailing parameter. The "n" index depend to the inter-band transitions mechanisms; the possible values for the index n are equal to 1/2, 2, 3/2 or 3 and each denotes respectively direct allowed, indirect allowed, direct forbidden and indirect forbidden transitions types. The E_g values were derived by the extrapolation of the tangential line from high photon energy to zero F(R) → 0. The type of inter-band transitions present in the samples corresponds to direct allowed transitions, **Fig-IV.P2.2** shows the calculated optical band gap using tauc plot method at F(R) → 0. The optical band gap of $SrTiO_3$ and $LaFeO_3$ were found to respectively be ~3.34 eV and ~2.19 eV, these results were close to the reported band gap in the literature [43]. The lowest optical band gap values obtained is equal to E_g= 2 eV. This value corresponds to the composition x = 0.8 and reflect the positive effect of the substitution on the optical property of perovskite materials.

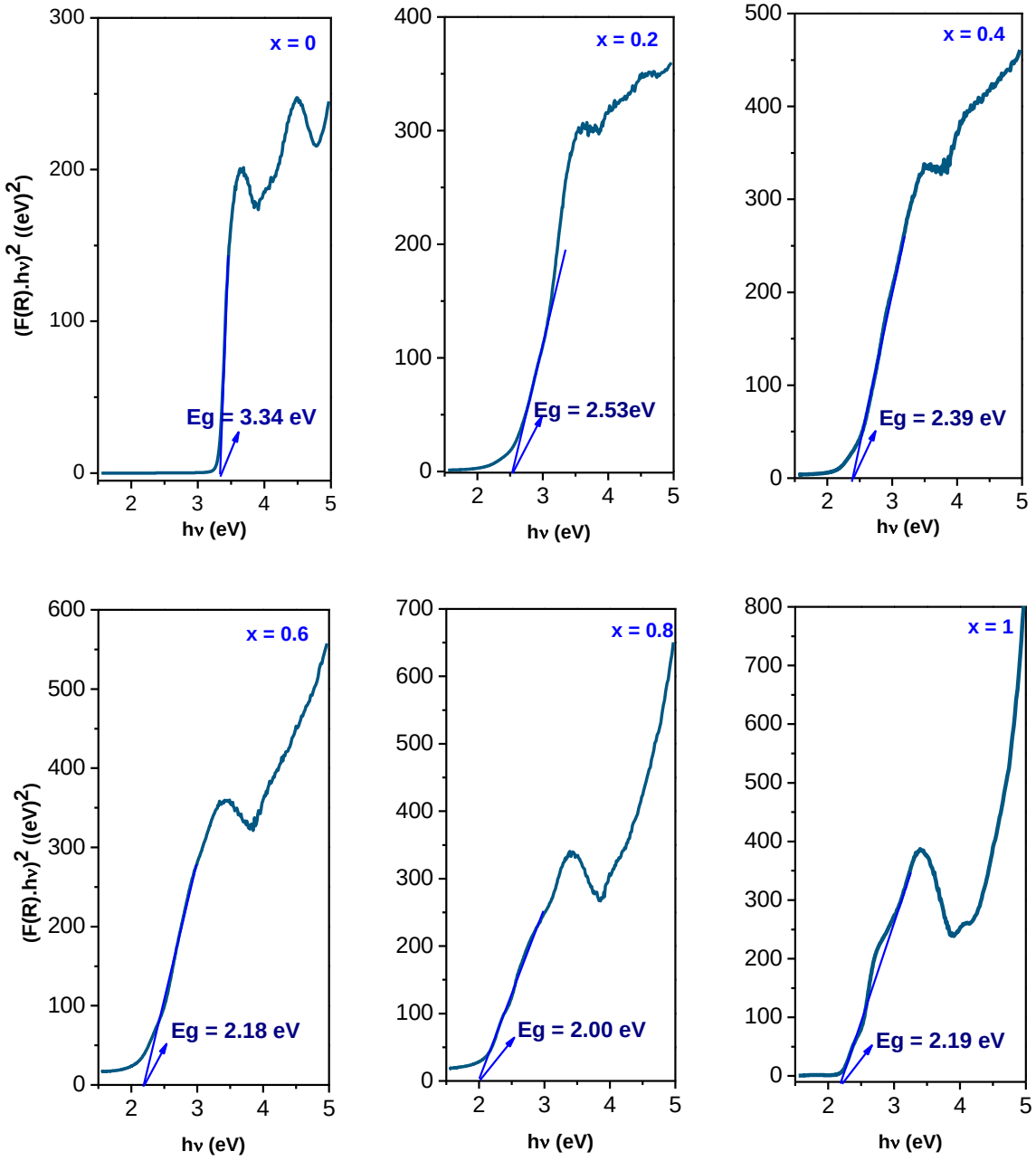

Fig-IV.P2.2: The kubelka-Munk function (F(R)hν)½ variation of the series $Sr_{1-x}La_xTi_{1-x}Fe_xO_3$ ($0 \leq x \leq 1$).

The evolution of the band gap as function of the composition "x" is shown in **Fig-IV.P2.3**. A continual decrease of the optical band gaps is observed for the new compositions in comparison the end members x=0 and x=1. The conduction band and the valence band consist of Ti(3d), Fe(3d) and O(2p) state respectively and under the effect of the distortion or the phase transitions, both states can overlap and mix [44]. The Figure **Fig-IV.P2.4a** presents the evolution of the volume and the band gap as function of the composition, the plot shows that the increase of the volume is followed by a decrease of the band gap, while the distortion variation shows no link to the band gap evolution as function of the composition as presented in **Fig-IV.P2.4b**. One other factor with a direct link to the energy level overlapping is shown in **Fig-IV.P2.4 (c, d)**. The two bond angles (Fe/Ti)-O_1-(Fe/Ti) and (Fe/Ti)-O_2-(Fe/Ti) continually deviate from their ideal value 180°, which is consistent with the transition from high symmetry to low symmetry systems. The continual deviation from 180° for (Fe/Ti)-O_1-(Fe/Ti) is followed by a continual decrease in the band gap energy. Nevertheless, the evolution of the bond angle (Fe/Ti)-O_2-(Fe/Ti) gives more insight on the effect of the structural parameters of the band gap evolution. It is demonstrated that as the amount the composition increases, the evolution of the bond angle and the band gap are in opposition. As shown in **Fig-IV.P2.4d** the further the bond angle deviates from 180°, the lower the band gap, which is in contradiction with the previously discussed results of **Part I** and literature [45]. Our investigations show that in this case of study and for the compositions $0.2 \leq x \leq 0.8$, the interatomic distances <Fe/Ti-O> and <Sr/La-O> show similar behavior of their evolution as function of the composition. It is demonstrated that the band gap values decreases as the interatomic distances increases as presented in **Fig-IV.P2.4 (e, f)**. These results open door for additional questions since they show no similarities to the previous results of **part I**. The shrink observed in the doped samples is also due

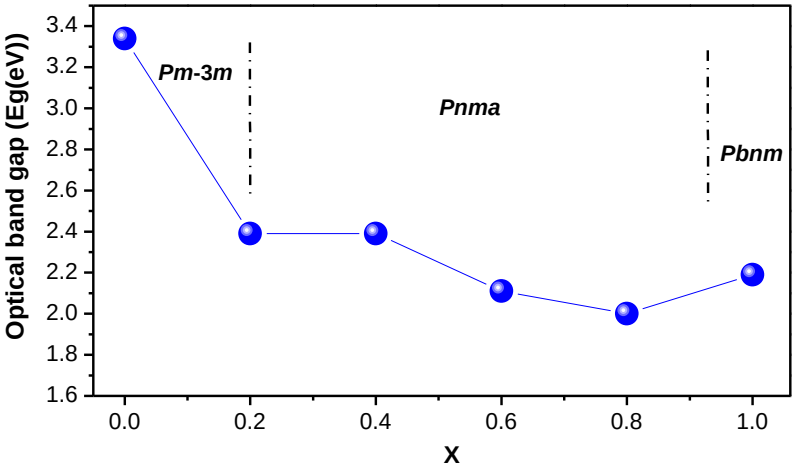

Fig-IV.P2.3: The evolution of the optical band gap as function of the composition of the series $Sr_{1-x}La_xTi_{1-x}Fe_xO_3$ ($0 \leq x \leq 1$).

to the new energy levels created in the middle of the conduction and valence band by La^{3+} and by Fe^{3+} above the valence band [42, 46]. We observe in this case that the composition effect is more presents that the structural effect in tuning the band gap values. **Table-IV.P2.1** summarizes the type of transitions present in the samples, the optical band gaps and the absorption regions.

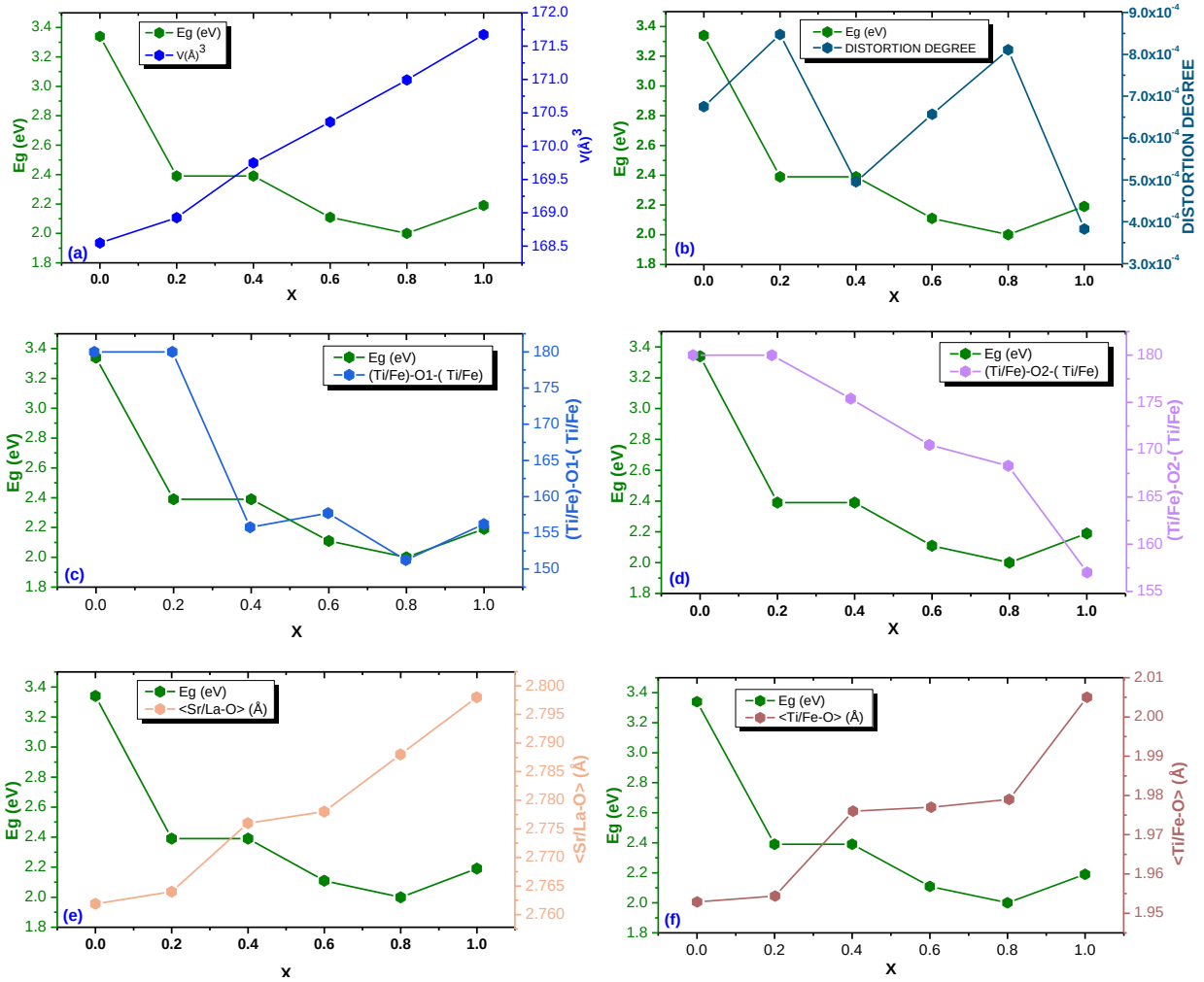

Fig-IV.P2.4: The optical band gap dependence to the crystallographic parameters. The evolution of E_g vs the volume **(a)**, the evolution of E_g vs the distortion degree **(b)**, the evolution of E_g vs the bond angles Fe/Ti-O_1-Fe/Ti **(c)** and Fe/Ti-O_2-Fe/Ti **(d)**, the evolution of E_g vs the interatomic distance <Sr/La-O>**(e)** and <Ti/Fe-O>**(f)**.

IV.3.4. Band gap edges estimation

The following empirical equation is used to estimate the edge of the conduction (CB) and the valence (VB) bands [32, 47].

$$E_{CB} = \chi - E_e - 0.5E_g \qquad \text{(Eq. 3)}$$

$$E_{VB} = E_{CB} + E_g \qquad \text{(Eq. 4)}$$

The parameters E_{CB} and E_{VB} are respectively the conduction band and the valence band potentials. E_g represents the band gap of each composition which is calculated previously. E_e is equal to 4.5 and represents the energy of the free electrons *vs* hydrogen [32, 47]. χ is the electronegativity of semiconductions and can be calculated as following [32, 47]:

$$\chi = [\chi(A)^a \chi(B)^b \chi(C)^c \chi(D)^d \chi(E)^e]^{\frac{1}{a+b+c+d+e}} \qquad \text{(Eq. 5)}$$

Where a, b, c, d and e are the number of atoms in each composition and $\chi(y)$ is the electronegativity of each elements of the compound. **Table-IV.P2.2.** summarizes the calculated electronegativity, the conduction band edge and the valence band edge potentials. **Fig-IV.P1.5** shows a descriptive schema of the calculated CB and VB edge potentials. The results obtained are in good agreements with the previous discussion. The substitutions with La^{3+}/Fe^{3+} has created new energy levels above the valence band and bellow the conduction band resulting in a shrink of the band gap.

Following the same interest of improving the photocatalytic characteristics of $SrTiO_3$ for water splitting and the degradation of organic molecules, the following paragraph is a synthetic study of the co-substitution effect on the light absorption, the valence (VB) and the conduction (CB) bands shift. As shown in **Fig-IV.P1.5**, $SrTiO_3$ conduction band edge is -0.84V lower than H^+/H_2 potential and thus $SrTiO_3$ presents a strong reducing ability. The calculated CBM and VBM are close to the values reported in literature [47]. The Valence band edge is more positive compared to O_2/H_2O. These results prove that $SrTiO_3$ satisfies the requirements of direct water splitting, but the fact that $SrTiO_3$ is only active under the UV-light drove us to enhance the visible light activity of this material and investigate the influence of co-substitution. For the compositions x=0.2, x=0.4 and x=0.8 the CB maximum shifts downward by 0.52V, 0.57V and 0.75V respectively. The VB maximum of x=0.2, x=0.4 and x=0.8 shifts upward by 0.43V and 0.38V and 0.48V respectively. Both the photo-reduction and the photo-oxidation capacities are greatly improved. Additionally to their optical band gap ranging within efficient utilization of visible light, both compositions have satisfied the characteristics required. For the composition x=0.8, the VB maximum move upward up to 0.94V proving the great enhancement of the photo-

oxidation, while the CB maximum shifts downward by 0.846V and lies at the oxidation level of water. The composition x=0.8 is to be expected as a photo-oxidation active material. Our results demonstrated that the co-substitution of $SrTiO_3$ by La^{3+} / Fe^{3+} extend the absorption edge to the visible light and are expected to improve the photocatalytic activity of $SrTiO_3$. **Fig-IV.P1.5** shows a schematic representation of the valence band and conduction band maximum of pure and doped compositions and **Table-IV.P2.2** summarizes the calculated values.

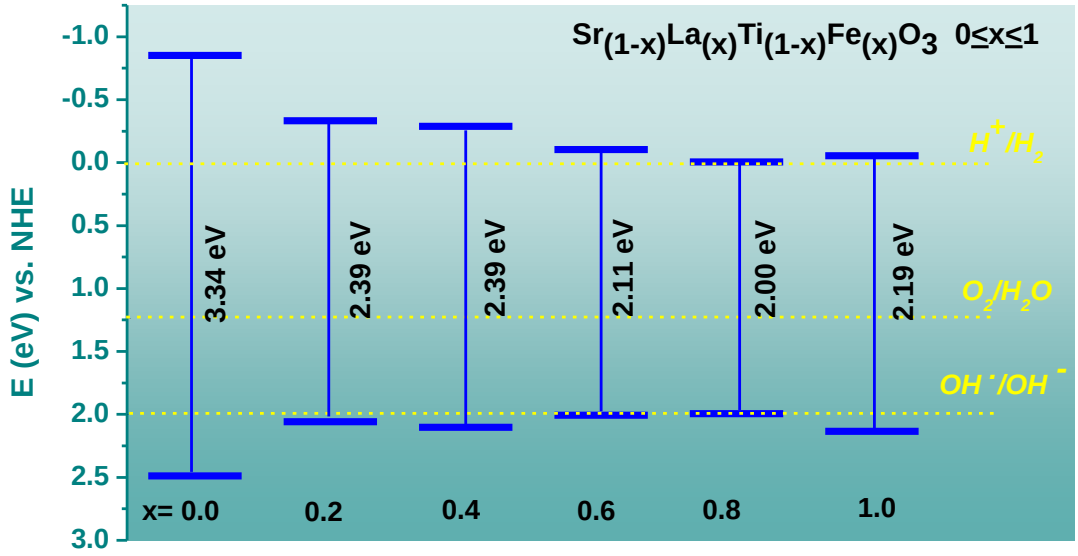

Fig-IV.P1.5: Schematic representations of the calculated conduction band minimum and the valence band maximum for the perovskite series $Sr_{1-x}La_xTi_{1-x}Fe_xO_3$ ($0 \leq x \leq 1$).

Table-IV.P2.2. The calculated values of the absolute electronegativity, the band gap Eg, and the CB and VB potentials for the perovskites series $Sr_{1-x}La_xTi_{1-x}Fe_xO_3$ ($0 \leq x \leq 1$).

Composition	χ	Eg	E_{CB}	E_{VB}
0	5.318779965	3.34	-0.85122	2.48878
0.2	5.362334185	2.39	-0.33267	2.057334
0.4	5.40624506	2.39	-0.28875	2.101245
0.6	5.450515511	2.11	-0.10448	2.005516
0.8	5.495148482	2	-0.00485	1.995148
1	5.540146942	2.19	-0.05485	2.135147

IV.3.5. Conclusion

Red-shift of the absorption band was observed for the new compositions. The UV-vis results demonstrate that the co-substitution of $SrTiO_3$ enhances their visible light absorption. As

the amount of the substitution increases, the absorption band of $SrTiO_3$ expand to the visible light and new absorption band appear around 455 – 527nm.

The calculated band gaps are between 2.39 eV and 2eV and are within the range of efficient utilization of the visible light. In comparison with the results of **part I**, the band gap of this case study decreases with the increase of the volume. Additionally, the further the Ti/Fe-O_1-Ti/Fe and Ti/Fe-O_2-Ti/Fe deviate from the ideal bond angle values 180° smaller band gap values are observed which is in contradiction with the results obtained in **part I**.

The composition had an impact on the position of the maximum of the valence band and the minimum of the conduction band. The upward shift of the valence band maximum VBM and the downward conduction band minimum CBM affect the performance of the materials. The photo-reduction and photo-oxidation ability of $SrTiO_3$ has been greatly improved for the compositions $0.2 \leq x \leq 0.6$, while we assume that the composition x=0.8 can only be photo-oxidation active since the CBM lies at the oxidation level of water. These improvements of the optical properties are mainly due to the creation of new energy level leading to a shift of the conduction band and valence band edges.

IV.4. Part III: Investigation of the composition and the structure effects on the optical properties of $Ba_{1-x}Sr_xTi_{1-x}Fe_xO_{3-\delta}$ perovskite system with $0 \leq x \leq 1$

IV.4.1. Introduction

The development of highly active photocatalyst semiconductors with broad light absorption of the visible light have been the topic of numerous studies. The wide band gaps of oxides photocatalysts prevent them from being active under the visible light. This limitation prevent their application under the sun light since the UV light constitute only 4% of the solar spectrum, additionally the use of artificial UV sources are costly and toxic. The wide band gap of oxides has a direct link to the bonding nature between the transition metals and oxygen. The works done to design semiconductors with narrow band gap consist mainly of doping the hosting structure with transition metals [48, 49]. Among the known semiconductors, perovskites oxides have proved their capability to be developed to meet the requirement of photocatalyst materials. Their structural flexibility gives rise to their hosting ability to different compositions and constituent, which provides the opportunity for tuning their physical properties. In the previous

parts, the band gap is seen to be dependent either to B-O interatomic distances between the B site elements and oxygen and/or to the bond angle B-O-B. The contribution to the shift of the conduction band and the valence band is mainly done by the B-site element orbitals and the O(2p) of oxygen. Moreover, we have demonstrated that the co-doping strongly influences the visible light response. The co-substitution of $BaTiO_3$ by La^{3+} in A-sites and Fe^{3+} in B-sites has induced a red shift of the UV light absorption while new absorptions peaks appeared in the visible domain. A shrink in the optical band gap was observed.

In this part we report the effect of the substitution of $BaTiO_3$ by Sr^{2+} in the A-site and Fe^{3+} in the B-sites on the structural and physical properties. The effect of the substitution on the optical response, the band gap and the conduction band and valence band edges are systematically studied.

IV.4.2. The UV-visible absorption performance

Reported experimental optical band gap of $BaTiO_3$ and $SrFeO_{2.5}$ are, respectively, ~3.17 eV and ~1.66 eV [17, 37]. It is known that the UV-Vis absorption bands of transition metals correspond mainly of charge transfer and/or electronic d-d transitions [50]. To study the effect of the substitution on the optical properties and the transition mechanisms, diffuse reflectance spectra were recorded at room temperature as shown in **Fig-IV.P3.1**. The spectra were recorded in the range of 250-800 nm. For the spectra analysis, the kubelka munk function theory was used as an approximate method to plot the UV-Vis absorption of the ceramics as follow:

$$\frac{K}{S} = \frac{(1-R)^2}{2R} \equiv F(R) \qquad (Eq.\,1).$$

Where, K, S and R, represent respectively the absorption coefficients, the scattering coefficient and the diffuse reflectance. $F(R) \equiv \alpha(\lambda)$, is the kubelka munk function representing the absorption coefficient in **Fig-IV.P3.1**. $BaTiO_3$ shows one absorption at around 352 nm corresponding to transitions between Ti(3d-t_{eg}) and O(2p) energy levels as seen in **Fig-IV.P3.1a**. $SrFeO_{2.5}$ in **Fig-IV.P3.1c** shows intense and broad absorption at 367 nm due to charge transfer between O2p non-bonding orbitals and the lowest empty orbital ($2t_{2g}$) and 731 nm corresponding to the spin forbidden ligand field transitions [37, 41, 51].

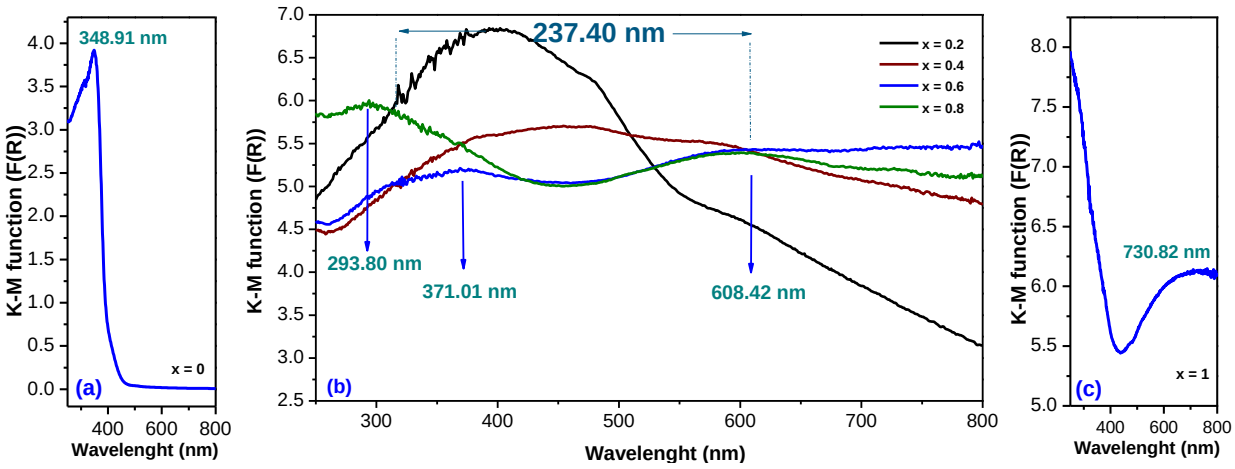

Fig-IV.P3.1: UV-vis Spectra of the series $Ba_{1-x}Sr_xTi_{1-x}Fe_xO_{3-\delta}$ ($0 \leq x \leq 1$), showing the evolution of absorption coefficient (K-M function) in the range of wavelength between 250 and 800 nm. The evolution of the absorption coefficient for the sample with x=0 **(a),** the samples with ($0.2 \leq x \leq 0.8$) **(b)** and for the samples with x = 1 **(c)**.

As the amount of the substitution increases, the UV absorption peak observed for $BaTiO_3$ shifts toward the visible light. Both composition x=0.2 and x=0.4 adopt the tetragonal structure and show very broad and intense absorption band as shown in **Fig-IV.P3.1b**. The width of this band is estimated to be higher than 314 nm as presented in **Fig-IV.P3.1b**. Above 40% of the substitution amount, the system undergoes a phase transition to cubic structure. We observed that the samples with composition x=0.6 and x=0.8 show similar absorption peaks for $SrFeO_{3-\delta}$ (**Fig-IV.P3.1c)**. The obtained UV-vis results show the effect of the substitution on the enhancement of the visible light absorption, while the structure variation gives an insight about the effect of symmetry on the behavior of the materials under UV-Vis excitation.

IV.4.3. Band Gap values determination

The optical band gap and the type of transition are determined according to the analysis method of McLean of the absorption edge using the equation (2):

$$F(R)h\nu = A(h\nu - E_g)^n \qquad (Eq.\,2)$$

Where, the coefficient "A" is the band tailing parameter, an energy independent parameter. The "n" index depends on the inter-band transitions mechanisms type; the possible values are equal to 1/2, 3/2, 2, or 3 each corresponds respectively to direct allowed, direct forbidden, indirect allowed and indirect forbidden transitions types. The final plots of $(F(R)h\nu)^x$ versus hν are

presented in **Fig-IV.P3.2**; the range of the absorption edge gives a straight line. The optical band gaps is estimated using tauc plot method by extrapolating the slope from high photon energy to zero F(R) → 0 as presented in **Fig-IV.P3.2**. The samples show direct band gap transition type. The extrapolated band gaps are presented in **Table-IV.P3.1**.

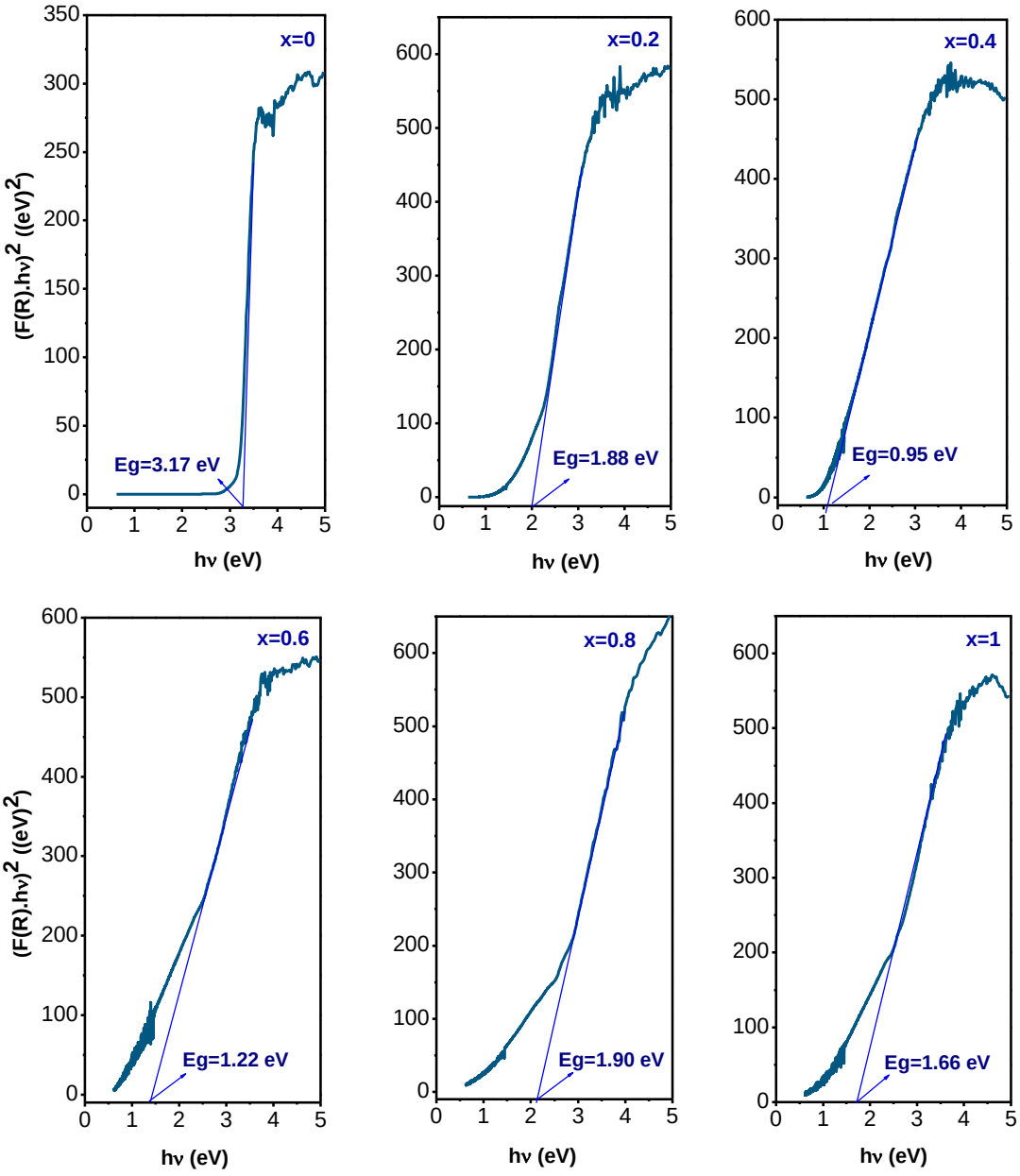

Fig-IV.P3.2: The kubelka-Munk function (F(R)hν)½ variation of the series $Ba_{1-x}Sr_xTi_{1-x}Fe_xO_{3-\delta}$ ($0 \leq x \leq 1$).

Table-IV.P3.1. The main absorptions peak in the UV-visible light (250 nm ≤ λ ≤ 800 nm), and the calculated optical indirect allowed energy gap using Tauc's relationship of the series $Ba_{1-x}Sr_xTi_{1-x}Fe_xO_{3-\delta}$ ($0 \leq x \leq 1$).

Composition	UV light absorption (nm)	visible light absorption (nm)	Eg (Tauc plot) (eV)
0	352	----	3.18
0.2	----	460	1.38
0.4	----	585	
0.6	371	608	1.61
0.8	294	608	2.33
1	----	731	2.46

Fig-IV.P3.3 shows the variation of E_g versus the substitution amount 'x'; a decrease in the optical band gap values is observed varying between 1.90 eV and 0.95 eV. In this case of study, a continual decrease is observed for the compositions between $0 \leq x \leq 0.4$ with P4/mmm; at the transition point from the tetragonal to cubic system, the band gap showed an increasing behavior as function of the composition between $0.6 \leq x \leq 0.8$. The observed variation of the band gap was systematically linked to the variation of the structural parameters. **Fig-IV.P3.4a** shows a close to linear behavior of the unit cell volume evolution, in this case, it is seen that the band gap is independently evolving with regards to the unit cell volume. The increase of the distortion degree is followed by an increase of the band gap value as shown in **Fig-IV.P3.4b.** The parameter of the bond angle is shown in **Fig-IV.P3.4 (c, d)** Both Ti/Fe-O_1-Ti/Fe and Ti/Fe-O_2-Ti/Fe are equal to 180°, nevertheless the band gap evolution shows no dependency or link to the mentioned parameter. On the other hand, the evolution of the interatomic distances

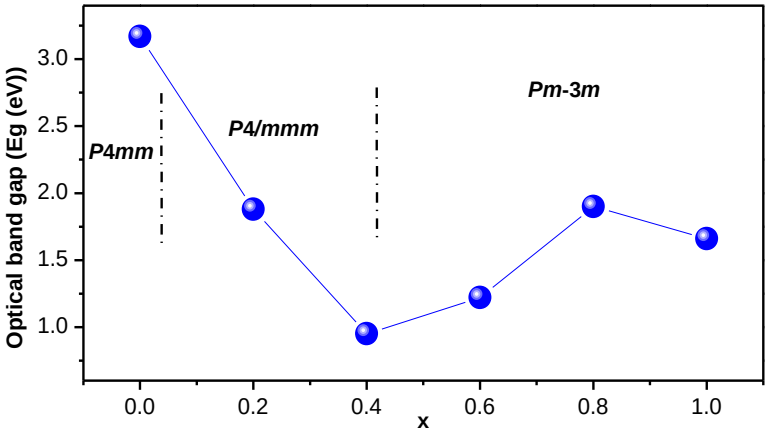

Fig-IV.P3.3: The evolution of the optical band gap as function of the composition of the series $Ba_{1-x}Sr_xTi_{1-x}Fe_xO_{3-\delta}$ ($0 \leq x \leq 1$).

gives insight on the evolution dependency of the band gap values. The **Fig-IV.P3.4 (e, f)** demonstrate that both interatomic distances behave similarly as function of the composition; besides it is observed that for high <Ba/Sr-O> and <Ti/Fe-O> distances, lower band gap values are obtained. Above the transition point, a continual decrease of the two distances <Ba/Sr-O> and <Ti/Fe-O> is observed, which is followed by an increase of the optical band gap. These results demonstrate that the band gap is sensitive to the amount of the substitution and the interatomic distances.

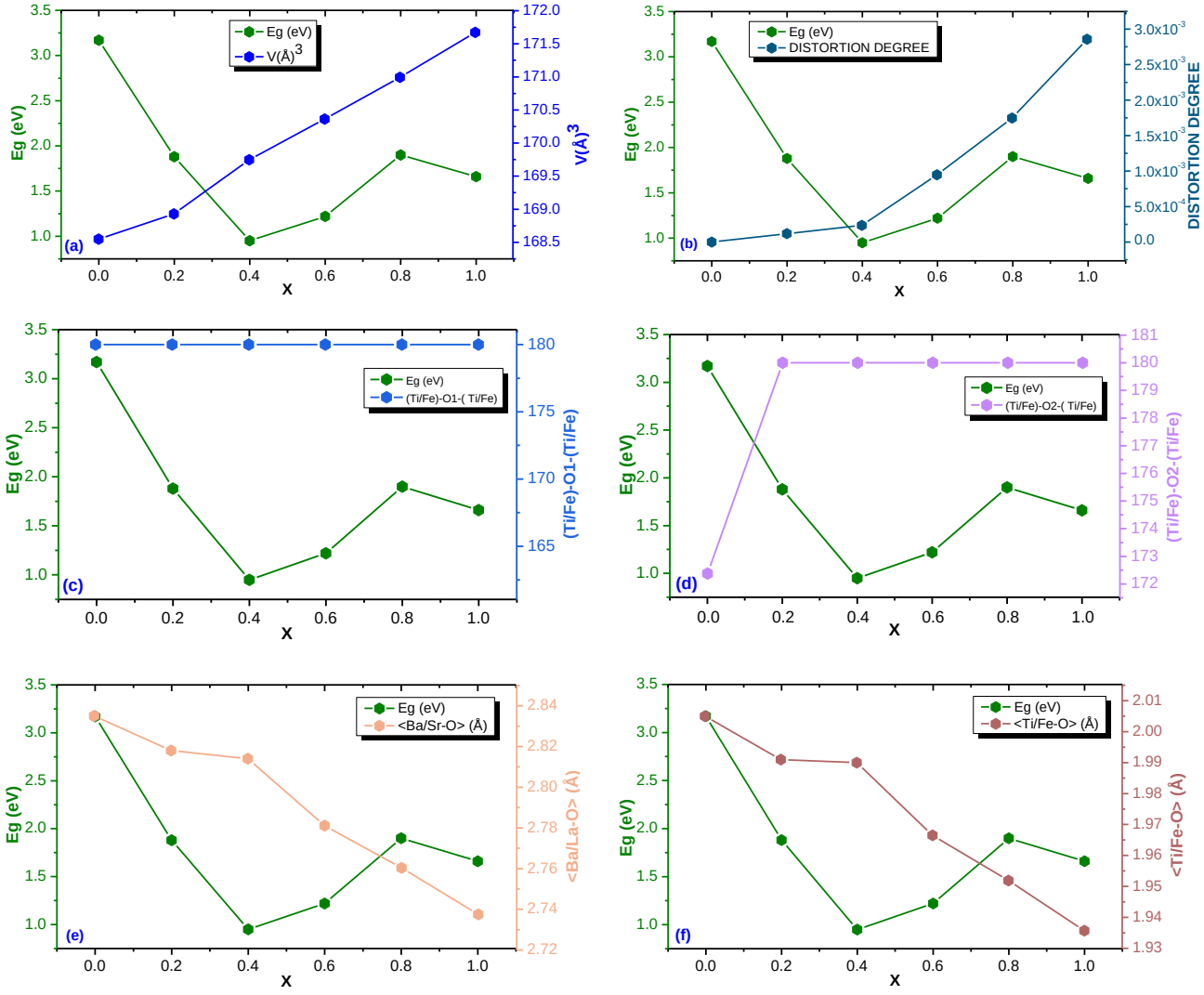

Fig-IV.P3.4: The optical band gap dependence to the crystallographic parameters. The evolution of E_g vs the volume **(a)**, the evolution of E_g vs the distortion degree **(b)**, the evolution of E_g vs the bond angles Fe/Ti-O_1-Fe/Ti **(c)** and Fe/Ti-O_2-Fe/Ti **(d)**, the evolution of Eg vs the interatomic distance <Ba/Sr-O> **(e)** and <Ti/Fe-O> **(f)**.

IV.4.4. Band Gap edges estimation

The conduction band and the valence band edges were calculated using the empirical equation:

$$E_{CB} = \chi - E_e - 0.5E_g \qquad \text{(Eq. 3)}$$

$$E_{VB} = E_{CB} + E_g \qquad \text{(Eq. 4)}$$

Where E_{CB}, E_{VB} and E_g are the conduction band potential, the valence band potential and the calculated band gap, respectively. E_e is equal to 4.5 and represents the energy of the free electrons vs hydrogen. χ is the absolute electronegativity of semiconductors and can be calculated by:

$$\chi = [\chi(A)^a \chi(B)^b \chi(C)^c \chi(D)^d \chi(E)^e]^{\frac{1}{a+b+c+d+e}} \qquad \text{(Eq. 5)}$$

The parameters a, b, c, d and e are the number of atoms in each composition and χ is the absolute electronegativity of each element of the compound. **Table-IV.P3.2** summarizes the calculated electronegativity, the conduction band edge and the valence band edge potentials. **Fig-IV.P3.5** shows a descriptive scheme of the calculated CB and VB edge potentials. A shift of the CBM and VBM is observed for all the new prepared compositions. The substitution Sr^{2+} and Fe^{3+} by Sr^{2+} and Fe^{3+} as well as the oxygen vacancies have contributed to the creation of new energy levels above the valence band and the bellow the conduction band which explains the small band gap reported earlier. Additionally to the new energy level created by the substitution with new elements in the A-site and the B-site, the oxygen vacancies create in-

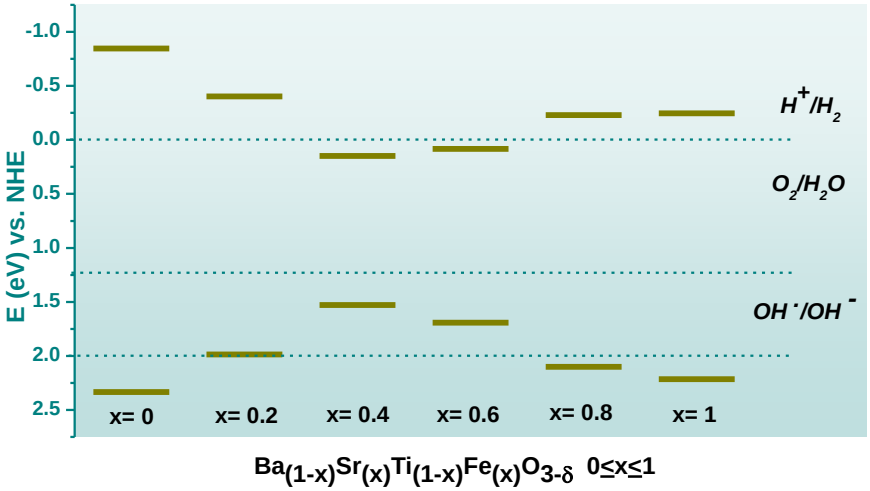

Fig-IV.P3.5: Schematic representations of the calculated conduction band minimum and the valence band maximum for the perovskite series $Ba_{1-x}Sr_xTi_{1-x}Fe_xO_{3-\delta}$ ($0 \leq x \leq 1$).

gap donor states that reduce the gap and induce a shift of the conduction band minimum and the valence band maximum [52]. The Prepared samples were successfully designed to be visible light absorber materials with low band gap. Yet, it was stated that the overall water splitting reaction and the photocatalytic activities are strongly dependent to the position of the CBM and the VBM. **Fig-IV.P3.5** describes the estimated CB and VB edges. For the composition x=0.2, the CBM shifts downward by 0.68 V, while the VBM shift upward by 0.6 V. These results indicate that both the photo-reduction and photo-oxidation capacities have greatly been improved and the material is expected to be active with a strong visible light absorption. It is noticed that the position of the VBM and CBM have an ideal level for the overall water splitting reaction. The compositions between $0.4 \leq x \leq 0.6$, present deep conduction band and are located at potential under the reduction potential of H^+ to H^2. The VB maximums are at suitable positions and are located at potential more positive than the oxidation potential of H_2O to O_2. For the composition x=0.8, the CBM shift downward and lies at the reduction potential position, while upward shift of the VBM is observed of about 0.44V. Among the presented materials of the solid solution $Ba_{1-x}Sr_xTi_{1-x}Fe_xO_{3-\delta}$ ($0 \leq x \leq 1$), the most affected materials are the compositions between $0.4 \leq x \leq 0.6$. While the composition x=0.8 and x=0.2 show promising characteristic for water splitting and photocatalysts.

Table-IV.P3.2. The calculated values of the absolute electronegativity, the band gap Eg, and the CB and VB potentials for the perovskites series $Ba_{1-x}Sr_xTi_{1-x}Fe_xO_{3-\delta}$ ($0 \leq x \leq 1$).

Composition	χ	E_g	E_{CB}	E_{VB}
0	5.244607848	3.18	-0.84539	2.334608
0.2	5.291770654	---	---	---
0.4	5.339357577	1.38	0.149358	1.529358
0.6	5.387372431	1.61	0.082372	1.692372
0.8	5.435819065	2.33	-0.22918	2.100819
1	5.484701362	2.46	-0.2453	2.214701

IV.4.5. Conclusion

The UV-vis results revealed the enhancement of the visible light absorption of the designed composition. The compositions with tetragonal structure showed a shift of the $BaTiO_3$

absorption band and an expansion equal to ~ 314 nm, where the compositions with cubic structure showed similarities to the absorption spectra of $SrFeO_{2.5}$.

A shrink of the optical band gap up to 0.95 eV was induced. Independency of the band gap evolution with regards to the variation of the volume and the bond angles is observed in this case of study. The variation of the band gap showed two different behaviors depending on the symmetry, a decrease of the band gap is observed for the tetragonal structure, and at the transition point an increasing behavior of the band gap is noticed. However, the evolution of the band gap was linked to the variation of the interatomic distances <Ba/Sr-O> and <Ti/Fe-O>. A decrease of the band gap values is observed for larger interatomic distances, above the transition point a continual decrease of this distances is followed by the increasing of the band gap.

The CBM and VBM were calculated and the shift of both bands was observed. These results were related to the creation of new energy levels by the substation at A-site and B-site, to count as well the contribution of the oxygen vacancies. For the tetragonal compositions, the results indicate that both the photo-reduction and photo-oxidation capacities have greatly been improved since the position of the VBM and CBM have an ideal level for the overall water splitting reaction and the material is expected to be active with a strong visible light absorption. Moreover, the compositions between $0.4 \leq x \leq 0.6$, present deep conduction band and are located at potential under the reduction potential of H^+ to H^2. The VB maximums are at suitable positions and are located at potential more positive than the oxidation potential of H_2O to O_2. For the composition x=0.8, the CBM shift downward and lies at the reduction potential position, while upward shift of the VBM is observed of about 0.44V.

IV.5. Chapter conclusion

The optical absorption in the UV-visible light of the three solid solutions labeled as BLTF, SLTF and BSTF was tested. The effect of the composition on the absorption and the evolution of the optical band gap are investigated. The results show that all the prepared samples show a red shift of the absorption band with good absorption performances under the UV and the visible light. This enhancement of the absorption is due to the shrink observed of the band gap as function of the composition.

The dependency of optical properties to the structural parameters is established. The different structural parameters used to understand the dependency of the opening of the band gap are the volume, the bond angles Ti/Fe-O_1-Ti/Fe and Ti/Fe-O_2-Ti/Fe, and the interatomic distances B-O and A-O. From the three cases, the band gap behavior in regards with the volume changed from a case to another, meaning that the volume does not constitute a critical parameter for the opening mechanism of the band gap. Knowing that the band gap in perovskites is mainly formed by the 2p (O2) and 3d level of transition metals at the B-site, we studied the dependency of the band gap variation to the bond angles Ti/Fe-O_1-Ti/Fe and Ti/Fe-O_2-Ti/Fe. The behavior of the band gap took different trends depending on the case, and no specific behavior was observed. However, the band gap evolution showed that the interatomic distance affect more the values of the band gap, larger values of <Ba/Sr-O> and <Ti/Fe-O> reflects lower values of the band gap. This was observed for the case of BSTF and SLTF solid solutions, for the solid solution BLTF, lower values of the optical band gap were only observed for large <Ti/Fe-O> distances.

The effect of the composition on the band gap is reflected by an upward shift of the valence band maximum VBM and the downward conduction band minimum CBM affecting the performance of the materials. These improvements of the optical properties are mainly due to the new energy level created by the substituting elements.

IV.6. References

1. Gagrani A, Sousa S, Monteiro OC, Tsuzuki T (2020) Solid state synthesis and photocatalytic activity of bio-inspired calcium manganese oxide catalysts. J Solid State Chem 288:121390. https://doi.org/10.1016/j.jssc.2020.121390

2. Feng Y, Wang N, Guo X, Zhang S (2020) Reaction mechanism of Ca2Fe2O5 oxygen carrier with CO in chemical looping hydrogen production. Appl Surf Sci 534:147583. https://doi.org/10.1016/j.apsusc.2020.147583

3. Watanabe M (2017) Dye-sensitized photocatalyst for effective water splitting catalyst. Sci. Technol. Adv. Mater. 18:705–723

4. Wang J, Yin S, Komatsu M, Sato T (2005) Lanthanum and nitrogen co-doped SrTiO3 powders as visible light sensitive photocatalyst. J Eur Ceram Soc 25:3207–3212. https://doi.org/10.1016/j.jeurceramsoc.2004.07.027

5. El Hachmi A, El Bachraoui F, Louihi S, et al (2020) Structural, Magnetic and Optical Properties Study of Tellurium-Based Perovskites: Sr3−xPbxFe2TeO9 ($0 \leq x \leq 2.25$). J Inorg Organomet Polym Mater 30:1990–2006. https://doi.org/10.1007/s10904-020-01446-4

6. Shin SS, Lee SJ, Seok SI (2019) Exploring wide bandgap metal oxides for perovskite solar cells. APL Mater 7:22401. https://doi.org/10.1063/1.5055607

7. Hu Z, Lin Z, Su J, et al (2019) A Review on Energy Band-Gap Engineering for Perovskite Photovoltaics. Sol RRL 3:1900304. https://doi.org/10.1002/solr.201900304

8. Chen L, Zheng G, Yao G, et al (2020) Lead-Free Perovskite Narrow-Bandgap Oxide Semiconductors of Rare-Earth Manganates. ACS Omega 5:8766–8776. https://doi.org/10.1021/acsomega.0c00138

9. Varignon J, Bibes M, Zunger A (2019) Origin of band gaps in 3d perovskite oxides. Nat Commun 10:1658. https://doi.org/10.1038/s41467-019-09698-6

10. Hu C-C, Tsai C-C, Teng H (2009) Structure Characterization and Tuning of Perovskite-Like $NaTaO_3$ for Applications in Photoluminescence and Photocatalysis. J Am Ceram Soc 92:460–466. https://doi.org/10.1111/j.1551-2916.2008.02869.x

11. Nowak M, Kauch B, Szperlich P (2009) Determination of energy band gap of nanocrystalline SbSI using diffuse reflectance spectroscopy. Rev Sci Instrum 80:4–7. https://doi.org/10.1063/1.3103603

12. Manzoor S, Husain S (2018) Analysis of Zn substitution on structure, optical absorption, magnetization, and high temperature specific heat anomaly of the nano-crystalline $LaFeO_3$. J Appl Phys 124:065110. https://doi.org/10.1063/1.5025252

13. Xiao P, Zhu J, Zhao D, et al (2019) Porous $LaFeO_3$ Prepared by an in Situ Carbon Templating Method for Catalytic Transfer Hydrogenation Reactions. ACS Appl Mater Interfaces 11:15517–15527. https://doi.org/10.1021/acsami.9b00506

14. Parida KM, Reddy KH, Martha S, et al (2010) Fabrication of nanocrystalline LaFeO3: An efficient sol–gel auto-combustion assisted visible light responsive photocatalyst for water decomposition. Int J Hydrogen Energy 35:12161–12168. https://doi.org/10.1016/J.IJHYDENE.2010.08.029

15. Tandon SP, Gupta JP (1970) Diffuse Reflectance Spectrum of Ferric Oxide. Spectrosc Lett 3:297–301. https://doi.org/10.1080/00387017008078624

16. Maity R, Sheikh MS, Dutta A, Sinha TP (2019) Visible Light Driven Photocatalytic Activity of Granular Pr Doped LaFeO3. J Electron Mater 48:4856–4865. https://doi.org/10.1007/s11664-019-07285-5

17. Xie P, Yang F, Li R, et al (2019) Improving hydrogen evolution activity of perovskite BaTiO3 with Mo doping: Experiments and first-principles analysis. Int J Hydrogen Energy 44:11695–11704. https://doi.org/10.1016/J.IJHYDENE.2019.03.145

18. Rai A, Thakur AK (2017) Effect of co-substitution on structural, optical, dielectric and magnetic behavior of LaFeO3. J Alloys Compd 695:3579–3588. https://doi.org/10.1016/J.JALLCOM.2016.11.407

19. Xiao Z, Zhou Y, Hosono H, et al (2018) Bandgap Optimization of Perovskite Semiconductors for Photovoltaic

Applications. Chem - A Eur J 24:2305–2316. https://doi.org/10.1002/chem.201705031

20. Ma S, Zhang Z, Harrison I (2018) Photoreduction of Hydrogen Cations on TiO2 and Its Impact on Surface Band Bending and the Charge Carrier Recombination Rate: A Photoluminescence Study under High Vacuum Conditions. J Phys Chem C 122:8288–8294. https://doi.org/10.1021/acs.jpcc.7b12624

21. Peerakiatkhajohn P, Butburee T, Yun JH, et al (2015) A hybrid photoelectrode with plasmonic Au@TiO2 nanoparticles for enhanced photoelectrochemical water splitting. J Mater Chem A 3:20127–20133. https://doi.org/10.1039/c5ta04137f

22. Kim J, Seo S, Lee J, et al (2021) Efficient and Stable Perovskite-Based Photocathode for Photoelectrochemical Hydrogen Production. Adv Funct Mater 2008277. https://doi.org/10.1002/adfm.202008277

23. Fu M, Xu H, Li X (2020) Mechanism of oxygen vacancy assisted water-splitting of LaMnO3: Inorganic perovskite prediction for fast solar thermochemical H2production. Inorg Chem Front 7:2381–2387. https://doi.org/10.1039/d0qi00338g

24. Chen HC, Huang CW, Wu JCS, Lin ST (2012) Theoretical investigation of the metal-doped SrTiO 3 photocatalysts for water splitting. J Phys Chem C 116:7897–7903. https://doi.org/10.1021/jp300910e

25. Kato K, Jiang J, Sakata Y, Yamakata A (2019) Effect of Na-Doping on Electron Decay Kinetics in SrTiO $_3$ Photocatalyst. ChemCatChem 11:6349–6354. https://doi.org/10.1002/cctc.201901669

26. Grinberg I, West DV, Torres M, et al (2013) Perovskite oxides for visible-light-absorbing ferroelectric and photovoltaic materials. Nature 503:509–512. https://doi.org/10.1038/nature12622

27. Li H, Yin S, Wang Y, et al (2013) Roles of Cr3+ doping and oxygen vacancies in SrTiO3 photocatalysts with high visible light activity for NO removal. J Catal 297:65–69. https://doi.org/10.1016/j.jcat.2012.09.019

28. Li W, Jiang K, Li Z, et al (2018) Origin of Improved Photoelectrochemical Water Splitting in Mixed Perovskite Oxides. Adv Energy Mater 8:1801972. https://doi.org/10.1002/aenm.201801972

29. Sedeek K, Said SA, Amer TZ, et al (2019) Band gap tuning in nanocrystalline SrTi0.9Fe0.1O2.968 perovskite type for photocatalytic and photovoltaic applications. Ceram Int 45:1202–1207. https://doi.org/10.1016/j.ceramint.2018.09.305

30. Sasikala C, Durairaj N, Baskaran I, et al (2017) Transition metal titanium (Ti) doped LaFeO3nanoparticles for enhanced optical structural and magnetic properties. J Alloys Compd 712:870–877. https://doi.org/10.1016/j.jallcom.2017.04.133

31. Smolin SY, Scafetta MD, Choquette AK, et al (2016) Static and Dynamic Optical Properties of La1-xSrxFeO3-δ: The Effects of A-Site and Oxygen Stoichiometry. Chem Mater 28:97–105. https://doi.org/10.1021/acs.chemmater.5b03273

32. Abdi M, Mahdikhah V, Sheibani S (2020) Visible light photocatalytic performance of La-Fe co-doped SrTiO3 perovskite powder. Opt Mater (Amst) 102:109803. https://doi.org/10.1016/j.optmat.2020.109803

33. Sun X, Wu Y, Wang Y, Li M (2019) Investigation of the effect of lanthanum oxide on the thermal stability of alumina aerogel. J Porous Mater 26:327–333. https://doi.org/10.1007/s10934-018-0599-y

34. Zhao Z, Liu Q (2008) Effects of lanthanide doping on electronic structures and optical properties of anatase TiO2 from density functional theory calculations. J Phys D Appl Phys 41:085417. https://doi.org/10.1088/0022-3727/41/8/085417

35. Faye J, Baylet A, Trentesaux M, et al (2012) Influence of lanthanum stoichiometry in La 1-xFeO 3-δ perovskites on their structure and catalytic performance in CH 4 total oxidation. Appl Catal B Environ 126:134–143. https://doi.org/10.1016/j.apcatb.2012.07.001

36. Zhu H, Zhang P, Dai S (2015) Recent Advances of Lanthanum-Based Perovskite Oxides for Catalysis. ACS Catal. 5:6370–6385

37. Perry NH, Kim N, Ertekin E, Tuller HL (2019) Origins and Control of Optical Absorption in a Nondilute Oxide Solid Solution: Sr(Ti,Fe)O 3- x Perovskite Case Study. Chem Mater 31:1030–1041. https://doi.org/10.1021/acs.chemmater.8b04580

38. Wang YQ, Liu Y, Zhang MX, Min FF (2018) Electronic, magnetic and optical properties of charge-compensated (Nb, TM = Fe, Cr)-codoped SrTiO3 from first principles. Ferroelectrics 537:68–78. https://doi.org/10.1080/00150193.2018.1528958

39. Jia T, Zeng Z, Lin HQ, et al (2017) First-principles study on the electronic, optical and thermodynamic properties of ABO3 (A = La,Sr, B = Fe,Co) perovskites. RSC Adv 7:38798–38804. https://doi.org/10.1039/c7ra06542f

40. Nowak M, Kauch B, Szperlich P (2009) Determination of energy band gap of nanocrystalline SbSI using diffuse reflectance spectroscopy. Rev Sci Instrum 80:046107. https://doi.org/10.1063/1.3103603

41. Samantaray CB, Sim H, Hwang H (2005) The electronic structures and optical properties of BaTiO3 and SrTiO3 using first-principles calculations. Microelectronics J 36:725–728. https://doi.org/10.1016/j.mejo.2005.03.001

42. Wang YQ, Liu Y, Zhang MX, Min FF (2017) Electronic Structure and Visible-Light Absorption of Transition Metals (TM=Cr, Mn, Fe, Co) and Zn-Codoped SrTiO3: A First-Principles Study. Chinese Phys Lett 35:017101. https://doi.org/10.1088/0256-307X/35/1/017101

43. Zhang C, Jiang N, Xu S, et al (2017) Towards high visible light photocatalytic activity in rare earth and N co-doped SrTiO3: a first principles evaluation and prediction. RSC Adv 7:16282–16289. https://doi.org/10.1039/c6ra27840j

44. Berger RF, Fennie CJ, Neaton JB (2011) Band gap and edge engineering via ferroic distortion and anisotropic strain: The case of SrTiO3. Phys Rev Lett 107:146804. https://doi.org/10.1103/PhysRevLett.107.146804

45. Hu C-C, Tsai C-C, Teng H (2009) Structure Characterization and Tuning of Perovskite-Like NaTaO 3 for Applications in Photoluminescence and Photocatalysis. J Am Ceram Soc 92:460–466. https://doi.org/10.1111/j.1551-2916.2008.02869.x

46. Robertson J (2003) Energy levels of point defects in SrTiO3 and related oxides. J Appl Phys 93:1054–1059. https://doi.org/10.1063/1.1525045

47. Xian T, Yang H, Di L, et al (2014) Photocatalytic reduction synthesis of SrTiO3-graphene nanocomposites and their enhanced photocatalytic activity. Nanoscale Res Lett 9:1–9. https://doi.org/10.1186/1556-276X-9-327

48. Malati MA, Wong WK (1984) Doping TiO2 for solar energy applications. Surf. Technol. 22:305–322

49. Peng S, Li Y, Jiang F, et al (2004) Effect of Be2+ doping TiO2 on its photocatalytic activity. Chem Phys Lett 398:235–239. https://doi.org/10.1016/j.cplett.2004.09.061

50. Yukito T, Satoru S (2013) On the Absorption Spectra of Complex Ions II. https://doi.org/101143/JPSJ9766 9:766–779. https://doi.org/10.1143/JPSJ.9.766

51. Galakhov VR, Kurmaev EZ, Kuepper K, et al (2010) Valence band structure and X-ray spectra of oxygen-deficient ferrites SrFeOx. J Phys Chem C 114:5154–5159. https://doi.org/10.1021/jp909091s

52. Boruah PJ, Khanikar RR, Bailung H (2020) Synthesis and Characterization of Oxygen Vacancy Induced Narrow Bandgap Tungsten Oxide (WO3−x) Nanoparticles by Plasma Discharge in Liquid and Its Photocatalytic Activity. Plasma Chem Plasma Process 40:1019–1036. https://doi.org/10.1007/s11090-020-10073-3

Chapter -V

Dielectric and electric studies at room and high temperature as function of the frequency of the solid solution system $A_{(1-x)}A'_xTi_{(1-x)}Fe_xO_{3-\delta}$ *for (A = Ba, La and Sr) with* $0 \leq x \leq 1$ & $\delta \geq 0$

V.1. Introduction

The majority of perovskite oxide materials are known as dielectric materials, this chapter shows to which extent the composition enhances or suppress this property. We study in this chapter the dielectric and electric properties of the three solid solutions BLTF, SLTF, and BSTF. The study is conducted under room and high temperature (290 – 390°C) at high, medium and low frequency (10Hz – 1MHz).

The dielectric properties in general depend strongly on the morphology of the material and on the composition. However, in this work, the objective is to study the effect of the composition, frequency, symmetry and temperature on the active region of the materials that participate in the transport mechanisms of charge carrier.

Part I – Chapter V presents the Impedance spectroscopy results: the dielectric and electrical properties of $Ba_{1-x}La_xTi_{1-x}Fe_xO_3$ perovskite system with the substitution amount varies between $0 \leq x \leq 1$. The dielectric properties namely, the relative dielectric constant and the tangent loss are presented at various frequencies under the effect of temperature ($\varepsilon(\omega)/\varepsilon''(\omega)$ *vs* T (°C)). The Nyquist plots known as Cole-Cole plots are systematically studied as function of the composition and temperature; the results reveals the active region such as the grain and the grain boundaries that participates in the conductivity as it also defines most resistive part of the material. The Nyquist plots are fitted to equivalent circuits combined of a resistance and impedance (RC or two RC connected in series), the shape of the plots gives insight on the homogeneity of the materials.

Part II – Chapter V presents the Impedance spectroscopy results: the dielectric and electrical properties of $Sr_{1-x}La_xTi_{1-x}Fe_xO_3$ perovskite system with the substitution amount varies between $0 \leq x \leq 1$. The dielectric properties namely, the relative dielectric constant and the tangent loss are presented at various frequencies under the effect of temperature ($\varepsilon(\omega)/\varepsilon''(\omega)$ *vs* T (°C)). The Nyquist plots known as Cole-Cole plots are systematically studied as function of the composition and temperature, the results reveals the active region as the grain and the grain boundaries that participates in the conductivity as it also defines most resistive part of the material. The Nyquist plots are fitted to equivalent circuits combined of a resistance and

impedance (RC or two RC connected in series), the shape the plots gives insight on the homogeneity of the materials.

Part III – Chapter V presents the Impedance spectroscopy results: the dielectric and electrical properties of $Ba_{1-x}Sr_xTi_{1-x}Fe_xO_{3-\delta}$ perovskite system with the substitution amount varies between $0 \leq x \leq 1$. The dielectric properties namely, the relative dielectric constant and the tangent loss are presented at various frequencies under the effect of temperature ($\varepsilon(\omega)/\varepsilon''(\omega)$ *vs* T (°C)). Additionally, the effect of the oxygen vacancies on the various studied parameters is emphasized. The Nyquist plots known as Cole-Cole plots are systematically studied as function of the composition and temperature, the results reveals the active region as the grain and the grain boundaries that participates in the conductivity as it also defines most resistive part of the material. The Nyquist plots are fitted to equivalent circuits combined of a resistance and impedance (RC or two RC connected in series), the shape the plots gives insight on the homogeneity of the materials.

V.2. Part I: The study of the dielectric and electric properties of the perovskite series $Ba_{1-x}La_xTi_{1-x}Fe_xO_3$ with $0 \leq x \leq 1$ at room and high temperature in a wide range of frequency

V.2.1. Introduction

The dielectric features of perovskites are due to the electric force originated from the attraction and the repulsion of electric charges [1]. Barium Titanate is a ferroelectric material bellow curie temperature (120 – 130 °C), and electric insulator at room temperature [2]. The dielectric and ferroelectric properties are related to the crystalline structure *i.e.* the size of particles. Z. Zhao et al. [2], studied the variation of the dielectric constant as function of the grain size, the group reported a shift of the temperature of transition from 120°C to around 100° as the particle size decreases from 1200 nm to 300 nm, they also observed that the peak of transition broaden with the decrease of the particle size. Additionally, a decrease of the ε_{max} is observed from 5000 at 1200 nm to 1000 for 50 nm where no phase transition was reported [2]. Another factor that influences the dielectric permittivity of $BaTiO_3$, and it is the insertion of foreign element that can reduces the resistivity of the material and lead to semiconducting features. *Masum B. et al*. [3] reported the effect of the composition on the electrical properties of Barium Titanate doped Lanthanum. The effect of the composition results in a shift of the transition temperature T_c to lower temperatures and a broadening of the transition peak as La^{3+} content increases. Similar behavior is reported by Z. Zhao et al. [2], a value as high as 12700 of the dielectric constant is obtained for grain size range between 0.85 – 1.3 μm unlike the samples with 0.3 and 0.6 mole % which show lower dielectric constant with grain size ranging between 0.75 and 1.2 μm [3]. M.M Vijatovic Petrovic et al. [4] studied the same series of lanthanum doped Barium Titanate with the same doping content of 0.3 and 0.5 mole%, the series however, was prepared using the modified Pechini process. The results confirm that lanthanum reduces the grain size from 2.5 μm for BT to 0.8 and 0.3 μm; the origin of the transition temperature found in various studies is reported to be due to the effect of lanthanum on the grain size, since T_c is connected with the grain size [4]. Co-doping of $BaTiO_3$ by La^{3+} and Ti^{4+} was reported by H.chaabane et al. [5] and Sushrisangita et al. [6], for different concentrations. H.chaabane et al. [5] results shows that all the samples with the substitution amount ranging from 0 to 0.15, show high dielectric constant of 7000 at 1kHz and a shift to lower temperature of the transition

temperature T_c is observed; moreover, the material's ferroelectricity was observed of classical type and at 0.1 of the substitution amount Relaxor ferroelectric features start to appear [5]. For larger amount of substitution $0 \leq x \leq 0.5$, Sushrisangita et al. [6] reported lower dielectric values in comparison with H.chaabane et al.; the highest dielectric constant was obtained for 0.3 at 1kKz equal to 6000, and the lowest dielectric values was shown for x=0.2 with 600 at 1 kHz. Additionally a shift to lower temperatures for the transitions related with $BaTiO_3$ is observed; Sushrisangita et al. [6] also reported the multiple phase transitions associated with the magnetic transitions of $LaFeO_3$ at 190°C, 270°C and 350°C. The transition related to Maxwell-wagner at the grain boundary is also reported by Y. Qiu et al. [7]; the highest dielectric constant of about 6×10^6 is observed for particles size of 150 nm and a decrease with the decrease of the particles size and as function of frequency. It is found that the resistance of the grain boundaries is much larger than that of the grains which makes $LaFeO_3$ a boundary-layer capacitor with conducting grains and resistive grain boundaries.

In this part, the BLTF solid solution was prepared by solid state reaction in wider amount of substitution between $0 \leq x \leq 1$. The aim is to complete the reported studies of BLTF perovskites series, and give in-depth studies on the effect of the substitution on the morphology which affect strongly the dielectric and electric properties of the materials. Additionally we aim to understand the effect of the composition on the activation of the grain and grain boundaries and their contribution to the conductivity, as we aim to confirm the observed transition of $LaFeO_3$ in the solid solution.

V.2.2. Frequency and temperature dependent of the relative permittivity & tangent loss

The solid solution labeled as BLTF is prepared to meet the requirement of semiconductors, thus investigating the persistence of dielectric feature is conducted. The dielectric measurements were conducted for the compositions x = 0.25, 0.3, 0.5, 0.6, 0.8 and 0.9. To illustrate the effect of the composition and the structure on the dielectric properties, the choice of the compositions was based on the symmetry.

$BaTiO_3$ is known to show high dielectric constant, The anomalies observed in general in the temperature dependent of the dielectric permittivity of $BaTiO_3$ have been reported at 20°C and 120°C corresponding respectively to the structural phase transitions: orthorhombic to

tetragonal and tetragonal to cubic symmetry [6]. Besides and according to literature, in the orthoferrite $AFeO_3$ (A = La, Sm, Gd, etc.), the exchange interaction between $Fe^{3+} \leftrightarrow Fe^{3+}$ is dominant in the temperature range between 150 – 250°C, thus Gaussian peak appears [6–10]. $LaFeO_3$ is reported as multiferroic materials with a curie temperature detected at around 200°C [11].

Fig-V.P1. (1, 2, and 3) display the relative dielectric constant ε_r and the dielectric loss tan(δ) as function of the temperature at various frequencies for the compositions x = 0.25, 0.3, 0.5, 0.6, 0.8 and 0.9. A decrease of the dielectric constant with increasing the frequency is observed for all the compositions, this behavior is common for dielectric materials due to the various polarization mechanisms. Different responses of the relative dielectric constant as function of the composition and temperature are observed. The composition x = 0.25 shows a peak at around 250°C then an increase of the relative dielectric constant as function of temperature is observed above 350°C **(Fig-V.P1.1a)**. The composition x = 0.3 shows a peak at 110°C after which an increase of the relative dielectric constant increases with temperature starting 250°C **(Fig-V.P1.2a)**. The compositions x = 0.25 and x = 0.3 adopt the tetragonal structure with *P*4/*mmm* and Cubic with *Pm*-3*m* respectively, thus, the peaks observed at 110°C for x = 0.3 is not related to the transition tetragonal ferroelectric phase to cubic paraelectric. The compositions with Fe^{3+} exceeding the quantity of Ti^{4+} in the B-sites, (i.e., x = 0.5, 0.6, 0.8 and 0.9) tend to show large anomalies at around 160°C, 190°C, 189°C and 150°C. The increasing behavior of the dielectric constant at high temperature is also observed. The compositions crystallizes under the cubic and orthorhombic system for x = 0.5, 0.6 and x = 0.8, 09 respectively. Due the increased amount of Fe^{3+} in the B-sites, the peaks observed are assigned to the exchange interaction between $Fe^{3+} \leftrightarrow Fe^{3+}$ as reported by Sushrisangita et al. [6]. Sushrisangita et al. [6] have reported that the polarization mechanism for the compositions x=0.0 to 0.3 is due to only bulk/grain. However, for the compositions x=0.4 and 0.5, the associated mechanism for the observed peak at around 190°C is that of Mawxell-Wagner. Similar results were found for $GdFeO_3$ and $SmFeO_3$ at 145 and 180°C. **Fig-V.P1.2** shows the dielectric constant at high frequencies for the compositions x=0.3, 0.5 and 0.6. The peak observed at around 150-190°C at low frequencies tend to fade with increasing the frequency, thus as in the reported case, the mechanism responsible is Maxwell-Wagner since it is only effective at low frequencies <10 kHz.

The mechanisms of polarization within the material under the effect of the applied field involve some dielectric loss tan(δ) as shown in **Fig-V.P1. (1, 2, and 3).** The dielectric loss accompanies the time varying field and the variation of the relative dielectric loss, thus at higher frequencies the materials tend to show low dielectric loss due to some inactive polarization mechanisms. The dielectric loss and the dielectric constant show an increase at high temperature. In term of composition we can observe that the highest dielectric value was observed for the composition x = 0.6 equal to 8000 at (10 Hz; 200°C) and it decreases with frequency; on the other hand the dielectric loss increases as function of the composition to reach values between 60 and 100 for the compositions x = 0.8 and 0.9.

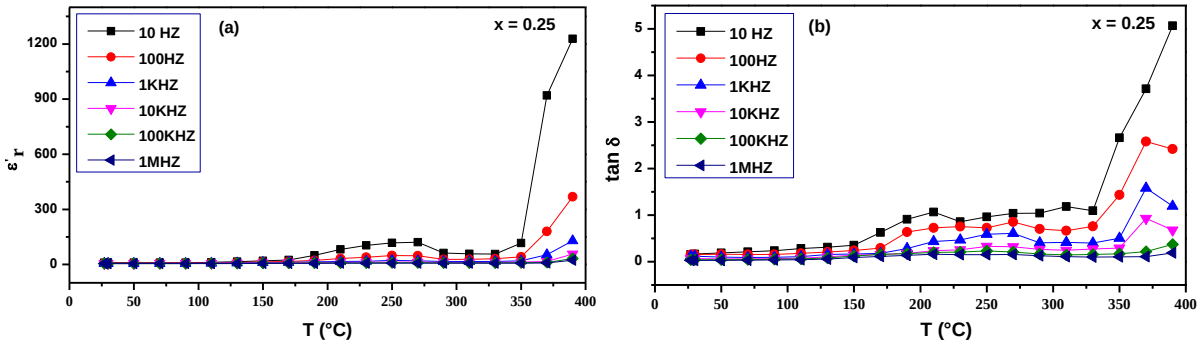

Fig-V.P1.1: Thermal variation of dielectric permittivity **(a)**, and dielectric losses **(b)** for $Ba_{1-x}La_xTi_{1-x}Fe_xO_3$ (x = 0.2; Tetragonal SG *P4/mmm*) at high, medium and low frequency (1Hz – 1MHz).

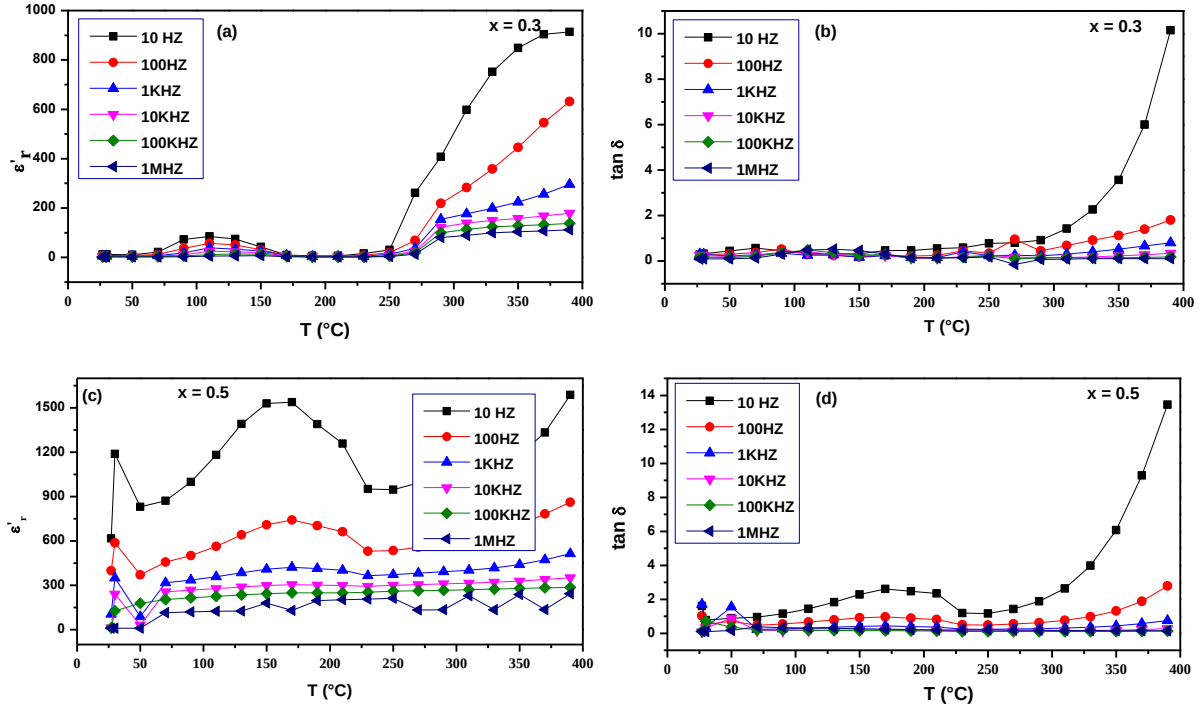

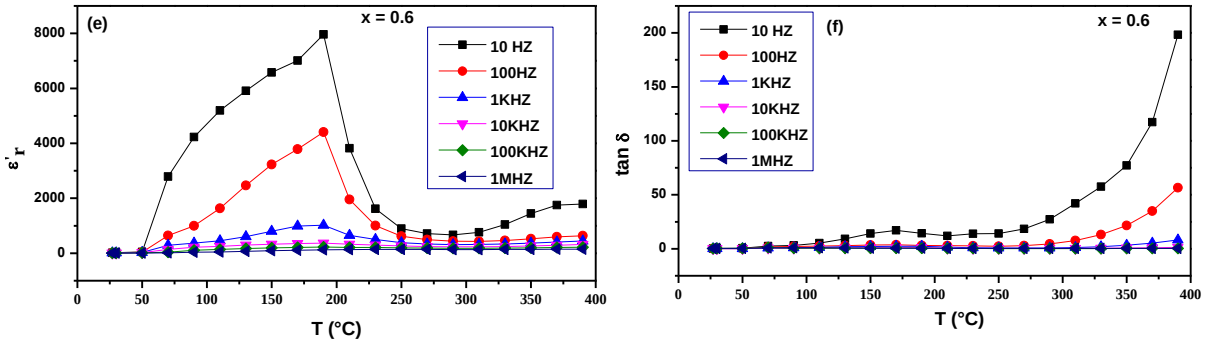

Fig-V.P1.2: Thermal variation of dielectric permittivity and dielectric losses for $Ba_{1-x}La_xTi_{1-x}Fe_xO_3$ (x = 0.3, 0.5 and 0.6; Cubic SG *Pm*-3*m*) at high, medium and low frequency (1Hz – 1MHz).

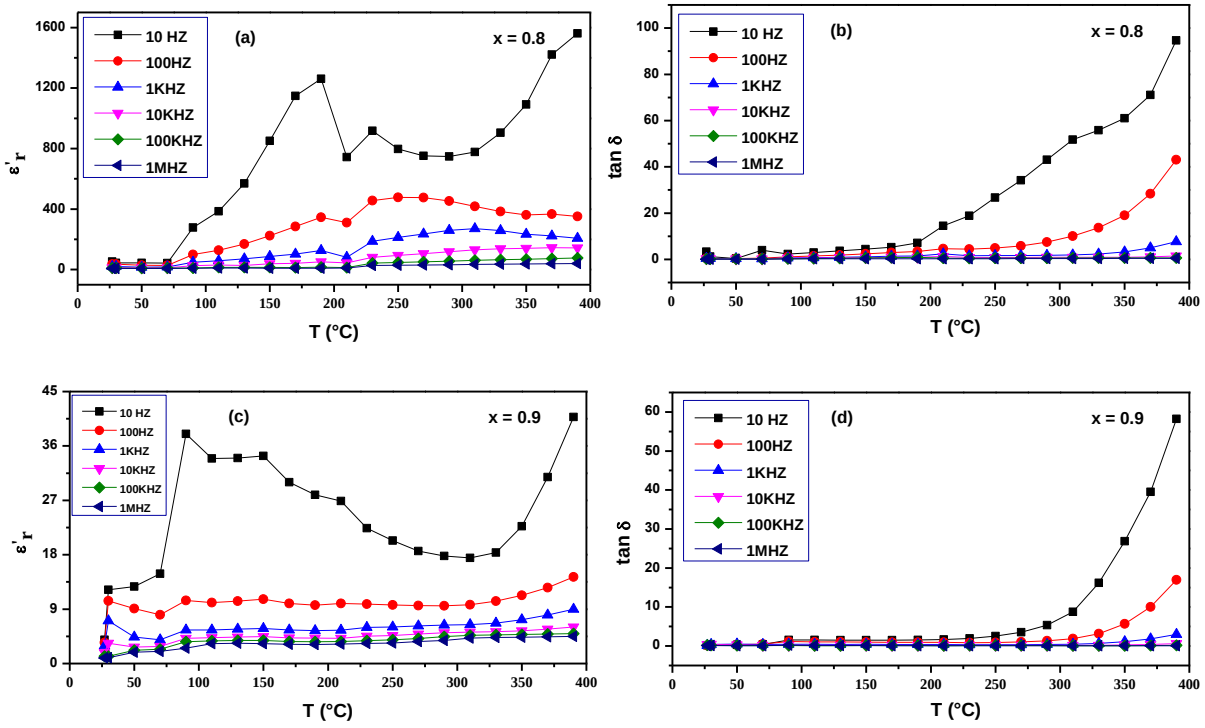

Fig-V.P1.3: Thermal variation of dielectric permittivity and dielectric losses for $Ba_{1-x}La_xTi_{1-x}Fe_xO_3$ (x = 0.8 and 0.9; Orthorhombic SG *Pnma/Pbnm*) at high, medium and low frequency (1Hz – 1MHz).

V.2.3. Analysis of Nyquist plots: Conductivity at room and high temperature

V.2.3.1. Fitting of Nyquist plots and determination of equivalent circuit

The impedance spectroscopy provides information about the electrical properties of the materials, and gives handful insights on the dependency of the transport properties of the charge carriers on the microstructural properties. **Fig-V.P1.4** shows the Cole-Cole or the Nyquist plots of the compositions x = 0.25, 0.3, 0.5, 0.6, 0.8, and 0.9 at room temperature. The effect of the

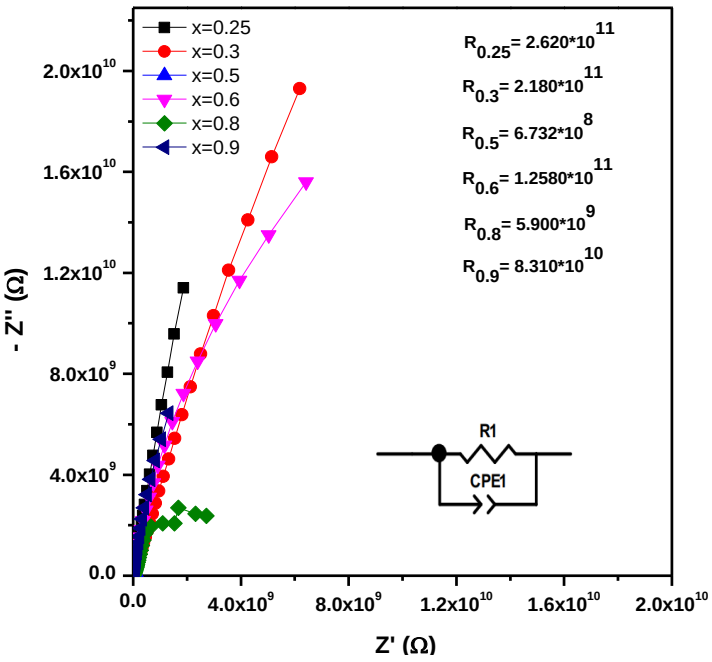

Fig-V.P1.4: Nyquist/Cole-Cole plots recorded at Room Temperature for $Ba_{1-x}La_xTi_{1-x}Fe_xO_3$ (x = 0.25, 0.3, 0.5, 0.6, 0.8, and 0.9) and the suitable equivalent circuit model.

composition on the electrical properties is clear as the material's resistance decreases; however, in low, medium, and high frequency and according to the incomplete semi-circles observed, the region active is that of the grains. The equivalent circuit found using Zview consists of a parallel RC circuit and which describes the bulk active region at room temperature. The compositions x=0.25, 0.3, and 0.6 shows a grain resistance in the order of 2.620 10^{11}, 2.180*10^{11}, and 1.258 10^{11} Ω, whereas the compositions x= 0.5, 0.8, 0.9 show lower resistance in the order of 6.732 10^8, 5.900 10^9, 8.310 10^{10} Ω. The single incomplete semicircle shows that the conductivity of these materials is very low at room temperature, and the contribution of the grains is low whereas the grain boundary does not participate in the transport mechanisms of charge carrier.

The **Fig-V.P1.5** presents the Nyquist plots of the compositions x = 0.25 and x = 0.3 at high temperatures, the experimental data shows an incomplete semicircles up to 350°C indicating the sole contribution of the grain, however a decrease in the resistance of the material is observed and presented in **Table-V.P1.1**; under the effect of the temperature the resistance of the grain region decreases from 3.980 x 10^9 at 290°C up to 9.009 x 10^6 Ω for the composition x=0.25, the same observation for the composition x=0.3, there is a decrease of the resistance under the effect of the temperature from 1.128 x 10^9 to 9.932 x 10^6 Ω. The single semicircle shows that the contribution of the grains is low whereas the grain boundary the grain boundaries are short circuited and thus the second semicircle doesn't appear due to the blocked ions in the grains which shows in the complex impedance the contribution of the grains only. However, above 370°C the samples under the effect of temperature are active in two regions, the grain and the grain boundaries and the grain boundaries resistance. The experimental results were fitted using

the circuit RC-RQC connected in series representing the active region of the grain corresponding to RC and the grain boundaries with RQC. The experimental results and the fitting model are presented in inset of **Fig-V.P1.5**, the results shows the resistance of the grain boundaries is in the order of 10^7 Ω which is higher than that of the grain as deduced from the higher radius of the semicircles presenting the grain boundaries.

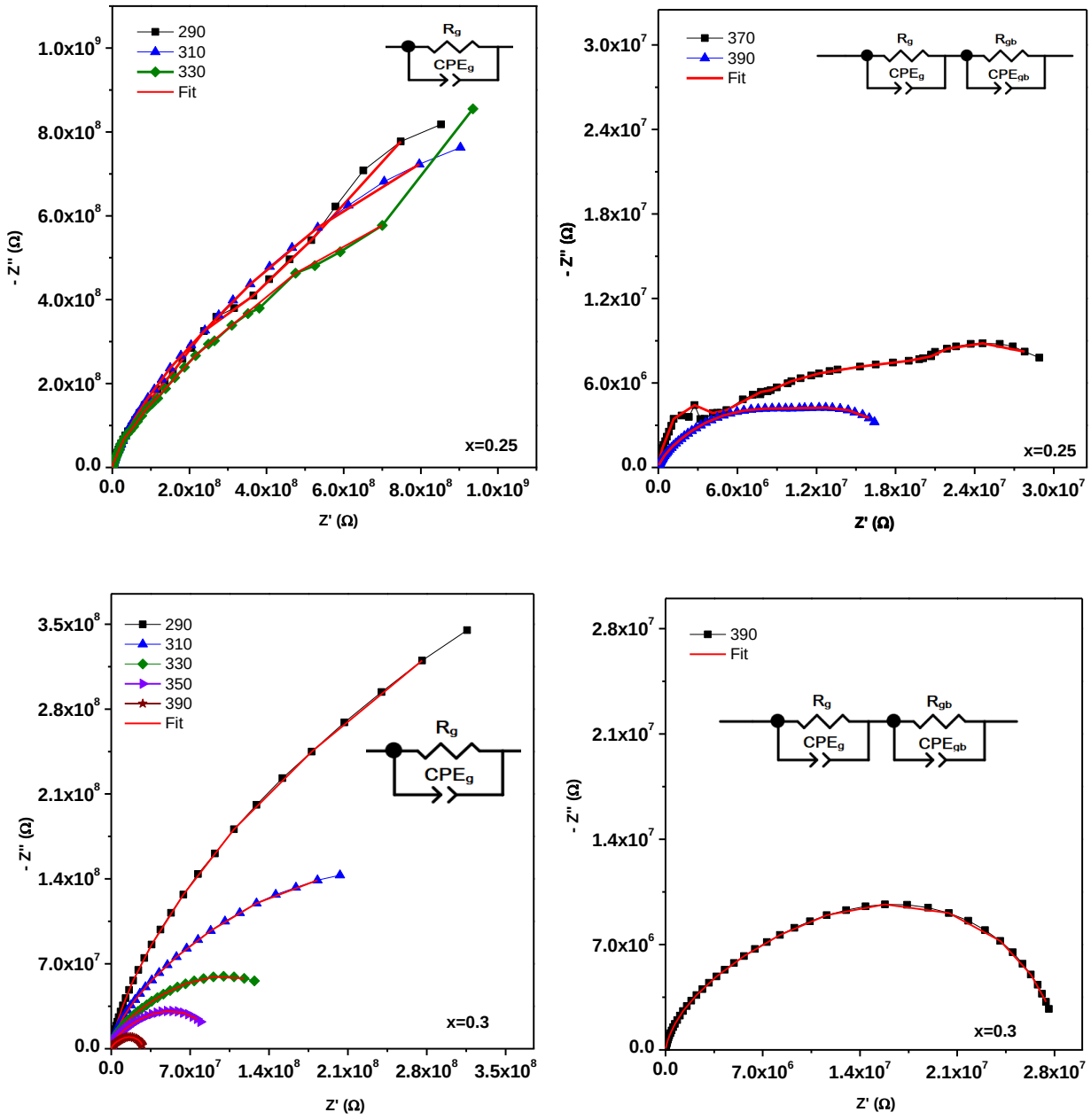

Fig-V.P1.5: Nyquist/Cole-Cole plots recorded at High Temperature for $Ba_{1-x}La_xTi_{1-x}Fe_xO_3$ (x = 0.25, and 0.3) and the suitable equivalent circuit model.

The Nyquist plots are shown in high temperatures from 290°C to 390°C in a wide range of frequency. For the compositions x = 0.5, 0.6, 0.8, and 0.9, the complex impedance fitting models matched two semicircles representing the contribution of grains and grain boundaries. The values of the grain and grain boundaries resistance in these samples are of the same amplitude however different behaviors are seen from the fitting results. For example the composition x = 0.5 the resistance of the two region increases from the order of 10^6 to 10^7 Ω for temperature between 310 and 350°C and then decreases, additionally the grain resistance seem to be slightly higher than the grain boundaries resistance. For the composition x = 0.6 the resistances of the two regions are of the same magnitude and decreases with temperature up to 4.7 x 10^5 Ω. The complex impedance results of composition x = 0.8 shows that the grain boundaries resistance becomes higher; however R_g and R_{gb} are of same magnitude giving one semicircle arc. At the composition x = 0.9 we observe an increase of the resistance up to 4.8 x 10^8 Ω at 290°C and decreases with temperature, the results are summarized in **Table-V.P1.1**. The varieties of behaviors are related to the morphology of the samples. The depressed semicircles obtained demonstrate the inhomogeneity of the samples, the same magnitude of resistances obtained shows that the grain and the grain boundary equally contribute to the transport mechanism of charge carrier in the samples.

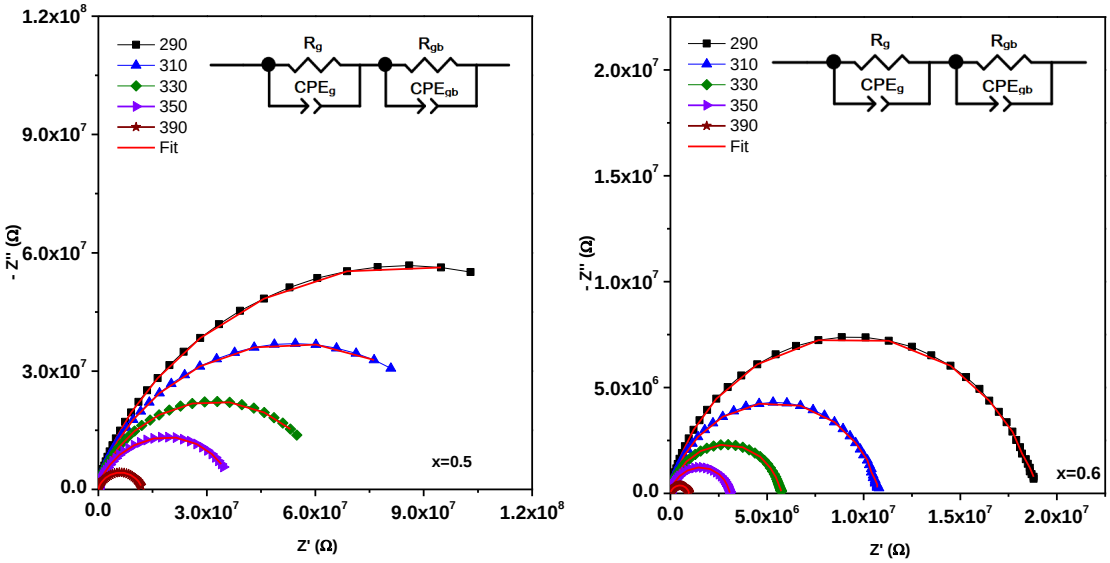

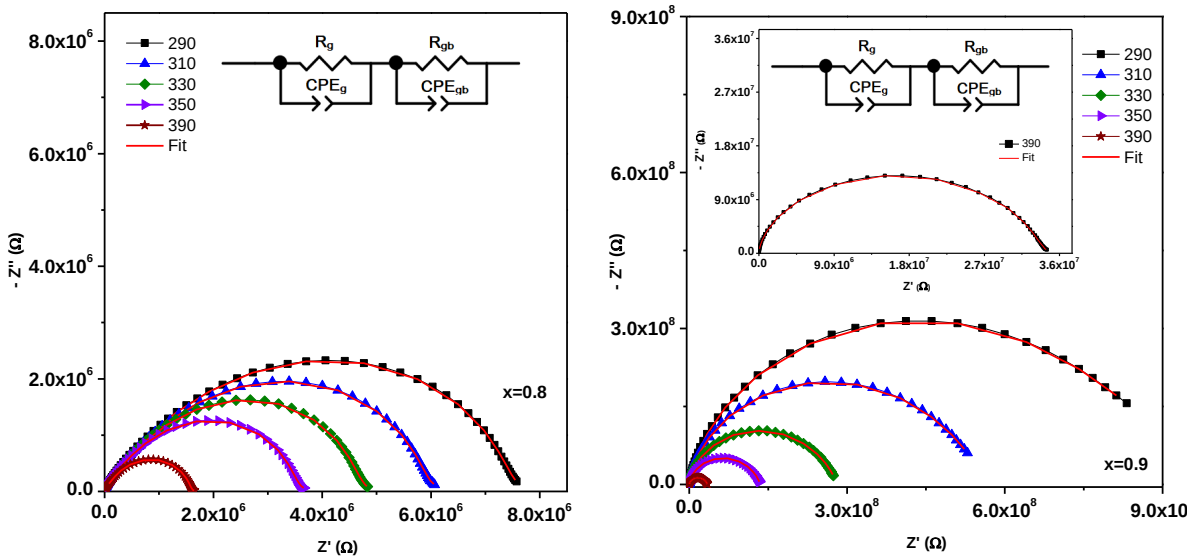

Fig-V.P1.6: Nyquist/Cole-Cole plots recorded at High Temperature for $Ba_{1-x}La_xTi_{1-x}Fe_xO_3$ (x = 0.5, 0.6, 0.8 and 0.9) and the suitable equivalent circuit model.

Table-V.P1.1. Different impedance circuits fitted parameters for BLTF compositions at different high temperatures.

		x=0.25	x=0.3	x=0.5	x=0.6	x=0.8	x=0.9
290	R_g (Ω)	3.980E+9	1.128E+9	7.958E6	9.488E6	3.402E6	4.899E+8
	CPE_g (Ω)	9.965E-12	9.165E-12	9.900E-11	9.900E-11	9.990E-12	9.980E-12
	R_{gb} (Ω)			4.18E6	9.428E6	4.2899E6	4.270E+8
	CPE_{gb} (Ω)			9.900E-11	9.300E-11	9.190E-11	4.280E-11
310	R_g (Ω)	2.700E+9	4.680E+8	7.88E7	5.288E6	2.802E6	2.690E+8
	CPE_g (Ω)	9.965E-12	9.165E-11	9.900E-12	9.900E-11	9.990E-12	9.980E-12
	R_{gb} (Ω)			2.5E7	5.428E6	3.2899E6	2.770E+8
	CPE_{gb} (Ω)			9.900E-11	9.500E-11	9.190E-11	3.980E-11
330	R_g (Ω)	2.300E+9	1.980E+8	4.58E7	2.58E6	1.902E6	1.790E+8
	CPE_g (Ω)	9.965E-12	9.965E-12	9.900E-11	9.900E-11	9.190E-11	9.980E-12
	R_{gb} (Ω)			1.8E7	3.128E6	2.9599E6	9.97E7
	CPE_{gb} (Ω)			9.900E-11	9.500E-11	6.890E-11	9.980E-11
350 / 370	R_g (Ω)	1.7009E6	9.98E7	2.58E7	1.81E6	1.502E6	6.199E7
	CPE_g (Ω)	7.688E-9	9.965E-12	9.900E-11	9.900E-11	6.090E-11	9.980E-12
	R_{gb} (Ω)	2.7219E7		1.18E7	1.27E6	2.086E6	7.187E7

	CPE_{gb} (Ω)	6.179E-8		9.900E-11	9.500E-11	2.690E-11	7.187E7
390	R_g (Ω)	9.0092E6	9.932E6	7.958E6	471000	530200	1.4349E7
	CPE_g (Ω)	9.998E-10	9.998E-11	9.900E-11	9.600E-11	9.190E-11	9.990E-12
	R_{gb} (Ω)	1.091E7	1.89E7	4.18E6	497000	1.086E6	2.0187E7
	CPE_{gb} (Ω)	8.199E-9	9.990E-11	9.900E-11	9.800E-11	5.190E-11	8.180E-11

V.2.3.2. Conductivity evolution as function of temperature and composition

Fig-V.P1.7 shows the evolution of the total conductivity (σ_{DC}) BLTF ceramics with x= 0.25, 0.3, 0.5, 0.6, 0.8, and 0.9 calculated using the following equation:

$$\sigma_{tot} = \frac{e}{(R_g + R_{gb}).S} \quad \text{(Eq. 1)}$$

Where **S** is the area of the sintered pellets, **e** is the thickness, R_g and R_{gb} are the grain and grain boundaries resistances respectively; R_g and R_{gb} value are obtained from the fit the Nyquist plots experimental data to the equivalent circuits.

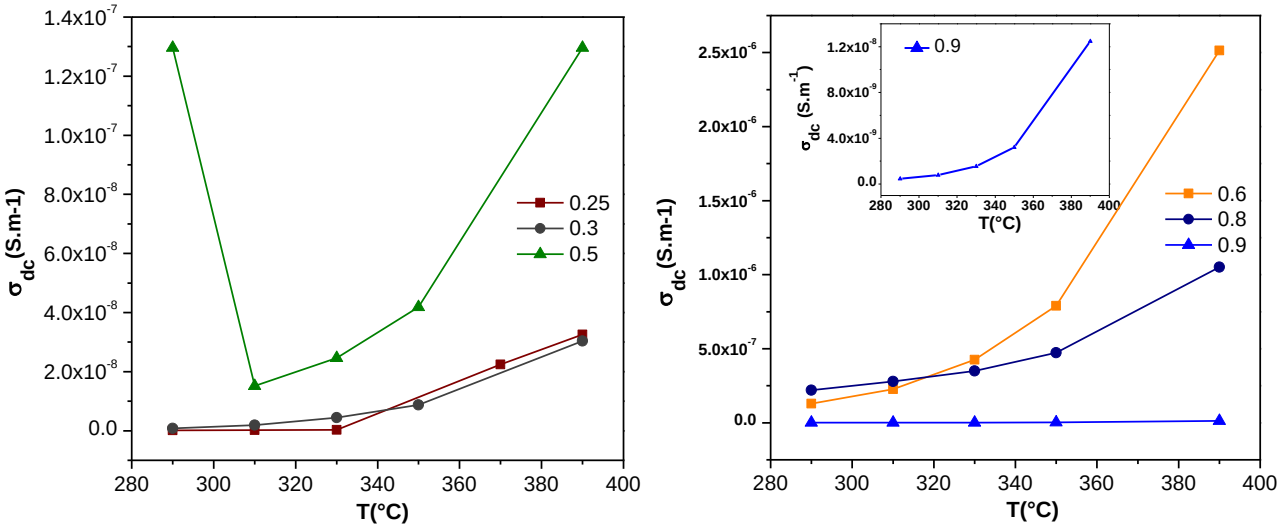

Fig-V.P1.7: Thermal variation of DC electrical conductivity of $Ba_{1-x}La_xTi_{1-x}Fe_xO_3$ (x = 0.25, 0.3, 0.5, 0.6, 0.8 and 0.9) compounds.

As function of temperature, the conductivity increases, and this is observed for all the samples; and exception for the composition with x = 0.5 is observed, the conductivity shows a

drop at temperatures between 300 and 310 °C, above which is shows close to linear increase. The effect of increasing temperature reduces the encountered barriers for the transport of the charge carriers by the thermal activation. As function of the compositions, we can observe that the insertion of La^{3+} and Fe^{3+} in $BaTiO_3$ enhances the conductivity.

V.2.4. Conclusion

The effect of the composition on the dielectric and electric properties in the BLTF system for the compositions x = 0.25, 0.3, 0.5, 0.6, 0.8 and 0.9, was investigated and reported. The dielectric and electric properties were studied in a wide range of temperature at various frequencies ranging from high, medium to low.

The results of the thermal variation of the dielectric constant illustrate the effect of the composition and temperature on the variation of the dielectric constant and dielectric loss. The incorporation of La^{3+} and Fe^{3+} in $BaTiO_3$ has induced a reduction of the dielectric constant and low dielectric loss for the compositions lower than $x \leq 0.3$; however an increase of the mentioned characteristics is observed at temperatures higher than 350°C. Additionally, two peaks were observed for x = 0.25 at 250°C related to the and at 110°C for x = 0.3. As the amount of the substitution increases, the thermal variation of the dielectric constant increases and shows broad peaks for the compositions (x = 0.5, 0.6, 0.8 and 0.9) at around 160°C, 190°C, 189°C and 150°C respectively. It is deduced that as the amount of Fe^{3+} exceeding that of Ti^{4+} in the B-sites, the exchange interaction between $Fe^{3+} \leftrightarrow Fe^{3+}$ becomes stronger and contributes to the increase of the dielectric constant value, the highest value reached is equal to 8000 for the composition x = 0.9 at 10 Hz. The samples show low dielectric loss which increases at high temperature T > 200°C. The reported peaks decreases with the frequency which a feature related to the mechanism responsible is Maxwell-Wagner since it is only effective at low frequencies <10 kHz.

The resistivity of the grains and the grain boundaries is investigated by the Nyquist plots for the compositions (x = 0.5, 0.6, 0.8 and 0.9). At room temperature the materials have very resistive grains, however as the amount of the substitution the resistivity decreases from 10^{11} to 10^{10}; the lowest grain resistance is obtained for x = 0.5 and $R_g = 5.9 \times 10^8$. At high temperature, the materials are less resistive and an increase of the conductivity is observed. The results of x = 0.25 and 0.3 show that at high temperature (T ≥ 370°C), the grains and the grain boundaries

contribute to the conductivity mechanisms. On the other hand, as the amount of the substitution increases, the Nyquist plots shows that complete semicircle appear and the equivalent circuits consists of RC-RQC connected in series representing the active region of the grain corresponding to RC and the grain boundaries with RQC.

The calculated total conductivity of the materials shows an increase as function of temperature and composition. These results prove that the incorporation of La^{3+} and Fe^{3+} in $BaTiO_3$ has induced an increase in the conductivity. The results show that as function of the composition, the conductivity decreased from the order of 10^{-10} to 10^{-7} ($S.m^{-1}$) at 290°C; while as function of temperature, the highest value was recorded for x = 0.6 at 390 for a value in the order of 10^{-6} ($S.m^{-1}$)

V.3.Part II: The study of the dielectric and electric properties of the perovskite series $Sr_{1-x}La_xTi_{1-x}Fe_xO_3$ with $0 \leq x \leq 1$ at room and high temperature in a wide range of frequency

V.3.1. Introduction

$SrTiO_3$ is a cubic perovskite structure with high dielectric constant and low dielectric loss; it is consequently an important ceramic to be used in sensors, microwave applications, and energy storage, etc [12]. $SrTiO_3$ also works as an ideal thin film growth substrate for high superconducting films, as integral component for oxide interfaces or as conducting interface between two insulators [13]. $SrTiO_3$ dielectric and optical properties were recently tested by Siliang Chen et al. [14]; a modification by doping La^{3+} into $Sr_{1-x}La_{2x/3}TiO_3$ ($0 \leq x \leq 1$) led to satisfactory results that meet the application requirement as a microwave device. The results of the doping proved that La^{3+} promote grain growth as growth striations are observed on the grain, which induced a decrease of the dielectric constant from 296 to 89.3 [14,15]. Colossal dielectric permittivity was induced by the effect of co doping Nb and Mg as reported by Bingjie Zhong et al. [15]; the dielectric ceramics $Sr(Mg_{1/3}Nb_{2/3})_xTi_{1-x}O_3$ showed good frequency stability, significant dielectric relaxation between -155 °C – 500 °C. Additionally, for the composition x = 5%, very low dielectric loss (0.0354, at 1 kHz) is observed and colossal permittivity of about 21026, at 1 kHz [15]. In comparison with other reported studies, colossal permittivity around 9100 with low dielectric loss was obtained by Mg and Nb co-doping of $SrTiO_3$, Bingjie Zhong

explained in their work the origin of this values is related to defect polarization and electron localization by defect dipoles [15]. J. Liu et al. [16] have attributed the colossal permittivity to the contribution of the grain boundary in the case of Cu and Nb co-doped $SrTiO_3$. However, Al and Nb co-doping was found to be unsuitable to enhance the dielectric permittivity of $SrTiO_3$ [17]. In the Case of $BaTiO_3$, doping has improved the dielectric properties, however the colossal permittivity was observed in a narrow temperature range [15]. This results reflect that Sr^{2+} play an important role on the dielectric properties of materials and mainly when it is doped with suitable elements like in the case of $SrNb_xTi_{1-x}O_3$, the group has reported high CP equal 59191 and low dielectric loss of 0.023.

The effect of Sr^{2+} substitution on the dielectric properties of $LaFeO_3$ was reported by D. Triyono [18]; the solid solution $La_{1-x}Sr_xFeO_3$ (x = 0.1, 0.2, 0.3, and 0.4) was prepared via sol gel methods and produced homogeneous nanoparticles in the order of 200 nm, meaning that the addition of Sr^{2+} does not contribute in the growth of the particles as La^{3+}. However, the incorporation of Sr^{2+} caused an increase of the dielectric and conductivity where the highest values were obtained for $La_{1-x}Sr_xFeO_3$ x=0.4 [18]. M. A. Gabal [19] studied the same solid solution for wider range of substitution $La_{1-x}Sr_xFeO_3$ (x = 0.1, 0.2, 0.3, 0.4, 0.6, 0.8, and 1.0), synthesized via sucrose auto-combustion route; the sample's size decrease with the content of Sr^{2+} (22 – 12 nm). However, The dielectric constant evolution as function of the composition at various temperature shows different results in comparison with D. Triyono et al.; in the work presented by M. A. Gabal et al. [19], the dielectric constant shows a broad peak as the temperature increases, however as function of temperature the dielectric constant decreases. The values of the dielectric constant are lower that the reported values of Triyono et al. [18]. However, the substitution of La^{3+} by Sr^{2+} enhanced the conductivity as results of increasing the electronic compensation, and or the ionic compensation [18–20].

This part presents the results of the dielectric and electric properties of the solid solution SLTF in a wide range of substitution. The effect of Ti^{4+} and Sr^{2+} on the particles growth process, the dielectric constant, and the conductivity properties will be systematically studied. Additionally, understanding the effect of the composition and structure on the activation regions and the mechanisms participating in the conductivity will be highlighted.

V.3.2. Frequency and temperature dependent of the relative permittivity and tangent loss

The dielectric measurement were carried it out for the composition of the perovskite series SLTF for x=0.2, 0.4, 0.6 and 0.8. **Fig-V.P2.1** and **Fig-V.P2.2** show the variation of the dielectric permittivity ε'_r and the dielectric loss tan $\delta = \varepsilon'/\varepsilon''$ as function of the temperature at different frequencies ranging from low to high frequency: 10 Hz to 1MHz. The decrease of the dielectric constant at high frequencies is observed for all the composition, as it is a common behavior for other studied perovskites compounds [9,21,22]. The results of Rietveld refinement demonstrated that the sample with x = 0.2 adopt the cubic structure while the compositions $0.4 \leq x \leq 0.8$, adopt the orthorhombic structure, *SG: Pnma.*

At low frequencies and for the composition x = 0.2, the dielectric constant variation as function of temperature does not show features of system transition, which is in accordance with the Rietveld refinement results. At low frequencies, from 27 °C to 280 °C, the dielectric permittivity remains steady and a sudden increase is observed above 280 °C, similar behavior is observed for the dielectric loss. At high frequencies a shoulder at around 100 °C is observed and shift toward 130 °C with frequency. The composition x = 0.4, shows that the sample might adopt more Centro-symmetric system since no anomaly is observed. Very low dielectric constant values are obtained for the composition x = 0.4, and the dielectric constant varies between 8 and 11 at high medium and low frequency. As function of temperature, the permittivity remains steady within the range 27 °C – 390 °C, and very low dielectric loss are observed.

For the compositions x = 0.6 and x = 0.8, broad anomalies appear respectively at around (111 and 248 °C), and at 145 °C. The peaks observed for x = 0.6 are more likely to be frequency dependent as they tend to shift and broaden as the frequency increases from 10 Hz to 100 KHz. The peak observed at around 111 °C is suspected to be a ferroelectric – paraelectric transition, however, the peak at around 248 °C is inactive at frequencies higher than 10 KHz which is a feature related with the mechanism of Mawxell-Wagner [6]. The dielectric anomalies observed are followed by an intense dielectric loss peak. The order of the dielectric loss is around 300 at low frequencies and decreases up to 8 at high frequencies. Similarly for the compositions x = 0.8 and due to the increased amount of Fe^{3+} in the B-sites, the peaks observed are assigned to the exchange interaction between $Fe^{3+} \leftrightarrow Fe^{3+}$ as previously reported. The dielectric loss accompanies the behavior of the dielectric constant and it increases in the region of the anomalies

and at high temperature, while it decreases at high frequencies. This behavior describes the dielectric properties of materials and reflects the activation of the polarization mechanisms within the material.

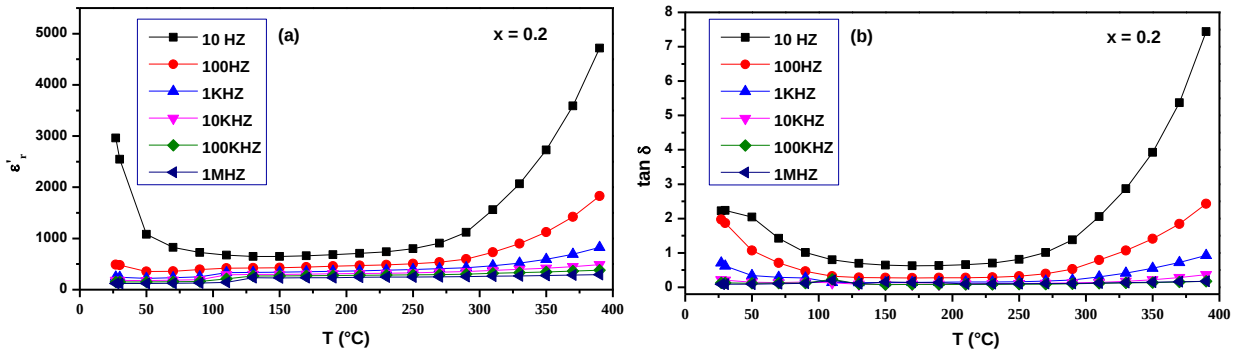

Fig-V.P2.1: Thermal variation of dielectric permittivity **(a),** and dielectric losses **(b)** for $Sr_{1-x}La_xTi_{1-x}Fe_xO_3$ (x = 0.2; Cubic SG *Pm*-3*m*) at high, medium and low frequency (1Hz – 1MHz).

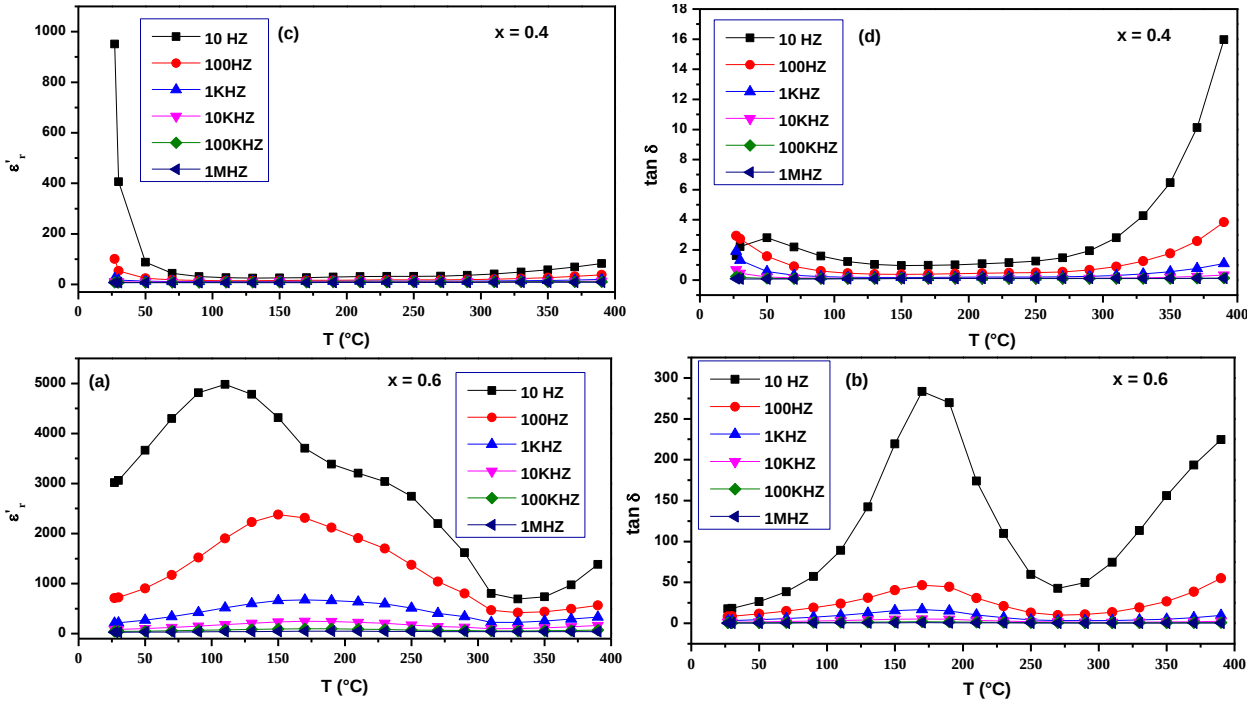

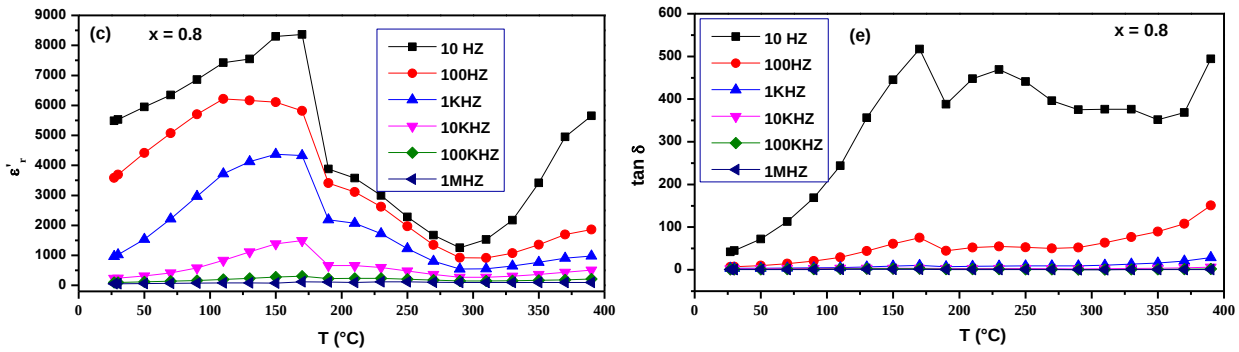

Fig-V.P2.2: Thermal variation of dielectric permittivity, and dielectric losses for $Sr_{1-x}La_xTi_{1-x}Fe_xO_3$ (x = 0.6 and 0.8; Orthorhombic SG *Pm*-3*m*) at high, medium and low frequency (1Hz – 1MHz).

V.3.3. Analysis of Nyquist plots: Conductivity at room and high temperature

V.3.3.1. Fitting of Nyquist plots and determination of equivalent circuit

Fig-V.P2.3 represents the impedance plots known as Nyquist plots for the compositions x = 0.2, 0.4, 0.6, and 0.8 at room temperature. The samples at room temperature show features of good conducting materials as they have close to complete or two semi circles as presented in **Fig-V.P2.3**.

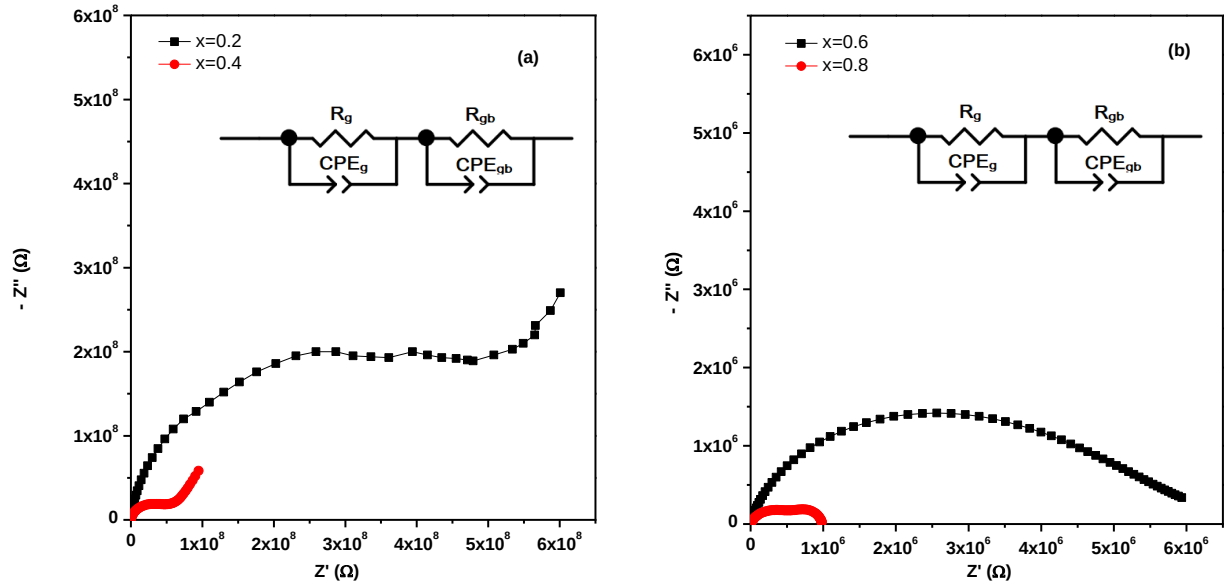

Fig-V.P2.3: Nyquist/Cole-Cole plots recorded at Room Temperature for $Sr_{1-x}La_xTi_{1-x}Fe_xO_3$ (x = 0.2, 0.4, 0.6, and 0.8) and the suitable equivalent circuit model.

The experimental results show that with the incorporation of La^{3+} and Fe^{3+} there is an enhancement in the electrical properties. As the amount of the substitution increases in SLTF, the semi circles are complete at concentrations: $x \geq 0.6$ (**Fig-V.P2.3b**). The experimental results were fitted using the circuit RC-RQC connected in series representing the active region of the grain corresponding to RC and the grain boundaries with RQC. Due to the inhomogeneity of the samples, the two semicircles representing the grain and grain boundaries are overlapping representing one large depressed semicircle.

The **Fig-V.P2.4(a, b)** presents the Nyquist plots of the compositions x = 0.2, and 0.4 at high temperatures, the experimental data shows an incomplete semicircles up to 350 °C, while at 390 °C the samples show complete semicircles. The experimental results were fitted using the circuit RC-RQC connected in series representing the active region of the grain corresponding to RC and the grain boundaries with RQC; the fitting results are summarized in **Table-V.P2.1**. It is observed that the radius of the semi-circle decreases as function of temperature and compositions. For the composition x = 0.2, and under the effect of the temperature the resistance of the grain decreases from 4.092 x 10^9 at 290°C up to 9.4194 x 10^6 Ω at 390 °C, and for the grain boundaries the resistance decreases from 9.930 x 10^8 at 310 to 5.039 x 10^7 Ω at 390°C. The same is observed for the composition x = 0.4, there is a decrease of the grain resistance under the effect of the temperature from 3.537 x 10^9 at 290 °C to 1.233 x 10^8 Ω at 390 °C, whereas, the grain boundaries resistance decreases from 2.940 x 10^8 at 330°C to 3.058 x 10^8 Ω at 390 °C. These results show that the two compositions present structures with grains and grain boundaries resistances of same order, expect at 350 and 390°C the grains are more resistive than the grain boundaries in the case of the sample with x = 0.4.

Fig-V.P2.4(c, d) displays the Nyquist plots of the compositions x = 0.6, and 0.8 and they show complete semicircles at high temperatures. The samples under the effect of temperature are active in two regions: the grain and the grain boundaries. The experimental results were fitted using the circuit RC-RQC connected in series representing the active region of the grain corresponding to RC and the grain boundaries with RQC. The fitting models are presented in inset of **Fig-V.P2.4(c, d)** and the results are summarized in **Table-V.P2.1.** For the composition x = 0.6, the results show that the resistance of the grain boundaries, in the order of 10^6, is higher than the grain. The value of the grain resistance decreases from 2.386 10^5 at 290°C to 9.487 10^4

Ω; on the other hand the resistance value of the grain boundaries is reducing from 3.7601 10^6 at 290°C to 9.401 10^5 Ω at 390 °C. The same observations for the sample with x = 0.8, the grain boundaries are more resistant in comparison with the grain, and decreases with temperatures, *e.g.*, the grain resistance decreases from 1.005 x 10^5 at 290 °C to 35430 x 10^4 Ω, and the grain boundaries resistance decreases from 3.760 x 10^6 at 290 °C to 4.51 x 10^4 Ω at 390°C.

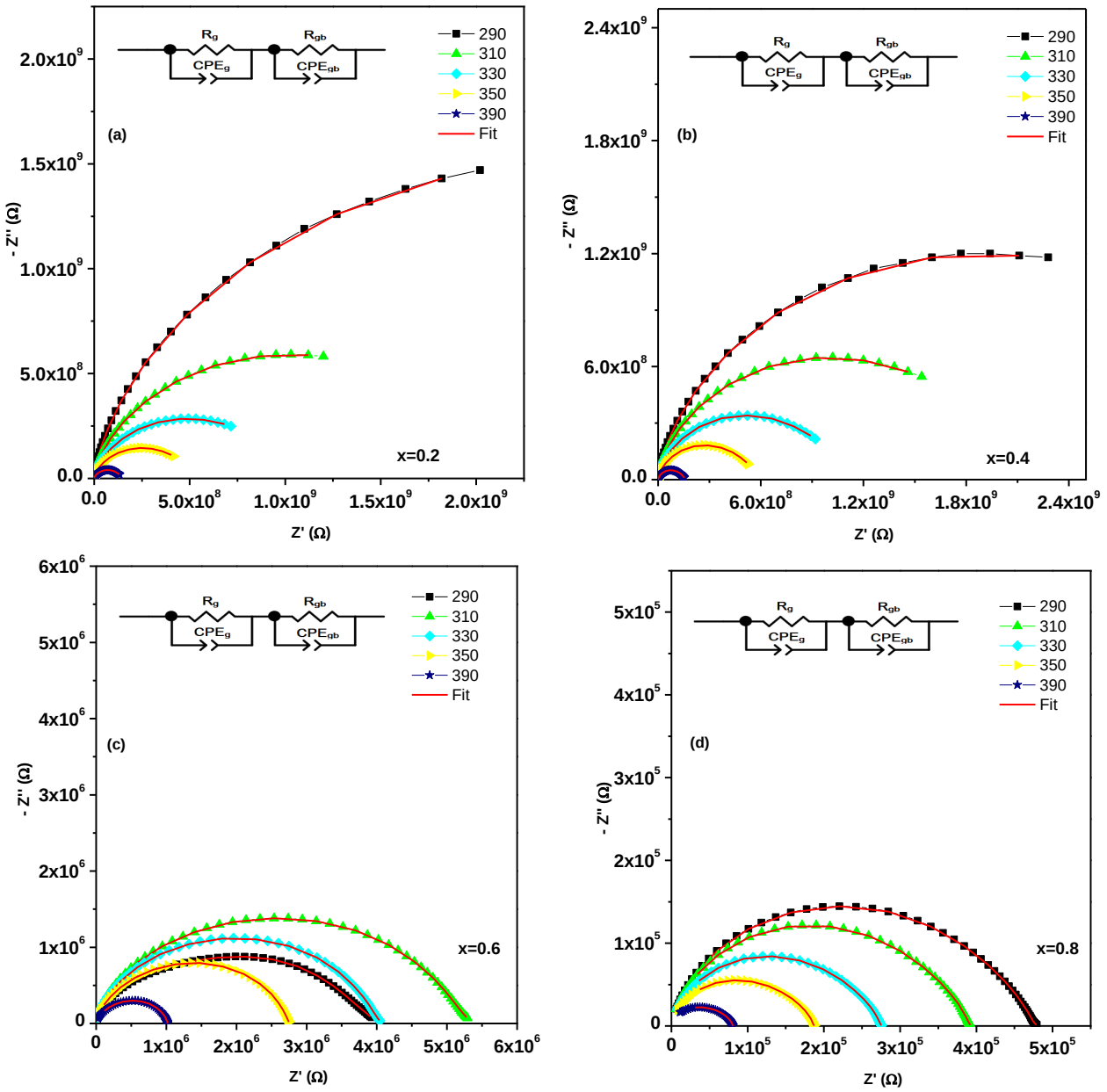

Fig-V.P2.4: Nyquist/Cole-Cole plots recorded at High Temperature for $Sr_{1-x}La_xTi_{1-x}Fe_xO_3$ (x = 0.2, 0.4, 0.6 and 0.8) and the suitable equivalent circuit model.

Table-V.P2.1. Different impedance circuits fitted parameters for SLTF compositions at different high temperatures.

		x=0.2	x=0.4	x=0.6	x=0.8
290	R_g (Ω)	4.092E+9	3.537E+9	238690	100530
	CPE_g (Ω)	9.937E-12	9.919E-12	8.590E-11	9.198E-12
	R_{gb} (Ω)			3.7601E6	376090
	CPE_{gb} (Ω)			9.970E-10	5.698E-10
310	R_g (Ω)	9.757E+8	1.980E+9	1.5982E6	97530
	CPE_g (Ω)	9.979E-12	9.919E-12	9.990E-12	9.998E-12
	R_{gb} (Ω)	9.930E+8		3.6401E6	292090
	CPE_{gb} (Ω)	3.900E-11		1.500E-10	5.998E-10
330	R_g (Ω)	5.158E+8	7.760E+8	9780	98530
	CPE_g (Ω)	8.959E-12	8.640E-12	9.990E-12	8.998E-12
	R_{gb} (Ω)	4.511E+8	2.940E+8	4.0401E6	178090
	CPE_{gb} (Ω)	3.987E-11	9.180E-11	3.470E-10	9.998E-10
350	R_g (Ω)	9.9899E7	5.330E+8	619870	50130
	CPE_g (Ω)	6.980E-12	9.940E-12	9.990E-12	6.798E-12
	R_{gb} (Ω)	3.978E+8	5.15E7	2.1401E6	137100
	CPE_{gb} (Ω)	2.793E-11	9.180E-10	1.970E-10	5.020E-10
390	R_g (Ω)	9.4194E7	1.233E+8	94870	35430
	CPE_g (Ω)	2.098E-12	9.870E-12	3.990E-11	9.998E-12
	R_{gb} (Ω)	5.039E7	3.058E7	940110	45100
	CPE_{gb} (Ω)	1.865E-11	9.760E-11	1.370E-10	9.990E-10

V.3.3.2. Conductivity evolution as function of temperature and composition

Fig-V.P2.5 shows the evolution of the total conductivity (σ_{DC}) BLTF ceramics with x= 0.2, 0.4, 0.6, and 0.8calculated using the following equation:

$$\sigma_{tot} = \frac{e}{(R_g + R_{gb}).S} \quad \text{(Eq. 1)}$$

Where **S** is the area of the sintered pellets, **e** is the thickness, R_g and R_{gb} are the grain and grain boundaries resistances respectively; R_g and R_{gb} value are obtained from the fit the Nyquist plots experimental data to the equivalent circuits.

The results of the thermal evolution of the conductivity show that there is and enhancement of as function of the composition. The conductivity increases from the order of 10^{-10} to 10^{-5} ($S.cm^{-1}$) as the amount of the substitution increases; the conductivity values are reported at 290°C. Moreover, as function of temperature, the conductivity increases, and this is

observed for all the samples. The effect of increasing temperature reduces the encountered barriers for the transport of the charge carriers by the thermal activation, thus an increase from the order of 10^{-10} to 10^{-8} ($S.cm^{-1}$) of the conductivity is observed from the compositions x = 0.2, and 0.4. Same observation for the compositions x = 0.6 and 0.8, the conductivity increases from 10^{-8} to 10^{-6} and 10^{-5} ($S.cm^{-1}$).

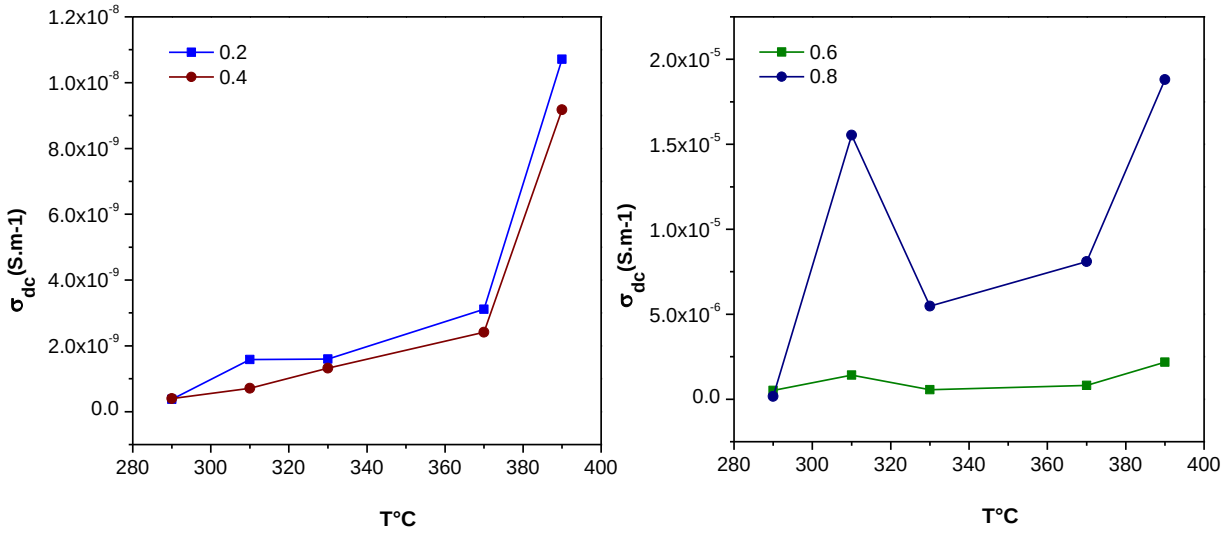

Fig-V.P2.5: Thermal variation of DC electrical conductivity of $Sr_{1-x}La_xTi_{1-x}Fe_xO_3$ (x = 0.25, 0.4, 0.6, and 0.8) compounds.

V.3.4. Conclusion

The effect of the composition on the dielectric and electric properties in the BLTF system for the compositions x = 0.2, 0.4, 0.6, and 0.8, was investigated and reported. The dielectric and electric properties were studied in a wide range of temperature at various frequencies ranging from high, medium to low.

The dielectric constant measurements show the effect of the composition and temperature on the thermal variation of the dielectric permittivity ε'_r and the dielectric loss tan $\delta = \varepsilon'/\varepsilon''$. The studies showed two type of results for x = 0.2 and 0.3 and for x = 0.6 and 0.8. Low values of the dielectric permittivity and dielectric loss were observed for x = 0.2 and 0.3, and no anomaly is reported as function of temperature which confirms that no ferroelectric – paraelectric transition has occurred. However different behavior if observed for compositions at x ≥ 0.6; the high content of Fe^{3+} in $SrTiO_3$ resulted in the appearance of the mechanism related to Mawxell-

Wagner resulting from the string exchange interaction between $Fe^{3+} \leftrightarrow Fe^{3+}$. It is observed that the contribution of the $Fe^{3+} \leftrightarrow Fe^{3+}$ exchange interaction enhances the dielectric constant and mainly at low frequencies, the highest value reached belongs to the compositions x = 0.8 which is in the range between 2000 at high frequency and 9000 at low frequency.

The Nyquist plots for the compositions x = 0.2, 0.4, 0.6, and 0.8 shows promising conductive properties of the materials at room temperature. The contribution of the grains and the grain boundaries appear in the Nyquist plots, moreover, the resistivity of the material decreases as function of the composition to reach values in the order of 10^6 Ω. At high temperature, the radius of the semi-circles decreases with temperatures for all the compositions. The Nyquist plots were fitted to the equivalent circuit consisting of RC-RQC connected in series representing the active region of the grain corresponding to RC and the grain boundaries with RQC. The compositions x = 0.2 and x = 0.4 fitting results show the two compositions present structures with grains and grain boundaries resistances of same order, expect at 350 and 390°C the grains are more resistive than the grain boundaries in the case of the sample with x = 0.4. The compositions x = 0.6, and 0.8 show complete semicircles at high temperatures the results show that the resistance of the grain boundaries, in the order of 10^6, is higher than the grain.

The calculated total conductivity of the materials shows an increase as function of temperature and composition. These results prove that the incorporation of La^{3+} and Fe^{3+} in $SrTiO_3$ has induced an increase in the conductivity from the order of 10^{-10} to 10^{-7} ($S.m^{-1}$). The highest value is observed for x = 0.8 at 390 with a conductivity in the order of 10^{-5} ($S.m^{-1}$).

V.4.Part III: The study of the dielectric and electric properties of the perovskite series $Ba_{1-x}Sr_xTi_{1-x}Fe_xO_{3-\delta}$ with $0 \leq x \leq 1$ at room and high temperature in a wide range of frequency

V.4.1. Introduction

In the perovskite structure, the effect of the substitution in A-site induces different change in the properties of the material in comparison with the B-site substitution and this difference is illustrated in several researches. When Ba^{2+} is substituted by Sr^{2+} the transition temperature from ferroelectric state to paraelectric state shifts to lower temperature [21,23,24]. D. R. Patil et al. [21] prepared $Ba_{1-x}Sr_xTiO_3$ ceramics (x = 0.1, 0.2 and 0.3) and reported on the evolution of the

dielectric properties with temperature at various frequencies. It is observed that the transition temperature shift to lower temperature from 333 °C to 308 °C, and an increase of the dielectric constant from 918 to 1195 as the content of Sr^{2+} increases. Broad peaks were observed indicating diffuse type behavior, which is attributed to the disorder in the arrangement of cations at the A-sites and the B-sites [21]. H. Abdelkefi et al. [23] have studied the same solid solution $Ba_{1-x}Sr_xTiO_3$ for x = 0.6 and 0.8; a difference in peak is observed where sharp peaks are obtained for the two compositions and no shift was reported. Additionally, Lower values of the dielectric constant in comparison with $BaTiO_3$ were obtained and lowered from around 14000 for $BaTiO_3$ to 9000 for the composition x = 0.8 [23]. Moreover, different results were presented by M. Arshad et al. [24] for the solid solution $Ba_{1-x}Sr_xTiO_3$ for x = 0, 0.25, 0.3 and 0.35. The anomaly or the peak characteristic of transition disappears as Ba^{2+} is substituted by Sr^{2+}, associating the fact that T_c temperature shifts to temperature lower than room temperature [24]. The substitution of Ba^{2+} by Sr^{2+} had induced a shrink in the volume due to the reduced average ionic radius; therefore the paraelectric phase with cubic structure is established leading to the disappearance of the transition peak. The dielectric loss decreased in all the reported work, and an increase in the conductivity with the content of Sr^{2+} is observed in all the reported samples [21,23,24]. The impedance spectroscopy revealed that the grain boundaries are more resistant than the grain, and the relaxation behavior are responsible for the conduction in $Ba_{1-x}Sr_xTiO_3$ ceramics [24]. On the other hand, the effect of Fe doped $BaTiO_3$ is presented by F.D. Cortès-Veg et al. [22]; the Fe doped $BaTiO_3$ with x = 0, 0.01, 0.02, 0.04 was prepared via ball milling and solid state reaction. As consequence of substituting Ti^{4+} by Fe^{3+}, fine grains were formed and a decrease in the size is observed, indicating that Fe^{3+} addition promotes a significant reduction of the crystal size, additionally, above x = 0.02 the samples show grains with hexagonal flake architectures [22]. The addition of Fe^{3+} had induced a decrease of the transition temperature up to 70°C which is due to the perturbation of the octahedral layers in the perovskite structure originating from the incorporation of Fe^{3+} into Ti^{4+} sites. In comparison with the effect of Sr^{2+} on $BaTiO_3$ dielectric properties, Fe^{3+} incorporation led to drastic shift of the transition temperature T_c, as it also lowered the values of the dielectric constant to 600 at T_c temperature. The aforementioned results show the effect of both elements on enhancing the electric properties of $BaTiO_3$ more than the dielectric properties, however above x = 0.04 is an interesting region to study the multiferroic properties as reported by [22]. Another parameter that can increases the transport properties of

perovskite material and it consists of creating oxygen deficient in the perovskite structure. V.V. Kharton et al. [25] report the effect of A-site deficiency in the solid solution $Sr_{1-y}Fe_{0.8}Ti_{0.2}O_{3-d}$ (y=0–0.06). Doping $SrTiO_3$ by Ti^{4+} creates A-site deficiency which leads to an increase of the unit cell volume, and the creation of oxygen vacancies. The total electrical conductivity was observed to be dominated by p-type electronic, however, the ionic conductivity seemed to increase with the increase of cation vacancy up to y = 0.03. The incorporation of moderate amount of Ti^{4+} of around ~ 20% results in high ionic conductivity and lower activation energy; above this value the samples tend to shows a decrease in the ionic type conductivity with Ti incorporation. A. Rothschild [26] reported similar results for $SrTi_{1-x}FexO_{3-d}$ (x=0.01, 0.35, and 0.50). The samples showed mixed ionic and electronic conductivity; at low temperature the electronic carriers are localized and trapped by the local minima in the potential field, thus, the mechanism of transport is that of hopping mechanism; however at high temperature they become delocalized and a band-like mechanism of conduction occurs.

The present work consists of studying the effect of the oxygen vacancies on the dielectric and electric properties of the solid solution BSTF in a wide range of substitution. The effect of Fe^{3+} and Sr^{2+} on the dielectric constant and the conductivity properties will be systematically studied. Additionally, understanding the effect of the composition and structure on the mechanisms participating in the conductivity will be highlighted.

V.4.2. Frequency and temperature dependent of the relative permittivity & tangent loss

Fig-V.P3.1 displays the variation of the dielectric constant as function of temperature at various frequencies for the compositions 0.2 and 0.4. The thermal variation of the dielectric constant shows that no phase transition occurred in the system, thus the BSTF system does not exhibit the ferroelectric – paraelectric transitions. Moreover, the peaks associated to interaction between $Fe^{3+} \leftrightarrow Fe^{3+}$ or Mawxell-Wagner effect are not observed [6]. The dielectric constant is observed to keep low values at all tested frequencies; however it shows an increase at around 200 °C and mainly at low frequencies. In the BSTF x = 0.2 and 0.4 compositions, the dielectric loss increases as functions of temperatures and compositions.

Similar behavior is observed for the cubic compositions x = 0.6 and 0.8, the dielectric constant seems to increase at high temperature mainly at low frequencies. The absence of

anomalies in the samples x = 0.6 and 0.8, demonstrate that no ferroelectric to paraelectric transition occurs in this samples within this range of temperature. The expected peaks around 260-300°C associated with the spin reorientation do not appear even at high content of Fe^{3+}. High dielectric loss is observed for the composition x = 0.6 in a wide range of temperature starting from 100°C and mainly at low frequency. Moreover, low dielectric loss is observed for the composition x = 0.8 and start increasing from 200°C at 10 Hz.

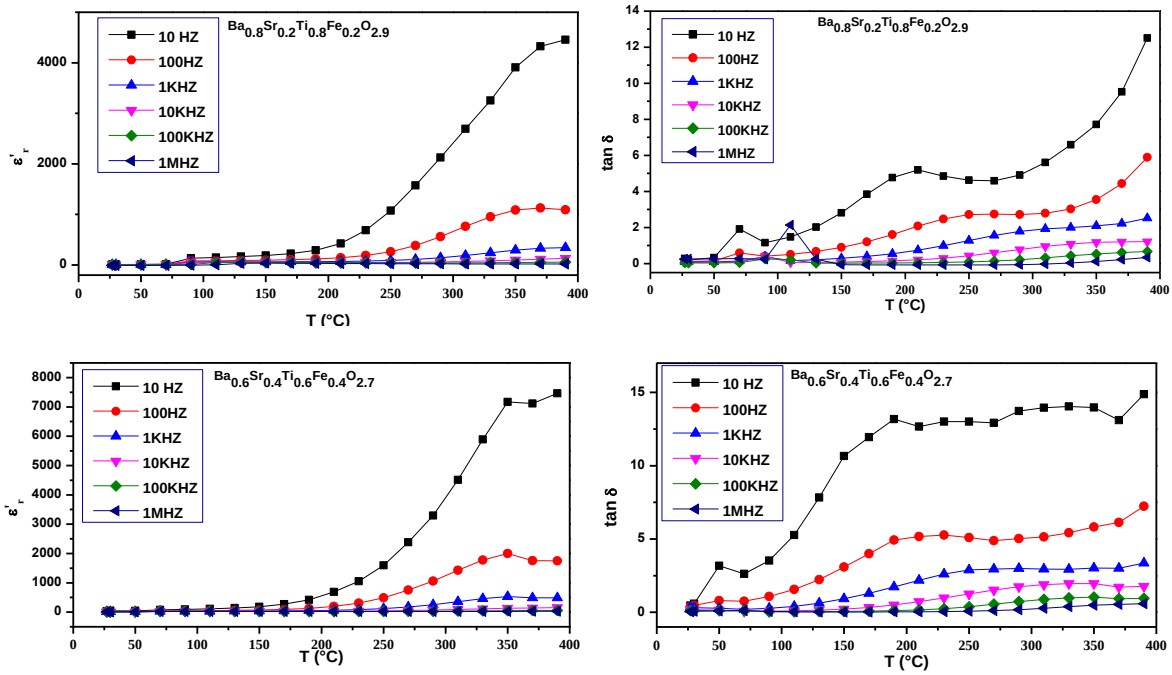

Fig-V.P3.1: Thermal variation of dielectric permittivity **(a),** and dielectric losses **(b)** for $Ba_{1-x}Sr_xTi_{1-x}Fe_xO_{3-\delta}$ (x = 0.2 and 0.4; Tetragonal SG *P4/mmm*) at high, medium and low frequency (1Hz – 1MHz).

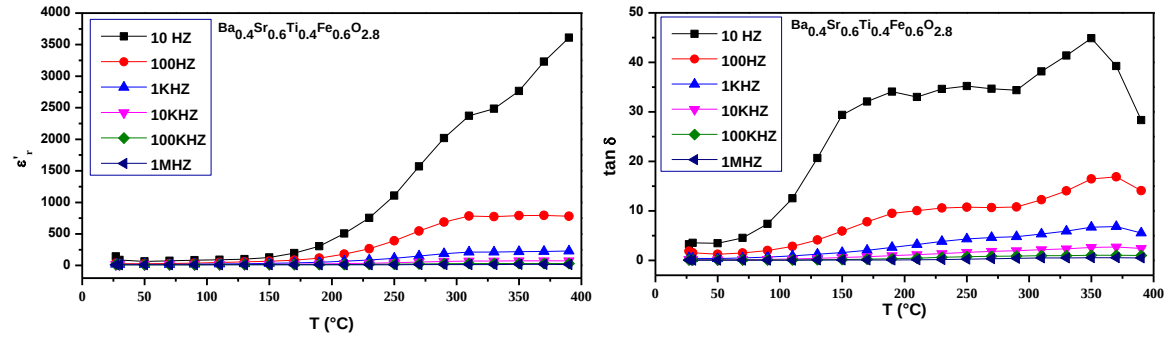

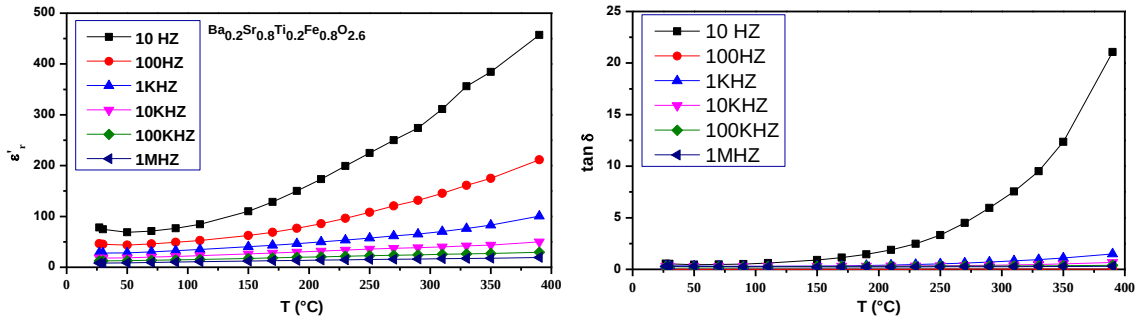

Fig-V.P3.2: Thermal variation of dielectric permittivity **(a),** and dielectric losses **(b)** for $Ba_{1-x}Sr_xTi_{1-x}Fe_xO_{3-\delta}$ (x = 0.6, and 0.8; Cubic SG *Pm*-3*m*) at high, medium and low frequency (1Hz – 1MHz).

V.4.3. Analysis of Nyquist plots: Conductivity at room and high temperature

V.4.3.1. Fitting of Nyquist plots and determination of equivalent circuit

Fig-V.P3.3 presents the Nyquist plots of the compositions x = 0.2, 0.4, 0.6, and 0.8 at room temperature. The effect of the composition on the electrical properties is observed on the decrease of the semicircle radius and thus the material's resistance decreases; however, at low, medium, and high frequency and according to the incomplete semi-circles observed, the region active is that of the grains, and this is valid only for the compositions x = 0.2, 0.4, and 0.8.

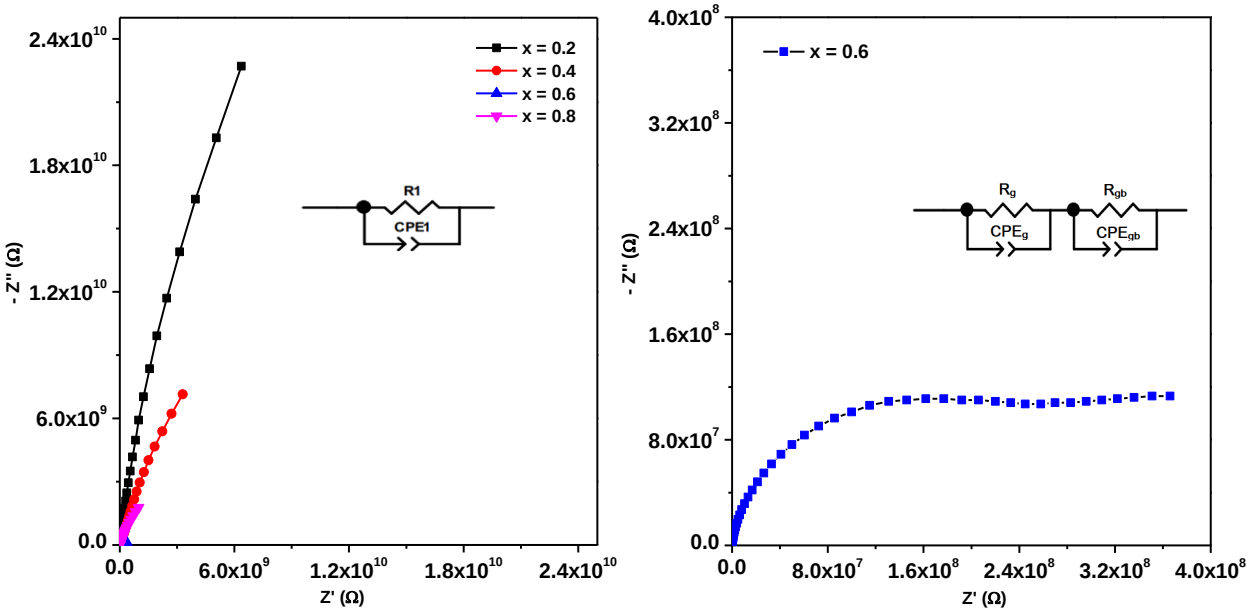

Fig-V.P3.3: Nyquist/Cole-Cole plots recorded at Room Temperature for $Ba_{1-x}Sr_xTi_{1-x}Fe_xO_{3-\delta}$ (x = 0.2, 0.4, 0.6, and 0.8) and the suitable equivalent circuit model.

The equivalent circuit found using Zview consists of a parallel RC circuit and which describes the bulk active region at room temperature. The Nyquist plot of the composition x = 0.6 shows two semicircles, one is of grain and the second consist of grain boundaries. The composition x = 0.6 in comparison with the rest of the samples shows good conducting properties at room temperature.

The Nyquist plots are presented in **Fig-V.P3.4** and **Fig-V.P3.4** for x = 0.2, 0.4, 0.6 and 0.8 at high temperatures. The Nyquist plots show two semi-circles for the compositions x = 0.2 and 0.4, while as function of temperatures there is an overlap of these semicircles, and only one depressed semicircles is observed. The radius of the semicircles reduces as function of temperatures, thus the resistance of the samples decreases, which is due to the easy mobility of the space charges. The Fitting of the Nyquist plots is compatible to the circuit RC-RQC connected in series representing the active region of the grain corresponding to RC and the grain boundaries with RQC. **Table-V.P1.1** resumes the obtained results; the grain and grain boundaries resistances are of the order 10^6 Ω, both regions show high resistance which decreases as function of temperature, this is valid for x = 0.2, 0.4, and 0.8. At x = 0.2, the resistance R_g decreases from 7.2757 x 10^6 at 290 °C to 4.35710^6 Ω at 390°C; the resistance R_{gb} decreases from 2.6593 x 10^7 at 290°C to 1.03 x 10^6 at 390 °C. On the other hand, the resistance R_g decreases from 2.2918 x 10^6 at 290 °C to 9.277 x 10^5 Ω at 390°C; the resistance R_{gb} decreases from 2.6593 x 10^7 at 290°C to 1.03 x 10^6 at 390 °C.

Fig-V.P3.4 displays the experimental of the impedance for x = 0.6 and 0.8. The Nyquist plots show one semicircle with a radius that decreases with temperature, thus the resistance. The plots reflect the inhomogeneity of the samples since the contribution of the grain and the grain boundaries overlap. The experimental results were fitted using the circuit RC-RQC connected in series representing the active region of the grain corresponding to RC and the grain boundaries with RQC, and the results are presented in **Table-V.P1.1**.The composition x = 0.6 shows a resistance in the order of 10^7 Ω which is higher in comparison with the resistance of the other compounds. The R_g decreases from 7.4709 x 10^7 to 1.099 x 10^7 Ω with the increase of temperature from 290 to 390 °C; also the R_{gb} decrease from 4.623 x 10^7 Ω to reach 9.529 x 10^5 Ω at 390°C. The results for x = 0.8 shows the resistance of the grain boundaries is in the order of

10^5 Ω which is lower than that of the grain; however, the R_g and R_{gb} decreases as function of temperature.

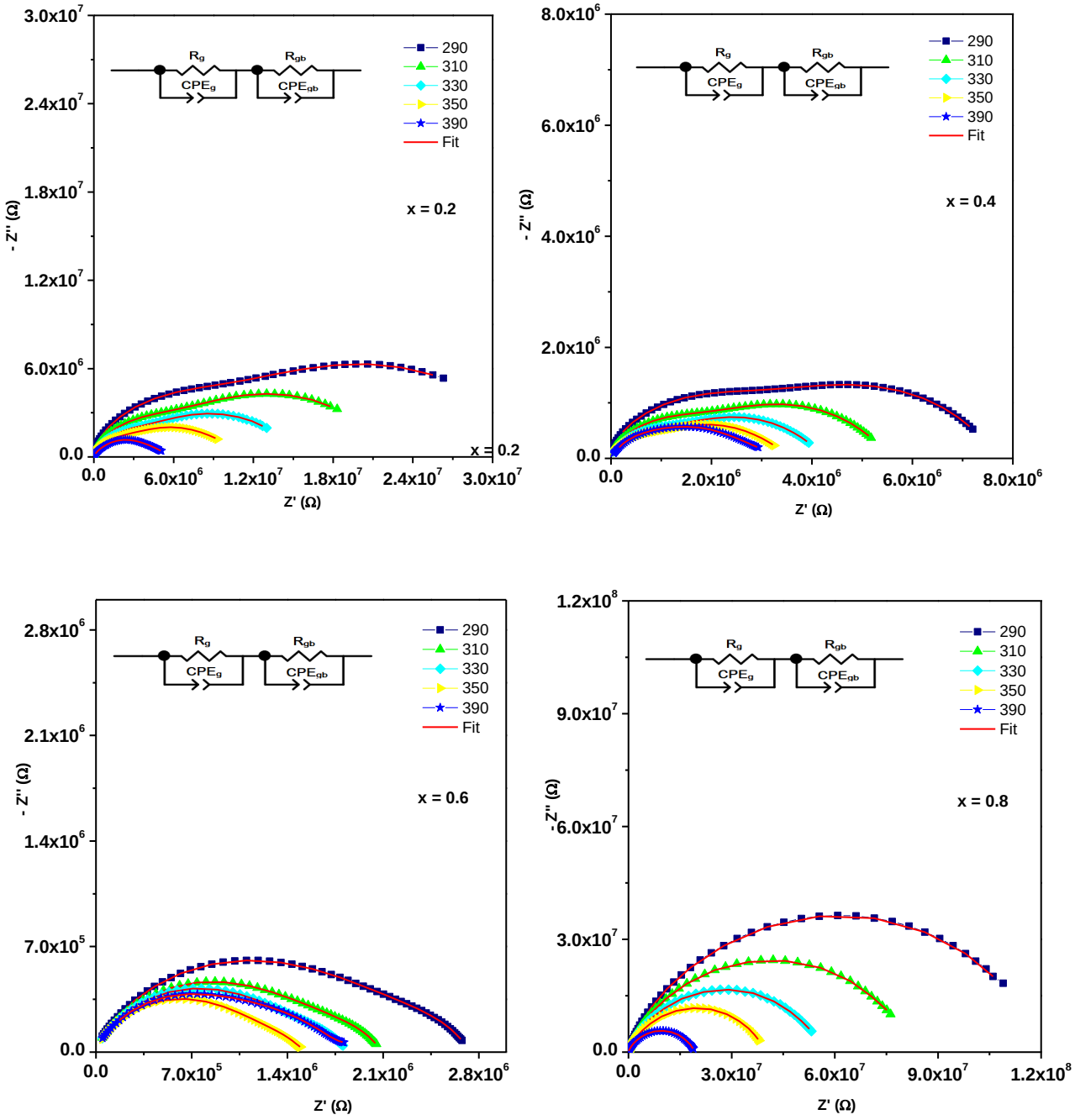

Fig-V.P3.4: Nyquist/Cole-Cole plots recorded at High Temperature for $Ba_{1-x}Sr_xTi_{1-x}Fe_xO_{3-\delta}$ (x = 0.2, 0.4, 0.6 and 0.8) and the suitable equivalent circuit model.

Table-V.P2.1. Different impedance circuits fitted parameters for BSTF compositions at different high temperatures.

		x=0.2	x=0.4	x=0.6	x=0.8
290	R_g (Ω)	7.2757E6	2.2918E6	7.4709E7	1.799E6
	CPE_g (Ω)	7.702E-10	5.590E-10	9.199E-11	2.190E-10
	R_{gb} (Ω)	2.6593E7	5.5739E6	4.6239E7	929840
	CPE_{gb} (Ω)	9.990E-9	9.999E-9	6.279E-11	9.999E-9
310	R_g (Ω)	4.357E6	1.5178E6	6.4709E7	1.329E6
	CPE_g (Ω)	7.702E-10	4.490E-10	9.199E-11	3.190E-10
	R_{gb} (Ω)	1.7993E7	4.139E6	1.8239E7	747390
	CPE_{gb} (Ω)	9.990E-9	9.299E-9	7.299E-11	9.999E-9
330	R_g (Ω)	3.257E6	1.0178E6	4.4709E7	1.129E6
	CPE_g (Ω)	7.702E-10	4.190E-10	9.199E-11	2.190E-10
	R_{gb} (Ω)	1.1993E7	3.239E6	1.2239E7	697390
	CPE_{gb} (Ω)	9.990E-9	9.999E-9	8.299E-11	9.999E-9
350	R_g (Ω)	2.157E6	857760	3.099E7	952920
	CPE_g (Ω)	7.702E-10	4.690E-10	9.999E-11	2.190E-10
	R_{gb} (Ω)	8.293E6	2.6659E6	9.2393E6	537390
	CPE_{gb} (Ω)	9.990E-9	9.999E-9	9.999E-11	9.999E-9
390	R_g (Ω)	4.357E6	927760	1.099E7	1.1919E6
	CPE_g (Ω)	5.319E-10	5.190E-10	9.999E-11	3.190E-10
	R_{gb} (Ω)	1.03E6	2.2159E6	8.2393E6	647390
	CPE_{gb} (Ω)	6.900E-9	9.999E-9	9.999E-11	9.999E-9

V.4.3.2. Conductivity evolution as function of temperature and composition

The conductivity as function of temperature is presented in **Fig-V.P2.5.** The conductivity is presented for all the compositions of BSTF ceramics with x = 0.2, 0.4, 0.6, and 0.8 calculated using the following equation:

$$\sigma_{tot} = \frac{e}{(R_g + R_{gb}).S} \quad \text{(Eq. 1)}$$

Where **S** is the area of the sintered pellets, **e** is the thickness, R_g and R_{gb} are the grain and grain boundaries resistances respectively; R_g and R_{gb} value are obtained from the fit the Nyquist plots experimental data to the equivalent circuits. The effect of the substitution on the conductivity properties of the BSTF system shows positive enhancement. An increase of the conductivity is detected from the order of 10^{-9} to 10^{-7} ($S.cm^{-1}$) as the amount of the substitution increases. The total conductivity also increases with temperature from 10^{-9} to 10^{-8} ($S.cm^{-1}$); 10^{-8}

to 10^{-7} (S.cm^{-1}) for the compositions x = 0.2 and x = 0.4 respectively. And it increases from the order of 10^{-7} to ~ 10^{-8} (S.cm^{-1}) at compositions x ≥ 0.6.

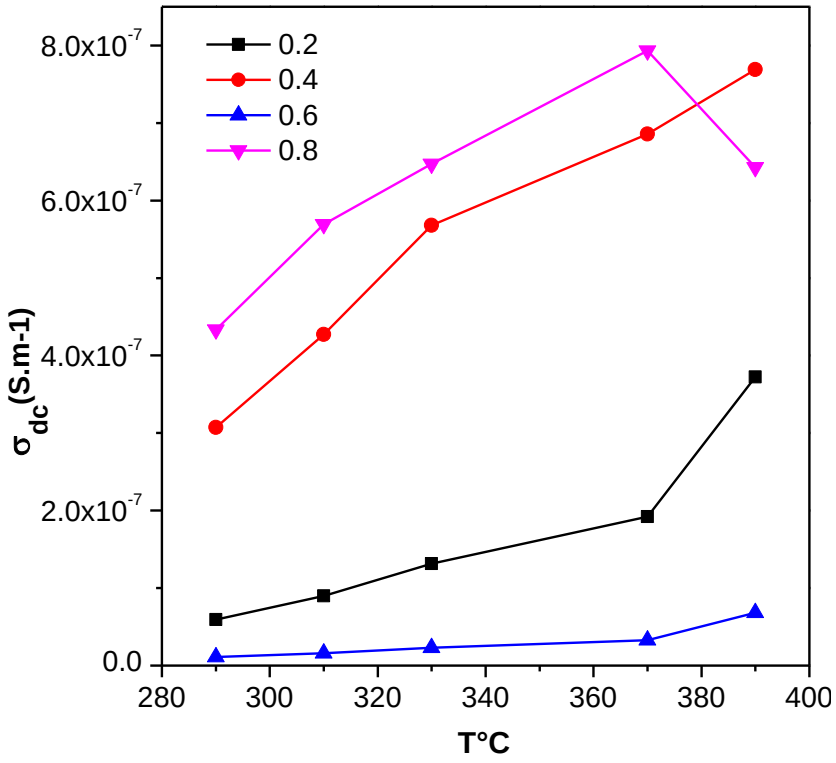

Fig-V.P3.5: Thermal variation of DC electrical conductivity of $Sr_{1-x}La_xTi_{1-x}Fe_xO_3$ (x = 0.25, 0.4, 0.6, and 0.8) compounds.

V.4.4. Conclusion

The effect of the composition on the dielectric and electric properties in the BSTF system for the compositions x = 0.2, 0.4, 0.6, and 0.8, was investigated and reported. The dielectric and electric properties were studied in a wide range of temperature (27 – 390°C) at various frequencies ranging from high, medium to low (1 Hz – 1 MHz).

The results obtained for the thermal variation of the dielectric constant and the effect of the composition show that the materials x = 0.2, 0.4, 0.6, and 0.8 show no anomalies and thus no ferroelectric – paraelectric transitions are present in the materials; additionally, at high content of Fe^{3+}, the interaction between $Fe^{3+} \leftrightarrow Fe^{3+}$ are inactive at all frequencies. The thermal variation of the dielectric permittivity ε'_r is shown to be very low for x = 0.2, 0.4, 0.6, and 0.8, however it

increases at temperatures above 200°C. The dielectric loss is observed to be low for x = 0.2, 0.4, and 0.8, and it increases in the temperature range (100 – 390°C) mainly at low frequencies. The highest dielectric loss ranging between 3 and 15 is observed for the composition x = 0.6, and it decreases with frequency.

At room temperature, the materials show low conductivity due incomplete semicircle, which is a sign of high resistant grain of the materials. However, the composition x = 0.6, shows good conductivity features at room temperature two semicircles of grain and grain boundaries. At high temperature, the compositions x = 0.2 and 0.4 shows two separate semicircles corresponding of the grain and the grain boundaries, the fitting of the Cole-Cole plots to RC-RQC connected in series represent the active region of the grain corresponding to RC and the grain boundaries with RQC. The fitting results show that the grain and grain boundaries resistances are of the order 10^6 Ω, both regions show high resistance which decreases as function of temperature, this is valid for x = 0.2, 0.4, and 0.8. The composition x = 0.6 shows a resistance in the order of 10^7 Ω which is higher in comparison with the resistance of the other compounds.

The calculated total conductivity of the materials shows an increase as function of temperature and composition. These results prove that the incorporation of Sr^{2+} and Fe^{3+} in $BaTiO_3$ has induced an increase in the conductivity from the order of 10^{-10} to 10^{-7} ($S.m^{-1}$) at 290°C. The highest value is observed for x = 0.8 at 370 with a conductivity in the order of 10^{-7} ($S.m^{-1}$). The

V.5. Chapter conclusion

The effect of the composition on the dielectric and electric properties was studied for the solid solution system $A_{1-x}A_xTi_{1-x}Fe_xO_3$ for (A = Ba, La, and Sr) with the substitution amount varies between $0 \leq x \leq 1$. The study was carried out in a wide range of temperature (27 – 390°C) and frequency (1 Hz – 1 MHz). The variable parameters in this study were mainly the composition at the A-site of the ABO_3 structure, and the content of the substituting elements.

In general the compositions of the three solid solutions BLTF, SLTF and BSTF showed low dielectric loss that decreases with frequency and increases at high temperatures (T > 200°C). It is observed that the substitution of the $BaTiO_3$ by either La^{3+}/Fe^{3+} or by Sr^{3+}/Fe^{3+} has suppressed the ferroelectric – paraelectric transitions known to appear at around 100 – 120°C in $BaTiO_3$. However, the incorporation of Fe^{3+} resulted in an enhancement of the dielectric constant and mainly at high content of Fe^{3+} at low frequencies. The solid solutions BLTF and SLTF have showed large peaks at content of Fe^{3+} exceeding $x \geq 0.3$ and $x \geq 0.4$ respectively. The peaks observed at high substitution amount of Fe^{3+} have greatly contributed to the dielectric permittivity values, the peaks were the result of the exchange interaction between $Fe^{3+} \leftrightarrow Fe^{3+}$ assigned to the mechanism of Maxwell-Wagner. The peaks are only effective at low frequencies <10 kHz. The highest value of the dielectric value was observed for the solid solution SLTF and is around for the composition x = 0.8 in the order of 9000 at 10 Hz, which decreases at higher frequencies. The BLTF solid solution shows dielectric constant around 8000 at 10 Hz which also decreases at higher frequencies. It is seen that the combination of Sr^{2+}/La^{3+} with high content of Fe^{3+} shows higher dielectric permittivity than Ba^{2+}/La^{3+} combination of element in the A site of ABO_3 structure. Moreover, BLTF in comparison with SLTF solid solution shows the lowest dielectric loss for all the compositions at all frequencies, while the SLTF shows a dielectric loss in the order of 100 at low frequencies for compositions $x \geq 0.6$. On the other hand the BSTF solid solution shows different results in comparison with BSTF and SLTF. BSTF solid solution thermal evolution of the dielectric constant shows no anomalies, which prove that no phase transition is occurring, and no spin orientation or the exchange interaction contribute are contributing to the dielectric constant $Fe^{3+} \leftrightarrow Fe^{3+}$. BSTF shows the lowest dielectric permittivity values in the order of 100 at low temperature and increases to reach a value between 400 and 500; the lowest dielectric loss is also observed in comparison with BLTF and SLTF

systems, the highest dielectric loss ranging between 3 and 15 is observed for the composition x = 0.6, and it decreases with frequency.

The Nyquist plots results at room temperatures and as function of the compositions shows that the SLTF shows promising conductive properties for all the studied compositions (x = 0.2, 0.4, 0.6, and 0.8), whereas the BSTF and BLTF samples show high resistive grains at room temperature, however, an exception for the composition = 0.6 is observed and shows good conductivity features. At high temperature the resistivity of the materials in general decreases, BSTF and SLTF solid solutions shows a resistance of the grain and the grain boundaries of the same order, however, the BLTF system shows higher resistive grain at compositions $x \leq 0.6$, above which the grain and the grain boundaries are of the same order.

The comparison of the calculated conductivities shows that at high temperatures, the total conductivity can be presented in the follow order SLTF (x = 0.8) > BLTF (x = 0.6) > BSTF (x = 0.8), for values in the order of 10^{-5} ($S.m^{-1}$), 10^{-6} ($S.m^{-1}$) and 10^{-7} ($S.m^{-1}$) respectively.

V.6. References

[1] K.C. Kao, Dielectric Phenomena in Solids, Dielectr. Phenom. Solids. (2004) 1–581. https://doi.org/10.1016/B978-0-12-396561-5.X5010-5.

[2] Z. Zhao, V. Buscaglia, M. Viviani, M.T. Buscaglia, L. Mitoseriu, A. Testino, M. Nygren, M. Johnsson, P. Nanni, Grain-size effects on the ferroelectric behavior of dense nanocrystalline <span class, Phys. Rev. B. 70 (2004) 024107. https://doi.org/10.1103/PhysRevB.70.024107.

[3] M. Billah, M.M. Rahman, Investigation on the Correlation between Structural and Electrical Properties of Lanthanum Doped Barium Titanate Ceramics, Appl. Mech. Mater. 860 (2017) 99–104. https://doi.org/10.4028/WWW.SCIENTIFIC.NET/AMM.860.99.

[4] M.M.V. Petrović, J.D. Bobić, T. Ramoška, J. Banys, B.D. Stojanović, Electrical properties of lanthanum doped barium titanate ceramics, Mater. Charact. 62 (2011) 1000–1006. https://doi.org/10.1016/J.MATCHAR.2011.07.013.

[5] H. Chaabane, N. Abdelmoula, H. Khemakhem, A. Simon, D. Michau, M. Maglione, Dielectric and ferroelectric properties of lead-free Ba1−xLaxTi1−xFexO3 ceramics, Phys. Status Solidi. 208 (2011) 180–185. https://doi.org/10.1002/PSSA.201026083.

[6] S. Sahoo, S. Das, P.K. Mahapatra, R.N.P. Choudhary, Fabrication and characterization of LaFeO3-BaTiO3 electroceramics, Mater. Chem. Phys. 216 (2018) 158–169. https://doi.org/10.1016/j.matchemphys.2018.05.032.

[7] Y. Qiu, Y.S. Luo, Z.J. Zou, Z.M. Tian, S.L. Yuan, Y. Xi, L.Z. Huang, Size effect on magnetic and dielectric properties in nanocrystalline LaFeO3, J. Mater. Sci. Mater. Electron. 2013 252. 25 (2013) 760–764. https://doi.org/10.1007/S10854-013-1642-Z.

[8] O. Rosales-González, F. Sánchez-De Jesús, C.A. Cortés-Escobedo, A.M. Bolarín-Miró, Crystal structure and multiferroic behavior of perovskite YFeO3, Ceram. Int. 44 (2018) 15298–15303. https://doi.org/10.1016/J.CERAMINT.2018.05.175.

[9] R. Maity, A.P. Sakhya, A. Dutta, T.P. Sinha, Effect of Sm doping on the structural, morphological and dielectric properties of EuFeO3 ceramics, Solid State Sci. 91 (2019) 28–35. https://doi.org/10.1016/J.SOLIDSTATESCIENCES.2019.03.007.

[10] M. Nakhaei, D. Sanavi Khoshnoud, Influence of particle size and lattice distortion on magnetic and dielectric properties of NdFeO3 orthoferrite, Phys. B Condens. Matter. 553 (2019) 53–58. https://doi.org/10.1016/J.PHYSB.2018.10.032.

[11] A. Mitra, A.S. Mahapatra, A. Mallick, A. Shaw, M. Ghosh, P.K. Chakrabarti, Simultaneous enhancement of magnetic and ferroelectric properties of LaFeO3 by co-doping with Dy3+ and Ti4+, J. Alloys Compd. 726 (2017) 1195–1204. https://doi.org/10.1016/J.JALLCOM.2017.08.074.

[12] B. Pongthippitak, P. Wongtha, P. Reabroy, P. Kunsuwan, S. Thountom, Dielectric properties of SrTiO3 ceramics synthesis by hybrid method, J. Phys. Conf. Ser. 1144 (2018) 012162. https://doi.org/10.1088/1742-6596/1144/1/012162.

[13] P.K. Gogoi, D. Schmidt, Temperature-dependent dielectric function of bulk <span class, Phys. Rev. B. 93 (2016)

075204. https://doi.org/10.1103/PhysRevB.93.075204.

[14] S. Chen, L. Li, S. Yu, H. Zheng, Z. Sun, W. Luo, The effects of inequivalent La3+ introduction on the structure and dielectric properties of SrTiO3 ceramic at microwave range, Mater. Chem. Phys. 216 (2018) 339–344. https://doi.org/10.1016/J.MATCHEMPHYS.2018.06.019.

[15] B. Zhong, Z. Long, C. Yang, Y. Li, X. Wei, Colossal dielectric permittivity in co-doping SrTiO3 ceramics by Nb and Mg, Ceram. Int. 46 (2020) 20565–20569. https://doi.org/10.1016/J.CERAMINT.2020.05.174.

[16] J. Liu, Q. Liu, Z. Nie, S. Nie, D. Lu, P. Zhu, Dielectric relaxations in fine-grained SrTiO3 ceramics with Cu and Nb co-doping, Ceram. Int. 45 (2019) 10334–10341. https://doi.org/10.1016/J.CERAMINT.2019.02.089.

[17] L. Tong, D. Zhang, H. Wang, Q.J. Li, Y. Yu, Y.D. Li, S.G. Huang, Y.M. Guo, C.C. Wang, High-temperature dielectric properties of (Al, Nb) co-doped SrTiO3 ceramics, Mater. Lett. 180 (2016) 256–259. https://doi.org/10.1016/J.MATLET.2016.06.001.

[18] D. Triyono, C.A. Kafa, H. Laysandra, Effect of Sr-substitution on the structural and dielectric properties of LaFeO3 perovskite materials, Https://Doi.Org/10.1142/S2010135X18500364. 8 (2018). https://doi.org/10.1142/S2010135X18500364.

[19] M.A. Gabal, F. Al-Solami, Y.M. Al Angari, A. Awad, A.A. Al-Juaid, A. Saeed, Structural, magnetic, and electrical characterization of Sr-substituted LaFeO3 perovskite synthesized via sucrose auto-combustion route, J. Mater. Sci. Mater. Electron. 2020 314. 31 (2020) 3146–3158. https://doi.org/10.1007/S10854-020-02861-6.

[20] E. V. Tsipis, M. V. Patrakeev, V. V. Kharton, A.A. Yaremchenko, G.C. Mather, A.L. Shaula, I.A. Leonidov, V.L. Kozhevnikov, J.R. Frade, Transport properties and thermal expansion of Ti-substituted La1−xSrxFeO3−δ (x=0.5–0.7), Solid State Sci. 7 (2005) 355–365. https://doi.org/10.1016/J.SOLIDSTATESCIENCES.2005.01.001.

[21] D.R. Patil, S.A. Lokare, R.S. Devan, S.S. Chougule, C.M. Kanamadi, Y.D. Kolekar, B.K. Chougule, Studies on electrical and dielectric properties of Ba1−xSrxTiO3, Mater. Chem. Phys. 104 (2007) 254–257. https://doi.org/10.1016/J.MATCHEMPHYS.2007.02.027.

[22] F.D. Cortés-Vega, C. Montero-Tavera, J.M. Yañez-Limón, Influence of diluted Fe3+ doping on the physical properties of BaTiO3, J. Alloys Compd. 847 (2020) 156513. https://doi.org/10.1016/J.JALLCOM.2020.156513.

[23] H. Abdelkefi, H. Khemakhem, G. Vélu, J.C. Carru, R. Von Der Mühll, Dielectric properties and ferroelectric phase transitions in BaxSr1−xTiO3 solid solution, J. Alloys Compd. 399 (2005) 1–6. https://doi.org/10.1016/J.JALLCOM.2005.03.007.

[24] M. Arshad, H. Du, M.S. Javed, A. Maqsood, I. Ashraf, S. Hussain, W. Ma, H. Ran, Fabrication, structure, and frequency-dependent electrical and dielectric properties of Sr-doped BaTiO3 ceramics, Ceram. Int. 46 (2020) 2238–2246. https://doi.org/10.1016/J.CERAMINT.2019.09.208.

[25] V. Kharton, A. Kovalevsky, E. Tsipis, A. Viskup, E. Naumovich, J. Jurado, J. Frade, Mixed conductivity and stability of A-site-deficient Sr(Fe,Ti)O3–δ perovskites, J. Solid State Electrochem. 2002 71. 7 (2002) 30–36. https://doi.org/10.1007/S10008-002-0286-3.

[26] *,† Avner Rothschild, ‡ Wolfgang Menesklou, † and Harry L. Tuller, E. Ivers-Tiffée‡, Electronic Structure, Defect Chemistry, and Transport Properties of SrTi1-xFexO3-y Solid Solutions, Chem. Mater. 18 (2006) 3651–3659. https://doi.org/10.1021/CM052803X.

General conclusion

This work reports on the composition effect on the morphology, structural phase transitions and the physical properties of the ABO_3 perovskite type materials. The different properties studied in this work are optical, dielectric and electric properties. The chosen systems of the ABO_3 simple perovskite are in the general formulas: $A_{(1-x)}A'_xTi_{(1-x)}Fe_xO_{3-\delta}$ (A = Ba, Sr, or La) in a wide range of substitution with $0 \leq x \leq 1$ and $\delta \geq 0$.

The three solid solutions were synthesized by the conventional solid state reaction, with high temperature treatment to ensure the quality of the powder. High purity precursors were mixed in the appropriate amount to produce the final products studied in this work.

The structural and morphological investigations were carried out for BLTF, SLTF, and BSTF by means of the X-ray diffraction and scanning electron microscopy. The X-ray patterns were collected at room temperature and all the samples are confirmed to adopt the perovskite structure. As function of the composition, it is reported that the composition effect has induced several phase transitions in the BLTF, SLTF, and BSTF systems. The Rietveld refinement results showed two main phase transitions, Tetragonal → Cubic → orthorhombic for the BLTF systems; one phase transition from cubic to orthorhombic, and same with BSTF system that shows a transition from tetragonal to cubic. The conducted studies allowed understanding the preferred structure in terms of structural parameters, it is concluded that the structure volume is more affected by the A-O interatomic distance, thus the size of the A-site element; on the other hand the symmetry is more related to the B-O interatomic distance, this the size of the B-site element.

The particles size is seen to decrease in some compositions BLTF, x = 0.25; SLTF, x = $0.2 \leq x \leq 0.4$; and BSTF, $0.2 \leq x \leq 0.4$. The morphology is observed to be dependent to the composition in the A site as Sr^{2+}/La^{3+} and Ba^{2+}/Sr^{2+} in the A-site can form flat plat like grains for a substitution amount ranging between $0.2 \leq x \leq 0.4$ and $0.2 \leq x \leq 0.6$ respectively. The substitution of $BaTiO_3$ in all the cases is found to form porous structures in comparison with the large agglomerated grains of $BaTiO_3$. However, the smaller grains size was obtained for BLTF at x = 0.25, while the larger particles were observed for BLTF at x = 0.8

The composition effect on the optical properties has showed good enhancement of light absorption in the three systems BLTF, SLTF and BSTF. The enhancement of the red shift

observed in the UV-Visible light absorption is associated with a shrink of the optical band gap as an effect of the composition. The study of dependency of optical properties to the structural parameters show that the band gap evolution is more related to the interatomic distances, larger values of <Ba/Sr-O> and <Ti/Fe-O> reflects lower values of the band gap. This was observed for the case of BSTF and SLTF solid solutions, for the solid solution BLTF, lower values of the optical band gap were observed for large <Ti/Fe-O> distances. Moreover, the insertion of new element in the ABO_3 creates new energy level and reduces which induce an upward and downward shift of the valence band and conduction band edges respectively.

The dielectric studied carried out by the complex impedance spectroscopy has shown that the composition affected the dielectric properties of the materials. The composition has induced a reduction of the dielectric permittivity and low dielectric losses were observed. Moreover, the incorporation of Sr, Ba, and La suppresses the ferroelectric-paraelectric transitions. The incorporation of Fe^{3+} is proven to enhance the dielectric constant at high content and the peaks are assigned to the mechanism of Maxwell-Wagner. The conductivity is seen to increase with temperature for all the compositions can be presented in the follow order SLTF (x = 0.8) > BLTF (x = 0.6) > BSTF (x = 0.8), for values in the order of 10^{-5} ($S.m^{-1}$), 10^{-6} ($S.m^{-1}$) and 10^{-7} ($S.m^{-1}$) respectively. The SLTF shows promising conductivity features at room temperature in comparison with BLTF and BSTF.

LIST OF PUBLICATIONS

PUBLISHED ARTICLES

1. **El bachraoui F.**, Chchiyai Z, Tamraoui Y, EL Mousaoui H., Alami J, And Manoun B. (2021) "Investigation of optical and magnetic properties of new perovskite materials: $Ba_{0.3}La_{0.7}Ti_{0.3}Fe_{0.7}O_3$ and $Ba_{0.1}La_{0.9}Ti_{0.1}Fe_{0.9}O_3$". Journal of Rare Earths. https://doi.org/10.1016/j.jre.2021.05.008
2. **El bachraoui F.**, Chchiyai Z, Tamraoui Y, Alami J, And Manoun B. (2021) "Effect of the composition and structure on the optical properties of $Ba_{1-x}La_xTi_{1-x}Fe_xO_3$ ($0 \leq x \leq 1$) solid solution: Correlation study using Rietveld refinement". J. Materials Characterization 175: 111058. https://doi.org/10.1016/j.matchar.2021.111058.
3. **El Bachraoui F.**, Tamraoui Y, Louihi S, et al (2021) Unusual superparamagnetic behavior in bulk $Ba_{0.198}La_{0.784}Ti_{0.096}Fe_{0.8}O_{3-\delta}$. Mater Res Bull 137:111187. https://doi.org/10.1016/j.materresbull.2020.111187.
4. Chchiyai Z., **El Bachraoui F.**, Tamraoui Y., El Mehdi Haily, Bih L., Lahmar A., Alami J. and manoun B. (2021) "Design, structural evolution, optical, electrical and dielectric properties of perovskite ceramics $Ba_{1-x}Bi_xTi_{1-x}Fe_xO_3$ ($0 \leq x \leq 0.8$)". Journal of Materials Chemistry and Physics. https://doi.org/10.1016/j.matchemphys.2021.125096
5. Tamraoui Y, **El Bachraoui F.**, Mirinioui F, et al (2021), "On the structural phase transitions and optical properties of $Sr_2Sr_{1-x}Ca_xTeO_6$ ($0 \leq x \leq 1$) ceramics". J Electroceramics 1–13. https://doi.org/10.1007/s10832-021-00237-8
6. Chchiyai Z, **El Bachraoui F**, Tamraoui Y, et al (2021) Synthesis, structural refinement and physical properties of novel perovskite ceramics $Ba_{1-x}Bi_xTi_{1-x}Mn_xO_3$ (x=0.3 and 0.4). Mater Chem Phys 262:. https://doi.org/10.1016/j.matchemphys.2021.124302.
7. Moutataouia M., **El bachraoui F.**, Tamraoui Y., et al (2021) Crystal structure and optical properties of a new nickel magnesium diphosphate. J Mol Struct 1223: https://doi.org/10.1016/j.molstruc.2020.128983.
8. Chchiyai Z., **El Bachraoui F.**, Tamraoui Y., et al (2020) Design and characterization of novel manganite perovskites $Ba_{1-x}Bi_xTi_{1-x}Mn_xO_3$ ($0 \leq x \leq 0.2$). Ceram Int. https://doi.org/10.1016/j.ceramint.2020.07.169.
9. El Hachmi A, **El Bachraoui F**, Louihi S, et al (2020) Structural, Magnetic and Optical Properties Study of Tellurium-Based Perovskites: $Sr_{3-x}Pb_xFe_2TeO_9$ ($0 \leq x \leq 2.25$).J Inorg Organomet Polym Mater 30: https://doi.org/10.1007/s10904-020-01446-4.

PUBLISHED ABSTRACT

1. **El Bachraoui F.**, Tamraoui Y, Louhi S, et al (2019) Structure design of novel $Ba_{3-x}Sr_xTeO_6$ double perovskites and the effect of temperature and composition on structure stability . Acta Crystallogr Sect A Found Adv 75:e282–e282. https://doi.org/10.1107/s205327331909274x.

SUBMITTED ARTICLES

1. **El Bachraoui F.**, Chchiyai Z., Tamraoui Y., Alami J., and Manoun B. "The design of high visible light absorption co-doped $SrTiO_3$ materials: structural and optical and dielectric properties investigation of the news synthesized perovskite series $Sr_{1-x}La_xTi_{1-x}Fe_xO_3$ $0 \leq x \leq 1$". Submitted to Journal of Ceramics International (2021).

2. **El Bachraoui F.**, Chchiyai Z., Tamraoui Y., Louihi S., EL Mousaoui H., Alami J., And Manoun B. "Reports on the ferromagnetic, optical and dielectric properties of $LaFeO_3$: (1-x) $SrTiO_3$ – $xLaFeO_3$ solid solution. Submitted to Journal of Materials Letters (2021).
3. **El Bachraoui F.**, Tamraoui Y., Louihi S., Alami J., and Manoun B. "Substitution inducing uniform structural variation enhanced optical and electrical properties: Oxygen-deficient perovskites case study $Ba_{1-x}Sr_xTi_{1-x}Fe_xO_{3-\delta}$ ($0 \leq x \leq 1$)". Submitted to Journal of Results in Physics (2021).
4. Tamraoui Y., **El Bachraoui F.**, Mirinioui F., Lazor P., Wenge Yang, Alami J., and Manoun B. "Structural Phase transitions mapping, self-doping mechanism, structural stability at high temperature and substitution effect on the optical properties of the double perovskites $Ba_{3-x}Sr_xTeO_6$: X-ray diffraction, High temperature Raman spectroscopy and UV-vis spectroscopy studies". Submitted to Optical Materials (2021)
5. Said louihi; Youssef TAMRAOUI; zakaria chchiyai; Anis Elaoud; **Fatima El Bachraoui**; Peter Lazor; Bouchaib Manoun "Molecular Structure, Vibrational Study and Optical Properties of New Lacunar Apatites; Series of $Na_{1-x}K_xPb_2CaCd(PO_4)_3$, with $0 \leq x \leq 1$". Submitted to Arabian Journal for Science and Engineering (2019).

TALKS AND AWARDS

AWARDS

BEST ORAL PRESENTATION TITLED:
Co-doped batio3 structural and physical properties investigation: rietveld refinement, uv-visible spectroscopy and impedance spectroscopy studies, 08/07/2021 – 8th edition of journée des doctorants, FST Settat-Morocco.

BEST ORAL PRESENTATION TITLED:
Understand the effect of the composition on the physical properties and the stability of ABO3-type perovskite structure:
Case study $Ba_{1-x}La_xTi_{1-x}FexO_3$, 28/06/2021 – 1st edition, Doctoral day at um6p, Benguerir-Morocco.

AWARD OF THE TOP TEN PROJECT:
The award of the best top ten projects at the Arabic Innovation Academy Entrepreneurship Program. The project has won a grant from HAG venture - accelerator program for startups to assist the continuity of the project. 7th - 20th january, 2020 - Qatar, Doha.

BEST ORAL PRESENTATION TITLED:
Investigation of the co-substitution effect on the structural, optical and magnetic properties of the ABO_3-type perovskite solid solution $Ba_{1-x}La_xTi_{1-x}Fe_xO_3$ ($0<x<1$). 02/05/2019 – 7th edition of journée des doctorants, FST Settat-Morocco.

BEST POSTER PRESENTATION TITLED:
Crystal structure, optical and electronic conductivity investigations of the new series of $Ba_{1-x}La_xTi_{1-x}Fe_xO_3$ ($0\leq x\leq 1$) perovskite oxides as cathode for sofcs. (12-13)/11/2018 Phoresnet-phospahte days at um6p, Benguerir-Morocco.

GRANTS

HAG venture - accelerator program for startup and Entrepreneurship, 1st April – 31st July

TALKS

ORAL PRESENTATIONS:

1. **Fatima EL BACHRAOUI**, Z. Chchiyai1, Y. Tamraoui, L. Bih, J. alami, and B. Manoun - Co-doped batio3 structural and physical properties investigation: rietveld refinement, uv-visible spectroscopy and impedance spectroscopy studies – 8th edition of journée des doctorants, JULY 8th, 2021 - FST Settat-Morocco
2. **Fatima EL BACHRAOUI**, Z. Chchiyai1, Y. Tamraoui, J. alami, and B. Manoun - Understand the effect of the composition on the physical properties and the stability of ABO3-type perovskite structure: Case study $Ba_{1-x}La_xTi_{1-x}FexO_3$, 28/06/2021 – 1st edition, Doctoral day at um6p, Benguerir-Morocco.
3. **Fatima EL BACHRAOUI**, Y. Tamraoui, Z. Chchiyai, S. Louihi, J. Alami and B.manoun - Analysis of substitution and temperature effect on structure stability and optical properties of novel $Ba_{3-x}Sr_xTeO_6$ double perovskites; The Second International Symposium on Energy & Materials (EM-II), March 24-26th, 2021, University Mohammed VI Polytechnic, Benguerir, Morocco.
4. **Fatima EL BACHRAOUI**, Z. Chchiyai, Y. Tamraoui, S. Louihi, J. Alami and B.manoun; Design of novel perovskites oxides materials for energy conversion and storage devices; Amatstic ii – advanced materials studies towards inverted classrooms – (16-18)/10/2019 – UM6P - Benguerir, Morocco.

5. **Fatima EL BACHRAOUI**, Z. Chchiyai, Y. Tamraoui, S. Louihi, H.el moussaoui, J. Alami and B.manoun; Co-substitution effect on tuning the physical properties in the new perovskite series $Ba_{1-x}La_xTi_{1-x}Fe_xO_3$ ($0\leq x\leq 1$): structural, magnetic and optical investigations toward high performance materials; International symposium nanomaterials: Microstructure and properties: tramp19 – (7-9)/10/2019 – Marrakech, Morocco.
6. **Fatima EL BACHRAOUI**, Y. Tamraoui, S. Louihi, I. Saadoune, J. Alami, P. Lazor and B. Manoun; Structure design of novel $Ba_{3-x}Sr_xTeO_6$ double perovskites: effect of temperature and composition on structure stability and optical properties investigations toward high performance materials, euro-mediterranean on materials and renewable energies emcmre, (17-20/06/2019) – Marrakech, Morocco.
7. **Fatima EL BACHRAOUI**, Y. Tamraoui, S. Louihi, I. Saadoune, J. Alami, P. Lazor and B. Manoun; structure stability and optical properties investigations in the novel designed $Ba_{3-x}Sr_xTeO_6$ double perovskites: toward high performance energy conversion materials; 1ère édition doctoriale – cerne2d 2019 sous le thème water, energy and environment nexus – (12-14/06/2019) – ENSET, Rabat, Morocco.
8. **Fatima EL BACHRAOUI**, Y. Tamraoui, S. Louihi, I. Saadoune, J. Alami and B. Manoun; Investigation of the co-substitution effect on the structural, optical and magnetic properties of the ABO_3-type perovskite solid solution $Ba_{1-x}La_xTi_{1-x}Fe_xO_3$ ($0\leq x\leq 1$). Journée doctorant - 7ième edition 02/05/2019 – FST Settat - UH1, Morocco.
9. **Fatima EL BACHRAOUI**, Y. Tamraoui, S. Louihi, I. Saadoune, J. Alami and B. Manoun; Crystal structure and optical investigations of the new series of $Ba_{1-x}La_xTi_{1-x}Fe_xO_3$ ($0\leq x\leq 1$) perovskite oxides, amatstic – advanced materials studies towards inverted classrooms workshop – (12-14)/12/2018 – UM6P - Benguerir, Morocco.
10. **Fatima EL BACHRAOUI**, B.manoun, Y.tamraoui, J.alami; $Ba_{1-x}La_xTi_{1-x}Fe_xO_3$ ($0\leq x\leq 1$) perovskite-type materials for solid oxide fuel cell cathodes: crystal structure, optical and electronic conductivity investigations, the second international conference on materials and environmental science (Icmes2018) – (26-27)/11/2018 – Saidia, Morocco.
11. **Fatima EL BACHRAOUI**, B.manoun, Y.tamraoui, J.alami; Crystallography and properties of perovskites, journée doctorant – 05/04/2018 – FST Settat - UH1, Morocco.

POSTERS:

1. **Fatima EL BACHRAOUI**, Z. Chchiyai, Y. Tamraoui, S. Louihi, J. Alami and B.manoun; Optical properties tenability and phase transitions induced by the substitution in the double perovskites series $Sr_2Sr_{1-x}Ca_xTeO_6$ ($0\leq x\leq 1$) amatstic – advanced materials studies towards inverted classrooms intenationale workshop– november (17-19)/12/2019 – University Koblenz-Landau (UKL) – Germany.
2. **Fatima EL BACHRAOUI**, Y. Tamraoui, S. Louihi, I. Saadoune, J. Alami and B. Manoun; Crystal structure and optical investigations of the new series of $Ba_{1-x}La_xTi_{1-x}Fe_xO_3$ ($0\leq x\leq 1$) perovskite oxides Amatstic – advanced materials studies towards inverted classrooms workshop – (19-21)/11/2018 – UM6P - Benguerir, Morocco.
3. **Fatima EL BACHRAOUI**, Y. Tamraoui, S. Louihi, I. Saadoune, J. Alami and B. Manoun; Crystal structure, optical and electronic conductivity investigations of the new series of $Ba_{1-x}La_xTi_{1-x}Fe_xO_3$ ($0\leq x\leq 1$) perovskite oxides as cathode for sofcs phoresnet – phosphate days 2018, international conference for research on phosphates and derivatives (12-13)/11/2018 – UM6P - Benguerir, Morocco.
4. Zakaria Chchiyai, Youssef Tamraoui. **Fatima EL BACHRAOUI**, Manoun Bouchaib; Synthesis, structural and optical studies of ba1-xbixti1-xfexo3 ($0\leq x\leq 0.8$) perovskite-type ceramics by x-ray diffraction and uv-vis spectroscopy journée doctorant - 7ième edition 02/05/2019 – FST Settat - UH1, Morocco.
5. **Fatima EL BACHRAOUI**, Y. Tamraoui, J. Alami and B. Manoun; Synthesis, Crystal structure and uv-vis measurement of the new perovskite $Ba_{0.5}La_{0.5}Ti_{0.5}Fe_{0.5}O_3$. 2eme edition de la conference internationale : materiaux fonctionnels et leurs applications technologiques, 13/10/2017 – ENS -uh2 - Casablanca, Morocco.